NON-EQUILIBRIUM QUANTUM DYNAMICS: INTERPLAY OF DISORDER, INTERACTIONS AND CONFINEMENT

Maximilian Schulz

A Thesis Submitted for the Degree of PhD
at the
University of St Andrews

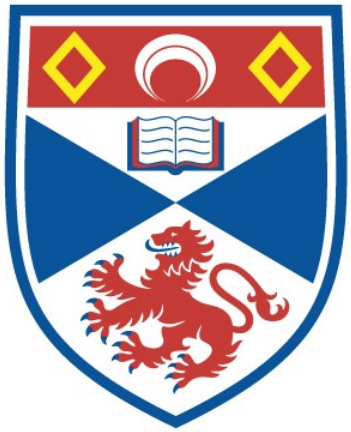

2019

Non-equilibrium quantum dynamics: interplay of disorder, interactions and confinement

Maximilian Schulz

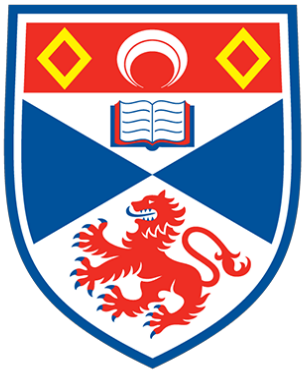

University of
St Andrews

This thesis is submitted in partial fulfilment for the degree of

Doctor of Philosophy (PhD)

at the University of St Andrews

September 2018

Candidate's declaration

I, Maximilian Schulz, do hereby certify that this thesis, submitted for the degree of PhD, which is approximately 42,263 words in length, has been written by me, and that it is the record of work carried out by me, or principally by myself in collaboration with others as acknowledged, and that it has not been submitted in any previous application for any degree.

I was admitted as a research student at the University of St Andrews in August 2014.

I received funding from an organisation or institution and have acknowledged the funder(s) in the full text of my thesis.

Date 01.02.2019 Signature of candidate

Supervisor's declaration

I hereby certify that the candidate has fulfilled the conditions of the Resolution and Regulations appropriate for the degree of PhD in the University of St Andrews and that the candidate is qualified to submit this thesis in application for that degree.

Date 01.02.2019 Signature of supervisor

Permission for publication

In submitting this thesis to the University of St Andrews we understand that we are giving permission for it to be made available for use in accordance with the regulations of the University Library for the time being in force, subject to any copyright vested in the work not being affected thereby. We also understand, unless exempt by an award of an embargo as requested below, that the title and the abstract will be published, and that a copy of the work may be made and supplied to any bona fide library or research worker, that this thesis will be electronically accessible for personal or research use and that the library has the right to migrate this thesis into new electronic forms as required to ensure continued access to the thesis.

I, Maximilian Schulz, have obtained, or am in the process of obtaining, third-party copyright permissions that are required or have requested the appropriate embargo below.

The following is an agreed request by candidate and supervisor regarding the publication of this thesis:

Printed copy

No embargo on print copy.

Electronic copy

No embargo on electronic copy.

Date 01.02.2019 Signature of candidate

Date 01.02.2019 Signature of supervisor

Underpinning Research Data or Digital Outputs

Candidate's declaration

I, Maximilian Schulz, understand that by declaring that I have original research data or digital outputs, I should make every effort in meeting the University's and research funders' requirements on the deposit and sharing of research data or research digital outputs.

Date 01.02.2019 Signature of candidate

Permission for publication of underpinning research data or digital outputs

We understand that for any original research data or digital outputs which are deposited, we are giving permission for them to be made available for use in accordance with the requirements of the University and research funders, for the time being in force.

We also understand that the title and the description will be published, and that the underpinning research data or digital outputs will be electronically accessible for use in accordance with the license specified at the point of deposit, unless exempt by award of an embargo as requested below.

The following is an agreed request by candidate and supervisor regarding the publication of underpinning research data or digital outputs:

No embargo on underpinning research data or digital outputs.

Date 01.02.2019 Signature of candidate

Date 01.02.2019 Signature of supervisor

NON-EQUILIBRIUM QUANTUM DYNAMICS: INTERPLAY OF DISORDER, INTERACTIONS AND CONFINEMENT

MAXIMILIAN SCHULZ

University of
St Andrews

FOUNDED
1413

A Thesis submitted for the degree of Doctor of Philosophy
January 2019

Maximilian Schulz: *Non-equilibrium quantum dynamics: interplay of disorder, interactions and confinement*, January 2019

In loving memory of my mother.
1954 – 2018

ABSTRACT

The study of collective behaviour in many-body systems often explores fundamentally new ideas absent from the mere constituents of such a system. A paradigmatic model for these studies is the spin-1/2 XXZ chain and its fermionic equivalent. This thesis can be broadly divided into the study of two fundamental aspects of this model. Firstly, we discuss localisation phenomena in one dimensional lattices as often experimentally realised in cold atom systems. Secondly, we investigate how disorder and symmetry influence heat transport in spin chains.

More specifically, in the first part we consider a system of non-interacting fermions in one dimension subject to a single-particle potential consisting of a strong optical lattice, a harmonic trap, and uncorrelated on-site disorder. We investigate a global inhomogeneous quantum quench and present numerical and analytical results for static and dynamical properties. We show that the approach to the non-thermal equilibrium state is extremely slow and that it implies a sensitivity to disorder parametrically stronger than that expected from Anderson localisation.

We also consider the above system in a strong non-uniform electric field. In the non-interacting case, due to Wannier-Stark localisation, the single-particle wave functions are exponentially localised without quenched disorder. We show that this system remains localised in the presence of nearest-neighbour interactions and exhibits physics analogous to models of conventional many-body localisation.

The second part explores the hydrodynamics of the disordered XYZ spin chain. Using time-evolving block decimation on open chains of up to 400 spins attached to thermal baths, we probe the energy transport of this system. Our principal findings are as follows. For weak disorder there is a stable diffusive region that persists up to a critical disorder strength that depends on the XY anisotropy. Then, for disorder strengths above this critical value energy transport becomes increasingly subdiffusive.

PUBLICATIONS

- **Maximilian Schulz**, Chris Hooley, Roderich Moessner. "*Slow relaxation and sensitivity to disorder in trapped lattice fermions after a quench*". Phys. Rev. A **94**, 063643 (2016).
- **Maximilian Schulz**, Scott R. Taylor, Chris Hooley, Antonello Scardicchio. "*Energy transport in a disordered spin chain with broken U(1) symmetry: diffusion, subdiffusion, and many-body localization*". Phys. Rev. B **98**, 180201(R) (2018).
- **Maximilian Schulz**, Chris Hooley, Roderich Moessner, Frank Pollmann. "*Stark Many-Body Localization*". Phys. Rev. Lett. **122**, 040606 (2019).

ACKNOWLEDGEMENTS

I would like to express my gratitude to my supervisor Chris Hooley. In the past eight years, from the first time we met in Fresher's week 2010, to the very end of this work, he has been a source of inspiration and a role model of what it means to be a scientist. Rarely will you find a person that is willing to spend an entire Sunday teaching a curious undergraduate student quantum field theory, whilst also ditching all evening plans in order to turn up with two bottles of wine at an end-of-year party. Through excellent teaching, infinite patience and a great sense of humour, he has guided me through my eight years of study and made me the physicist that I am today. He is the very definition of a teacher and also a good friend. Thank you!

I would equally like to express my gratitude to my second supervisor Roderich Moessner. I am grateful to have been so warmly received at his institute, a place that continues to be an inspiration of how science should be organised. The open and intellectual atmosphere that I experienced during my time in Dresden has been invaluable; my exceptional coworkers and very generous funding for travel allowed me to begin my transition from a student to a scientist. I remain impressed that despite his busy schedule, he was always available to answer any questions and worries. His physical intuition and view of the bigger picture, together with precise questioning, have guided and helped me through even the most difficult times during this PhD. It is with a heavy heart that I will be leaving Dresden, and I hope to be welcomed in the future as a guest.

I would further like to thank my collaborators. Firstly I want to mention Scott Taylor, with whom I shared the workload of one project and who has become a dear friend over the past few years. Working with him was a pleasure, not only because of his mathematical ability, but also his unique sense of humour. Additionally I would like to thank my senior collaborators, Frank Pollmann and Antonello Scardicchio. Frank is a true inspiration, especially when it comes to numerics. His 'toy codes' made even the most complicated algorithm look simple. Antonello has been a great guidance in my first project going beyond the familiar surroundings of my PhD. I am looking forward to working with him in the coming year.

I would not be where I am today without the unique experience and outstanding education I received from the University of St Andrews. My four years as an undergraduate and the first year of my PhD have enriched me with memories and skills that I will cherish for the rest of my life. None of this would have been possible without the support from CM-CDT and EPSRC (UK) under grants

EP/G03673X/1 and EP/L015110/1. Also, special thanks to Christine Edwards and Julie Massey who were always there when I needed assistance. Additionally, I must extend warm thanks to all of the physics department in St Andrews and the CM-CDT especially who made the PhD more interesting and enjoyable. I would especially like to thank Andy Mackenzie, Jonathan Keeling, Natalia Korolkova, Donatella Cassetari, Bruce Sinclair, Friedrich König, Ryan Amiri, Ian Van Beek, Matthew Trott, Stephanie Matern and many others!

Equally, I would like to thank the people in Dresden, the Visitors program, the Administration department and IT department at the Max-Planck Institute for the Physics of Complex Systems who made my time hugely enjoyable and memorable. Thank you also to my fellow physicists, many of whom have become friends. In particular I would like to thank Jan Behrends, Talía Lezama Mergold Love, Cécile Repellin, Omar Adame Arana, Matthias Gohlke, Johannes Hauschild, Peter Fulde, Jens Bardarsson, Younes Javanmard, Jorge Rehn and many more. A special thanks also to my great two office mates Daniel Vorberg and Heiko Burau. It has been a pleasure and you have both taught me a great deal.

I would also like to express my gratitude to the people that have provided comments on the manuscript: Chris Hooley, Roderich Moessner, Pamela Sandford, Norbert Schulz, Jesse Scherwitz, Heiko Burau, Matthias Gohlke, Scott Taylor and Jack Bartlett.

I am very grateful for the great friends for life that I have made during my time in St Andrews, in particular Charles Field, Jake Ramsden and Felix Kress. It was an incredible experience and there is so much more to come. All of this would not have been possible without you. I am equally grateful to my 'old' friends from Cologne. It is an incredible source of comfort to have such long-lasting and loyal friends. Even six years abroad did not change our friendship in the slightest. I would also like to thank the many non-physics friends that shaped my time in Dresden and that made my return to Germany such a great experience. It was truly outstanding to live another student life with you guys, and I know for sure that this is not the end. Especially I would like to thank my wonderful flatmates David Siebrasse, Jack Bartlett and Hella Van Lengerich.

Finally, I would like to address a special thanks to those closest to my heart. Pam, the summer day we met in St Andrews turned out to be one of the luckiest days of my life. You have been an incredible support during these past months and I cannot wait to share all my dreams and happiness with you. The final word goes to my family and in particular my parents. I am more grateful to you two than words can describe. Your unconditional support, guidance and love are the dearest treasures and have made me the person I am today. Unsere Seilschaft waren wir drei und das wird auch immer so bleiben. Mama, du weißt, dass diese Arbeit dir gewidmet ist und ich

bin dankbar, dass ich dir dies noch erzählen konnte. Du wirst mich immer begleiten. Danke für alles.

CONTENTS

LIST OF FIGURES

Part I

INTRODUCTION & BACKGROUND

1

INTRODUCTION

Much of human expectation about their surroundings is in fact based on some natural intuition about *equilibrium thermodynamics*. If for instance our morning tea is too hot, we can be sure that if we wait long enough, it will reach the correct temperature. If we wait too long, it might cool to room temperature and no longer be appetising to us. At the same time we know that it will not continue to cool and eventually turn into a block of ice! Had we prepared a frozen tea in the freezer (for scientific reasons only, of course!), we know that it would also eventually reach room temperature, even more interestingly change its constitution from a solid to a liquid. It seems that time very naturally flows in one direction, and the final state of systems (such as our cup of tea) is only dependent (in this example) on one variable; the all-important room temperature.

The physicist's task begins when trying to understand the workings of this phenomenon. The main challenge of any attempt to study the thermodynamics of a macroscopic object such as our cup of tea lies in the difficulty of dealing with an enormously large number of constituent particles ($\sim 10^{23}$). Following each of them around is certainly impossible, so we resort to statistics instead of tracking trajectories of every particle. We shall focus on very few average quantities which we believe characterise the equilibrium properties of the system. Formally we take a substance, subject to a number of constraints (e. g. volume V) with some conserved quantities (e. g. number of particles N, internal energy U) and let it evolve in time. The assumption is that the system will seek to maximise its *entropy* S, a concept originally introduced by Rudolf Clausius in his analysis of the Carnot cycle[1], in order to reach its thermodynamic equilibrium. In this case the system, said to be in a certain *macrostate*, can indeed be described by very few thermodynamic quantities. The study of the phenomenological relations between those, e. g. that $dU = PdV - TdS$ (here P denotes pressure and T stands for temperature), defines the field of equilibrium thermodynamics and is the knowledge of the late 19th century. The limit to this theory is the macroscopic world, yet the power of these discoveries helped to reshape the face of the Earth in a way never seen before. The invention of the steam engine and the beginning of the industrial revolution are deeply linked to the un-

1 The Carnot cycle is a thermodynamic cycle introduced by Sadi Carnot in 1824 which puts an upper bound on the efficiency of any classical engine that converts heat into mechanical work. Clausius set out to reconcile some inconsistencies of this work in 1850.

derlying theory, and to this day thermodynamics remains one of the most successful and complete physical theories.

The next step taken was to connect and derive these thermodynamic quantities from microscopic descriptions of the system, a field that is known as *statistical mechanics*. But as already mentioned, it is not practical nor even theoretically possible to know at a microscopic level the simultaneous position and velocities of the $\sim 10^{23}$ particles involved. For this reason, one introduces the concept of a statistical *ensemble*, a large collection of virtual independent copies of the system in various states. It is thus a probability distribution over all states of the system. Statistical equilibrium denotes the point not at which the particles have stopped moving, but at which the ensembles do not change any longer. For an isolated system, there are three equilibrium ensembles which are usually considered. The simplest is called the *microcanonical ensemble* and it describes a system with a precisely fixed energy and particle number. It is motivated by the *equal a priori probability postulate*, which states that in the microcanonical ensemble, the probability for every possible microscopic configuration, often called a microstate, is the same. It takes the value of $p_i = 1/W$, where W is the total number of available microstates. The famous Boltzmann equation, $S = k_B \log W$, carved on Boltzmann's gravestone in Vienna, relates the thermodynamic property entropy with the microscopic description of the system. The logarithm naturally arises, as for two combined systems, the number of possible microstates should multiply, while the entropy as an extensive quantity should be additive, $S = k_B \log W_1 W_2 = S_1 + S_2$.

Relaxing the strict constraint of fixed energy, one could imagine the system to be in thermal equilibrium (constant, but no net flow of energy) with a much larger heat bath at a precise temperature T. In this case, the system is best described by the *canonical ensemble*. It contains microstates with different total energy (as it can exchange energy with the bath) whose probability to occur is weighted by the temperature of the bath. It can be derived to take the form $p_i = \frac{1}{Z} \exp(-\frac{e_i}{k_B T})$, where the normalisation factor $Z = \sum_i \exp(-\frac{e_i}{k_B T})$ is called the partition function. The e_i describe the energy of an individual microstate and it is very common to take $\frac{1}{k_B T} \equiv \beta$. The probability distribution is used to again connect to macroscopic quantities. The average internal energy U for example may be written as $U = \langle E \rangle = -\frac{\partial}{\partial \beta} \ln Z$, where the angle brackets denote an ensemble average. Finally, the *grand canonical ensemble* describes a system in thermal and chemical (exchanging particles) equilibrium with a thermodynamic reservoir. In the case of many particles, the thermodynamic limit, all ensembles tend to give identical answers, proven in the theorem of equivalence of ensembles. It is then a mathematical convenience which ensemble is used.

Closely linked to the postulate of equal a priori probabilities and often invoked to bridge the gap between the irreversibility of thermodynamics and the reversibility of the underlying microscopics is the so-called *ergodic hypothesis* formulated by Boltzmann. An ergodic system is a system that evolves over time to explore all accessible microstates with the same particle number and total energy. According to the ergodic hypothesis, typical systems studied in statistical mechanics are ergodic in this sense. An ensemble average and a time average, defined by $\overline{\Theta} \equiv \frac{1}{\tau}\int_0^\tau dt\Theta(t)$, should be equal if $\tau \to \infty$,

$$\langle\Theta\rangle = \overline{\Theta} \quad \text{for} \quad \tau \to \infty. \tag{1.1}$$

Here Θ denotes some macroscopic quantity we are interested in. Systems violating the ergodic hypothesis are quickly found; masses connected by springs (with linear spring constant) would be one, for instance. If we excite a single mode of motion, then this mode will not equipartition its initial energy between all available modes, even after very long times. In this case, the natural arrow of time seems to be absent as we can easily track the system back to its initial state, as opposed to the example of the cup of tea. These systems, whose equations of motion we can integrate and hence exactly solve were for a long time believed to be isolated points in parameter space, such that a small non-linear perturbation to their Hamiltonian would make them ergodic. However, in one of the first numerical simulations in physics, the now celebrated Fermi-Pasta-Ulam problem [62], on one of the first ever computers in Los Alamos, this assumption was shown not to be true. Anharmonic perturbations to the spring constants did not make the system ergodic. This prompted intense research on the roots of classical thermalisation, culminating in many important discoveries such as the KAM theorem, solitons and chaos at the root of thermalisation (see [147]). It was later shown that there is an energy threshold below which chaotic behaviour is not produced and therefore the system cannot be described by the usual statistical physics. The simulation of Fermi, Pasta and Ulam (by chance) happened to be below this threshold.

In that sense we have concluded our journey through classical thermodynamics and statistical physics. The knowledge presented suffices to predict and explain almost all of the known physical phenomena at the time. In fact, a well known historical fact is that Max Planck was advised by a physics professor from Munich not to continue with physics as all fundamental laws had been discovered [111]. One of the major remaining challenges was to explain the spectrum of black-body radiation: thermal electromagnetic radiation within or surrounding a body in thermodynamic equilibrium with its environment, or emitted by a black body (an opaque and non-reflective body). Its spectrum and intensity only depends on the body's temperature. Luckily Max Planck ignored his professor's advice and solved the

above problem in 1901 in the formalism now known as Planck's law of black-body radiation. Planck had to assume that energy was actually quantised in units of $\hbar\omega$, an idea Albert Einstein later built on to explain the photoelectric effect, thus establishing the field of *quantum mechanics*. These important theoretical advances eventually resulted in the superseding of classical electromagnetism by quantum electrodynamics. In relation to the previous discussion, it led to the development of quantum probability distributions, called Fermi-Dirac statistics and Bose-Einstein statistics, each applicable to a different class of particles, fermions and bosons.

It is at this point that this thesis aims to explain the necessary background theory in more detail. Ch. 2 gives a basic introduction to the necessary tools in quantum mechanics, while Ch. 3 uses these ideas to revisit the question of thermalisation in a quantum mechanics context. The final chapter of this introductory part (Ch. 4) introduces the necessary numerical tools needed to investigate ideas around quantum thermalisation (or failures thereof): in a way, the modern kind of Fermi-Pasta-Ulam research.

The second part of this thesis investigates quantum quenches in cold atom systems. Cold atom systems constitute one of the most suitable candidates to experimentally verify quantum mechanical predictions and quenches are a convenient tool to bring systems out of equilibrium. In Ch. 5, we investigate a particular instance of inhomogeneous quantum quench in a non-interacting system. Following that, in Ch. 6 we build on some of the insights gained to show quantum non-ergodicity in a disorder-free idealised interacting system. We conclude this part by bringing ideas from the previous two chapters together giving an overview of some unpublished results in Ch. 7.

The last part is concerned with the investigation of special notions of quantum ergodicity, hydrodynamics and the role of underlying symmetries. We show in Ch. 8 that energy transport in quantum systems can be anomalous in the ergodic phase and show the influence of symmetry breaking therein.

2 QUANTUM THEORY

2.1 BASIC QUANTUM THEORY

Max Planck's work on black-body radiation started a veritable revolution in theoretical physics. In the decades that followed, many well established concepts of classical mechanics had to be rejected. A few of the most important and intuitive to human experience of the macroscopic world are that particles and fields possess well defined dynamic variables (position and momentum) at all times and in the case of point-like particles follow predictable trajectories. Luckily not everything had to be rejected, as for example symmetries and resulting conservation laws remain valid concepts. And similar to classical mechanics, quantum mechanics too can be formulated in many different ways. Whether one chooses a wave-description (Schrödinger) based on the Hamilton formalism, or a path integral approach based on the Lagrangian formalism, or the matrix mechanics approach (Heisenberg) to describe nature and more specifically a quantum system does not matter. They are all formally equivalent [128].

2.1.1 *Quantum states*

In quantum mechanics, the state of a closed system can be described by a *state vector* $|\psi\rangle$ in a complex vector space called Hilbert space $\mathcal{H}$ of dimension $\mathcal{D}$. It can be represented by a $\mathcal{D} \times 1$-matrix. Normalisation ensures that the inner product gives $\langle\psi|\psi\rangle = 1$, where $\langle\psi| = (|\psi\rangle)^\dagger$ is the Hermitian conjugate of the state. With n particles each having $d > 1$ internal states (local Hilbert space dimension), the dimension $\mathcal{D} = d^n$ of the whole Hilbert space can be enormous if again $n \sim 10^{23}$. It is a truly colossal number. We will discuss the implications of this later (see Ch. 4).

In order to cope with it, we may again introduce statistics using the concept of a *density matrix* or density operator $\hat{\rho}$. The density matrix is an extension to the state vector $|\psi\rangle$, because similar to classical statistical mechanics, it represents an ensemble of possible pure quantum states. We denote the set of possible pure states by $\{|\psi_i\rangle\}$ and the associated probabilities in the ensemble as p_i. The density matrix is then given by the outer product

$$\hat{\rho} = \sum_i p_i \, |\psi_i\rangle \, \langle\psi_i| \,, \tag{2.1}$$

and can be represented by a $\mathcal{D} \times \mathcal{D}$ matrix. Operators (matrices) that can act on states (vectors) are conventionally denoted by a hat, but

for the rest of this thesis, we will omit this notation, unless explicitly useful in distinguishing them from other quantities. The probabilistic description of the ensemble follows the usual statistical rules. The probabilities have to sum up to one, $\sum_i p_i = 1$. Importantly, they have nothing to do with the quantum mechanical uncertainty of measurement prediction. This statistical element is the reason why density matrices that have a non-zero probability p_i for more than one pure state $|\psi_i\rangle$ are called a statistical mixture (of pure states). For a spin-$\frac{1}{2}$ system, where the only possible states are $|\uparrow\rangle$ and $|\downarrow\rangle$, the pure-state density matrix for $|\psi_1\rangle = |\uparrow\rangle$ would be,

$$\rho = \begin{pmatrix} 1 & 0 \\ 0 & 0 \end{pmatrix}, \tag{2.2}$$

while a completely mixed state could be represented via the matrix,

$$\rho = \frac{1}{2}\begin{pmatrix} 1 & 0 \\ 0 & 1 \end{pmatrix}. \tag{2.3}$$

Some useful properties of the density matrix are *positivity*, $\langle\phi|\,\rho\,|\phi\rangle \geq 0 \quad \forall\,|\phi\rangle \in \mathcal{H}$, *hermiticity*, $\rho^\dagger = \rho$, and a *unit trace*, $\mathrm{Tr}\,(\rho) = 1$.

2.1.2 *Time evolution and observables*

If we can describe our system by a state vector, then we can time-evolve this quantum state in the Schrödinger picture by integrating the well known Schrödinger equation,

$$i\hbar\frac{\partial}{\partial t}\,|\psi\rangle = H\,|\psi\rangle\,, \tag{2.4}$$

where i is the imaginary unit, $\hbar$ the reduced Planck constant and H an operator acting on $\mathcal{H}$, representing the total energy of the system. It is commonly referred to as the Hamiltionian of the system. This yields the solution,

$$|\psi(t)\rangle = U(t, t_0)\,|\psi(t_0)\rangle\,, \tag{2.5}$$

where the evolution is determined by the time-evolution operator,

$$U(t, t_0) = e^{-\frac{i}{\hbar}H(t-t_0)}. \tag{2.6}$$

In the density formalism, the Schrödinger equation takes the form of the von Neumann equation, which is the corresponding equation for density matrices,

$$\frac{\partial\rho}{\partial t} = -\frac{i}{\hbar}\,[H, \rho]\,. \tag{2.7}$$

Here $[.,.]$ denotes the *commutator*. It is a key concept in physics, and in quantum mechanics defined as $[A, B] \equiv AB - BA$. If $[A, B] = 0$, then

A and B are said to commute. Commuting operators share a common set of eigenfunctions and as such, observables represented by such operators can have definite values at the same time. As mentioned above, one of the striking differences between classical and quantum mechanics is that the dynamical variables position and momentum indeed cannot do that. As a consequence, the commutator of the position operator $\hat{x}$ and momentum operator $\hat{p}$ is nonzero, $[\hat{x}, \hat{p}] = i\hbar$ (see [128] for details). In this way, one may regard classical mechanics as a limit of quantum mechanics where $\hbar \to 0$.

2.1.3 *Expectation values*

It is now evident that quantum theory is inherently probabilistic. Importantly, this has nothing to do with a lack of knowledge, but is the most common interpretation of the quantum mechanical state or wave function as a probability wave. This interpretation, commonly known as the Copenhagen interpretation of quantum mechanics, states in essence that quantum systems do not have definite properties prior to measurement. Quantum mechanics can only predict the probabilities that a measurement will give a certain result. The act of measurement will affect the system and reduce the state of the system to one of the eigenstates of the operator representing the measurement; the probability of this state then becomes one. In this interpretation, it is clear that commuting operators can take definite values in the same measurement, while non-commuting operators cannot. In this sense, the quantum mechanical wave function is not a physical object, but a mere mathematical construction. Physical observables are calculated as expectation values, the weighted average of all the possible outcomes of a measurement. In the case of a pure state $|\psi\rangle$, the expectation value of an observable Θ is denoted by

$$\langle\Theta\rangle = \langle\psi|\Theta|\psi\rangle\,. \tag{2.8}$$

The angle brackets are reminiscent of the ensemble average introduced above, but for pure states this is not the case. Even in the full knowledge of the state, we can only calculate an expectation value. This changes when we use the density matrix formalism, in which case the expectation value of an observable is defined as

$$\langle\Theta\rangle = \mathrm{Tr}\,(\Theta\rho)\,. \tag{2.9}$$

Lastly, one may also use this tool in order to evaluate how a certain property of a system is correlated either in space or in time within the system. If for example we are interested in the correlation of Θ at the spatial points $x = 0$ and $x = i$, then we evaluate the expression

$$C(0,i) = \langle\psi|\Theta_i\Theta_0|\psi\rangle - \langle\psi|\Theta_i|\psi\rangle\,\langle\psi|\Theta_0|\psi\rangle\,. \tag{2.10}$$

It is often called the two-point correlation function and may equally be used for correlations in time.

2.1.4 *Composite and open quantum systems*

In addition to the study of statistical mixtures of pure states, one may also be interested in composite and consequently even open systems. In the former case, this means that the Hilbert space of the combined system may be partitioned such that degrees of freedom in the basis of choice only have support in one respective partition. In the latter case, part of the system takes the role of a bath, and thus the dynamics of the system as a whole is no longer unitary and information preserving.

The connection of respective Hilbert spaces $\mathcal{H}_A$ and $\mathcal{H}_B$ is given by a basic postulate of quantum mechanics [128]. It states that the composite Hilbert space of the combined system is given by the *tensor product* of the Hilbert spaces of the single quantum systems, i. e. by $\mathcal{H}_{AB} = \mathcal{H}_A \otimes \mathcal{H}_B$. From this follows that if we join two quantum systems A and B with respective bases $\{|i\rangle_A\}$ and $\{|j\rangle_B\}$, then every possible state $|\psi\rangle_{AB}$ of the composite system can be represented as,

$$|\psi\rangle_{AB} = \sum_{i,j} d_{ij} |i\rangle_A \otimes |j\rangle_B \,, \tag{2.11}$$

where d_{ij} are complex expansion coefficients in $\mathcal{H}_{AB}$. We may extend this to N composite systems in a straightforward manner by adding any additional subsystem via another tensor product. Similarly one can obtain the same result for density matrices where the composite density matrix for a N-body quantum system would take the form (here assuming $d = 2$, and that σ^i are Pauli matrices - see (2.17))

$$\rho = \sum_{\{i_1,i_2,\ldots,i_N\}} c_{i_1,i_2,\ldots,i_N} \bigotimes_{j=1}^{N} \sigma_j^i. \tag{2.12}$$

A key theoretical tool to describe specific parts of the full system is the *partial trace*. For a quantum system that consists of two smaller subsystems A and B, the density matrix for e. g. subsystem B can be extracted by tracing out subsystem A from the full density matrix ρ^{AB} via,

$$\rho^B = \mathrm{Tr_A}(\rho^{AB}). \tag{2.13}$$

So far we have only been concerned with closed systems. However, in open/dissipative systems, the time-evolution (2.7) is no longer valid. To include e. g. pumping from or losses to an environment, we require non-unitary time evolution. In the case of Markovian dynamics (i. e. the bath has no memory, which is a highly non-trivial assumption in many cases), then the most general dynamics is given by the Lindblad equation,

$$\frac{\mathrm{d}\rho}{\mathrm{d}t} = -i[H,\rho] + \sum_{\mu} \left(L_\mu \rho L_\mu^\dagger - \frac{1}{2} L_\mu L_\mu^\dagger \rho - \frac{1}{2} \rho L_\mu L_\mu^\dagger \right) \equiv \mathcal{L}\,[\rho]\,, \tag{2.14}$$

where the first term on the right-hand side is the usual unitary Hamiltonian time-evolution (2.7) and the second term contains the information regarding the bath. $\mathcal{L}$ is often called the Liouville operator or Liouvillian. The L_μ denote the relevant pumping/dissipation operators, sometimes called Lindblad or jump operators.

2.2 EFFECTIVE MODELS FOR STRONGLY CORRELATED SYSTEMS

In the area of condensed matter physics, one is ultimately interested in real materials. The Hamiltonians of such systems are far too complicated to ever solve or in many cases even to write down. As such, theorists have to resort to effective models for strongly correlated materials in order to capture the essential relevant physical phenomena. In this section, we briefly introduce three of the most well known effective models in condensed matter physics.

2.2.1 *Hubbard model*

The Hubbard model is considered the paradigm for strongly correlated electron systems. It allows us to describe a variety of strongly correlated phenomena. For instance, in two dimensions it represents the simplest model that captures the transition from a metallic to a Mott-insulating ground state at half filling [161]. In addition, it is also believed to contain important aspects of high-T_c superconductors in the presence of hole doping. 'Solving' the Hubbard model in more than one dimension is sometimes considered the holy grail of condensed matter physics. The Hamiltonian of the one-band Hubbard model takes the form

$$H = -t \sum_{\langle i,j\rangle,\sigma} \left(c^\dagger_{i\sigma} c_{j\sigma} + c^\dagger_{j\sigma} c_{i\sigma} \right) + U \sum_i c^\dagger_{i\uparrow} c_{i\uparrow} c^\dagger_{i\downarrow} c_{i\downarrow}, \tag{2.15}$$

where t denotes the strength of the nearest-neighbour hopping and U the on-site Coulomb repulsion. The operators $c^\dagger_{i\sigma}$ and $c_{i\sigma}$ create or annihilate fermions (obeying Fermi-Dirac statistics as mentioned above) with spin (a quantum mechanical magnetic property that in the simplest case, spin-1/2, can take two values) $\sigma \in \{\uparrow, \downarrow\}$ respectively on site i. They obey the fermionic anti-commutation relations $\{c^\dagger_{i\sigma}, c^\dagger_{j\sigma'}\} = 0$, $\{c_{i\sigma}, c_{j\sigma'}\} = 0$, and $\{c_{i\sigma}, c^\dagger_{j\sigma}\} = \delta_{ij}\delta_{\sigma\sigma'}$, where $\{A, B\} \equiv AB + BA$ denotes the *anti-commutator*, as opposed to the commutator introduced in Sec. 2.1.2. The angle brackets denote the summation over all possible nearest-neighbour pairs. For small U, the system shows metallic behaviour as the electrons are relatively free to move around. With increasing interaction strength U/t, less electrons are able to doubly occupy a lattice site and thus their mobility is suppressed. At half filling, i. e. exactly one electron per site, the system transitions into a Mott-insulating state for $U > U_c$, where each site

contains a single localised electron. One may observe d-wave superconductivity at finite hole doping [162].

2.2.2 *Heisenberg model*

The Heisenberg model is another very famous example of an effective model for strongly correlated systems. It is often used to describe the magnetic properties of materials [84]. In fact it can be derived from the Hubbard model in the limit of very large U at half filling. In this case, we may describe the low energy physics of the Hubbard model by replacing the fermionic fields with a dynamic spin degree of freedom (local Hilbert space dimension of $d = 2$) on every site. The Heisenberg Hamiltonian is then obtained by expanding (2.15) in powers of t/U and keeping only the leading term,

$$H = J \sum_{\langle i,j \rangle} \mathbf{S}_i \cdot \mathbf{S}_j, \tag{2.16}$$

where $\mathbf{S}_i$ represents a vector of spin-1/2 operators on site i and $J \sim t^2/U$. The components of $\mathbf{S}_i$ are $\{S^x, S^y, S^z\}$, where $S^\alpha = \frac{\hbar}{2}\sigma^\alpha$ and $\alpha \in \{x, y, z\}$. In the case in which the prefactors of the individual components $\{J_x, J_y, J_z\}$ vary, i. e. $J \neq J_x \neq J_y \neq J_z$, (2.16) is referred to as the XYZ model (or XXZ in the case of $J_x = J_y$). The σ's denote 2×2 Hermitian matrices that go under the name of Pauli matrices and take the form,

$$\sigma^x = \begin{pmatrix} 0 & 1 \\ 1 & 0 \end{pmatrix}, \quad \sigma^y = \begin{pmatrix} 0 & -i \\ i & 0 \end{pmatrix}, \quad \sigma^z = \begin{pmatrix} 1 & 0 \\ 0 & -1 \end{pmatrix}. \tag{2.17}$$

In fact, together with the identity, for convenience denoted by $\sigma^0 = \mathbb{1}$, they are an orthonormal basis of operators spanning the vector space of 2×2 Hermitian matrices. Quantum mechanical 2-level systems live in this vector space. Indeed the eigenvalues of σ^z are $\{+1, -1\}$ and are associated with the magnetic spin pointing either up or down along the z-axis, i. e. $\{\uparrow, \downarrow\}$. In the case of $J > 0$, the ground state of this seemingly simple model favours anti-parallel spin order on neighbouring sites, which we call anti-ferromagnetic order. This is easily pictured as we would, in order to minimise (2.16), try to maximise the anti-alignment of the $\mathbf{S}$ vectors. Yet, the model can also exhibit a variety of different phases depending on the underlying lattice geometry. For example, some lattices induce frustration which strongly suppresses magnetic order, leading to exotic phases of matter such as spin liquids [16]. Furthermore the Heisenberg model is an extremely important toy model for theoretical concepts such as topology [75, 76], quantum magnetism [16, 151] and many-body localisation [127]. It is also under much better numerical control than its fermionic counterparts (see Ch. 4).

2.2.3 *Transverse field Ising model*

An even simpler spin model can be formulated: the transverse field Ising model. Its Hamiltonian reads:

$$H = -\sum_i \sigma_i^z \sigma_{i+1}^z + g\sigma_i^x, \tag{2.18}$$

where σ^z and σ^x are the Pauli matrices introduced above and $g > 0$. This simple model has a quantum phase transition (the quantum counterpart of the transition from ice to water in the example given in the introduction) at $g = g_c = 1$. It has two very simple limits. For $g = 0$, the ground state is a simple ferromagnet in which all the spins are aligned. This state is actually two-fold degenerate, as all the spins could point up or down. On the other hand, at $g \to \infty$ the ground state is a state in which all spins are polarised by the transverse field in the x-direction. For intermediate values of g, the ground states are more complicated, however a special property introduced later makes them numerically very tractable (except at $g = g_c$). We introduce this model at this point, as it serves very well to introduce concepts of entanglement and symmetry. It also remains to this day the only one in which many-body localisation is rigorously proven (see Ch. 3).

2.2.4 *Local Hamiltonians*

In the above examples, we presented some of the most widely used effective models in condensed matter physics. They all share the property of being local Hamiltonians. This means that their Hamiltonian, defined on a lattice $\mathcal{L}$, can be decomposed as

$$H = \sum_{i \in \mathcal{L}} h_i, \tag{2.19}$$

where h_i are few-body operators that only include terms that are from a local subcluster of sites around i. While not attempting to present a mathematically rigid definition of locality, one may typically take h_i to consist consist of operators located on nearest- or next-nearest-neighbour sites on $\mathcal{L}$. Often we are interested in the ground-state (corresponding to the lowest eigenvalue of the Hamiltonian H) and low-energy physics of Hamiltonians such as (2.15) and (2.16), so one may wonder how the locality of the Hamiltonian is reflected in the ground-state properties of such a system. A straightforward measure for locality was introduced above. Two-point correlation functions are expected to decay with increasing lattice distance due to the local nature of the interaction terms. This can indeed be observed in the corresponding ground-state wave functions. In gapped models, which are characterised by a finite energy gap separating the ground state and the first excited state in the thermodynamic limit, these correlation functions show a so-called 'clustering of correlations'. This means

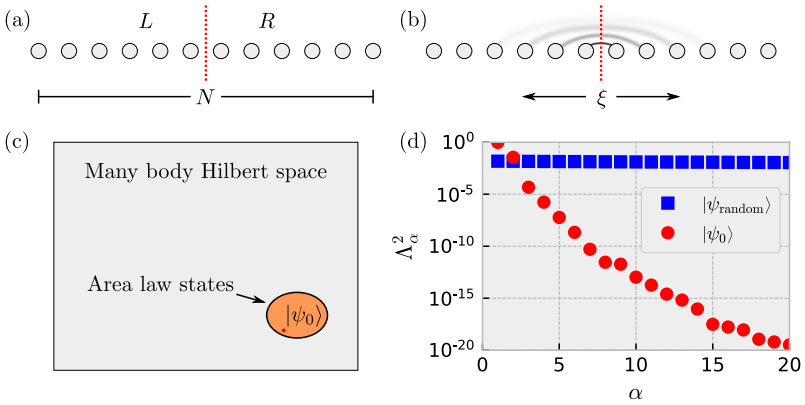

Figure 2.1: a) We split a system of N sites into two parts, namely L and R. b) In one-dimensional, local and gapped systems, it is known that correlations decrease exponentially. Significant quantum fluctuations should therefore occur only on short length scales. c) Area law states occupy a very small fraction of the entire Hilbert space. d) We compare the largest Schmidt values of the ground state of the transverse field Ising model ($g = 1.5$) and a state selected from a random position in the spectrum for a system consisting of $N = 16$ spins. The index α labels different Schmidt values. Adapted from [82].

that correlations decay exponentially with increasing lattice distance. As usual with exponential decay, one can define a length-scale ξ, on which correlations effectively drop to zero [81], often called the correlation length. In contrast, correlations behave differently in models without an energy gap (so-called gapless or critical models). These models still exhibit a decay of correlation functions with increasing lattice distance, however, this is no longer an exponential but rather an algebraic decay [58].

2.3 ENTANGLEMENT

Entanglement is a fundamental property only found in quantum systems. There is no classical analogue. It implies that different degrees of freedom of the system in question cannot be described independently. Its roots date back to Schrödinger [170, 171] and the famous 'Gedankenexperiment' by Einstein, Podolski and Rosen [57]. In the following we review some important implications of this peculiar quantum property, mostly following the reviews [58, 59].

Hand in hand with the notion of entanglement comes the concept of entanglement entropy. The most often used entropy is the so-called von Neumann entropy. It measures the degree to which a subsection or part of a system is entangled with the remainder. Given a pure

state ($|\rho^{\mathcal{BC}}\rangle = |\psi\rangle\langle\psi|$), the von Neumann entropy of subsystem $\mathcal{C}$ is defined as

$$S(\rho^{\mathcal{C}}) = -\mathrm{Tr}\left(\rho^{\mathcal{C}} \log\left(\rho^{\mathcal{C}}\right)\right), \tag{2.20}$$

where $\rho^{\mathcal{C}}$ is the reduced density matrix of subsystem $\mathcal{C}$ obtained by tracing out its complement $\mathcal{B}$. Thus if there is entanglement between the regions $\mathcal{C}$ and $\mathcal{B}$, then the entropy $S(\rho^{\mathcal{C}})$ is nonzero and positive. It is an interesting feature of this quantum entropy that it does not signify an objective lack of information about the system as a whole. In classical concepts of entropy this is not the case. In classical statistical mechanics, entropy is representative of the amount of information lacking to identify the microstate of a system compatible with its macrostate. We simply cannot know the exact state of all water molecules in a cup of tea (see example in the introduction, Ch. 1) that are compatible with the macrostate, namely room temperature.

In quantum mechanics however non-zero entropies may arise even without an objective lack of knowledge. Let us envisage some lattice system $\mathcal{L}$. At zero temperature, when the system is in its non-degenerate (pure) ground state $|\psi_0\rangle$, it has a vanishing von Neumann entropy as a whole ($S(\rho) = 0$), but a subregion within it generally does not. If for simplicity we take $\mathcal{L}$ to be one-dimensional, then a useful subregion could be a bipartition of $\mathcal{L}$ into two halves (see Fig. 2.1a). The reduced density matrix for the left part, ρ^L (ρ^R for the right part), is mixed, which leads to $S(\rho^L) > 0$ (and $S(\rho^R) > 0$). Thus, even at zero temperature, when the system is in its (non-degenerate) ground state alone, we may encounter non-zero entropy (for a subsystem). It does not originate from ignorance about the microstate of the whole system, but rather from entanglement; the fact that parts of the systems are not independent from each other. If they are, the two parts are said to form a product state.

Let the Hilbert space of our system $\mathcal{L}$ be split into two parts according to our chosen bipartition, i. e. $\mathcal{H} = \mathcal{H}_L \otimes \mathcal{H}_R$. Can we bring any wave function of a (pure) state $|\psi\rangle \in \mathcal{H}$ into a form which displays this intricate coupling? The answer is yes, and the method for that is the so-called *Schmidt decomposition*. For any pure $|\psi\rangle \in \mathcal{H}$ it works as follows. Let us write $|\psi\rangle$ as

$$|\psi\rangle = \sum_{m,n} A_{m,n} |\psi_m^L\rangle \otimes |\psi_n^R\rangle, \tag{2.21}$$

where the $\{|\psi_m^L\rangle\}$ and $\{|\psi_n^R\rangle\}$ are orthonormal bases in the two Hilbert spaces $\mathcal{H}_L$ and $\mathcal{H}_R$. In practice, we have reshaped the state vector $|\psi\rangle$ with the number of entries equal to the size of the whole Hilbert space into a matrix with the same number of entries. The rectangular ($\mathcal{D}_L \times \mathcal{D}_R$) matrix A (as the sizes of $\mathcal{H}_L$ and $\mathcal{H}_R$ may differ) can

be brought into diagonal form using a singular value decomposition (SVD):

$$A_{m,n} = \sum_{\alpha} U_{m,\alpha} S_{\alpha,\alpha} V^{\dagger}_{\alpha,n}, \tag{2.22}$$

where the matrix $\mathbf{U}$ has orthonormal columns and dimension $(\mathcal{D}_L \times \min(\mathcal{D}_L, \mathcal{D}_R))$, the matrix $\mathbf{S}$ is diagonal and has a respective dimension $(\min(\mathcal{D}_L, \mathcal{D}_R)) \times \min(\mathcal{D}_L, \mathcal{D}_R))$ with non-zero entries Λ_α along the diagonal and $\mathbf{V}^\dagger$ has orthonormal rows and consequently a dimension of $(\min(\mathcal{D}_L, \mathcal{D}_R)) \times \mathcal{D}_R)$. This gives, combining $\mathbf{U}$ and $\mathbf{V}^\dagger$ with the respective basis,

$$|\psi\rangle = \sum_{\alpha} \Lambda_\alpha |\Phi^L_\alpha\rangle \otimes |\Phi^R_\alpha\rangle, \tag{2.23}$$

where $\Lambda_\alpha = S_{\alpha,\alpha}$ are called the Schmidt values. This form features a single sum that is limited by the smaller of the two Hilbert spaces and new orthonormal sets in both parts. If $|\psi\rangle$ is normalised, then $\sum_\alpha \Lambda^2_\alpha = 1$. A simple calculation shows that the Schmidt states $|\Phi_\alpha\rangle$ are the eigenfunctions of the reduced density matrix of the respective bipartition. The Schmidt values are the square roots of the corresponding eigenvalues, i. e. $\rho^L = \sum_\alpha \Lambda^2_\alpha |\Phi^L_\alpha\rangle \langle\Phi^L_\alpha|$ and similar for ρ^R. This actually means that ρ^L and ρ^R have the same non-zero eigenvalues. We can thus express the entanglement entropy (2.20) in terms of the Schmidt values Λ_α:

$$S(\rho^L) = -\mathrm{Tr}\left(\rho^L \log(\rho^L)\right) = -\sum_{\alpha} \Lambda^2_\alpha \log\left(\Lambda^2_\alpha\right) = S(\rho^R). \tag{2.24}$$

In the form of (2.24), entanglement is much easier to understand. If there is only one single nonzero Schmidt value $\Lambda = 1$, then there is no entanglement between the two parts and $S = 0$, i. e. a product state. On the contrary, if all Schmidt values have equal weight, then the subsystem is maximally entangled with its complement. It becomes thus clear that abstractly speaking the fewer Schmidt values we have, the less information we need to aptly describe the quantum state in question.

2.3.1 *Area law*

An interesting question that follows therefore is how entanglement scales with the size $|\mathcal{C}|$ of some subregion $\mathcal{C}$. This will in fact be crucial with regards to the applicability of tensor networks introduced in Ch. 4. Naively, one would expect that the entanglement entropy is an extensive quantity that grows with the volume of $\mathcal{C}$, i. e.

$$S(\rho^{\mathcal{C}}) = \mathcal{O}(|\mathcal{C}|), \tag{2.25}$$

and this is indeed true for most states of the Hilbert space. In this case, we speak of a *volume law* scaling of the entanglement. In fact it has

been shown that a state selected from a random position in the spectrum $|\psi_{\text{random}}\rangle$ has an entanglement entropy close to the maximum value of $S \approx |\mathcal{C}| \log(d)$ [58]. This maximum is quite intuitive as the smallest possible subsystem clearly must have a maximum entanglement entropy of $S = \log(d)$. In one spatial dimension, this means that the entanglement entropy grows linearly as a function of the position of the bipartition (except for some boundary effects).

This intuition is however not correct for a small subset of states in the low-energy sector of gapped, local Hamiltonians (see Sec. 2.2.4), in particular the ground state itself. They instead follow a so-called *area law*, which indicates that the entanglement instead scales with the area of the subsystem's boundary

$$S(\rho^{\mathcal{C}}) = \mathcal{O}(\partial|\mathcal{C}|). \tag{2.26}$$

This has been rigorously proved for gapped systems with a unique ground state in one spatial dimension [80]. There is further a lot of evidence that the area law also holds for higher dimensional gapped systems [42, 59, 144].

In one spatial dimension for an N-site subsystem this has the consequence that $S(N)$ is approximately constant for $N > \xi$, where ξ is the correlation length of the system (see Sec. 2.2.4). Intuitively a gapped ground state should only contain fluctuations within the correlation length ξ and hence only degrees of freedom near the bipartition can become entangled (see Fig. 2.1b). Ground states are in this respect special and can be found in a very small corner of the entire Hilbert space (see Fig. 2.1c). As shown in Fig. 2.1d, an only slightly entangled state can be extremely useful in compressing quantum states, as most of the information is contained in very few Schmidt states. In that case, we show a comparison of the ground state and state selected from a random position in the spectrum of the transverse field Ising model (2.18). For $\epsilon > 0$ we can define some finite χ_{max}, which for area law states is *independent* of system size such that

$$\left\| |\psi\rangle - \sum_{\alpha=1}^{\chi_{\text{max}}} \Lambda_\alpha |\Phi_\alpha^L\rangle \otimes |\Phi_\alpha^R\rangle \right\| < \epsilon, \tag{2.27}$$

where $\sum_{\alpha=1}^{\chi_{\text{max}}} \Lambda_\alpha |\Phi_\alpha^L\rangle \otimes |\Phi_\alpha^R\rangle = |\psi_{\text{truncated}}\rangle$. This particular property makes area law states ideally suited to a matrix-product state representation which will be introduced in Sec. 4.2.

2.4 SYMMETRY

As opposed to the entanglement studied in the previous section, an intrinsically quantum mechanical object, symmetry is already a central concept in classical physics. In broad terms, a symmetry is a transformation of a physical system under which the action of that system

remains unchanged. One of the most beautiful theorems of mathematical physics was proven by Emmy Noether in 1915 and often goes simply by the name of Noether's theorem [129]. Technical points aside, it states that if a system has a continuous symmetry property, then there are corresponding quantities whose values are conserved in time, or in other words, unchanged. This is one of the most fundamental insights into nature. A continuous symmetry that is obviously present in the Hamiltonians presented above is time-translational invariance. This is easy to see as they do not depend on time at all, hence $H(t) = H(t_0) = H$. The resulting conserved quantity is a single scalar that usually goes by the name energy. Many Hamiltonians in condensed matter physics are time-translation invariant and as such energy conservation is one of the most important features of them. There is an interesting class of systems, called Floquet systems, whose Hamiltonians are only periodic in time, i. e. $H(t+T) = H(t)$, which have recently received much attention in the condensed matter community due to their possibility of forming 'time crystals' [206], where energy is merely conserved modulo $2\pi/T$, but this discussion would certainly be beyond the scope of this thesis.

Beyond their fascinating insight into the fundamental working of nature, symmetries and their associated conserved quantities also provide a huge technical advantage in the study of systems. The reason for this is that conserved quantities vastly limit the amount of accessible phase space (space of dynamic variable such as position and momentum), or in the case of quantum mechanics, Hilbert space. An example is the XXZ Hamiltonian, a special case of (2.16), which is $U(1)$ symmetric. The group $U(1)$, sometimes referred to as the circle group, may be represented by all complex numbers with absolute value 1, or in other words the unit circle in the complex plane. We can parametrise the circle group by the angle θ, such that all group members can be written as $z = e^{i\theta} = \cos(\theta) + i\sin(\theta)$. For the model in question, we note that the Hamiltonian in fact remains unchanged if we rotate all the spins by some angle θ around a common axis (z-axis in the case of the XXZ model). The corresponding conserved quantity is the total magnetisation, $M = \sum_i S_i^z$. Conservation entails that H and M must share a common set of eigenfunctions and thus commute. Indeed, one can easily show that $[M, H] = 0$. This in turn means that the Hamiltonian cannot have matrix elements between states that correspond to different values of M, in other words that differ by the quantum number M. This splits the Hamiltonian matrix into a number of smaller blocks corresponding to a distinct quantum number. One can then diagonalise the often much smaller block in order to obtain the eigenstates and eigenvalues of the Hamiltonian and thus the solution to the problem. In Ch. 4 we will further discuss why this may still be a very challenging task.

3

QUANTUM THERMALISATION AND ITS FAILURES

As described in the introduction (Ch. 1), the question of thermalisation is one of the most profound mysteries of nature. Not only is thermalisation a striking display of simplicity in physical systems, but it allows us to determine the fate of almost every such system at long times. Perhaps even the universe will ultimately be thermal, although this is a philosophical rather than scientific question. With the establishment of dynamical chaos at the root of classical thermalisation, the question of its quantum counterpart naturally arises. After all, at the smallest of lengthscales, all systems are quantum. Dynamical chaos cannot occur in an isolated system in which the governing equation of motion is linear, such as the Schrödinger equation (2.4), and the spectrum discrete [155]. Up until the beginning of the past decade, answering this question was a purely mathematical effort. However, in recent years there has been a significant increase in the level of theoretical activity on questions of thermalisation, especially for isolated quantum systems [23, 60, 70, 90, 127, 146, 155]. There are several reasons for this. One is the growing availability of experimental realisations, for example in cold-atom systems [29, 100, 103, 156, 167] and in the nuclear spins of solid-state dopants [40]. Another is the growing theoretical understanding of how quantum-mechanical systems approach thermal equilibrium. In this chapter we will discuss the mechanism behind quantum thermalisation as well as the possible ways in which this process can fail.

We begin (see Sec. 3.1) by defining the concept of quantum thermalisation. We then review the currently understood generic mechanism for quantum thermalisation, namely the *eigenstate thermalisation hypothesis* (ETH) in Sec. 3.1.1. There are however examples in which this hypothesis does not hold. One class of these occurs in integrable systems, where the large number of conserved quantities prevents thermalisation and the long-time state is described by the so-called *generalised Gibbs ensemble* (GGE) (see Sec. 3.2). A second class occurs in disordered systems via localisation. In the non-interacting case (which cannot thermalise by definition), where the single-particle eigenfunctions are localised, this goes by the name of *Anderson localisation* (AL). It has been discovered more recently that the concept of localisation extends to the case of interacting particles, where it goes by the name of *many-body localisation* (MBL). We look at these failures of thermalisation in Sec. 3.3 and Sec. 3.4. We finish this chapter by reviewing some of the recent results in the ergodic region preceding MBL (see Sec. 3.5).

3.1 QUANTUM THERMALISATION

We consider a strongly interacting isolated (closed) quantum many-body system of some volume V. By isolated we mean that the system is not coupled to some external bath with which it can exchange energy or particles. The system is described by a local Hamiltonian H (see Sec. 2.2.4 for examples), and we are generally concerned with its highly excited eigenstates, not just the ground state and some low-lying excitations. Let the system be in some initial pure state described by the density matrix $\rho_0 = |\psi_0\rangle \langle\psi_0|$. We then evolve it in time according to (2.7), such that we obtain

$$\rho(t) = U(t)\rho_0 U^\dagger(t), \tag{3.1}$$

which importantly is also a pure state, as it is a single quantum state under unitary time-evolution.

If the system were to thermalise, then the memory of the initial state will be lost. In that case, the long-time dynamics of the system will be described by an equilibrium statistical density matrix ρ_{th} which only depends on a few thermodynamic parameters like the temperature T or the chemical potential μ. Hence, thermalisation means that

$$\lim_{\tau\to\infty}\lim_{V\to\infty}\frac{1}{\tau}\int_0^\tau dt\rho(t) \to \rho_{\text{th}}, \tag{3.2}$$

where ρ_{th} takes the following form in the canonical ensemble (see Introduction for a discussion of ensembles):

$$\rho_{\text{th}} = \frac{1}{Z}e^{-\beta H}. \tag{3.3}$$

Here, Z denotes the partition function $Z = \text{Tr}(e^{-\beta H})$ and $\beta = 1/T$ (we have set the Boltzmann factor k_B to 1). Importantly, the two limits need to be taken simultaneously (i. e. $V/\tau =$ constant), because at finite V, $\rho(t)$ would be quasi-periodic and thus have no limit as $\tau \to \infty$, while at finite τ, due to the locality of H, conserved quantities can only be transported a finite distance, and hence infinite systems cannot thermalise. We note that the temperature T is not a well defined concept in a finite closed system out-of-equilibrium with a discrete energy spectrum as there is no external bath and the concept of entropy does not translate straightforwardly (as in (3.50)) such that we could write $\frac{1}{T} = \frac{dS}{dE}$. In this case we refer to T as the parameter that controls the energy density.

We note however that a pure state can in fact never thermalise. Indeed, even at infinite times (3.1) is still a pure state and a rank-one operator cannot converge to an equilibrium density operator, which has rank larger than one [17]. This might come as a surprise after having defined thermalisation in great detail above, but we have already

seen in Sec. 2.3 that pure states have zero von Neumann entropy at all times ($S(\rho(t)) = 0$). We resolve this apparent paradox of 'losing' information of initial conditions under thermalisation and the preservation of information under unitary evolution as follows. A closed system is meant to thermalise if 'it acts as its own bath' [43, 127]. This means that a subsystem will thermalise locally, and so (local) information is not erased, but just hidden. At long times, the subsystem will get heavily entangled with the whole system such that initial local information becomes inaccessible. In that sense, we let $\mathcal{C}$ be a finite portion or subsystem of the system in question. Following (2.13) we obtain the reduced density matrix by tracing out its complement $\mathcal{D}$. In general $\rho^{\mathcal{C}}$ is not a pure state. Thus, a closed system thermalises if

$$\lim_{\tau\to\infty}\lim_{\mathcal{D}\to\infty}\frac{1}{\tau}\int_0^\tau dt\rho^{\mathcal{C}}(t) \to \rho^{\mathcal{C}}_{\text{th}}. \tag{3.4}$$

Now let $\{|\nu\rangle\}$ be the eigenstates of H with eigenenergies $\{E_\nu\}$; then any time-evolved initial state $|\psi_0\rangle$ can be written as

$$|\psi(t)\rangle = \sum_\nu C_\nu e^{-iE_\nu t}|\nu\rangle\,. \tag{3.5}$$

The coefficients $\{C_\nu\}$ result from the overlap with the initial state and are given by $\{\langle\nu|\psi_0\rangle\}$. Thus all the information about the initial condition is encoded in the $\{C_\nu\}$. The time evolution of the quantum-mechanical mean of any observable A can be written as

$$\begin{aligned} A(t) = \langle\psi(t)|A|\psi(t)\rangle &= \sum_\nu |C_\nu|^2 A_{\nu,\nu} \\ &+ \sum_{\nu,\mu\neq\nu} C^*_\mu C_\nu e^{-i(E_\nu - E_\mu)t} A_{\mu,\nu}, \end{aligned} \tag{3.6}$$

where the matrix element $A_{\mu,\nu} = \langle\mu|A|\nu\rangle$. Now if there is no special symmetry or energy degeneracy (we discuss in Sec. 3.4.2 why we do not expect levels to cross in general), then

$$\lim_{\tau\to\infty}\frac{1}{\tau}\int_0^\tau dt A(t) = \sum_\nu |C_\nu|^2 A_{\nu,\nu}. \tag{3.7}$$

If the system relaxes at all, it *must* be to this value. Equation (3.7) is often said to predict a 'diagonal ensemble', where the coefficients $|C_\nu|^2$ correspond to the weight that $|\nu\rangle$ has in this ensemble [155].

3.1.1 *Eigenstate thermalisation hypothesis*

As mentioned above, by thermalisation we understand the settling of macroscopic observables to an appropriate statistical ensemble. We should therefore demand that the diagonal ensemble (3.7) and the microcanonical ensemble give the same predictions for the relaxed value of $\hat{A}^{\mathcal{C}}$, such that

$$\sum_\nu |C_\nu|^2 A_{\nu,\nu} = \langle A\rangle_{\text{microcan}}(E_0) \equiv \frac{1}{\mathcal{N}_{E_0,\Delta E}}\sum_{|E_0 - E_\nu|<\Delta E} A_{\nu,\nu}. \tag{3.8}$$

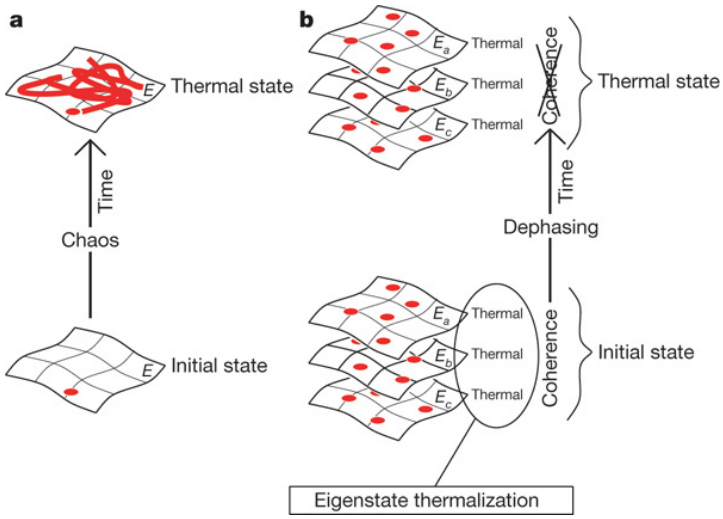

Figure 3.1: The fundamental difference between thermalisation in classical systems and quantum systems is illustrated here. a) In classical mechanics, the eventual thermal state is constructed from an initial state through dynamical chaos which results from non-linear equations evolved in time. b) On the contrary, in quantum systems following the ETH, the initial state, which is a superposition of energy eigenstates, already implicitly contains a thermal state in every eigenstate. It is phase-coherence which initially hides the thermal nature, but dephasing though time-evolution eventually reveals it. Adapted from [155].

In the above equation, E_0 is the mean energy of the initial state. ΔE is the width of an appropriately (see [155]) chosen energy window (such that it contains at least a few eigenstates, but that the actual width does not become relevant) which is centred at E_0. $\mathcal{N}_{E_0,\Delta E}$ is the normalisation factor counting the number of energy eigenstates with energies in the window $\left[E_0 - \frac{\Delta E}{2}, E_0 + \frac{\Delta E}{2}\right]$. Equation (3.8) clearly exhibits the thermodynamic universality we are looking for. The left hand side remembers the initial conditions via the $\{C_\nu\}$ while the right hand side only depends on the total energy, which is the same for many different initial states.

The *eigenstate thermalisation hypothesis* (ETH) provides a mathematical route through which this is made possible. It was independently proposed by Deutsch [53] and Srednicki [179]. The ansatz is that the matrix elements of $\hat{A}^{\mathcal{C}}$ have the following statistical properties:

$$\langle \mu | \hat{A}^{\mathcal{C}} | \nu \rangle = \overline{A}(\overline{E})\delta_{\mu\nu} + e^{-S(\overline{E})/2} f_A(\overline{E}, \omega)\mathcal{R}_{\mu,\nu}, \tag{3.9}$$

where $\overline{E} = \frac{1}{2}\left(E_\mu + E_\nu\right)$, $\omega = \left(E_\mu - E_\nu\right)$, $S(\overline{E})$ is the entropy of the system which scales with the volume ($S \sim V$) and $\mathcal{R}_{\mu,\nu}$ are random variables with zero mean and unit variance. Furthermore, $\overline{A}$ and f_A are smooth functions of their argument and importantly, $\overline{A}(\overline{E}) = A^{\mathcal{C}}_{\text{th}}$, where $A^{\mathcal{C}}_{\text{th}}$ is the expectation value of $\hat{A}^{\mathcal{C}}$ at equilibrium, calculated with the appropriate ensemble. In (3.8) we have chosen the microca-

nonical ensemble. It follows then indeed that (3.7) and (3.9) imply that any initial state, constructed from eigenstates within an energy window of ΔE around some E_0, will give expectation values as predicted by the microcanonical ensemble. This holds for local few-body operators $\hat{A}$. Further, in the limiting case of ΔE only containing a single eigenstate, we see the remarkable property of the ETH. As the name suggests, we do not need an ensemble anymore: any eigenstate already possesses the thermal properties of any other traditional statistical mechanics ensemble. With the ETH, we can thus view the process of quantum thermalisation as 'dephasing' the phase-coherent initial state and hence exposing the thermal nature of the underlying eigenstates. Classical and quantum systems thermalise therefore in fundamentally different ways as illustrated in Fig. 3.1.

There are a few important things to note. First, in order for the time-average (3.7) leading to the diagonal ensemble to be meaningful (i. e. that the value actually stays close to the average), we require that the time-averaged fluctuations of $\langle A \rangle$ vanish in the thermodynamic limit. Second, we note that formally the time for equilibration τ will scale exponentially with the volume $\tau_{\text{th}} \sim e^V$ since one needs to resolve the smallest difference between two eigenenergies ($\min_{\mu,\nu} |E_\nu - E_\mu| \sim e^{-cV}$). Both issues turn out to be resolved using the property of (3.9) that the off-diagonal terms are exponentially small in volume compared to the diagonal elements. The fluctuations are directly linked to the off-diagonal elements because the diagonal terms ($\mu = \nu$) cancel in the subtraction,

$$\sigma_A^2 \equiv \lim_{\tau\to\infty} \frac{1}{\tau} \int_0^\tau dt \left(\langle A(t) \rangle - \langle A \rangle_{\text{thermal}} \right)^2 \leq e^{-S(\overline{E})}, \tag{3.10}$$

and thus indeed vanish in the thermodynamic limit.

3.1.2 *Failure of thermalisation*

While the ETH provides a widely accepted mechanism for quantum thermalisation in generic systems, it is equally well known that certain systems simply do not thermalise [100, 127, 167]. Formally this means that

$$\lim_{\tau\to\infty} \frac{1}{\tau} \int_0^\tau dt A^{\mathcal{C}}(t) \neq \langle A \rangle_{\text{thermal}} \,. \tag{3.11}$$

While thermalising systems can be described using only a temperature and a chemical potential, non-thermalising systems need more information, as they somehow store knowledge about the initial condition. The two main concepts linked to the failure of thermalisation are *integrability* and *localisation*, both of which we will discuss in the following sections.

3.2 INTEGRABILITY AND THE GENERALISED GIBBS ENSEMBLE

In classical physics the notion of integrability is well defined. An integrable system with n degrees of freedom will possess n independent first integrals of motion that are Poisson-commuting and can thus be called 'integrable'. The terminology follows from the fact that it is then possible to integrate the resulting differential equations describing the time evolution and the solutions will display periodic motion on tori in phase space where ergodicity is absent. This clear definition is not possible in quantum mechanics where already the definition of degrees of freedom is very different. In fact it was shown by Caux and Mossel [36] that we currently do not possess a commonly accepted and self-consistent definition of quantum integrability. It is however possible to define integrability in a practical sense. We therefore call a quantum system integrable if it is Bethe Ansatz solvable [61] or non-interacting (its Hamiltonian is quadratic in the fermionic (bosonic) creation and annihilation operators). Strictly speaking, the latter already entails the former. Usually integrable systems constitute isolated points in parameter space meaning that when we add weak perturbations, they become generic. They further contain a large number (extensively many) of conserved quantities. Lastly we note that integrability in quantum systems is linked to Poisson level statistics [36], something we discuss further in Sec. 3.4.2.

Directly linked to integrability is the concept of the *generalised Gibbs ensemble* (GGE). The GGE is a natural extension of the canonical ensemble[1] to the many conserved quantities expected in integrable systems. It is conjectured that integrable systems 'thermalise' to the GGE [154]. While technically this is a generalisation of thermalisation, it does not really carry the same spirit any more. In generic systems, where one thermalises to a standard ensemble, one only requires very few variables ($\mathcal{O}(1)$) to describe the thermal state. The GGE can be obtained in the standard procedure of maximising the entropy with constraints. Let us suppose we write the density operator as $\rho = \sum_\nu p_\nu \left|\nu\right\rangle \left\langle\nu\right|$ and seek to maximise the entropy $S = -\sum_\nu p_\nu \log p_\nu$ with respect to a large number of constraints. This is best done by employing the method of Lagrange multipliers. Here we seek to maximise a Lagrangian function $\mathcal{L}(\{p_\nu\}, \{\lambda_i\}) = S(\{p_\nu\}) - \sum_i \lambda_i \, g_i(\{p_\nu\})$, where the function $g_i(\{p_\nu\}) = \sum_\nu p_\nu I^i_\nu - G_i$ is the expectation value of some conserved quantity I^i, an integral of motion, subject to a constrained value G_i. λ_i is the corresponding Lagrange multiplier and conjugate variable to that conserved quantity. We note that we always require normalisation, that the probabilities sum to unity, $\sum_\nu p_\nu = 1$.

1 Historically, the canonical ensemble was first introduced by Boltzmann, but later revisited and further investigated by Josiah Willard Gibbs.

For time-independent Hamiltonians and thus energy conservation, we also have that $\sum_\nu p_\nu E_\nu = E$. We therefore obtain that

$$\frac{\partial \mathcal{L}}{\partial p_\nu} = -(\log p_\nu + 1) + \beta E_\nu + \sum_i \lambda_i I_\nu^i \stackrel{!}{=} 0, \tag{3.12}$$

where we have relabelled the Lagrange multiplier of the energy as $\beta \equiv 1/T$. Solving for p_ν, we find that

$$p_\nu = C e^{-\beta E_\nu - \sum_i \lambda_i I_\nu^i}, \tag{3.13}$$

where C is some constant. We can now write an equilibrium density matrix in the GGE as follows

$$\rho_{\text{th}} = \frac{1}{Z} e^{-\beta H - \sum_i \lambda_i I^i}. \tag{3.14}$$

Here the normalisation factor is the usual partition function $Z = \text{Tr}\left[\exp\left(-\beta H - \sum_i \lambda_i I^i\right)\right]$, and $\{I^i\}$ is the full set of integrals of motion. There are still many open questions remaining after the formulation of the GGE. Far from integrability (in terms of parameters), systems should thermalise according to the ETH, while approaching integrability and certainly at the integrable point, they are suspected to relax to a state described by the GGE (3.14). It is however not always clear what conserved quantities to use [36], and whether the GGE only holds for local observables. A good overview can be found in [146].

3.3 ANDERSON LOCALISATION

Another way to prevent thermalisation is when localisation occurs. Indeed if particles cannot even explore all of real space or momentum space, they must clearly violate the ETH. We begin reviewing localisation starting with the non-interacting case, now known as Anderson localisation. A non-interacting system trivially cannot thermalise as every single-particle occupation is a non-trivial constant of motion; the system has no means of changing that occupation. It is however at the root of localisation in interacting systems, which we will discuss in the following.

Anderson localisation is a wave phenomenon in which transport in a non-interacting system can be suppressed due to the presence of an uncorrelated quenched disorder potential [10, 189]. Its realisation for particles is intimately connected to the particle-wave duality in quantum mechanics [128]. Let us consider a classical particle first. It is subjected to some random potential $U(x)$, and it will have a different velocity depending on its kinetic energy $K(x)$. If the particle's total energy $E = U(x) + K(x)$ is larger than $U(x)$ everywhere, the particle will propagate through the system. If, on the contrary, the total energy is smaller than $U(x)$ at any position, the particle will only be able

to visit a bounded portion of the system and it will oscillate back and forth in this allowed region. The particle is said to be classically localised.

Quantum mechanics drastically changes this picture. A simple calculation using (2.4) shows that the probability density of a quantum particle does not become strictly zero in potential regions *larger* than its total energy ($U(x) > E$) and as such it will be able to tunnel through potential barriers. At the same time, a part of it will also be reflected at potential barriers *smaller* than the total energy E. Reflected and transmitted parts can interfere constructively or destructively. At first approximation, this phenomenon will take place randomly and as such the motion may be approximated by a random walker where the particle diffuses through the system. As usual with great discoveries in physics, this intuition turns out to be incorrect in the presence of strong disorder (or even any disorder in one and two dimensions), where destructive interference may dominate and transport will be suppressed even in regions where ($E > U(x)$). This phenomenon, now termed Anderson localisation, was first discovered by P.W. Anderson in this seminal work [10]. The following review is based on [163].

The model he considered is now known as the Anderson model (of localisation), and its Hamiltonian reads

$$H = -J \sum_{\langle ij \rangle} c_i^\dagger c_j + \sum_i \epsilon_i c_i^\dagger c_i, \tag{3.15}$$

where the operators $c_i^\dagger$ and c_i denote the fermionic creation and annihilation operators at site $i \in \mathbb{Z}^d$ and d denotes the dimension of the chosen lattice geometry. Further, $J \geq 0$ denotes the hopping amplitude which applies only to nearest-neighbours as denoted by the angle brackets. The on-site energies ϵ_i are uncorrelated random variables that are uniformly drawn from a box distribution $[-W, W]$, so that we call W the disorder strength. Since H commutes with $N = \sum_i c_i^\dagger c_i$, it conserves, as shown in Sec. 2.4, the number of fermions. Since it is quadratic in the fermionic operators, it is a non-interacting model and we can thus restrict the analysis to the one-fermion subspace $\mathcal{H}_1$. A simple version of (3.15) can thus be written as

$$H|_{\mathcal{H}_1} = -J \sum_{\langle ij \rangle} |i\rangle \langle j| + \sum_i \epsilon_i |i\rangle \langle i|, \tag{3.16}$$

where $|i\rangle$ denotes the particle located on site i. For any state $|\psi\rangle \in \mathcal{H}_1$ we can introduce the wave function $\psi(i) = \langle i|\psi\rangle$.

Anderson was initially not concerned with complete localisation of single particle states. He presented a simple model for conduction in the 'impurity band', which describes diffusion in a lattice that is in some sense random. After choosing a suitable geometry for (3.16), the only free parameter in the model becomes the dimensionless degree

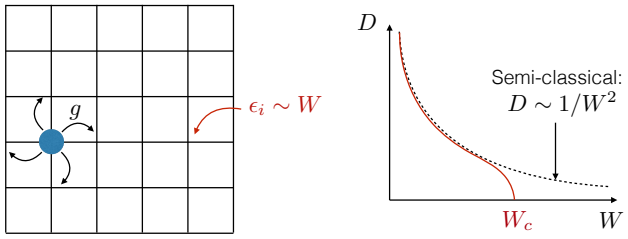

Figure 3.2: Left panel: A sketch of the system in question. We ask if a quantum particle starting somewhere on a d-dimensional lattice (here $d = 2$) can in fact become localised as opposed to simply be diffusing away (here $g = J$). Right panel: Semi-classical considerations suggest that diffusion is expected, with the diffusion coefficient D being proportional to the square inverse of the disorder strength. It was Anderson who first proposed that D might in fact become zero for some $W_c < \infty$. It was later shown that $W_c = 0$ for the case of $d = 2$ in the left panel. Adapted from [163]

of disorder W/J. We will start by carefully analysing the two trivial extreme cases of no disorder ($W = 0$) and infinite disorder ($J = 0$). Regarding the localisation of this model, we will ask for two main observables: the return probability

$$p(t) \equiv |\psi(t,0)|^2, \tag{3.17}$$

if $\psi(t = 0, i) = \delta_{i,0}$, in other words the chance that a particle initially localised around the origin will revisit that place, and the mean-square displacement

$$\Delta x^2(t) \equiv \langle \psi(t,j)|X^2|\psi(t,j)\rangle = \sum_{j\in\mathbb{Z}^d} j^2 |\psi(t,j)|^2, \tag{3.18}$$

where X denotes the position operator. The latter in particular lets us assess transport properties of the Anderson model.

3.3.1 *Zero disorder, infinite disorder and the case in between*

For a clean system ($W = 0$) and on a finite (hypercubic) d-dimensional lattice of linear size L with periodic boundary conditions, the Hamiltonian (3.16) is invariant under discrete translations and therefore conserves crystal momentum [129]. Its eigenstates are the usual Bloch-type plane waves of the form

$$\psi_k(j) \equiv \frac{1}{\sqrt{L^d}} e^{ikj} \quad , \quad E_k = -2J \sum_{n=1}^{d} \cos(k_n), \tag{3.19}$$

where the quasi-momentum components obey the condition $k_n L = 2\pi m_n$ with $m_n \in \{0, 1, \ldots, L-1\}$. Attaching the time-evolution to an eigenstate in the usual way, we write the solution to (3.16) with

$\psi(t=0,i)=\delta_{i,0}$ in the clean case as a superposition of all plane wave eigenstates

$$\psi(t,j)=\frac{1}{L^d}\sum_k e^{ikj+2itJ\sum_{n=1}^d cos(k_n)}. \tag{3.20}$$

In the thermodynamic limit, taking $L\to\infty$, we can show that the wave function converges to a Bessel function of the first kind

$$\psi(t,j)=\int_{k\in[0,2\pi]^d}\frac{d^dk}{(2\pi)^d}e^{ikj+2itJ\sum_{n=1}^d cos(k_n)}=i^d\prod_{n=1}^d\mathcal{J}_{j_n}(2tJ), \tag{3.21}$$

where we have transformed the sum over discrete k states into an integral over the first Brillouin zone. A simple shift of variables yields the integral definition of the Bessel function of the first kind $\mathcal{J}_\alpha(x)$. It is then easy to obtain the return probability for the clean case,

$$p(t)=|\psi(t,0)|^2\sim\frac{1}{t^{d/2}}, \tag{3.22}$$

where we used the fact that $\mathcal{J}_0(t)\sim t^{-1/2}$ when $x\to\infty$. While the centre of the wave packet, $x(t)\equiv\sum_{j\in\mathbb{Z}^d}j|\psi(t,j)|^2$, will remain at the origin, $x(t)=0$, the mean-square displacement diverges ballistically as

$$\Delta x^2(t)\equiv\sum_{j\in\mathbb{Z}^d}j^2|\psi(t,j)|^2=2dJ^2t^2. \tag{3.23}$$

To show (3.23), we note first that we can reduce the calculation for any dimension d to a product of $d=1$ terms, $\Delta x^2(t,d)=d\Delta x^2(t,d=1)$. Making use of the Schrödinger equation (2.4), we also note that

$$\partial_t\Delta x^2(t)=i\left\langle\psi(t,j)\right|\left[H,X^2\right]\left|\psi(t,j)\right\rangle. \tag{3.24}$$

Further we then obtain $\partial_t^2\Delta x^2(t)=-\left\langle\psi(t,j)\right|\left[H,\left[H,X^2\right]\right]\left|\psi(t,j)\right\rangle$ as well as $\partial_t^3\Delta x^2(t)=-i\left\langle\psi(t,j)\right|\left[H,\left[H,\left[H,X^2\right]\right]\right]\left|\psi(t,j)\right\rangle$. Calculating these terms explicitly shows that

$$\begin{aligned}\left[H,X^2\right]\phi(j)&=-H\phi(j)+2jJ\left(\phi(j+1)-\phi(j-1)\right)\\ \left[H,\left[H,X^2\right]\right]\phi(j)&=-2H^2\phi(j),\end{aligned} \tag{3.25}$$

from which immediately follows that $\partial_t^3\Delta x^2(t)=0$. We are now in a position to perform a Taylor expansion of $\Delta x^2(t)$ around $t=0$ in which all but the third term are zero, such that we obtain (3.23). The reason for this ballistic transport is that the initial wave packet is made of plane waves that propagate themselves ballistically in every direction and is a consequence of the translational invariance of the system [163]. We note that ballistic transport has also been linked to integrability of the underlying model [120].

The opposite case of infinite disorder/zero hopping is described by the limit in which $J/W = 0$. In this limit, the position basis is the eigenbasis of the system, such that

$$H|i\rangle = \epsilon_i |i\rangle , \tag{3.26}$$

and the Hamiltonian thus generates no dynamics: $|\psi(t,j)\rangle = e^{-i\epsilon_0 t}|0\rangle$. It follows then that the return probability remains unity $p(t) = 1$ and that the wave-packet does not spread as $\Delta x^2(t) = 0$. As opposed to the ballistic transport seen before, we now speak of localisation and the absence of transport.

The key question is now what happens in between, in the case of finite hopping and finite disorder. It is intuitively clear that we have a form of competition between the delocalising influence of the hopping and the localising effect of the disorder. If we imagine the time evolution of a quantum particle from a classical perspective, we would expect the motion to consist of a succession of ballistic propagation in between elastic scattering against some random impurities. This picture is immediately reminiscent of a random walk, which results in diffusive motion.

In order to show this let us first define the parameters for a random walk in one dimension. Let l be the step-length of some classical particle (the walker) propagating, and τ be the time for a single step. Further we define the probability to find the walker at position $x = ml$ at time $t = N\tau$, where m and N are integers, as $P_N(m)$. Then in the case of equal probability of traveling to the left and right, we can write

$$P_{N+1}(m) = \frac{1}{2}\left(P_N(m-1) + P_N(m+1)\right). \tag{3.27}$$

Subtracting $P_N(m)$ and taking the case of infinitesimal l and τ, we obtain the diffusion equation

$$\frac{\partial P}{\partial t} = \underbrace{\frac{1}{2}\frac{l^2}{\tau}}_{\equiv D}\frac{\partial^2 P}{\partial x^2}, \tag{3.28}$$

where $D = \frac{1}{2}\frac{l^2}{\tau} = \frac{1}{2}v^2\tau$, for velocity $v \equiv l/\tau$. A solution to (3.28) can be written as

$$P(t,x) = \frac{1}{\sqrt{2\pi\sigma^2}}\exp\left(-\frac{x^2}{2\sigma^2}\right), \tag{3.29}$$

with $\sigma^2 = 2Dt$. It follows immediately that the return probability goes as $P(t,0) \sim (Dt)^{-1/2}$ and the mean-square displacement $\langle x^2(t)\rangle = 2Dt$.

Returning to the quantum case, in the random walk picture, we would therefore obtain

$$\Delta x^2(t) \simeq Dt \quad \text{for} \quad t \gg \tau, \tag{3.30}$$

with a diffusion coefficient $D = v^2\tau$. Here v is the typical velocity of the quantum particle in between scattering events and τ the typical time between those events. The return probability would then take the form

$$p(t) = \frac{1}{(Dt)^{d/2}}. \tag{3.31}$$

Clearly the diffusion coefficient D must depend on the disorder strength W, which is responsible for the scattering. It can be obtained calculating the scattering rate by perturbatively adding disorder to the clean, plane wave case. In this semi-classical analysis, the particle may have a definite momentum k such that we can obtain the scattering rate Γ_k using a Fermi golden rule calculation

$$\frac{1}{\tau} = \Gamma_k = \frac{2\pi}{\hbar}\sum_{k'} |\langle k|V|k'\rangle|^2 \delta(E_k - E_{k'}), \tag{3.32}$$

where $V = \sum_i \epsilon_i |i\rangle\langle i|$ denotes the potential. Splitting the sum into diagonal and off-diagonal terms, we obtain

$$\Gamma_k = \frac{2\pi}{\hbar}\sum_{k'}\left(\sum_j \epsilon_j^2 \frac{1}{L^{2d}} + \sum_{j\neq j'} \epsilon_j \epsilon_{j'} \frac{e^{i(k-k')(j-j')}}{L^{2d}}\right)\delta\left(E_k - E_{k'}\right). \tag{3.33}$$

Taking the disorder average, the terms for which $j \neq j'$ drop out and we are left with

$$\begin{aligned}\Gamma_k &= \frac{2\pi}{\hbar}\sum_{k'}\frac{W^2}{3L^d}\delta\left(E_k - E_{k'}\right) \\ &= \frac{2\pi}{\hbar}\int \frac{d^dk'}{(2\pi)^d}\frac{W^2}{3}\delta\left(E_k - E_{k'}\right) \\ &= \frac{2\pi}{\hbar}\int dE'\rho(E')\frac{W^2}{3}\delta\left(E_k - E_{k'}\right) \sim W^2\rho(E_k).\end{aligned} \tag{3.34}$$

Here ρ denotes the density of states, and we have used the fact that the variance of a box distribution of width $2W$ equals $W^2/3$. Taking as v the group velocity $v = \partial_k E_k \sim g$, we obtain a diffusion coefficient

$$D \sim \frac{g^3}{W^2}. \tag{3.35}$$

The diffusion coefficient thus turns out to be inversely proportional to the disorder strength, but never zero.

Remarkably, Anderson predicted in 1958 that contrary to (3.35), D can become strictly zero for sufficiently strong (but finite) $W > W_c$ in his seminal paper [10] and as such the return probability $p(t)$ would not decay to zero.

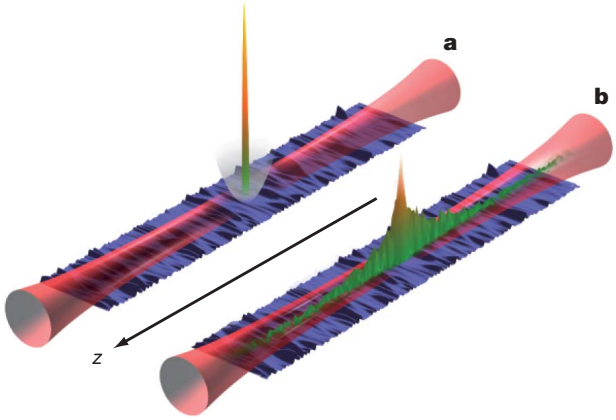

Figure 3.3: Experimental realisation of Anderson localisation for matter waves. In a) a small Bose-Einstein condensate (BEC) of 1.7×10^4 atoms is formed in a combination of a horizontal optical waveguide, ensuring a strong confinement in the transverse direction, and a loose magnetic trap in the longitudinal direction that prevents the BEC from expanding in the z-direction. b) At time $t = 0$ the magnetic trap is removed and the BEC starts expanding, but quickly localises due to the weak disorder potential that is superimposed via laser speckle. We note that a) and b) are not exactly to scale for illustration purposes. Adapted from [29].

3.3.2 *Absence of diffusion and transport*

Anderson, who was initially not concerned with complete localisation of single states, noticed this absence of diffusion for his proposed model (3.15) on a cubic lattice. The original calculation is fairly elaborate (see reviews [65, 125]) and involves a number of assumptions, some of which are not easy to motivate [2] or turned out to be mathematically incorrect [184]. At its core however lies the remarkable realisation that for strong enough disorder, the quantum amplitudes associated with the tunnelling paths through the disordered system cancel each other, resulting in a localised wave function. Equivalently, an incoming wave may be scattered from disorder potentials and at high enough disorder, the scattered wavelets interfere destructively in the forward direction, causing the wave to decay exponentially [11]. A great deal has been discovered since the original proposal, especially that the dimensionality of the lattice is crucial. It therefore makes sense to group the known results by dimension d and not chronologically.

LOCALISATION AT STRONG DISORDER IN ANY d is known rigorously [89]. This means that in any dimension d there exists $W_c < \infty$ beyond which the system is localised. While localisation has been proven for sufficiently strong disorder, the absence of it has not been

proven even for cases where delocalisation appears to be present on numerical grounds.

LOCALISATION IN $d = 1$ is rigorously known, while localisation in $d = 2$ is strongly expected and supported by many numerical studies for *any* amount of uncorrelated disorder. In one dimension it was first conjectured by N.F. Mott and W.D. Twose [124] following the work of Anderson. This statement was later given a rigorous mathematical proof by M. Goldshtein *et al.* [68]. The argument uses the fact that we can rewrite the Schrödinger equation for the tight-binding model as (setting $J = 1$)

$$-\psi_{i-1} - \psi_{i+1} + \epsilon_i \psi_i = E\psi_i. \tag{3.36}$$

This may be rewritten using so called transfer-matrices T_i as

$$\begin{pmatrix} \psi_{i+1} \\ \psi_i \end{pmatrix} = \prod_{i'=1}^{L} T_{i'} \begin{pmatrix} \psi_1 \\ \psi_0 \end{pmatrix}, \quad T_{i'} = \begin{pmatrix} \epsilon_{i'} - E & -1 \\ 1 & 0 \end{pmatrix}, \tag{3.37}$$

where $\begin{pmatrix} \psi_1 \\ \psi_0 \end{pmatrix}$ is the boundary condition of the Schrödinger equation. Using the Oseledec-Ruelle Theorem (multiplicative ergodic Theorem) [150] and Fürstenberg's Theorem for products of random matrices [66] one can prove rigorously that for $L \to \infty$ the overall shape of the wave function is $\psi_i \sim \exp(-i/\xi)$. Here, ξ is the localisation length in units of the lattice constant. Formally it is known as the Lyapunov exponent of the product of matrices T_i. As a consequence, all eigenstates are not extended over the entire lattice, but are exponentially confined to certain areas of the lattice, hence localised. We stress again that remarkably any amount of uncorrelated disorder suffices for this to happen. This implies that any 1D material will lose its diffusion or conduction capabilities if the system size is $L \gg \xi$. Numerically one can show that the disorder dependence of the localisation length ξ is well described by the power law $\xi \propto W^{-2}$ for weak disorder [104].

The same result is in fact expected in two dimensions. Although a completely rigorous solution is missing, the claim was first based on the scaling theory of localisation [3] after the concept of renormalisation group was introduced [207]. The main idea is that close to the transition between localised and extended states, there is only one relevant scaling variable. This variable should be sufficient to describe the conductance on the metallic side of the transition and the localisation length on the insulating side [104].

LOCALISATION AND DELOCALISATION are possible in $d = 2 + \epsilon$ for $\epsilon > 0$, where the phenomenology becomes much richer. We expect a true phase transition at a finite value of the disorder strength $W_c > 0$ above which the entire spectrum becomes localised. Furthermore, it

turns out that for smaller disorder strengths there may be a value W_c' which depends on the energy E of the eigenstates at which parts of the spectrum might be localised (usually the tails of the spectrum, often called 'Lifshitz tails' [104]), while other parts remain delocalised. In other words, we obtain $W_c' = W_c'(E)$. This defines the concept of 'mobility edges', a concept first introduced by Mott [123]. The fact that both localised and delocalised eigenfunctions at the same energy are forbidden is known as Mott's argument. Any delocalised state with the same energy will hybridise with the localised states at that energy making them in turn delocalised.

EXPERIMENTS that show Anderson localisation are sparse and often disputed. Among other attempts, a recent highlight has been achieved by the group of Bouyer & Aspect [29]. This experiment is an impressive manifestations of Anderson localisation for matter waves, something not previously observed, unlike in other media [47, 205]. In Fig. 3.3, we show the results of [29], where a Bose-Einstein condensate (BEC) is released for expansion in an entirely uncorrelated disordered landscape achieved by laser speckle. As predicted, the particles or matter waves making up the BEC are exponentially localised.

To summarise, we note that in the now decades-long history of Anderson localisation many aspects of the problem have been discussed and are now clear. In addition to the original proposal, that the *return probability* of a particle starting at a fixed position may not decay, it was shown that in one and two dimensions, we further find *exponentially localised wave functions* in the entire spectrum which results in the *absence of diffusion and transport*. In higher dimensions there can be localisation for strong enough disorder, but depending on the energy, parts of the spectrum may still be delocalised. This separation is called a *'mobility edge'*. Further diagnostics of Anderson localisation include the characterisation of the *spectral properties* of the system, something which we will inspect more closely in the following section.

3.4 MANY-BODY LOCALISATION

Many-body localisation (MBL) is in many ways even more surprising than Anderson localisation, a phenomenon physicists today have, in general, become very accustomed to. MBL is currently a subject of intense research [127], for both practical reasons (such as possible advances in the technology of quantum computing [9, 15, 109]), as well as in the context of fundamental questions in physics (such as the thermalisation of quantum systems [127] or phase transitions at finite temperature [130]). In the most simple terms, MBL is the stability of Anderson localisation to the addition of interactions between

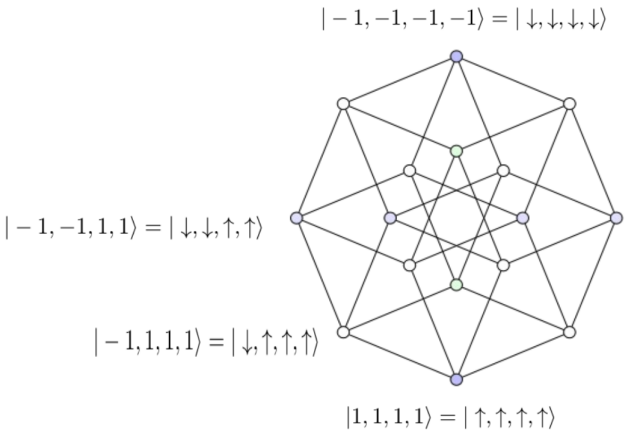

Figure 3.4: Graphical representation of the Fock space graph of an $L = 4$ lattice onto which (3.40) may be mapped. Every corner represents an eigenstate of the non-interacting Hamiltonian (3.38), which is a product state in the σ^z basis. The vertices denote the effective hopping introduced by (3.39).

the particles. In this section we review some of the known results, especially in the context of work presented later in this thesis.

3.4.1 *Localisation in Fock space and Imbrie's proof*

It was widely believed that interactions between particles would destroy the Anderson insulator making the system a metal, albeit a 'bad one' [115]. In order to show why one would assume this, we consider the following example. Take the following Hamiltonian in one dimension

$$H^{(0)} = \sum_{i=1}^{L} h_i \sigma_i^z + \sum_{i=1}^{L-1} J_i \sigma_i^z \sigma_{i+1}^z, \tag{3.38}$$

where σ^z denotes the usual Pauli matrix (2.17), the $\{h_i\}$ and $\{J_i\}$ are independent and identically distributed random variables, and L is the length of the chain. This model is integrable in the sense introduced in Sec. 3.2, and can be easily diagonalised. Its eigenstates are simply product states in the σ^z-basis and therefore equivalent to the basis states of Fock space. This model is therefore trivially localised in space. Localisation in the spin context is harder to picture as naively nothing moves. We may however visualise the eigenstates of this system as sites of a hypercube on a Fock space graph as shown in Fig. 3.4 (for $L = 4$). The number of sites is equal to the dimension D of the Hilbert space ($D = 2^L = 16$). The localisation in Fock space is evident as there are no matrix elements in this Hamiltonian that would

connect the points. We now weakly perturb $H^{(0)}$ with the following Hamiltonian

$$H^{(1)} = \sum_{i=1}^{L} \gamma_i \sigma_i^x, \tag{3.39}$$

where again $\{\gamma_i\}$ are independent identically distributed random variables. We thus define the complete perturbed Hamiltonian as

$$H = H^{(0)} + \delta H^{(1)}, \tag{3.40}$$

where $\delta > 0$ is the strength of the perturbation. When turning on the perturbation, we create an effective hopping on the hypercube in Fig. 3.4 produced by the term $\sum_j \gamma_j \sigma_j^x$. This hopping occurs on the hypercube between sites that only differ by one spin flip operation and is denoted by edges connecting the sites. The on-site energies on this graph are given by $\sum_i h_i a_i + \sum_i J_i a_i a_{i+1}$ with $a_i \in \{-1, 1\}$. Thus H can be mapped onto an Anderson model on a complicated graph with very high connectivity, i. e. that sites are connected to many other sites (usually of $\mathcal{O}(L)$). The question of MBL can in one sense be defined as the question of Anderson localisation in Fock space. Intuitively one would expect the system *not* to localise, because the on-site energies are correlated random variables and also, perhaps, because the coordination number is so high. This is easily seen as we use $2L$ random variables (h_i, J_i) to create 2^L on-site energies on the graph.

It was D.M. Basko, I.L. Aleiner and B.L. Altshuler (BAA) who first proposed in their seminal work [23] that localisation in the Anderson sense on a graph constructed by the non-interacting eigenstates is possible. In their paper they demonstrate for a model of weakly-interacting disordered fermions that the system is localised in the sense of Anderson localisation on a graph constructed taking the eigenstates of the non-interacting problem as in Fig. 3.4. Remarkably, they also showed that a delocalisation-localisation happens as a function of disorder strength and energy density. This transition, often called the MBL transition, is a novel type of phase transition that may occur at finite temperature T, something previously thought impossible for a one-dimensional system (although the work of BAA was concerned with $d = 3$) [116]. It distinguishes an ergodic phase where the eigenstates are delocalised on this Fock space graph and are thermal and a MBL phase in which the system is localised. We note there are several works that claim a genuine localisation in Fock space is not possible [24, 48, 116].

In 2016, J.Z. Imbrie was able to show under minimal assumptions on the energy level statistics of H, that for small $\delta (\delta \ll 1)$ the system (3.40) is still localised in space [92]. In his proof, he defines a map between the eigenstates of $H^{(0)}$ and the eigenstates of H by constructing a unitary operator W given by the product of local unitary

operators such that the Hamiltonian can be rewritten in terms of a set of local integrals of motions (LIOMs) τ_i^z

$$\tilde{H} = W^\dagger H W = \sum_\alpha \tilde{E}_\alpha \tau_\alpha^z + \sum_{\alpha<\beta} J_{\alpha,\beta} \tau_\alpha^z \tau_\beta^z + \sum_{\alpha<\beta<\gamma} J_{\alpha,\beta,\gamma} \tau_\alpha^z \tau_\beta^z \tau_\gamma^z + \dots . \tag{3.41}$$

These LIOMs, often also referred to as 'l-bits', obey several properties. They are constructed from the original (diagonal) spin operators as $\tau_i^z = W \sigma_i^z W^\dagger$. They are functionally independent and commute with one another $\left(\left[\tau_i^z, \tau_j^z\right] = 0\right)$ and with the Hamiltonian $\left(\left[\tilde{H}, \tau_i^z\right] = 0\right)$. Further, they are quasi-local operators, such that we can associate a localisation centre with them, $\tau_i^z = Z_i \sigma_i^z + \sum_{r\neq i} C_{i+r} \sigma_r^z$, where $Z_i < 1$ and the norm of the correction C decays exponentially in space as $||C||_{i+r} \leq e^{-|r|/\xi_{\text{op}}}$ for some localisation length ξ_{op}. The interaction terms $J_{\alpha,\beta}$ (and higher order terms) between the LIOMs also decay exponentially with the distance between the localisation centres, $J_{\alpha,\beta} \leq e^{-|\alpha-\beta|/\xi_{\text{int}}}$, with some possibly different localisation length ξ_{int}. One can think of them as dressed versions of the non-interacting σ_i^z operator, with corrections vanishing as $\delta \to 0$ [38, 92, 139, 149, 157].

The existence of a set of LIOMs implies further properties of the MBL phase which we will non-exhaustively discuss in the next section [163]. Regarding entanglement, it has been shown that the existence of LIOMs is related to the area-law nature of eigenstates, something previously only found in or near ground states. Also, the growth of entanglement after a quench has been shown to be unbounded although logarithmic in time. The proximity of the true eigenstates to product states (the non-interacting eigenstates) also implies a breaking of the ETH and hence an absence of thermalisation. In addition, one can relate the existence of LIOMs to Poisson spectral statistics and the absence of transport. Lastly we note that while most of the work on MBL has been done on one-dimensional systems, MBL is generally expected also in higher dimensions [23]. Beyond the analytical work sketched out above, most of the above mentioned evidence for the existence of two phases, a localised and a delocalised one, is numerical. In the remainder of the chapter we will discuss the results most relevant to this thesis. For other reviews, we refer to [1, 6, 127].

3.4.2 *Numerical evidence*

Due to the exponential growth of the Hilbert space, something that we will discuss in more detail in Sec. 4.1, most of the numerical work focuses on one-dimensional systems. Arguably the most studied model with an MBL transition is the spin-1/2 Heisenberg chain [38, 116, 127, 138, 177], which has the Hamiltonian (see (2.16)):

$$H = \sum_i^L h_i S_i^z + \sum_i^{L-1} J \mathbf{S}_i \cdot \mathbf{S}_{i+1}, \tag{3.42}$$

where $\mathbf{S}_i = \{S_i^x, S_i^y, S_i^z\}$, with $S_i^\alpha = \frac{1}{2}\sigma_i^\alpha$. Here σ_i^α are the Pauli matrices (2.17). The fields $\{h_i\}$ are independent random numbers equally distributed between $[-W, W]$ and L denotes the length of the chain. In this model, the total magnetisation $S^z_{\text{tot}} = \sum_i^L S_i^z$ is conserved (we recall that then $[H, S^z_{\text{tot}}] = 0$), which implies the conservation of magnetisation in the z-direction. So far the parameters of all the spin components took the same value J, but it is common to vary them (J_x, J_y, J_z), in which case we may speak of the spin-1/2 XYZ chain. As long as $J_x = J_y$, the model will still conserve S^z_{tot}. This model can be mapped to a system of spinless fermions using the Jordan-Wigner transformation:

$$\begin{aligned} \sigma_j^+ &= e^{-i\pi \sum_k^{j-1} c_k^\dagger c_k} c_j^\dagger, \\ \sigma_j^- &= e^{+i\pi \sum_k^{j-1} c_k^\dagger c_k} c_j, \\ \sigma_j^z &= 2n_j - 1, \end{aligned} \tag{3.43}$$

where $c_j^\dagger$ and c_j are the usual fermionic creation and annihilation operators, and $n_j = c_j^\dagger c_j$. Using (3.43), we obtain

$$\begin{aligned} H = &- \frac{J_\perp}{2} \sum_{i=1}^{L} c_i^\dagger c_{i+1} + h.c. + \sum_{i=1}^{L} h_i \left(n_i - \frac{1}{2} \right) \\ &+ J_z \sum_{i=1}^{L-1} \left(n_i - \frac{1}{2} \right) \left(n_{i+1} - \frac{1}{2} \right), \end{aligned} \tag{3.44}$$

where $J_x = J_y = J_\perp$. This Hamiltonian describes spinless fermions hopping on a lattice, while experiencing nearest-neighbour interactions J_z.

3.4.2.1 *Level statistics*

So far we have mostly associated MBL with localisation in space, but this is of course only one basis. A powerful, basis independent method to distinguish an ergodic phase from a localised one lies in the statistical properties of the energy spectrum of the Hamiltonian. This approach to studying the properties of a system has its root in nuclear physics and the consequently developed random matrix theory. The basic idea that Eugene Wigner introduced was that the spectrum of a heavy atom nucleus (whose Hamiltonian would be too complicated to ever write down) should resemble the spacings between the eigenvalues of a random matrix, and should only depend on the symmetry properties of the underlying evolution. More recently it has become also a key diagnostic of MBL systems [5, 20, 101, 108, 116, 138, 175, 178, 180] and has further been linked to integrability [36].

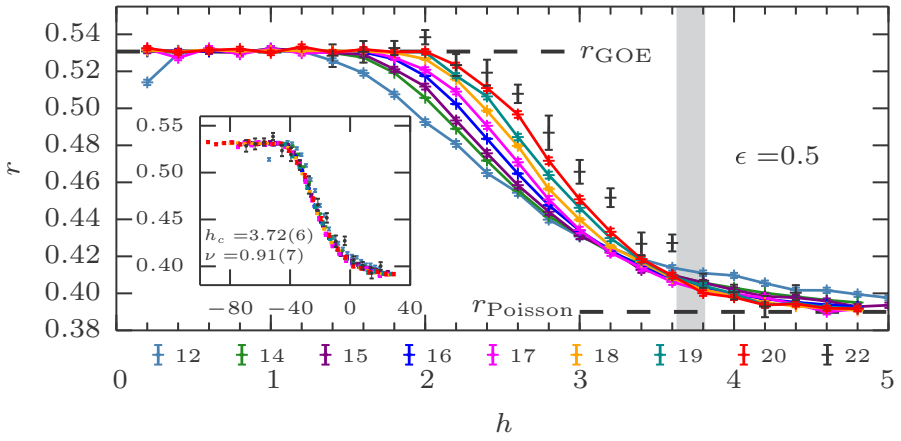

Figure 3.5: The average gap-ratio parameter $\bar{r}$ as a function of the disorder strength W (here $h \equiv W$) for different system sizes L (here denoted by different colours). For weak disorder, we clearly see that the level statistics follow those of random matrices in the Gaussian orthogonal ensemble, while at strong disorder there is a transition to Poisson statistics. The inset shows the scaled curves with an approximate transition point (here labelled h_c). Adapted from [116].

The main quantity of interest is the gap between adjacent energy levels δ_n and the more recently introduced gap-ratio parameter r_n [130]. They are defined as

$$\begin{aligned} \delta_n &= E_{n+1} - E_n \\ r_n &= \min\left(\delta_n, \delta_{n+1}\right) / \max\left(\delta_n, \delta_{n+1}\right). \end{aligned} \tag{3.45}$$

The latter conveniently removes the dependence on the density of states. The statistics of level spacings of an ergodic system is expected to be the same as that of a random matrix belonging to the same symmetry class [74], which is, in the case of real Hamiltonians, the so called Gaussian Orthogonal Ensemble (GOE). Its associated probability distribution for the level spacings is the Wigner-Dyson distribution [13] of the form

$$P_{\mathrm{GOE}}(\delta) = \beta\delta \exp(-\gamma\delta^2), \tag{3.46}$$

where β and γ are appropriately chosen constants.

In general, we may derive the probability distribution $P(r)$, where $r \equiv \delta_1/\delta_2$, the ratio of two values, by considering the *joint* probability distribution for values $P(\delta_1, \delta_2)$. This can be expressed as

$$P(r) = \int P(\delta_1, \delta_2)\delta(r - \frac{\delta_1}{\delta_2}) d\delta_1 d\delta_2 = \int P(r\delta_2, \delta_2)\delta_2 d\delta_2. \tag{3.47}$$

In the case that δ_1 and δ_2 are independent, $P(\delta_1, \delta_2) = P(\delta_1)P(\delta_2)$, and $P(r)$ can be easily found by evaluating (3.47). If this is not the case, one must find the joint probability distribution, which can be highly non-trivial [13].

For the gap-ratio parameter in the GOE, where neighbouring level spacings δ_n and δ_{n+1} are correlated, it can be shown that the probability distribution of r is well described by the following, with only small residual corrections to numerical data [13]:

$$P_{\mathrm{GOE}}(r) = \frac{27}{4}\frac{r + r^2}{(1 + r + r^2)^{5/2}}. \tag{3.48}$$

This can be condensed into a single number by taking the average such that one obtains $\bar{r}_{GOE} \approx 0.5307$. In the case of Wigner-Dyson statistics, it is commonly said that the system exhibits 'level repulsion' because the probability for two levels to be degenerate, i. e. to have precisely the same energy ($\delta = 0$), is zero. Physically one can gain some intuition by considering an eigenfunction in the ergodic phase, hence by definition an extended state. If another extended state happens to have the same energy, the two states will hybridise and their energies be shifted apart. It is the general belief that this is true for generic (non-integrable) systems. As a cautionary note, it has to be mentioned that special care needs to be taken in the presence of symmetries. The eigenstates in each symmetry sector are not influenced by those in other sectors, so their eigenenergies will not be correlated, and the distribution of level spacings can have significant weight near zero.

This directly leads us to a prominent counter example, in which Wigner-Dyson statistics are absent in the spectrum. In the case of integrability (see Sec. 3.2), the presence of a large, extensive number of integrals of motion that cannot be divided into symmetry sectors allows energy levels to cross each other, i. e. δ to be zero. It has also been discovered that the LIOMs in the context of MBL equally cause this level-crossing [130]. As such, the level statistics in this case may be an indicator of integrability [36] or localisation. Due to the absence of level repulsion, the eigenenergies in this case are effectively independent random numbers, and are thus described by a Poisson distribution:

$$P_P(\delta) = \frac{1}{\Delta}\exp\left(-\frac{\delta}{\Delta}\right) \quad \text{and} \quad P_P(r) = \frac{2}{(1+r)^2}, \tag{3.49}$$

where Δ denotes the average level spacing. Again condensing this into a single number gives us $\bar{r}_P = 2\log 2 - 1 \approx 0.3863$ [130].

Fig. 3.5 (where $h \equiv W$) shows the average gap-ratio parameter $\bar{r}$ of (3.42) as a function of the disorder strength W for several system sizes L. $\bar{r}$ has been obtained by averaging over disorder and over eigenstates at a fixed energy density ϵ, which can be defined as $\epsilon = (E - E_{\mathrm{min}})/(E_{\mathrm{max}} - E_{\mathrm{min}})$. It is indeed found that for weak disorder $\bar{r} \approx \bar{r}_{\mathrm{GOE}}$, indicating that the system is ergodic. When W is increased, the value of $\bar{r}$ drops monotonically to $\bar{r}_P$. The curves for different L cross each other at a value around $W_c \approx 3.7$, giving strong

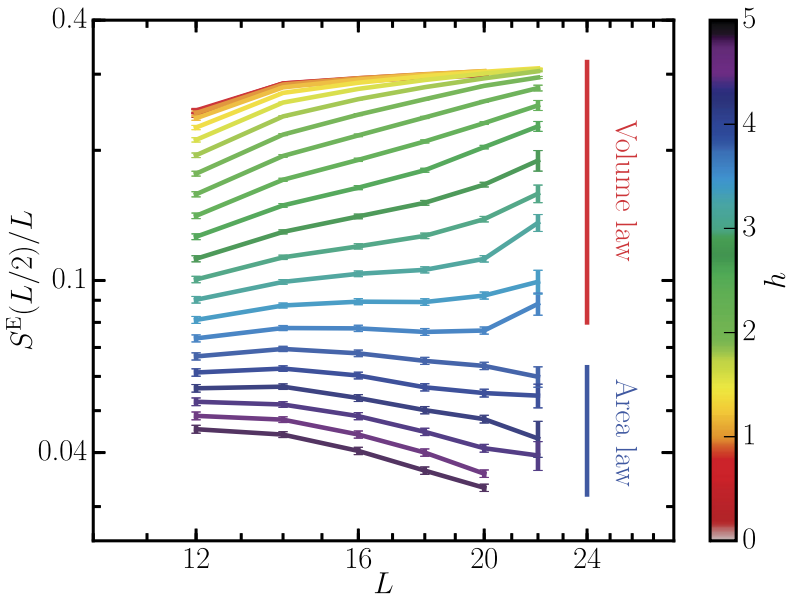

Figure 3.6: A study of the disorder-averaged half-chain entanglement entropy for (3.42) at a fixed energy density in the middle of the many-body spectrum ($\epsilon = 0.5$) with $L = 12, \ldots, 22$. One can observe a qualitative change from volume law at small disorder $h \equiv W$ to an area law at $h > h_c = 3.8$. Adapted from [6].

evidence of a possible transition. It is also possible to collapse the curves for different L performing a finite size scaling analysis using a scaling function of the form $g\left[L^{1/\nu}\left(W - W_c\right)\right]$, as shown in the inset of Fig. 3.5, where $\nu \approx 0.91$.

Nonetheless it can be shown that $\bar{r}$ can have the value of $\bar{r}_{\mathrm{GOE}}$ even if the probability distribution is not the Wigner-Dyson distribution [105]. This is one of the reasons that an analysis of the gap-ratio parameter $\bar{r}$ alone is not sufficient to distinguish an ergodic from a localised phase. One must therefore apply other measures as introduced below.

3.4.2.2 *Entanglement entropy*

Another key result regarding the MBL transition is that the bipartite entanglement entropy (see Sec. 2.3) behaves differently in the ergodic and localised phases. Firstly, one can show that the von Neumann en-

tropy (2.20) is equal to the thermodynamic entropy S_{th} for a thermal subsystem density matrix $\rho_{\text{th}}^{\mathcal{C}} \sim \exp(-\beta H^{\mathcal{C}})$:

$$\begin{aligned} S_{\text{vN}}(\rho_{\text{th}}) &= -\text{Tr}\,(\rho_{\text{th}} \ln \rho_{\text{th}}) \\ &= -\text{Tr} \sum_{\alpha} \frac{1}{Z} e^{-\beta E_\alpha} \ln\left(\frac{1}{Z} e^{-\beta E_\alpha}\right) |\alpha\rangle \langle\alpha| \\ &= \beta \sum_{\alpha} \frac{1}{Z} e^{-\beta E_\alpha} E_\alpha + \ln Z \sum_{\alpha} \frac{1}{Z} e^{-\beta E_\alpha} \\ &= \beta E + \ln Z = \beta U - \beta F = \beta T S_{\text{th}} \\ &= S_{\text{th}}, \end{aligned} \tag{3.50}$$

where all the symbols have their usual thermodynamic meaning. S_{th} is an extensive quantity and as a consequence $S_{\text{vN}}(\rho_{\text{th}})$ should also be extensive. Fig. 3.6 (where $h \equiv W$) shows the normalised bipartite entanglement S/L for several L and for different values of W again averaged over eigenstates in the middle of the spectrum ($\epsilon = 0.5$). A change in the behaviour of the entanglement properties at $W_c \approx 3.7$ is visible. For disorder values smaller than W_c, S/L is almost constant as a function of system size, while for $W > W_c$, S/L starts to decrease for larger L, implying that the entanglement entropy is at least sub-extensive, in contrast to S_{th} and the ETH. In summary it can be seen on numerical grounds that a system that is many-body localised in space exhibits area-law entanglement properties ($S \sim L^{d-1} \sim \mathcal{O}(1)$), and thus clearly fails to thermalise, while the ergodic side of the system shows volume law entanglement ($S \sim L^d \sim \mathcal{O}(L)$) consistent with thermalisation.

It can be further shown that the fluctuations of the entanglement entropy have a maximum at the MBL transition, which then serves as another diagnostic of the transition point itself [101, 116]. This peak can be understood in the following way. Close to the MBL transition, a small difference in disorder strength can cause the entanglement properties to change (as seen above), such that the variance of the entanglement entropy will diverge as a function of system size over a window that contains the MBL transition. This is because it includes both localised and extended states [101]. This concludes another key diagnostic of the MBL transition.

3.4.2.3 *Other eigenvector measures*

Next to the von Neumann entropy, one can obtain further diagnostics of MBL based on the eigenvectors, which we will briefly summarise in this section. Perhaps the most intuitive of those is the inverse participation ratio (IPR) defined as follows,

$$I_q^\alpha = \sum_n |\langle n|\alpha\rangle|^{2q} \sim \mathcal{N}^{D_q(1-q)}. \tag{3.51}$$

Here $|\alpha\rangle$ denotes an eigenstate of the system, $\{\langle n|\}$ is a set of basis states in a chosen basis (often position) with dimension $\mathcal{N}$, the size of

the Hilbert space. D_q is called the generalised fractal dimension and the case of a nonlinear dependence of D_q on q indicates that the eigenstates have become multifractal [185]. The intuitive picture behind the IPR is the following. We ask how much an eigenstate participates in the basis states of some chosen basis. If $I_q^\alpha \sim \mathcal{O}(1)$ remains approximately constant as a function of $\mathcal{N}(L)$, then the system may be localised in the chosen basis as adding basis states does not affect the overlaps and hence the eigenstate cannot have any support in that part of the Hilbert space. In the case of an ergodic system, where the eigenstate is expected to be delocalised and to sample most of the Hilbert space without preference, D_2 is expected to be close to unity. Indeed, the case of random matrices following the GOE give $I_2^\alpha \simeq 3\mathcal{N}^{-1}$ [186, 209]. In the delocalised but not fully ergodic case, we would find $0 < D_2 < 1$. Importantly, the IPR is basis dependent, so one needs to be careful in drawing conclusions from the IPR alone. Related to the IPR and D_q is the so-called Renyi entropy

$$S_q^{(R),\alpha} \equiv \frac{1}{1-q}\ln\left(I_q^\alpha\right) \sim D_q \ln\left(\mathcal{N}\right), \tag{3.52}$$

which in the limit of $q \to 1$ is called the Shannon entropy,

$$S_{\text{Sh}}^\alpha = -\sum_n |\langle n|\alpha\rangle|^2 \ln\left(|\langle n|\alpha\rangle|^2\right). \tag{3.53}$$

The Shannon entropy allows us to calculate D_1 (as I_1^α).

Lastly, we could directly verify the ETH via the calculation of expectation values for local observables for eigenstates which belong to the same energy density in the thermodynamic limit. If for example we define for the local magnetisation,

$$\begin{aligned} m_i^\alpha &\equiv \langle\alpha|S_i^z|\alpha\rangle, \\ |m_i^\alpha - m_i^{\alpha+1}| &\equiv |\langle\alpha|S_i^z|\alpha\rangle - \langle\alpha+1|S_i^z|\alpha+1\rangle|, \end{aligned} \tag{3.54}$$

then if the eigenstate $|\alpha\rangle$ is thermal, the expectation value of S_i^z is just described by the energy density ϵ, and thus by the ETH,

$$|m_i^\alpha - m_i^{\alpha+1}| \sim e^{-cL} \quad c > 0. \tag{3.55}$$

On the contrary, if the system is localised, then $|m_i^\alpha - m_i^{\alpha+1}|$ can and will be finite even for eigenstates of the same energy density in the thermodynamic limit.

3.4.2.4 *Mobility edge*

In this section, we summarise some of the static results that we have reported so far and show the complete phase diagram for the chosen MBL system (3.42). The study of eigenstates and of the spectral properties of (3.42) give evidence for the existence of two phases: an ergodic phase in which the eigenstates are ergodic and the ETH holds,

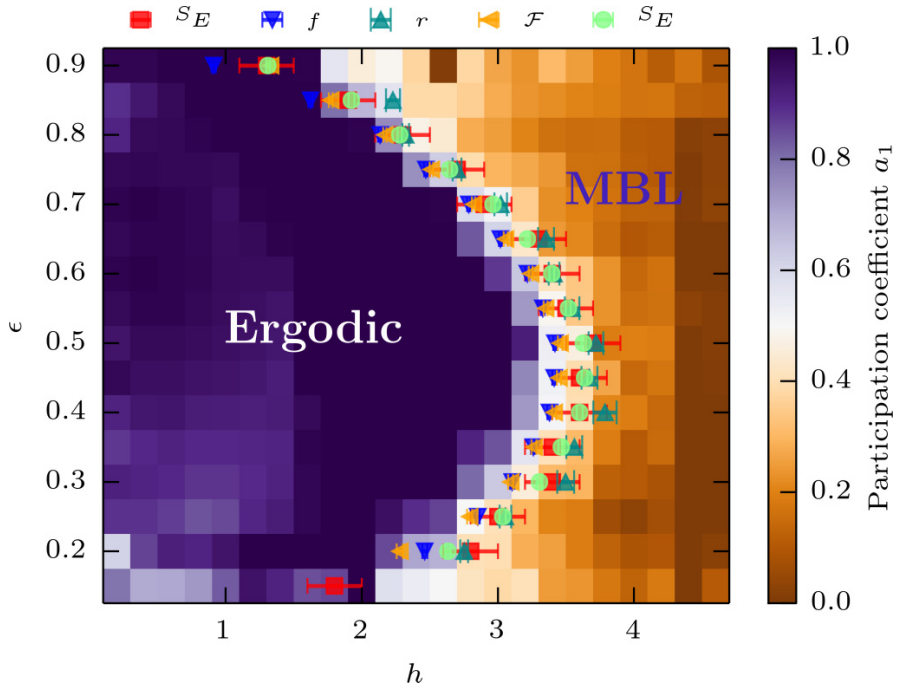

Figure 3.7: Complete phase diagram of the random field spin-1/2 Heisenberg chain (3.42) as a function of disorder W (here $h \equiv W$) and energy density ϵ displaying the two phases and the mobility edge. The diagram was produced by an exact diagonalisation study of system sizes up to $L = 22$. The diagnostic tools involve the spectral statistics (turquoise upwards-pointing triangles), entanglement entropy (red squares) and fluctuations thereof (green circles), the decay of a long-wavelength spin density (blue downward-pointing triangles), and the fluctuations of the half-chain magnetisation (yellow left-pointing triangles). The last two measures are not discussed in the text. The colour scheme is obtained from the scaling of the Shannon entropy with system size (here denoted as a_1). Adapted from [116].

and another phase called MBL phase where the eigenstates are localised and ergodicity breaks down. Furthermore, the ergodic phase is characterised by having Wigner-Dyson level statistics ($r \approx r_{\text{GOE}}$) and the eigenstates are volume-law ($S \sim L$). The MBL phase has Poisson level statistics ($r \approx r_{\text{Poisson}}$) and its eigenstates are area-law ($S \sim L^0$). The localised phase is also characterised by the existence of an extensive number of quasi-local integrals of motion, often called LIOMs or l-bits, $\{\tau_i^z\}$.

Moreover, we have also seen that the critical value of the MBL transition (W_c) is energy density dependent $W_c'(\epsilon)$. The collection of these results gives rise to the phase diagram for the MBL transition of (3.42). Fig. 3.7 shows the phase diagram for disorder strength (W) vs energy density (ϵ) [116]. It gives evidence for the existence of an MBL transition also at a finite energy density (highly-excited quantum phase transition) and thus for the existence of a *many-body mobility edge*

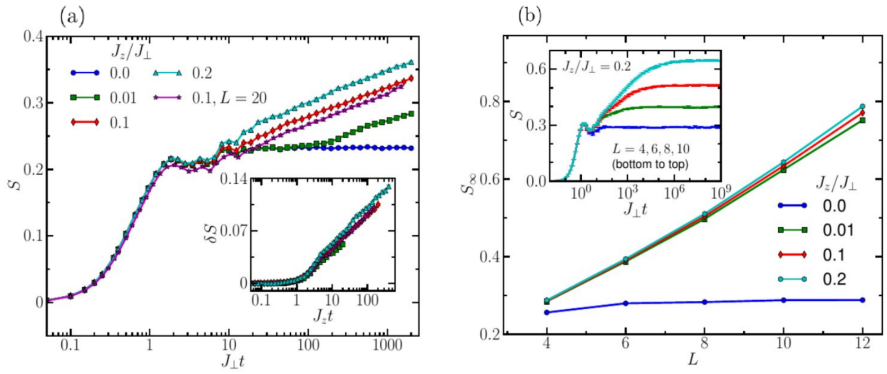

Figure 3.8: a) The entanglement entropy $S(t)$ as a function of t for several interaction strengths J_z for a fixed L. In this panel the system is always in a localised phase. For $J_z = 0$ the system is Anderson localised and entanglement propagation is absent, while for $J_z \neq 0$ the system is interacting and $S(t) \sim \log(t)$. b) The saturation value of $S(t)$ in the interacting case follows a volume-law ($S_\infty \sim L$). Adapted from [21].

(MBME). In the literature, energy density and the word temperature are used interchangeably. In other words, for large values of W, the system is always localised ($W \geq W_c(\epsilon = 0.5) \approx 3.7$). For smaller values of W, the energy spectrum can host separate bands which are composed of ergodic states or of localised states.

Nevertheless, it is important to point out that recently the existence of MBME has been questioned [51]. Using perturbation theory and assuming that ETH holds in the ergodic phase, it was argued that thermal local-fluctuations in eigenstates could destabilise the localised phase, forbidding the existence of MBME. In the next section, we show some properties of the quantum dynamics of many-body localised systems.

3.4.2.5 *Entanglement growth*

As we have already discussed, localised systems are characterised by the absence of transport. Nevertheless, MBL systems have the peculiarity that entanglement can still propagate, contrary to a localised non-interacting system, in which entanglement propagation is absent.

Starting with a random product state in the σ^z-basis and evolving it, the bipartite entanglement entropy grows logarithmically with time ($S(t) \sim \log(t)$) in the MBL phase. On the contrary, for the non-interacting case, no propagation occurs ($\lim_{t\to\infty} S(t) \sim$ constant). In Fig. 3.8a, we show $S(t)$ as a function of t for several interaction strengths [21] for a fixed system size. As anticipated, $S(t)$ for the non-interacting case just saturates to a constant. Upon switching on the interaction strength, a slow logarithmic propagation of entanglement is visible. An important note to take (see Fig. 3.8b [21]) is that the long-time saturation value of $S(t)$ scales linearly with system size

($S_\infty = \lim_{t\to\infty} S(t) \sim L$). If the system is ergodic, then the entanglement will spread ballistically [114]. At long times for finite systems, it will saturate to the value, $S_\infty = L\log 2 - \frac{1}{2} + \mathcal{O}(\frac{\log L}{L})$ [137]. In fact, the evolved random product state (a point on a graph such as in Fig. 3.4) in an ergodic system spreads in Fock space, and its long-time limit can be approximated with a random state in Fock space. The bipartite entanglement entropy of such a random state is $L\log 2 - \frac{1}{2} + \mathcal{O}(\frac{\log L}{L})$. Nevertheless, for an MBL system, S_∞ is smaller than the value expected for an ergodic system, indicating that even if the long-time evolved state is a volume-law state, it is non-thermal.

Following the discovery of logarithmic entanglement growth during time-evolution of 1D disordered XXZ spin chains, Serbyn *et al.* [177] study a possible mechanism that would explain such a phenomenon. They find that even arbitrarily weak interactions lead to a bipartite entanglement entropy growth, $S_{\text{ent}}(t) \propto \xi \log(Vt/\hbar)$, where V is the interaction strength and ξ the single-particle localisation length. Very importantly they also state that the saturation value of S_{ent} is of the order of the 'diagonal entropy' S_{diag} [146] of the given initial state. The diagonal entropy is determined by the participation ratios of the initial state in the basis of eigenstates of the system for $V = 0$. This is also described as $S_{\text{diag}} = -\sum P_i(x)\,\ln(P_i(x))$, where $P_i(x)$ are the probabilities of different states in a segment size x calculated from the wave function of the initial state — basically the diagonal elements of a reduced density matrix of a subsystem x.

The Hamiltonian that they use is (apart from constants) equivalent to (3.42) and describes spinless fermions hopping on a disordered chain with nearest-neigh-bour interactions:

$$H = J\sum_{\langle ij\rangle} c_i^\dagger c_j + \sum_i W_i n_i + V\sum_{\langle ij\rangle} n_i n_j, \tag{3.56}$$

where the symbols carry their usual meaning. We mention this version for the purpose of keeping the same notation.

The main ingredient for the calculation is the realisation that for very weak interactions, the many-body eigentstates of the system are not significantly changed but their energies are altered slightly. If we were to fix all but two particles situated at a distance $x \gg \xi$, they will experience an interaction energy of $\approx Ve^{-x/\xi}$ (c.f. exponentially decaying single particle wave functions in the Anderson insulator). This corresponds to a dephasing time of $t_{\text{deph}} \approx \hbar/\Delta E = \hbar e^{x/\xi}/V$. If we look at the system on the whole we discover that there is a resulting hierarchy of dephasing times ranging from $t_{\min} = \hbar/V$, when the particles are next to each other, to $t_{\max} = \hbar e^{L/\xi}/V$, when they are the furthest away possible. Since initial states that were considered e. g. in [21] are superpositions of many eigenstates, the interactions will induce a slow dephasing between these (due to the

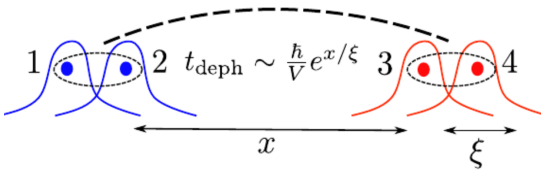

Figure 3.9: Illustration of the initial state (3.57). Here, x denotes the distance between the two particles, while ξ describes the single-particle localisation length. Initially the two particles are made up by two single-particle eigenstates respectively. The dephasing time between many-body states involving these states goes as $t_{\text{deph}} \sim \frac{\hbar}{V} e^{x/\xi}$, due to interactions mediated by the exponentially small tails. Adapted from [177].

energy shift) and thus create entanglement between remote parts of the system. The hierarchy of scales means that a subsystems of length x becomes near maximally entangled with the rest of the system after $t_{\text{deph}} \approx \hbar e^{x/\xi}/V$ and so the bipartite entanglement entropy S_{ent} grows logarithmically.

How does this work in the two particle case? Here we start without interactions or hopping ($V = J = 0$) in an initial state that describes a product state of two distant particles, each prepared in a superposition of two eigenstates that are localised near a specific site. Orbitals 1,2 and 3,4 are taken to be far apart:

$$|\psi_0\rangle = \frac{1}{2}\left(A_1\, c_1^\dagger + A_2\, c_2^\dagger\right)\left(A_3\, c_3^\dagger + A_4\, c_4^\dagger\right)|0\rangle\,, \tag{3.57}$$

where A_1, A_2, A_3, A_4 are coefficients that allow us to vary the strength of the superposition and that have to obey a normalisation condition. The diagonal many-body Hamiltonian in the two-particle subspace would look like (ignoring V's) the following. We choose a many-body basis of $\{|13\rangle, |14\rangle, |23\rangle, |24\rangle, |12\rangle, |34\rangle\}$, with $|ij\rangle \equiv c_i^\dagger c_j^\dagger |0\rangle$:

$$H = \begin{pmatrix} \epsilon_{1,3} & & & & & \\ & \epsilon_{1,4} & & & & \\ & & \epsilon_{2,3} & & & \\ & & & \epsilon_{2,4} & & \\ & & & & \epsilon_{1,2} & \\ & & & & & \epsilon_{3,4} \end{pmatrix}, \tag{3.58}$$

where $\epsilon_{i,j} = \epsilon_i + \epsilon_j$, the single-particle energies, and all other entries are zero. For very weak interactions, the many-body eigenstates are not significantly altered [177] and so the Hamiltonian (3.58) can still be written in diagonal form with only perturbative energy corrections to the many-body eigenenergies ($V_{i,j}$). These perturbative corrections go as $V_{\alpha,\beta} = C_{\alpha\beta} V e^{-x/\xi}$ and hence we obtain an effective 4×4 Hamiltonian due to the large interaction energy ($\sim V$) for states $\{|12\rangle, |34\rangle\}$.

The next question is whether in our effective two particle, small V description we can actually obtain a slow entanglement growth between the particles. We start with the time-evolution of our initial state:

$$|\psi(t)\rangle = \sum_{\alpha,\beta} A_\alpha A_\beta e^{-iE_{\alpha\beta}t} |\alpha\beta\rangle \,, \tag{3.59}$$

with $\alpha, \beta = 1, 2$ and $3, 4$ and $E_{\alpha\beta} = \epsilon_{\alpha,\beta} + V_{\alpha,\beta}$ can be conveniently read off our diagonal Hamiltonian. We can now write the time-dependent reduced density matrix for the left particle ρ_L, which has spatial support near single-particle orbitals 1 and 2. This is done by simply tracing out the right particle with its support at 3 and 4:

$$\rho_L = \frac{1}{4} \begin{pmatrix} A_1^2 (A_3 + A_4)^2 & F(t) \\ F^*(t) & A_2^2 (A_3 + A_4)^2 \end{pmatrix}, \tag{3.60}$$

where $F(t) = A_1 A_2 \left(A_3^2 e^{-i(E_{13} - E_{23})t} + A_4^2 e^{-i(E_{14} - E_{24})t} \right)$. This extended form, compared to [177], allows us to investigate the role of the initial condition a bit more closely. In the simple case of $A_1 = A_2 = A_3 = A_4 = 1$ (and $V \neq 0$), we recover the simple form from [177]:

$$\rho_L = \frac{1}{2} \begin{pmatrix} 1 & F(t)/2 \\ F^*(t)/2 & 1 \end{pmatrix}, \tag{3.61}$$

where $F(t) = e^{-i\Omega t} \left(1 + e^{-i\delta\Omega t}\right)$, $\delta\Omega = V_{14} - V_{24} - V_{13} + V_{23}$, and $\Omega = \epsilon_1 - \epsilon_2 + V_{13} - V_{23}$. We therefore see that the eigenstates of ρ_L oscillate with a very long period, and so we have a very slow growth towards maximum entanglement of $S_{\text{diag}} = \ln(2)$.

The first thing that we can analyse conveniently from the form of (3.60) is that the initial condition has a large impact on S_{diag}, and hence presumably on the form of the entanglement growth. Let us focus on the distribution of the superposition making up the left particle. If we keep A_3, A_4 and the time-dependence in the off-diagonal elements fixed for now, then the distribution of A_1 and A_2 will let us interpolate between two forms of ρ_L, namely:

$$\rho_L = \frac{1}{2} \begin{pmatrix} 1 & 1 \\ 1 & 1 \end{pmatrix} \qquad \text{and} \qquad \rho_L = \begin{pmatrix} 1 & 0 \\ 0 & 0 \end{pmatrix}. \tag{3.62}$$

So while an uneven superposition in the left particle seemingly would reduce the off-diagonal elements (and hence create equal eigenvalues and entanglement), it does not, as we again recover a pure state yielding an eigenvalue distribution of 0 and 1. The homogeneity of the initial condition, or in other words how evenly spread an 'l-bit' is, gives us a measure of the effective size of the reduced density matrix and therefore of the maximum entanglement achievable, which

is called S_{diag}. Since $-\sum_{n=1}^{N} \frac{1}{N} \log(\frac{1}{N}) = \log(N)$, this grows logarithmically with effective matrix size N and hence subsystem size for a given initial state in which we have a completely equal superposition of states (and where small interactions do not change these states).

We conclude that in order to be even able to achieve entanglement, we need to have an effective matrix size that is larger than one, in which case our reduced density matrix has only one non-zero component. Yet this does not yield any entanglement as long as we cannot *independently* make the off-diagonal elements zero. As was very nicely shown in [177], this cannot be done as long as interactions do not change the energies. In that case, $\delta\Omega = 0$ and while $F(t)$ is thus oscillating, it can never be zero. It becomes now immediately obvious that the ratio of A_3 and A_4, as seen from the form of $F(t)$, determines to what degree the off-diagonal elements can become zero. Only in the limit $\frac{A_3}{A_4} \to 1$, can we get perfect cancellation (at a very long period) and hence maximal entanglement. In other words, the less equal a superposition we have for the right particle, the closer we are to $F(t)$ being a pure exponential, which yields eigenvalues of 0 and 1.

3.4.2.6 *Absence of transport*

In the non-interacting case, diffusive transport is naively expected upon adding disorder to the system but proven to be absent for any disorder in one and two dimensions. The interacting many-body case is more complicated not least because it admits a mobility-edge even in one-dimension. The question then is how transport behaves in the ergodic region (see Sec. 3.5), and whether it is absent in the MBL regime. The answer to the latter is of course that it is. Indeed this has been shown in the seminal works on MBL [23, 70]. A vanishing conductivity also follows from the existence of LIOMs that are strictly local (without exponential tails), as can be seen by using the Kubo formula [157]. A numerical demonstration of the absence of transport has been given in [211], in which they show that for an MBL system, the spin-spin correlation function, defined as

$$C(r,t) = \frac{1}{2^L} \text{Tr}\left[S^z_{L/4}(t) S^z_{L/4+r}\right], \tag{3.63}$$

becomes an exponentially decaying function in space at large times: $C(r, t \to \infty) \sim e^{-r/\xi}$, where $\xi > 0$ is a localisation length.

3.5 THE ERGODIC SIDE OF MANY-BODY LOCALISATION

Most of the work concerning MBL has focused on the study of the localised, non-ergodic regime. Very little attention was paid to the ergodic phase [8, 127, 191]. The reason for this is that following the seminal work of [23], it was largely accepted that the ergodic phase in

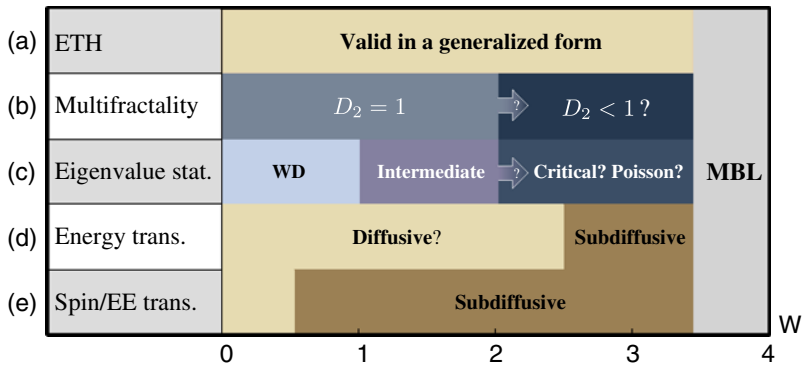

Figure 3.10: A recent overview of some of the phenomena in the ergodic region preceding the MBL transition. a) While the ETH is expected to hold in a generalised form, other features suggest an intermediate phase. b) The generalised fractal dimension D_q is not constant, but takes multiple values, while c) the energy level statistics have been shown to exhibit intermediate features. Lastly, the transport of d) energy and e) spin exhibits features of anomalous subdiffusive transport. Adapted from [115].

systems exhibiting an MBL transition was a trivial metal, albeit a bad one [23]. In recent years it has become increasingly evident that this might in fact not be the case. For a detailed discussion, we refer to the excellent review [115], from which Fig. 3.10 was adapted. It provides a detailed overview over the different diagnostics of anomalous behaviour in the ergodic region. In this section, we briefly discuss relevant observables, which are by no means an exhaustive list (see e. g. [69] for further indicators).

A) ETH Ergodic systems are generally believed to obey the ETH. However, in systems exhibiting MBL, it was shown that there can be anomalous, subdiffusive transport (for details see below). In this case it was found that the system satisfies a modified version of the ETH, in which the scaling of the variance of the off-diagonal matrix elements with system size requires power-law corrections to the exponential in (3.9) [114].

B) MULTIFRACTALITY The generalised fractal dimension D_q, introduced in Sec. 3.4.2, was studied in detail in [116, 178, 185]. It was shown that there seems to be a broad critical region preceding the MBL transition in which the IPR cannot be described by a single fractal dimension, but instead requires a multitude of exponents. A similar feature has been shown for Anderson localisation. The multifractal region seems to shrink with increasing system size, suggesting that it might be a finite size effect.

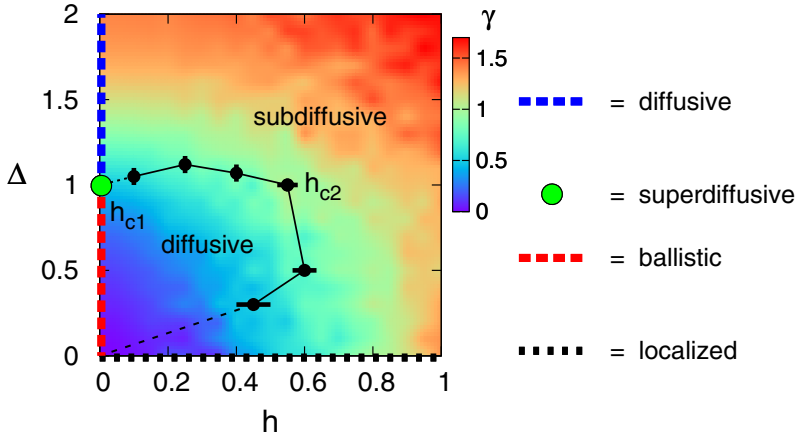

Figure 3.11: A study of the spin transport in the spin-1/2 XXZ chain (3.42) for which in this figure $J_x = J_y = 1$ and $J_z = \Delta$. The disorder strength W is denoted by h. By driving currents in and obtaining a non-equilibrium steady state, a coefficient describing transport may be obtained. $\gamma = 0$ signifies ballistic transport, while $\gamma = 1$ stands for regular diffusion. Other coefficients entail anomalous super- and subdiffusive transport. The colour scheme is a guide to the eye suffering severe finite size effects in the small h, Δ regime. The black line denotes the transition from diffusive to subdiffusive transport. Adapted from [212].

C) EIGENVALUE STATISTICS The gap-ratio parameter (3.45) has proven to be a useful measure in determining the broad distinction between a localised and a delocalised regime. However, recent studies indicate that the flow from Wigner-Dyson to Poisson statistics may be a two-stage process. Coming from the delocalised side, one still has long-ranged interaction between the energy levels, but with shrinking correlation length. Coming from the localised side, the interactions between the levels are already local, and belong to the same or similar critical family as Poisson statistics and thus give a similar gap-ratio parameter $\bar{r}$. Finite size effects may not be excluded in this case [28, 176, 185]. It is conjectured that the boundary between those regions coincides with the onset of a Griffiths phase [72, 196] or subdiffusive transport.

D),E) SPIN AND ENERGY TRANSPORT The Hamiltonian (3.42) conserves energy and total magnetisation (or particle number in the case of (3.44)), such that those quantities may be transported. The expectation in an ergodic region would be, to some degree for the same reasoning presented for the Anderson case, diffusive transport. After first evidence [18] of anomalous diffusion, it has been shown in several numerical studies that for intermediate disorder preceding MBL there exists a region in which subdiffusive spin (or particle) transport prevails. The boundaries of this region are disputed, but the most compelling evidence so far has been obtained by [212]. They show

that for $J_\perp = 1$ and $J_z > 1$ (strong interactions), subdiffusive transport prevails for all finite disorder strengths, while for $J_z < 1$, there is a transition between diffusive and subdiffusive transport at weak W.

This slower form of transport (see Ch. 8) has been speculated to be linked to long-tailed (i. e. non-Gaussian) distributions for the off-diagonal matrix elements of local spin operators in the ergodic phase [113, 114]. In any case the phenomenology is complex, as there seems to be a mechanism that causes spin excitations (or particles) to 'get stuck', something potentially linked to rare Griffiths regions [72, 196]. Recently it has also been suggested that the subdiffusion may be transient [27]. The situation is again different in the case of energy transport, which is much harder to envision physically. However, recent results have also reported diffusive and subdiffusive transport for energy transport [190]. A part of this thesis is dedicated to studying energy transport in the case of a broken $U(1)$-symmetry. Results in higher dimensions are challenging and remain sparse to this day [19].

In conclusion we can say that the region preceding MBL is indeed fascinating, and in many ways much richer than just the 'bad metal' as it was dubbed by Altshuler [115]. Not least if we inspect Fig. 3.10, we see that these phenomena need *not* coincide. Further, some of these features are believed to disappear in the thermodynamic limit, while others seem to persist. Some of this thesis is dedicated to answering this question further.

4

NUMERICAL TECHNIQUES

4.1 INTRODUCTION

Since one of the first numerical experiments, the celebrated Fermi-Pasta-Ulam problem at Los Alamos in 1955 (see Introduction) [62], computational physics has come a long way. With the ever growing power of desktop and supercomputers, the possibilities for numerical investigation of physical problems have equally reached new boundaries in the past decades. Nonetheless the fundamental problem of numerical quantum physics remains. What is ubiquitous to any physicist today, is often hard to grasp for an outsider or newcomer: the exponential explosion of the Hilbert space describing the physical system in question. The sheer immensity of the task becomes very clear however if we consider a simple example. Let's imagine a quantum system that can only be in two states, say up or down, such as shown in Fig. 4.1. This is often called a qubit, a 'quantum bit', alluding to its classical analogue the 'bit', which can be one of two things and is often expressed as 0 or 1 in binary notation. Following the notation of Sec. 2.1.1, we would describe the state of this qubit as

$$|\psi\rangle = c_0 |\uparrow\rangle + c_1 |\downarrow\rangle , \tag{4.1}$$

where the c's are complex coefficients that ensure normalisation. And this is already the entirety of the problem, namely the superposition principle of quantum mechanics. The qubit can be in a superposition of up and down as long as no measurement is performed in the $\{|\uparrow\rangle , |\downarrow\rangle\}$ basis. This is because the wave function is not a physical quantity and cannot be extracted in an experiment. The well known 'Schrödinger cat' [168, 169], supposedly dead and alive at the same time, was devised to show the absurdity of the superposition principle in the macroscopic world. In any case, storing this state on a computer is certainly no difficult task. The two decimal numbers required to describe (4.1) occupy 2×8 bytes of storage when using double precision. The problem arises when coupling several qubits together, i. e. when enlarging the system. Again borrowing from Sec. 2.1.4, our system of two qubits now reads

$$|\psi\rangle = c_0 |\uparrow\rangle \otimes |\uparrow\rangle + c_1 |\downarrow\rangle \otimes |\uparrow\rangle + c_2 |\uparrow\rangle \otimes |\downarrow\rangle + c_3 |\downarrow\rangle \otimes |\downarrow\rangle . \tag{4.2}$$

Adding a third spin would in turn require to store 4 coefficients and so on. This $\mathcal{D} = 2^N$ scaling of the Hilbert space (the c's make up the state vector), where N describes the number of qubits, is the root of the exponential explosion. The wave function $|\psi\rangle$ of a system of

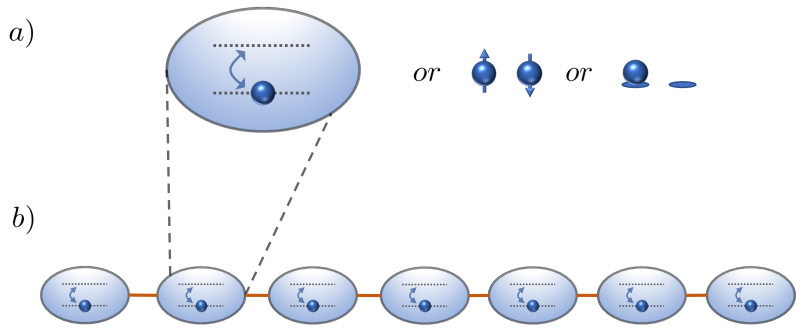

Figure 4.1: a) A cartoon of a typical quantum 2-level system. This can be an object such as an atom that only has two internal states like its ground and first excited state. It could however also be a magnetic system, with the magnetisation pointing along or against some fixed axis. Lastly of course, particles and holes also allow for a natural occurence of 'two-levels'. b) The exponential explosion of the Hilbert space necessary to describe the state of a larger system (here $N = 7$) scales in the case of a two-level system as 2^N. This makes brute-force numerical treatments impossible for even moderate system sizes.

$N = 27$ qubits, not quite the formidable system size, would require of the order of Gigabytes of storage. Adding a mere 6 spins necessitates already of the order of Terabytes. And so far we are only concerned with storing the information of *one* quantum state, let alone manipulating it in any way. Is therefore all hope lost of ever simulating the quantum dynamics of realistic physical systems?

The answer is as expected not so simple. Richard Feynman addressed this question in 1981, in a keynote speech later titled 'Simulating Physics with Computers' [63]. He concludes that if we do not want a machine that grows exponentially with the desired simulated volume of space and time, then we need an entirely new device, one that is itself quantum. And if this device would be a universal one, not a simulator for special purposes, then it could truly be called a 'quantum computer'. The field of quantum computing [52, 112, 128] and special purpose quantum simulators is a very active one [12, 31, 34, 67, 88, 98, 164], not least since the advent of cold atom physics in optical lattices [32, 94, 110]. However, while there have been considerable advances in recent years, we are still *very* far from having a working useful universal quantum computer. And so in the meantime there is considerable need for alternative theoretical methods to circumvent or reduce the exponential scaling of the Hilbert space.

The most straightforward way to tackle the problem is of course to brute-force it. This entails generating the full many-body Hamiltonian, in our example a $2^N \times 2^N$ matrix, and use *exact diagonalisation* [198] (ED) to obtain all or a subset of the eigenvalues and eigenvectors. In this procedure the exponential scaling is even worse than the simplified example above as with current implementations

the complexity of a numerical diagonalisation procedure scales as $\approx \mathcal{O}(d^{3N})$, where d is the size of the local Hilbert space ($d = 2$ for our qubit). While we have just affirmed the need for alternative approaches, there are already a few possibilities within the framework of ED. For instance, if we are only interested in the ground state, then we can somewhat ease the exponential scaling by a Lanczos algorithm which only targets the ground state of the system [107]. We can further exploit underlying symmetries of the system which make the Hamiltonian matrix block diagonal and hence effectively smaller. And ultimately there are a series of useful finite-size scaling techniques which allow at times to extrapolate to the thermodynamic limit (here $N \to \infty$) [116]. All in all these methods are nonetheless limited to system sizes of $\mathcal{O}(10)$, and hence fail for systems with long correlation lengths or severe finite-size effects.

Other, more approximative methods are *series expansion techniques*, which expand a specific quantity in terms of a power series of one or more parameters [132]. The main limitation of these techniques is to achieve high enough expansion order so that the quantity of interest converges. This turns out to be most difficult at thermal phase transitions, where the physics is dominated by long-ranged correlations.

Arguably the most powerful and widely used numerical technique for strongly correlated quantum systems in the past is *Quantum Monte-Carlo* (QMC). In the now long history of this algorithm there have been developed many facets of this method [64, 73, 181], but they all share a common feature, which is the Monte Carlo algorithm whose modern version was invented by Stanislaw Ulam in the late 1940s. The main concept of solving a model stochastically by a random sampling technique is best described by an unpublished remark Ulam made allegedly in 1983:

> *'The first thoughts and attempts I made to practice [the Monte Carlo method] were suggested by a question which occurred to me in 1946 as I was convalescing from an illness and playing solitaires. The question was what are the chances that a Canfield solitaire laid out with 52 cards will come out successfully? After spending a lot of time trying to estimate them by pure combinatorial calculations, I wondered whether a more practical method than 'abstract thinking' might not be to lay it out say one hundred times and simply observe and count the number of successful plays.'* [56]

The method was first put to use in the Manhattan Project and in the development of the hydrogen bomb. QMC in turn uses this framework to tackle difficult many-body problems beyond a mean-field approximation for large systems with only polynomial size scaling. For many systems, QMC can be implemented highly efficiently and proved to be a method to circumvent the exponential scaling. However, for most frustrated magnets and models of itinerant fermions,

QMC techniques are plagued by the so-called sign problem [187] (to which there are certain exceptions [7, 85]). In those cases we again face an exponential scaling of the algorithm.

A recent powerful alternative has arisen with the invention of so-called *Tensor Network techniques* (TN) [58, 134, 166]. They are a different approach to QMC in tackling the many-body problem. Their common framework builds on parameterising the quantum mechanical wave function as a collection of connected tensor objects. These networks can often, most notably for one-dimensional systems, be stored and manipulated efficiently. The introduction of the TN framework is a formalisation of the pioneering work of Steve White in 1992, when he introduced the density matrix renormalisation group (DMRG) [200, 201]. It is an algorithm for obtaining the ground state of a one-dimensional lattice model in the form of a matrix product state (MPS) [78, 165].

After initial studies of static properties such as energy, order parameter and correlation functions of ground states and low lying eigenfunctions of strongly correlated Hamiltonians (Heisenberg, $t - J$ and Hubbard models), it was quickly extended to investigate dynamic properties [77, 95, 106]. The immense success of DMRG in investigating one-dimensional systems stems from the fact that it does not suffer from a sign problem, its non-perturbative character and the access to large system sizes. In fact often the accuracy of the result is only limited by machine precision even for moderate computational resources.

Unsurprisingly the feasibility for an extension to higher dimensions and real-time dynamics was quickly investigated. It turns out that both aspects are closely related. DMRG only proved moderately successful for two dimensional lattices and long time evolution [202]. In both cases it was then found that the success of the DMRG approach was built on the low entanglement structure [193] of many quantum ground-states of interest (area law) [59], which could only then be efficiently represented by a MPS. In the case of higher dimensions even an area law scaling is problematic while in real time-evolution the entanglement essentially grows linear in time, both culminating in an exponential increase of required numerical resources.

After some previous work [4, 25, 55, 135], the connection between DMRG and MPS, hence the establishment of the TN field was formalised by Vidal and co-workers [44, 192, 194, 195]. This allowed for more abstract development and extensions hard to express in conventional DMRG language [79, 148] of which one example is the time-evolving block decimation (TEBD) algorithm for time-evolution.

While TN methods are currently the most widely used numerical technique for one-dimensional quantum lattice systems, and seem far from having saturated in innovation, there are already interesting new proposals. In line with the current excitement around artifi-

cial intelligence and deep learning in all areas of research and daily life applications, there are already promising proposals that neural networks can be an integral part in future numerical applications in physics [35].

Much of the work in this thesis has been performed using numerics. In condensed matter physics, where correlations dominate the systems of interest, one finds some of the most interesting challenges of modern quantum mechanics. These challenges however come at a cost. Exact analytical solutions to more complex problems are rare. And even though numerics have, as described above, severe limitations too, they often provide the only road for theory to make meaningful predictions. The techniques used in this thesis are ED and TN methods. While the former needs no further introduction than has already been given, a numerical solver finds the eigenvalues and eigenvectors of a given (Hamiltonian) matrix, the remainder of this chapter is used to introduce the latter.

We start by introducing the most commonly used TN in one-dimension, the matrix product state (MPS), as well as its diagrammatic representation. Widely used algorithms for ground state search (DMRG) and time-evolution (TEBD) follow. We finish by introducing the changes necessary to simulate open-system dynamics and to drive thermal currents.

4.2 MATRIX PRODUCT STATES

We already encountered the area-law of entanglement and the fact that this allows us to parametrise a quantum state very efficiently. Indeed, we may cite [58] to show that this law lies at the root of the success of TN:

> *'Many natural quantum lattice models have ground states that are little, in fact very little, entangled in a precise sense. This shows that 'nature is lurking in some small corner of Hilbert space', one that can be essentially efficiently parametrised. [...] In the end, the reason for tensor network methods to provide such powerful tools is rooted in the fact that natural ground states satisfy area laws (or show small violations thereof).'*

In the following we want to look at MPS from two angles. On the one hand they emerge as an interesting class of quantum states for analytic study, or we can in fact rewrite *any* pure state as a MPS via the Schmidt decomposition introduced in (2.21). Historically MPS were discovered in the former sense, well before a connection to TN was made [166]. Before however, we are going to introduce a diagrammatic representation of MPS and TN in general, that simplifies the abundant use of explicitly written out matrix multiplications and tensor contractions. In the spirit of Feynman diagrams in field theory,

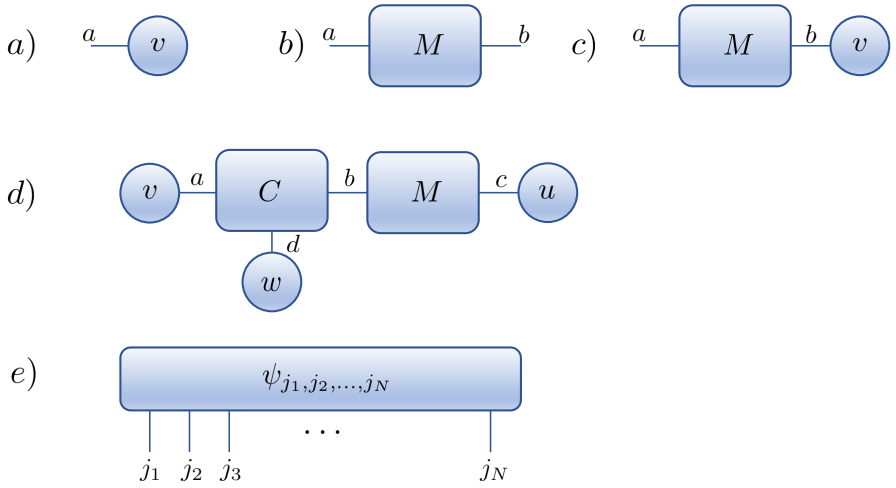

Figure 4.2: a) A rank-1 tensor v_a (i. e. a vector) represented graphically. The object is some shape, while its index is represented by a line emerging from the shape. b) A rank-2 tensor or matrix M_{ab}, with two open indices. c) A tensor contraction between a matrix and a vector, i. e. a matrix multiplication: $\tilde{v}_a = \sum_b M_{ab} v_b$. d) More complex arbitrary TN: $\gamma = \sum_{a,b,c,d} C_{abd} M_{bc} v_a w_d u_c$. The result of the contracted network is a single scalar number γ. e) The wave function $\psi_{j_1 j_2 \ldots j_N}$ with 2^N possible entries (if $d = 2$).

these diagrams are pictorial representations of mathematical expressions and help grasping the essence of an algorithm.

In this approach, we represent every tensor object by a shape (circle, square, triangle). Each individual index of a tensor is represented by a line that originates from the shape and is open ended. A contraction of two tensor is then expressed by a line connecting two shapes. This signifies a sum over the respective index of the two tensors. In this notation, we can express arbitrarily complicated tensor networks and contractions with simple shapes connected by lines. An example of this notation can be found in Fig. 4.2.

4.2.1 *Basics and notation*

We will start by describing how to decompose a generic quantum state $|\psi\rangle$ into a matrix product state by successive application of the Schmidt decomposition. From now on and for the rest of this thesis we will work in one dimension. We consider a chain of N sites, where we label the local basis on site i by $|j_i\rangle$, where $j_i = 1, \ldots, d$. In the example in Sec. 4.1, we had a local basis of dimension $d = 2$, which we denoted by $|\uparrow\rangle$ and $|\downarrow\rangle$. As previously seen, we can then write a generic state as

$$|\psi\rangle = \sum_{\{j_i\}} \psi_{j_1 j_2 \ldots j_N} |j_1, j_2, \ldots, j_N\rangle \,. \tag{4.3}$$

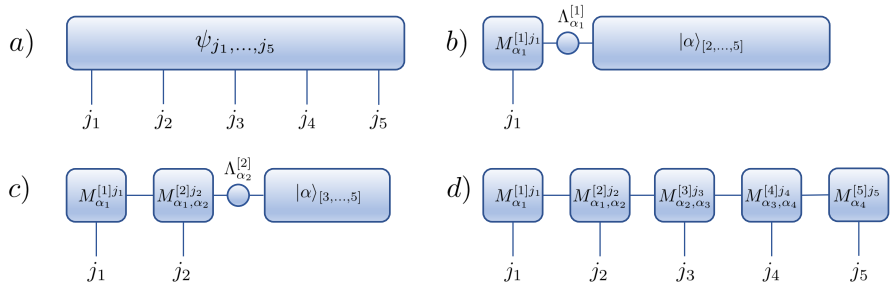

Figure 4.3: a) An example wave function for a system of $N = 5$ sites. b) We start the successive decomposition into a MPS by a Schmidt decomposition at the first bond. The matrix $M^{[1]j_1}_{\alpha_1}$ links the Schmidt states of the first site to the local basis and $\Lambda^{[1]}$ are the Schmidt values at that bond. c) We proceed to the second bond and apply a Schmidt decomposition again. $M^{[2]j_2}_{\alpha_1,\alpha_2}$ now links the Schmidt states of the left two sites to the local basis $|j_2\rangle$ *and* the Schmidt states at the first site. These are linked to the to local basis using the results from the previous step. d) We continue the procedure along the entire chain in order to obtain a MPS formulation of the arbitrary quantum state $|\psi\rangle$.

We start by applying a Schmidt decomposition (2.23) to (4.3), such that we split the state $|\psi\rangle$ into the first site and the rest such that (now and for the rest of this thesis omitting the $\otimes$ symbol)

$$|\psi\rangle = \sum_{\alpha_1=1}^{d} \Lambda^{[1]}_{\alpha_1} |\alpha_1\rangle_{[1]} |\alpha_1\rangle_{[2,\ldots,N]} . \tag{4.4}$$

The states $|\alpha_1\rangle_{[1]}$ and $|\alpha_1\rangle_{[2,\ldots,N]}$ form the new orthogonal basis for the left and right part, here first site and rest, as previously done in Sec. 2.3. The square brackets denote the relation of the object to the local site. The diagonal matrix $\Lambda^{[1]}_{\alpha_1}$ contains the Schmidt values between the first site and the rest of the system. In order to restore a relation to the physical basis $\{|j_n\rangle\}$, we invert the part of the Schmidt decomposition where $\mathbf{U}$ (see Sec. 2.23) is combined with the original basis and write (4.4) as

$$|\psi\rangle = \sum_{j_1=1}^{d} \sum_{\alpha_1=1}^{d} M^{[1]j_1}_{\alpha_1} \Lambda^{[1]}_{\alpha_1} |j_1\rangle |\alpha_1\rangle_{[2,\ldots,N]} , \tag{4.5}$$

where $M^{[1]j_1}_{\alpha_1}$ is the first matrix of the MPS and relates the Schmidt states $|\alpha_1\rangle_{[1]}$ with the local states $|j_1\rangle$. It is given by $M^{[1]j_1}_{\alpha_1} = \langle j_1|\alpha_1\rangle_{[1]}$, where j_1 is called the physical index or bond while α_1 is internal or virtual index or bond. The name *matrix* product state refers to the virtual bonds alone and the first matrix (as well as the last) is in fact a vector. We then perform a Schmidt decomposition of the state on the second bond, such that

$$|\psi\rangle = \sum_{\alpha_2=1}^{d^2} \Lambda^{[2]}_{\alpha_2} |\alpha_2\rangle_{[1,2]} |\alpha_2\rangle_{[3,\ldots,N]} . \tag{4.6}$$

We then proceed as above and invert part of the Schmidt decomposition and write (4.6) as

$$|\psi\rangle = \sum_{\alpha_1=1}^{d} \sum_{\alpha_2=1}^{d^2} \sum_{j_1,j_2=1}^{d} M_{\alpha_1}^{[1]j_1} M_{\alpha_1,\alpha_2}^{[2]j_2} \Lambda_{\alpha_2}^{[2]} |j_1, j_2\rangle_{[1,2]} |\alpha_2\rangle_{[3,\ldots,N]}, \quad (4.7)$$

where $M_{\alpha_1,\alpha_2}^{[2]j_2}$ is the second matrix of the MPS and relates mixed basis states $|\alpha_1\rangle_{[1]} |j_2\rangle$ with the left Schmidt states $|\alpha_2\rangle_{[1,2]}$. It is given by $M_{\alpha_1,\alpha_2}^{[2]j_2} = \left[\langle\alpha_1|_{[1]} \langle j_2|\right] |\alpha_2\rangle_{[1,2]}$. We can continue this procedure along the chain for each individual site as depicted in Fig. 4.3. The last matrix $M_{\alpha_{N-1}}^{[N]j_N}$, like the first, relates the Schmidt states $\Lambda_{\alpha_{N-1}} |\alpha_{N-1}\rangle_{[N]}$ to the local basis j_N. We therefore arrive at a final MPS representation of an arbitrary quantum state $|\psi\rangle$ as

$$|\psi\rangle = \sum_{\{j_i\}} \sum_{\{\alpha\}} M_{\alpha_1}^{[1]j_1} M_{\alpha_1,\alpha_2}^{[2]j_2} \ldots M_{\alpha_{N-2},\alpha_{N-1}}^{[N-1]j_{N-1}} M_{\alpha_{N-1}}^{[N]j_N} |j_1, j_2, \ldots, j_N\rangle . \quad (4.8)$$

Fig. 4.3 illustrates much better why this is a MPS. We still keep the original physical indices j_i, corresponding to the local Hilbert space of size d, but the tensor $\psi_{j_1,\ldots,j_N}$ has been transformed into a product of matrices, hence the name, connected by virtual or bond indices α. For every site n, we have a set of d matrices $M_{\alpha_n,\alpha_{n+1}}^{[n]}$ of dimension $\chi_n \times \chi_{n+1}$ that are usually grouped into rank-3 tensors. We further note that the matrices at the boundary are vectors, such that when we contract (multiply out) the MPS we arrive at a single 1×1 scalar number $\psi_{j_1 j_2 \ldots j_N}$.

The above representation alone does not circumvent the exponential scaling of the Hilbert space, in fact (4.8) requires more coefficients to be stored than (4.3). The key to compressing the state lies in the possibility to restrict the sizes of the matrices M while controlling the introduced error. If we, as defined in Sec. 2.3.1, choose $\chi_{\max}$ as some upper limit for the size of matrix M, then the total number of coefficients needed to be stored increases only polynomially with system size. In numerical simulations, $\chi_{\max}$ then becomes the main parameter that controls the accuracy of the simulation. As (4.8) was constructed by successive Schmidt decomposition, which in turn is deeply related to the entanglement of a state, it becomes quite intuitive that $\chi_{\max}$ puts an upper bound to the entanglement captured by the MPS representation of $|\psi\rangle$. Specifically for any subset $\mathcal{C}$ of consecutive sites, it can be easily shown that the entanglement entropy is bounded as $S(\rho^{\mathcal{C}}) \leq 2\,(\log(\chi_{\max}))$. The entanglement entropy of the MPS describing the system is therefore bounded from above by some constant in the number of sites N [58].

This is a reformulation of the area-law (see Sec. 2.3.1), which in turn means that a MPS is particularly suited to describe area law states, i. e. for example ground states of 1D gapped systems. Since many powerful algorithms such as DMRG or TEBD, as well as the

procedure to calculate expectation values can be implemented very efficiently in the MPS or TN framework, this formulation has become so important and widely used.

4.2.2 *Historical appearance of matrix product states*

As previously mentioned, so-called MPS were already discovered as an interesting class of quantum states for analytical study. Here we just briefly want to mention the most prominent examples in ascending complexity, namely (i) a trivial product state, (ii) a product of singlets and (iii) the one-dimensional spin-1 AKLT state.

(i) A *product state* $|\psi\rangle = |\phi^{[1]}\rangle \otimes |\phi^{[2]}\rangle \otimes \cdots \otimes |\phi^{[N]}\rangle$ can easily be written in the form of (4.8). Because it has no entanglement, all bond dimensions are simply $\chi_n = 1$ and hence the $M^{[n]}$ are simply 1×1 'matrices' given by $M^{[n]j_n} = \left(\phi^{[n]}_{j_n}\right)$. As a concrete example, we can consider the product state $|\leftarrow \cdots \leftarrow\rangle \equiv \left(\frac{1}{\sqrt{2}}|\uparrow\rangle - \frac{1}{\sqrt{2}}|\downarrow\rangle\right) \otimes \cdots \otimes \left(\frac{1}{\sqrt{2}}|\uparrow\rangle - \frac{1}{\sqrt{2}}|\downarrow\rangle\right)$, which is approximately the ground state for the transverse field Ising model (2.18) for $g \gg 1$. It is represented by a MPS with uniform matrices

$$M^{[n]\uparrow} = \begin{pmatrix} \frac{1}{\sqrt{2}} \end{pmatrix} \qquad \text{and} \qquad M^{[n]\downarrow} = \begin{pmatrix} -\frac{1}{\sqrt{2}} \end{pmatrix}. \tag{4.9}$$

Another product state such as the well-known Neel state $|\uparrow\downarrow\uparrow\downarrow\ldots\rangle$, which does not have a uniform local state, is described by different matrices on odd and even sites

$$\begin{aligned} M^{[2n-1]\uparrow} &= M^{[2n]\downarrow} = (1) \\ M^{[2n-1]\downarrow} &= M^{[2n]\uparrow} = (0)\,, \end{aligned} \tag{4.10}$$

where $n = 1, \ldots, N/2$.

(ii) As a first example of a state with entanglement, we can consider a *product of singlets* $\left(\frac{1}{\sqrt{2}}|\uparrow\downarrow\rangle - \frac{1}{\sqrt{2}}|\downarrow\uparrow\rangle\right) \otimes \cdots \otimes \left(\frac{1}{\sqrt{2}}|\uparrow\downarrow\rangle - \frac{1}{\sqrt{2}}|\downarrow\uparrow\rangle\right)$. On every other bond we thus have a maximally entangled singlet, while the global state is a product state of such singlets. This state is represented by a MPS with 1×2 matrices on odd sites and 2×1 matrices on even sites given by

$$\begin{aligned} M^{[2n-1]\uparrow} &= \begin{pmatrix} \frac{1}{\sqrt{2}} & 0 \end{pmatrix}, M^{[2n-1]\downarrow} = \begin{pmatrix} 0 & -\frac{1}{\sqrt{2}} \end{pmatrix} \\ M^{[2n]\uparrow} &= \begin{pmatrix} 0 \\ 1 \end{pmatrix}, M^{[2n]\downarrow} = \begin{pmatrix} 1 \\ 0 \end{pmatrix}. \end{aligned} \tag{4.11}$$

(iii) The *Spin-1 AKLT state* was introduced by Affleck, Kennedy, Lieb and Tasaki (AKLT) after they constructed an exactly solvable $S = 1$ Hamiltonian

$$H = \sum_j \mathbf{S}_j \mathbf{S}_{j+1} + \frac{1}{3}\left(\mathbf{S}_j \mathbf{S}_{j+1}\right)^2, \tag{4.12}$$

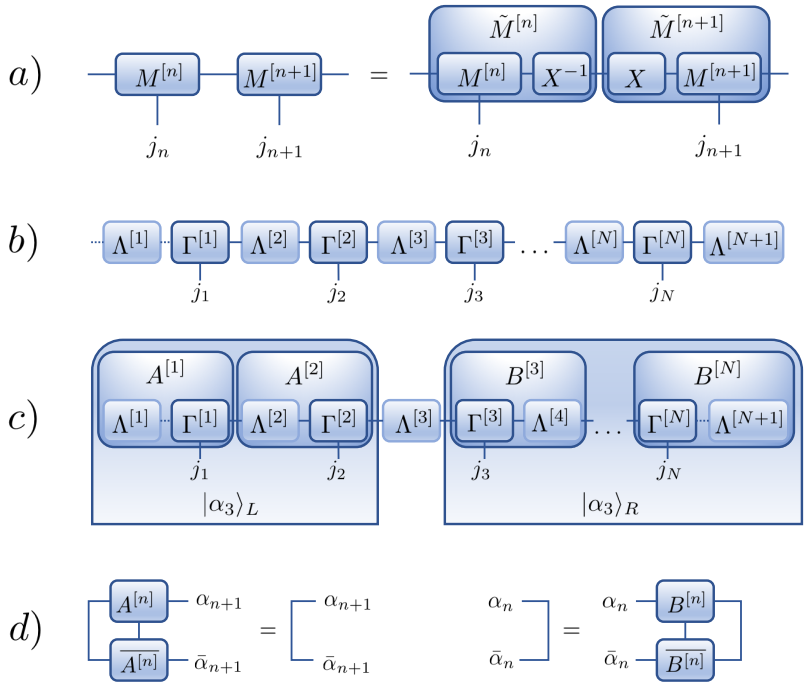

Figure 4.4: a) The choice of M matrices to describe $|\psi\rangle$ is not unique. Inserting an identity $I = X^{-1}X$ transforms the M, but leaves the global state unchanged. b) We use this gauge freedom to define a canonical form, where $\Lambda^{[n]}$ are diagonal matrices containing the Schmidt values of a Schmidt decomposition between sites n and $n+1$. c) The mixed canonical form allows to for the Schmidt decomposition to be read off for any bipartition, here between the sites 2 and 3. d) Orthonormality properties of the left and right canonical forms of the MPS.

where $\mathbf{S}$ are spin-1 operators (with spin projection $+1, 0, -1$). For open boundary conditions, the ground state is four-fold degenerate and can be represented by the three (as $d = 3$ for spin-1) uniform matrices $M^{[n]}$ with bond dimension $\chi = 2$ as

$$M^{[n]+1} = \sqrt{\frac{4}{3}} \begin{pmatrix} 0 & 0 \\ \frac{1}{\sqrt{2}} & 0 \end{pmatrix} \qquad M^{[n]0} = \sqrt{\frac{4}{3}} \begin{pmatrix} \frac{1}{2} & 0 \\ 0 & -\frac{1}{2} \end{pmatrix}$$
$$M^{[n]-1} = \sqrt{\frac{4}{3}} \begin{pmatrix} 0 & -\frac{1}{\sqrt{2}} \\ 0 & 0 \end{pmatrix}, \tag{4.13}$$

where $1 < n < N$ for the bulk and where the edge sites actually cause the four-fold degeneracy. For more details, we refer to [82].

4.2.3 *Canonical form*

The representation (4.8) is not unique however. Let us consider a bond between sites n and $n+1$ which defines a bipartition of the lattice in

$L = \{1, \ldots, n\}$ and $R = \{n+1, \ldots, N\}$. Given an invertible $\chi_{n+1} \times \chi_{n+1}$ matrix X, we can insert the identity $I = X^{-1}X$ between the matrices $M^{[n]}$ and $M^{[n+1]}$, such that

$$\begin{aligned} M^{[n]j_n} &\to \tilde{M}^{[n]j_n} := M^{[n]j_n} X^{-1} \\ M^{[n+1]j_{n+1}} &\to \tilde{M}^{[n+1]j_{n+1}} := X M^{[n+1]j_{n+1}}. \end{aligned} \tag{4.14}$$

Under this transformation, which we can perform at all sites, $|\psi\rangle$ still represents the same state (see Fig. 4.4a). This gauge freedom exists on every virtual bond α of the M matrices and can be used to define a very convenient 'canonical' form following [193] in which the bond index corresponds to the Schmidt decomposition at that bond, for all bonds simultaneously. Without loss of generality, we can write the matrices $M^{[n]j_n}$ as a product of $\chi_{n-1} \times \chi_n$ matrices $\Gamma^{[n]j_n}$ and positive, real, square diagonal matrices $\Lambda^{[n]}$,

$$|\psi\rangle = \sum_{j_1,\ldots,j_N} \Lambda^{[1]} \Gamma^{[1]j_1} \Lambda^{[2]} \Gamma^{[2]j_2} \Lambda^{[3]} \ldots \Lambda^{[N]} \Gamma^{[N]j_N} \Lambda^{[N+1]} |j_1, \ldots, j_N\rangle \,, \tag{4.15}$$

as shown in Fig. 4.4b. We have introduced trivial 1×1 matrices $\Lambda^{[1]} \equiv \Lambda^{[N+1]} \equiv (1)$ for uniform representation (which also means that the label of the Λ has increased by one). This form allows us to rewrite the MPS in terms of the bipartition into L and R. Contracting the tensors Γ and Λ on both sides of the bipartition, we can define a set of χ_n wave functions $|\alpha\rangle_{[1,\ldots,n]}$ and $|\alpha\rangle_{[n+1,\ldots,N]}$ to the left and right of the bond (see Fig. 4.4c), such that $|\psi\rangle$ takes the form

$$|\psi\rangle = \sum_{\alpha=1}^{\chi} \Lambda^{[n]}_{\alpha} |\alpha\rangle_{[1,\ldots,n]} \otimes |\alpha\rangle_{[n+1,\ldots,N]} \,. \tag{4.16}$$

This looks tantalizingly close to the original definition of a Schmidt decomposition (2.23). However, in general $|\alpha\rangle_{L/R}$ need not form an orthonormal set, i. e. $\langle\alpha'|\alpha\rangle_{L/R} \neq \delta_{\alpha',\alpha}$. We therefore define the canonical form of an MPS in the representation of $\{\Gamma^{[1]}, \Lambda^{[1]}, \ldots, \Gamma^{[N]}\}$ such that for every bond n, the set of Schmidt states $|\alpha\rangle_{[1,\ldots,n]}$ and $|\alpha\rangle_{[n+1,\ldots,N]}$ along with the Schmidt values $\Lambda^{[n]}$ form a Schmidt decomposition of $|\psi\rangle$. This means that $\langle\alpha'|\alpha\rangle_{[1,\ldots,n]} = \delta_{\alpha',\alpha}$ and equally that $\langle\alpha'|\alpha\rangle_{[n+1,\ldots,N]} = \delta_{\alpha',\alpha}$ along with $\sum \left(\Lambda^{[n]}_{\alpha}\right)^2 = 1$ on every bond n. In that sense we interpret X in (4.14) as a basis transformation for $|\alpha\rangle_{L/R}$ such that it maps them to the correct orthonormal Schmidt basis. In practice this is much more easily achieved by successive application of an SVD to the M matrices moving along the chain as is depicted in Fig. 4.3.

While the canonical form (4.15) is very useful by allowing us to read off the Schmidt decomposition at any bond, in practice the Schmidt values $\Lambda^{[n]}$ are grouped with either $\Gamma^{[n]j_n}$ or $\Gamma^{[n]j_{n+1}}$ such that we define

$$A^{[n]j_n} \equiv \Lambda^{[n]} \Gamma^{[n]j_n} \qquad \text{and} \qquad B^{[n]} \equiv \Gamma^{[n]j_n} \Lambda^{[n+1]}. \tag{4.17}$$

A and B matrices fulfill different orthonormality conditions such as depicted in Fig. 4.4d. If we write an MPS entirely in terms of A tensors (B tensors), then it is said to be left (right) canonical. Note that the MPS obtained from successive Schmidt decomposition from the left of a general state resulted in a left-canonical MPS, while the examples given in Sec. 4.2.2 were all in right-canonical form. For (4.16) to be a Schmidt decomposition, the matrices to the left of the bipartition need to be in left-canonical form while the matrices to the right need to be in right canonical form. The resulting MPS in then said to be in a 'mixed'-canonical form as depicted in Fig. 4.4c for a bipartition between sites $n = 2$ and $n = 3$, where the A and B tensors transform the Schmidt basis from one bond to the next.

As already noted, *any* state can be represented in the form of an MPS if we allow an arbitrary bond dimension $\chi_{\max}$. In order to avoid an explosion in needed computational resources, we truncate the matrices to a moderate $\chi_{\max}$. It turns out that a simple truncation of the Schmidt decomposition is optimal locally to that bond in that it minimises the error ϵ in (2.27). As a consequence, when our MPS is in (mixed) canonical form, we can simply discard the rows of $A^{[n]j_n}$ and columns of $B^{[n+1]j_{n+1}}$ that correspond to the smallest Schmidt values of $\Lambda^{[n+1]}$. To preserve the norm of the wave function, we renormalise the remaining Schmidt values $\Lambda^{[n+1]}$ such that $\sum_{\alpha_{n+1}} \left(\Lambda^{[n+1]}_{\alpha_{n+1}}\right)^2 = 1$. While this strictly changes the Schmidt vectors and values on others bonds and thus destroys the canonical form, this can be ignored as long as the discarded weight $\sum_{\alpha>\chi_{\max}} \Lambda^2$ is small enough.

4.2.4 *Overlaps and expectation value*

One great advantage of the canonical form, and more precisely its orthonormality properties, is that it allows to evaluate expectation values of local operators very easily. A very natural thing to demand from a numerical method aiming to represent complete wave functions is how to evaluate an overlap. To this end, we need a way to represent the bra-state $\langle\psi|$. It is a widely accepted convention to depict the complex-conjugate of ket-state $(|\psi\rangle)^\dagger = \langle\psi|$ in the graphical tensor network representation with the physical indices j_n pointing *upwards* (see Fig. 4.5a). The scalar product or overlap of two different wave functions $|\psi\rangle$ and $|\psi'\rangle$ amounts to contracting over all physical indices and all bond indices of the two MPS representations of the state and takes the form

$$\begin{aligned}\langle\psi'|\psi\rangle = \sum_{\{j_i\}}\sum_{\{\alpha\}}\sum_{\{\alpha'\}} & M'^{[N]j_N\dagger}_{\alpha'_{N-1}} \dots \\ & \dots M'^{[2]j_2\dagger}_{\alpha'_2,\alpha'_1} M'^{[1]j_1\dagger}_{\alpha'_1} M^{[1]j_1}_{\alpha_1} M^{[2]j_2}_{\alpha_1,\alpha_2} \dots M^{[N]j_N}_{\alpha_{N-1}}.\end{aligned} \tag{4.18}$$

This is quite a formidable expression and it becomes very quickly clear why from this point on we will mostly use the graphical nota-

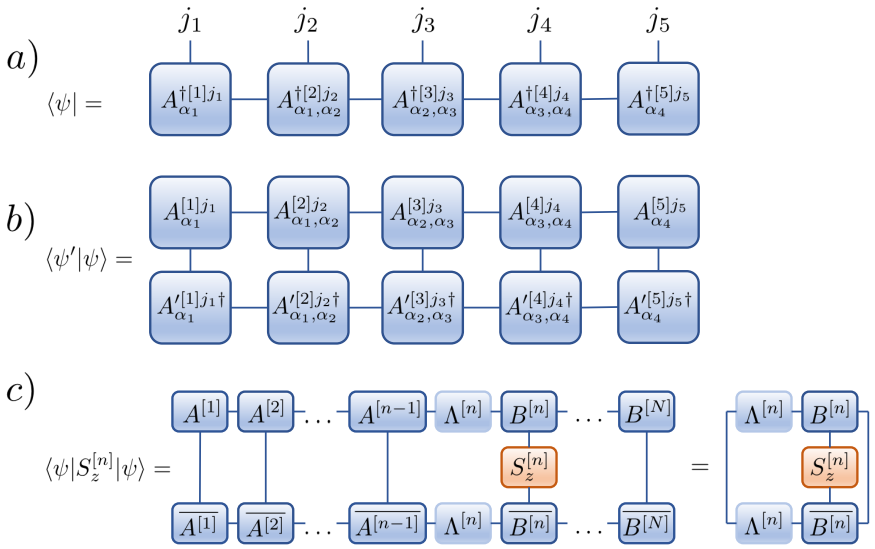

Figure 4.5: a) By convention, we depict the state $\langle\psi|$ with the physical indices pointing upwards. b) The graphical representation of (4.18), here in right canonical form. c) The expectation value for local operators is very convenient to evaluate when in canonical form. We simply need to contract the TN around the operator due to the orthonormality properties.

tion to represent expressions such as (4.18). Fig. 4.5b depicts this scalar product. In order to evaluate it, one needs to contract all the tensors. While not immediately intuitive, the order of contraction matters for numerical feasibility. In the worst case one can possibly end up with computational costs that scale exponentially with the system size [166].

Equally important to an overlap is the evaluation of an expectation value such as the magnetisation M at a specific site $M_n = \langle\psi|\,\hat{S}_z^{[n]}\,|\psi\rangle$, or even a two-point correlation function $O_{i,j} = \langle\psi|\,\hat{S}_z^{[i]}\hat{S}_z^{[j]}\,|\psi\rangle$ (see Sec. 2.1.3). Fully writing out either expression would again look rather messy, so that we simply illustrate the magnetisation M_n in Fig. 4.5c. Again, contracting the entire TN can be a numerically demanding task, but if the MPS representation of $|\psi\rangle$ is in its canonical form then we can use the orthonormality properties to save a lot of efforts. This is depicted in Fig. 4.5c. Instead of performing an overlap calculation for the entire MPS, we only have to evaluate the TN around the applied local operators.

4.3 TIME EVOLVING BLOCK DECIMATION

Historically the DMRG algorithm for obtaining ground states was introduced well before TEBD, which is an extension of the former [166]. In this chapter however, we introduce the TEBD algorithm prior because it can be formulated much more easily. It enables us

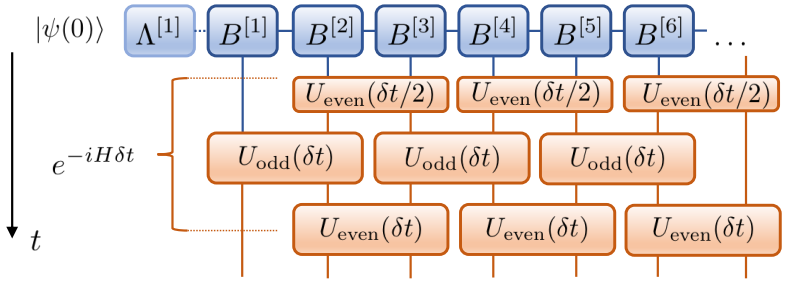

Figure 4.6: The application of two-site operators obtained via a *second* order Trotter decomposition in order to advance the initial state $|\psi(0)\rangle$ in time. We have depicted how, as long as no measurement needs to be performed, we obtain the second order decomposition at no computational cost, as the half-steps can be grouped into full ones.

to simulate the action of the unitary time-evolution operator $e^{-i\hat{H}t}$ on the MPS representation of a generic quantum many-body state $|\psi\rangle$. While the danger of uncontrolled entanglement growth poses a serious limitation to what one can achieve with TEBD, it nonetheless introduces the capability to study a variety of dynamical features, going far beyond extracting ground-state properties with standard (original) DMRG. It has to be noted that the terms TEBD, tDMRG (time-dependent DMRG) and tMPS (time-dependent MPS) describe, bar small variations, the same methodology. They are often used interchangeably even if they technically differ slightly. Among some of the achievements of the time-evolution of MPS are the simulation of local, and global quenches [54, 102], the calculation of dynamic correlators [22, 203, 204], the approximation of steady states in dissipative systems [45, 46], as well as finite-temperature techniques (where time-evolution appears in the form of an imaginary-time-evolution operator $e^{-\beta\hat{H}}$) [214].

In the following we will describe in detail the TEBD algorithm for systems with short-ranged interactions, mostly following [82]. In practice we are interested in the evaluation of the following term

$$|\psi(t)\rangle = U(t)\,|\psi(0)\rangle\,. \tag{4.19}$$

The time evolution operator U can either take the form $U(t) = e^{-iHt}$ yielding a real time evolution, or $U(\tau) = e^{-\tau H}$, which in turn stands for an imaginary time evolution. The latter allows us to find the ground state of the Hamiltonian H through the relation

$$|\psi_{\text{GS}}\rangle = \lim_{\tau\to\infty} \frac{e^{-\tau H}\,|\psi_0\rangle}{||e^{-\tau H}\,|\psi_0\rangle\,||}, \tag{4.20}$$

where $|\psi_0\rangle$ is some arbitrary initial state with non-zero overlap with the ground-state $|\psi_{\text{GS}}\rangle$. In practice this procedure is not very efficient and an iterative variational DMRG procedure yields much faster and

more precise results. It is nonetheless fascinating that TEBD is able to obtain and time-evolve ground states. In order to apply $U(t)$, be it in real or imaginary time, we have to approximate the exponential of an operator (here the Hamitonian H). The need to do this arises from the fact that different terms in the Hamiltonian sum might be non-commutative. Let us suppose we have a local Hamiltonian, as previously discussed in Sec. 2.2.4, that contains only nearest-neighbour terms of the form $H = \sum_n h^{[n,n+1]}$. Exponentiating this expression, we write

$$\exp(H) = \exp\left(\sum_n h^{[n,n+1]}\right) = \prod_n \exp\left(h^{[n,n+1]}\right), \tag{4.21}$$

where the last equality only holds as long $\left[h^{[n-1,n]}, h^{[n,n+1]}\right] = 0$ for all n, i. e. when every nearest-neighbour term commutes. This however is not the case in general. To this end we make use of the so-called Suzuki-Trotter decomposition [183], which approximates the exponent of a sum of operators with a product of exponents of the same operators as long as the exponent is small. For example the first and second order expansions can be written as

$$e^{(X+Y)\delta} = e^{X\delta}e^{Y\delta} + \mathcal{O}(\delta^2) \tag{4.22}$$

$$e^{(X+Y)\delta} = e^{X\delta/2}e^{Y\delta}e^{X\delta/2} + \mathcal{O}(\delta^3) \tag{4.23}$$

Here X and Y are non-commuting operators, while δ is a small parameter. Since terms in our local Hamiltonian that do not share a common site trivially commute, we can split H into two sums of mutually commuting terms

$$H = \underbrace{\sum_{n \text{ odd}} h^{[n,n+1]}}_{H_{\text{odd}}} + \underbrace{\sum_{n \text{ even}} h^{[n,n+1]}}_{H_{\text{even}}}. \tag{4.24}$$

The above, together with (4.21) and the Trotter decomposition (4.22), allows us to write out the time evolution $U(\delta t)$ to first order as

$$U(\delta t) \approx \left[\prod_{n \text{ odd}} U^{[n,n+1]}(\delta t)\right]\left[\prod_{n \text{ even}} U^{[n,n+1]}(\delta t)\right] + \mathcal{O}(\delta t^2), \tag{4.25}$$

where $U^{[n,n+1]}(\delta t) = e^{-i\delta t\, h^{[n,n+1]}}$. In order to obtain a small argument for the exponent, we have divided time into small slices $\delta t \ll 1$. The relevant time scale is in fact the inverse gap [82]. This Trotter decomposition of a local Hamiltonian is pictorially shown in Fig. 4.6. While in (4.25) we have used a first order Trotter decomposition for simplicity, we note that the form of (4.23) allows us to use the second order decomposition at no increased computational cost. As long as we do

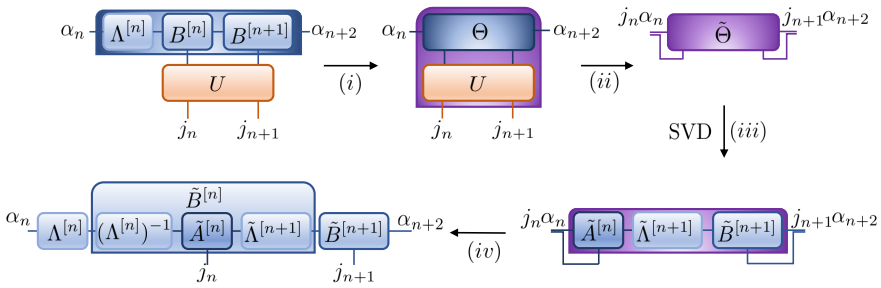

Figure 4.7: Graphical illustration of one update step in the TEBD algorithm. We begin (i) by using the canonical form to formulate the wave function Θ. We then (ii) apply the two-site unitary time-evolution operator U to obtain the wave function evolved in time $\tilde{\Theta}$. In order to return to the canonical form we (iii) perform a SVD of $\tilde{\Theta}$. Lastly, in order to obtain the correct canonical form (iv) again, we multiply the inverse of the left Schmidt value.

not require to perform a measurement after every time-step δt, we can group the half-step in (4.23) of consecutive time steps such that we in practice end up with the computational costs of a first order decomposition such as illustrated in Fig. 4.6. A similar feature holds for the Trotter decompositions of third and fourth order, which are more complicated in form, but still feasible for implementation [166].

The error introduced via the Trotter decomposition is next to the limitation of the maximal bond dimension χ the only error source of the TEBD algorithm. The successive application of the two-site unitary operators $U(\delta t)$ is at the heart of TEBD and will be described in the following. The spirit and also the advantage of TEBD in the MPS representation is similar to what we already encountered when calculating expectation values. It is extremely easy and efficient to apply local operators to a state written as an MPS. Moreover, the canonical form is preserved if the applied operator is unitary [166]. As already graphically shown in Fig. 4.5 for the expectation value, a one-site unitary U simply transforms the MPS locally, i. e.

$$\tilde{\Gamma}^{j}_{\alpha,\beta} = \sum_{j'} U^{j}_{j'} \Gamma^{j'}_{\alpha,\beta}. \tag{4.26}$$

If we want to make use of the Hamiltonian however, which is now in the form of a series of two-site unitaries U, we need to learn how to apply the latter. The procedure for a two-site unitary transformation acting on two neighbouring sites n and $n+1$ is depicted in Fig. 4.7. For this matter, we assume that the MPS representation of the wave function is in its right canonical form. Everything would analogously work in the left or mixed canonical form with slight modifications. We begin by expressing the wave function $|\psi\rangle$ in the basis spanned by the left Schmidt states, the local basis (necessary to apply U) and the right Schmidt states. Together they form an orthonormal basis $\{|\alpha_n\rangle_L \otimes$

$|j_n\rangle \otimes |j_{n+1}\rangle \otimes |\alpha_{n+2}\rangle_R\}$. We label the wave function coefficients Θ, and thus obtain an expression for $|\psi\rangle$:

$$|\psi\rangle = \sum_{\alpha_n, j_n, j_{n+1}, \alpha_{n+2}} \Theta^{j_n, j_{n+1}}_{\alpha_n, \alpha_{n+2}} |\alpha_n\rangle |j_n\rangle |j_{n+1}\rangle |\alpha_{n+2}\rangle_R . \tag{4.27}$$

Using the definitions of $|\alpha\rangle_{L/R}$, as explained previously and shown in Fig. 4.4, Θ takes the form

$$\Theta^{j_n, j_{n+1}}_{\alpha_n, \alpha_{n+2}} = \sum_{\alpha_{n+1}} \Lambda^{[n]}_{\alpha_n, \alpha_n} B^{[n] j_n}_{\alpha_n, \alpha_{n+1}} B^{[n+1] j_{n+1}}_{\alpha_{n+1}, \alpha_{n+2}}. \tag{4.28}$$

So in essence we have made convenient use of the Schmidt decomposition at either side of the sites in questions and reduced our wave function to the coefficients Θ to which we can apply a two-site unitary operator as easily as it was in the single site case. This will be the second step in the algorithm, so that the transformed wave function has coefficients $\tilde{\Theta}$ that read

$$\tilde{\Theta}^{j_n, j_{n+1}}_{\alpha_n, \alpha_{n+2}} = \sum_{j'_n, j'_{n+1}} U^{j_n, j_{n+1}}_{j'_n, j'_{n+1}} \Theta^{j'_n, j'_{n+1}}_{\alpha_n, \alpha_{n+2}}. \tag{4.29}$$

In order to return to a canonical form of the MPS, we then have to extract the new, transformed tensors $\tilde{\Lambda}^{[n+1]}$, $\tilde{B}^{[n]}$ and $\tilde{B}^{[n+1]}$. For that matter, we 'reshape' the rank-4 tensor $\tilde{\Theta}$ into a $d\chi_n \times d\chi_{n+2}$ dimensional matrix $\tilde{\Theta}_{j_n \alpha_n, j_{n+1} \alpha_{n+2}}$. Due to the orthonormality of the bases $\{|\alpha_n\rangle_L \otimes |j_n\rangle\}$ and $\{|j_{n+1}\rangle \otimes |\alpha_{n+2}\rangle_R\}$, it is natural to decompose $\tilde{\Theta}_{j_n \alpha_n, j_{n+1} \alpha_{n+2}}$ using an SVD into

$$\tilde{\Theta}_{j_n \alpha_n, j_{n+1} \alpha_{n+2}} = \sum_{\alpha_{n+1}} \tilde{A}^{[n]}_{j_n \alpha_n, \alpha_{n+1}} \tilde{\Lambda}^{[n+1]}_{\alpha_{n+1}, \alpha_{n+1}} \tilde{B}^{[n+1]}_{\alpha_{n+1}, j_{n+1} \alpha_{n+2}}, \tag{4.30}$$

where $\tilde{A}^{[n]}$,$\tilde{B}^{[n+1]}$ are isometries and $\tilde{\Lambda}^{[n+1]}$ is a diagonal matrix. By choosing to write the obtained matrices as A and B, we have suggested that the wave function obtained after the SVD be in mixed canonical form. This is indeed the case, as the SVD yields the first step of a Schmidt decomposition (2.22) of the wave function between sites n and $n+1$, where the isometry $\tilde{A}^{[n]}$ relates the new Schmidt states $|\alpha_{n+1}\rangle_L$ to the combined bases $|\alpha_n\rangle_L \otimes |j_n\rangle$. In fact this is precisely a step (see (4.7)) in our previous decomposition of a general state, where the obtained MPS was in left canonical form. Analogously, the same holds for $\tilde{B}^{[n+1]}$ and the Schmidt states on the right. Therefore, the diagonal matrix $\tilde{\Lambda}^{[n+1]}$ contains precisely the Schmidt values of the transformed state. Finally, we need to reshape the obtained matrices into the usual rank-3 tensors and recover the correct canonical form by

$$\begin{aligned} \tilde{B}^{[n] j_n}_{\alpha_n, \alpha_{n+1}} &= (\Lambda^{[n]})^{-1}_{\alpha_n, \alpha_n} \tilde{A}^{[n]}_{j_n \alpha_n, \alpha_{n+1}} \tilde{\Lambda}^{[n+1]}_{\alpha_{n+1} \alpha_{n+1}} \quad \text{and} \\ \tilde{B}^{[n+1] j_{n+1}}_{\alpha_{n+1}, \alpha_{n+2}} &= \tilde{B}^{[n+1]}_{\alpha_{n+1}, j_{n+1} \alpha_{n+2}}. \end{aligned} \tag{4.31}$$

So after the unitary two-site update, we have obtained a MPS that is still in canonical form. However the entanglement at the updated bond between sites n and $n+1$ has changed and the bond dimension increased to $d\chi$. As such, the information we keep about a wave function would increase exponentially with every unitary update. To overcome this problem, we approximate the state by only keeping the largest Schmidt values, often a fixed number $\chi_{\max}$, as previously discussed. As a consequence this limits the dimension of the MPS and the tensors B, which have a dimension of at most $\chi_{\max} \times d \times \chi_{\max}$. As long as the truncated weight is small, the normalisation conditions for the canonical form will be fulfilled to a good approximation. The normalisation of the wave function is ensured by dividing by the norm after truncation, i. e. by $\mathcal{N} = \sqrt{\sum_{j_n, j_{n+1}, \alpha_n, \alpha_{n+2}} |\Theta^{j_n, j_{n+1}}_{\alpha_n, \alpha_{n+2}}|^2}$.

In the case of an imaginary time evolution of the state, the operator U is not unitary and thus it does not conserve the canonical form. However, the successive application of the SVD proved to assure a relatively good approximation as long as the time step is small enough. A possible way to obtain accurate results is to reduce the step size successively [82]. In terms of numerical performance we note that the simulation cost of this algorithm scales as $d^3\chi^3_{\max}$, where the SVD is the most time consuming part. Should the applied Hamiltonian contain any symmetries, one can considerably speed up the calculation exploiting the block diagonal structure of $\Theta_{j_n \alpha_n, j_{n+1} \alpha_{n+2}}$, similar to Sec. 2.4. In this case the SVD can be performed for each block individually yielding a considerable speed up to the algorithm. For implementations, see [82].

4.4 DENSITY MATRIX RENORMALISATION GROUP

Real time evolution of a particular initial state is at the center of this thesis, however for some part finding the ground state is also relevant. As previously mentioned this can in theory be achieved with an imaginary time evolution, but in practice this is rather slow. We used the DMRG procedure in the context of MPS instead. While historically this was invented first, has much wider applications and implications, we will only devote a small section to it, proportionally to how much it has been applied in this thesis. For a more in depth review, we refer to the excellent publication of [166].

The DMRG algorithm in the language of MPS relies on the reformulation of the Hamiltonian as a matrix product operator (MPO). It is a natural generalisation of a MPS to the space of operators, given by

$$O = \sum_{j_1,\ldots,j_N} \sum_{j'_1,\ldots,j'_N} v^L W^{[1] j_1, j'_1} W^{[2] j_2, j'_2} \ldots \\ \ldots W^{[N] j_N, j'_N} v^R \, |j_1, \ldots, j_N\rangle \langle j'_1, \ldots, j'_N| \,, \tag{4.32}$$

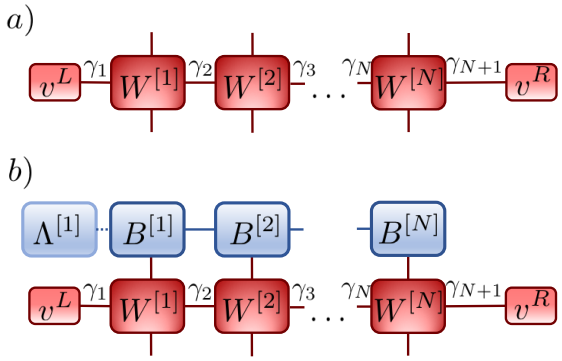

Figure 4.8: a) An operator O acting on the entire chain expressed as a MPO. This representation is *exact* and as long as O contains only short range interactions, the dimension D of the virtual γ bond is small. b) An MPO acting on a MPS in right canonical form. The virtual bond dimension of the MPS usually increases after such an update.

where $W^{[n]j_n,j'_n}$ are $D \times D$ matrices with virtual bonds γ, and $|j_n\rangle, |j'_n\rangle$ represent the local basis states at site n, similar to the MPS case. Again, we terminate the TN by some left and right vectors v^L and v^R. This new kind of tensor network is illustrated in Fig. 4.8, where we also demonstrate that it can be efficiently applied to a state in MPS form. Another great advantage of the MPO is that all local Hamiltonians with only short range interactions can be represented *exactly* via an MPO with only small dimension D. A widely used Hamiltonian in this thesis is the anisotropic Heisenberg (XXZ) chain in the presence of a field h_n that can vary from site to site. We will introduce this Hamiltonian at a later stage again, but it takes the form

$$H_{\mathrm{XXZ}} = \sum_n \left(S^x_n S^x_{n+1} + S^y_n S^y_{n+1} + \Delta S^z_n S^z_{n+1} \right) + \sum_n h_n S^z_n. \tag{4.33}$$

Here S^α_n with $\alpha = x, y, z$ is the $\alpha-$component of the spin operator $\vec{S}$ at site n. Δ is some anisotropy parameter that corresponds to interparticle interaction in the fermion picture. Fully expressed as a tensor product, the Hamiltonian would take the following rather large form:

$$\begin{aligned} H = {} & S^x \otimes S^x \otimes \mathbb{1} \otimes \cdots \otimes \mathbb{1} + \mathbb{1} \otimes S^x \otimes S^x \otimes \cdots \otimes \mathbb{1} + \ldots \\ & + S^y \otimes S^y \otimes \mathbb{1} \otimes \cdots \otimes \mathbb{1} + \mathbb{1} \otimes S^y \otimes S^y \otimes \cdots \otimes \mathbb{1} + \ldots \\ & + \Delta S^z \otimes S^z \otimes \mathbb{1} \otimes \cdots \otimes \mathbb{1} + \ldots \\ & + h_1 S^z \otimes \mathbb{1} \otimes \mathbb{1} \otimes \cdots \otimes \mathbb{1} + \ldots \end{aligned} \tag{4.34}$$

The corresponding *exact* MPO only has dimension $D = 5$ and takes the form

$$W^{[n]} = \begin{pmatrix} \mathbb{1} & S^x & S^y & S^z & h_n S^z \\ 0 & 0 & 0 & 0 & S^x \\ 0 & 0 & 0 & 0 & S^y \\ 0 & 0 & 0 & 0 & \Delta S^z \\ 0 & 0 & 0 & 0 & \mathbb{1} \end{pmatrix}, \tag{4.35}$$

where the entries of this matrix are themselves matrices that act in the space of $|j_n\rangle$ on site n and

$$v^L = (1,0,0,0,0), \qquad v^R = (0,0,0,0,1)^T. \tag{4.36}$$

It is remarkable that by multiplying these matrices (and taking tensor products of the operator entries) according to (4.32), one finds that they *exactly* give the Hamiltonian as written in (4.33). Further details, especially on how to formulate more complicated Hamiltonians, can be found in [119]. We are now in a position to schematically describe the process of the DMRG algorithm, as depicted in Fig. 4.9.

Very similar to TEBD, we require that at each step the state be represented by a MPS. We then variationally optimise pairs of neighbouring sites to minimise the ground state energy $\langle\psi| H |\psi\rangle$ while keeping the rest of the chain fixed.

As previously defined in (4.28), we describe the wave function $|\psi\rangle$ with the two-site tensor $\Theta^{j_n,j_{n+1}}_{\alpha_n,\alpha_{n+2}}$. We then require to project the Hamiltonian into the space spanned by the usual basis set $\{|\alpha_n\rangle_L \otimes |j_n\rangle \otimes |j_{n+1}\rangle \otimes |\alpha_{n+2}\rangle_R\}$, i. e. obtain an effective Hamiltonian H_{eff} that acts on $\tilde{\psi} = \sum \tilde{\Theta}^{j_n,j_{n+1}}_{\alpha_n,\alpha_{n+2}} |\alpha_n j_n j_{n+1} \alpha_{n+2}\rangle$ (assuming implicit summation) and then aim to minimise $E = \langle\tilde{\psi}| H_{\text{eff}} |\tilde{\psi}\rangle$. We recall from Fig. 4.4c that the product of $A^{[1]}A^{[2]}\dots A^{[n-1]}$ gives exactly the mapping from the physical space $|j_1 j_2 \dots j+n-1\rangle$ to $|\alpha_n\rangle_L$ and likewise for the B's that map to $|\alpha_{n+1}\rangle_R$. Therefore, H_{eff} is given by the contracted network as shown in Fig. 4.9b.

Often the contractions to the left and right of sites n and $n+1$ are called 'environments' and are labelled $L^{[n]}$ and $R^{[n+1]}$ respectively. Each environment has three open indices, namely the MPO bond index γ, and the two virtual bond indices α_n and $\bar{\alpha}_n$ of the bra and ket MPS. Similar to the TEBD algorithm, we can group the indices in H_{eff} as well as Θ and view the construct as the well-known combination of an operator matrix multiplying a state vector. Minimising the energy means therefore finding the ground-state 'vector' $\tilde{\Theta}$ of H_{eff}. This can be done by ED, however since this minimisation step is the most costly in the DMRG algorithm, and we really only need the ground state, it makes sense to employ an iterative procedure such as the Lanczos algorithm [107].

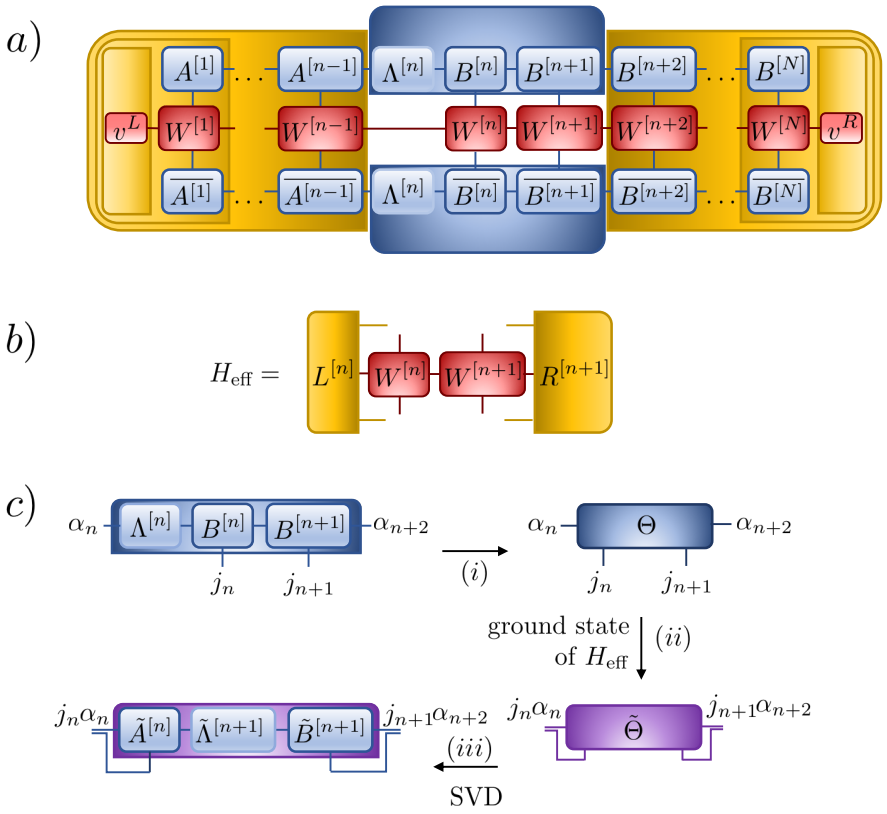

Figure 4.9: a) The energy $E = \langle\psi|H|\psi\rangle$ given for a MPS in mixed canonical form and the Hamiltonian written as a MPO. As explained in the main text, we contract the (yellow) parts to the left of site n and to the right of site $n+1$ to form the environments $L^{[n]}$ and $R^{[n+1]}$ respectively. b) The effective Hamiltonian with respect to which we seek to optimise the two-site wave function Θ on sites n and $n+1$. It is the MPO projected onto the basis $\{|\alpha_n\rangle_L \otimes |j_n\rangle \otimes |j_{n+1}\rangle \otimes |\alpha_{n+2}\rangle_R\}$. c) An update step in DMRG is very similar to TEBD. The main difference lies in step (ii), where we obtain the updated wave function $\tilde{\Theta}$ by minimising the energy with respect to H_{eff}. After this update, we repeat the process for a pair of sites to the right or left.

The newly obtained $\tilde{\Theta}$ can be viewed similar to the obtained wave function after one Trotter step. We therefore also split the new $\tilde{\Theta}$ using an SVD and again need to truncate to some maximal virtual bond dimension $\chi_{\max}$. At this point, we have an improved 'guess' for the tensors $\tilde{A}^{[n]}$,$\tilde{\Lambda}^{[n+1]}$ and $\tilde{B}^{[n+1]}$ with the center of the mixed canonical form moved one site to the right, at which point we move on to the next bond. We note that depending on which direction we move to (right or left), we need to reshape the tensors into the correct canonical form. This 'sweeping' procedure is performed until the change in ground state energy E is smaller than some desired threshold.

4.5 OPEN SYSTEMS

So far we have been concerned with finding the ground state or time-evolving a single pure state out-of-equilibrium. Historically this has posed already much of a challenge and in many cases TN were the first method to break through the surface of what seemed to be simply unsolvable problems. That being said, we have already stated at length that there are many issues present in TN techniques as well.

One is certainly that we have (at worst) a linear build-up of entanglement in time in an out-of-equilibrium quantum state that translates itself into an (at worst) exponential increase in required bond dimension $\chi_{\max}$ to describe the state properly. Similar problems arise in finite temperature calculations, a possible extension which we have not discussed yet.

A second issue which has not been covered so far concerns dissipative or open systems, where we are not studying a closed system under unitary Hamiltonian dynamics, but an open quantum system. As discussed in Sec. 2.1.4, if the dynamics are Markovian, not always a trivial assumption, then the most general form of the dynamics is given by the Lindblad master equation (2.14). In this section we want to explain the alterations that need to be made to the existing algorithm in order to accommodate for open dissipative systems.

While there are other methods known to simulate driven/dissipative dynamics such as the method of quantum trajectories [45], we will apply a so-called superoperator formalism [133, 148, 214]. The superoperator formalism makes maximal reusage of pure state TEBD possible as it simply encodes the density matrix (needed to describe mixed states and therefore open systems) as a (super-)vector. Since the Lindbladt master equation is a linear equation we are able to encode every term in that equation as superoperator acting on a superket. A simple example of the superoperator formalism follows. Let us

examine the product of matrices A and ρ, a term we would encounter e. g. in the Lindblad equation:

$$A = \begin{pmatrix} a_{11} & a_{12} \\ a_{21} & a_{22} \end{pmatrix} \quad \text{and} \quad \rho = \begin{pmatrix} \rho_{11} & \rho_{12} \\ \rho_{21} & \rho_{22} \end{pmatrix}. \tag{4.37}$$

The resulting matrix $A\rho$ takes the form of

$$A\rho = \begin{pmatrix} a_{11}\rho_{11} + a_{12}\rho_{21} & a_{11}\rho_{12} + a_{12}\rho_{22} \\ a_{21}\rho_{11} + a_{22}\rho_{21} & a_{21}\rho_{12} + a_{22}\rho_{22} \end{pmatrix}. \tag{4.38}$$

Writing the resulting matrix $A\rho$ simply as a column vector, we notice that we could have achieved a similar result by the following matrix-vector multiplication:

$$\begin{aligned} \tilde{A}\rho &= \begin{pmatrix} a_{11}\rho_{11} + a_{12}\rho_{21} \\ a_{21}\rho_{11} + a_{22}\rho_{21} \\ a_{11}\rho_{12} + a_{12}\rho_{22} \\ a_{21}\rho_{12} + a_{22}\rho_{22} \end{pmatrix} = \begin{pmatrix} a_{11} & a_{12} & 0 & 0 \\ a_{21} & a_{22} & 0 & 0 \\ 0 & 0 & a_{11} & a_{12} \\ 0 & 0 & a_{21} & a_{22} \end{pmatrix} \begin{pmatrix} \rho_{11} \\ \rho_{21} \\ \rho_{12} \\ \rho_{22} \end{pmatrix} \\ &= A^{\#} |\rho\rangle^{\#}. \end{aligned} \tag{4.39}$$

The # denotes that density matrix ρ and the operator A have been promoted to a *superoperator* $A^{\#}$ and a *superket* $|\rho\rangle^{\#}$. In this spirit we are able to rewrite (2.14) as

$$\frac{d}{dt} |\rho\rangle^{\#} = A^{\#} |\rho\rangle^{\#}, \tag{4.40}$$

and thus can formulate a time-evolution operator $U(t)$. In order to utilise the TEBD algorithm, we further require that the Liouville operator $\mathcal{L}$ decomposes into terms involving at most two contiguous sites, i. e.

$$\mathcal{L}[\rho] = \sum_j \mathcal{L}_{j,j+1}[\rho]. \tag{4.41}$$

We note that in the above example, for the sake of simplicity, we kept the expansion of ρ to the Euclidean basis, which is spanned by the four matrices with a single unit entry at the respective position. This is equivalent to writing the matrix as a simple column vector. In order to represent complex matrices, such as the density operator, we require a basis set to span the vector space of complex Hermitian matrices.

The Pauli matrices (2.17) introduced in Sec. 2.2 are the ideal choice for this. Together with the identity they span the vector space of 2×2 Hermitian matrices. In this space, the scalar product of two matrices A and B is denoted by $\langle A|B\rangle := \mathrm{Tr}(A^\dagger B)$. The expansion coefficients (and thus the entries of the superket $|\psi\rangle^{\#}$) are as usual obtained via

$c_i = \langle \sigma_i | A \rangle$, where A is an arbitrary operator which we seek to expand in the Pauli basis. Consequently, we can express any Hermitian operator A as

$$A = \sum_i \langle \sigma_i | A \rangle \, \sigma_i. \tag{4.42}$$

At this point we are able to apply the above in order to simulate an open system via for example the Lindblad equation with the TEBD algorithm. We note again that non-unitary time-evolution does not preserve the canonical form such that truncation may not be optimal. This can be circumvented by re-orthogonalising the state. For small enough time-step, and when approaching a steady-state (similar to imaginary time TEBD) the introduced error may however be kept small. Since (2.14) is a linear equation, thus only involves products of $A\rho$ and ρA (everything else can be brought into this form), we can write the time-evolution (not necessarily unitary) as $U(\delta t) = \exp\left(A^{\#}\delta t\right)$. We therefore only need to work out the coefficients of the (here 4×4) matrix $A^{\#}_{i,j}$. Let us use $\eta = A\rho$ as an example. We will not omit hats in this case to make the distinction from coefficients clearer. We can expand this general Hermitian operator $\hat{\eta}$ in terms of the Pauli basis:

$$\hat{\eta} = \hat{A}\hat{\rho} = \sum_i d_i \hat{\sigma}_i. \tag{4.43}$$

Generally our state evolves from $\hat{\rho} \to \hat{A}\hat{\rho}$, where we can also expand the unevolved state, i. e. write:

$$\hat{\rho} = \sum_j c_j \hat{\sigma}_j. \tag{4.44}$$

Given that $\mathrm{Tr}\left(\hat{\sigma}_i \hat{\sigma}_j\right) = 2\delta_{ij}$, we get that

$$\mathrm{Tr}\left(\hat{\sigma}_j \hat{\eta}\right) = \mathrm{Tr}\left(\sum_i d_i \hat{\sigma}_j \hat{\sigma}_i\right) = \sum_i d_i 2\delta_{ij}. \tag{4.45}$$

From this we can deduce that

$$d_i = \frac{1}{2}\mathrm{Tr}\left(\hat{\sigma}_i \hat{\eta}\right) = \frac{1}{2}\mathrm{Tr}\left(\sum_j \hat{\sigma}_i c_j \hat{A} \hat{\sigma}_j\right) = \frac{1}{2}\sum_j c_j \underbrace{\mathrm{Tr}\left(\hat{\sigma}_i \hat{A} \hat{\sigma}_j\right)}_{=\hat{A}^{\#}_{ij}}. \tag{4.46}$$

Similar derivations show that:

1. $\hat{\rho}\hat{A} \ \to (\hat{A}^{\#}_{ij})^{\top}$
2. $\hat{A}^{\dagger}\hat{\rho} \to (\hat{A}^{\#}_{ij})^{\dagger}$
3. $\hat{\rho}\hat{A}^{\dagger} \to (\hat{A}^{\#}_{ij})^{*}$.

This concludes the necessary changes one needs to make in order to accommodate for density matrix time-evolution. To reiterate, we take our desired Lindblad equation (2.14) with corresponding nearest-neighbour Lindbladian (4.41) and derive the corresponding superoperator $A^{\#}$ via (4.46). We then perform the time-evolution with the TEBD algorithm using $U(\delta t)$.

We note that there is one important distinction to pure state MPS techniques. When performing a Schmidt decomposition of the superket $|\psi\rangle^{\#}$, the Schmidt values $\Lambda^{[n]}$ are a measure not of the entanglement, but the amount of correlations between the two subsystems [214] or operator space entanglement [148].

Part II

QUANTUM QUENCHES IN COLD ATOM SYSTEMS

5

NON-INTERACTING TRAP JUMP

In this chapter, we consider a global quantum quench applied to a one-dimensional system of spinless, non-interacting fermions in a potential consisting of a strong optical lattice, a harmonic trap, and sometimes also uncorrelated site disorder [174]. The term quench, which we will precisely define below, refers to the abrupt change of the system at a certain point in time. A more commonly known form of quenching occurs in material sciences, where rapid cooling of a workpiece in water, oil or air is employed to obtain certain material properties. This question is theoretically interesting because it concerns a quantum system relaxing under the influence of bulk but inhomogeneous forces. It is also of interest because of its direct relevance to experiment: indeed, reports of experiments exhibiting two or even all three of these ingredients (lattice, trap, disorder) may already be found in the literature [29, 41, 83, 96, 118, 172, 199].

The quench protocol consists of letting the system equilibrate, and then, at the moment of the quench, suddenly displacing the centre of the harmonic trapping potential from its initial position by Δj lattice sites. Such quenches were first studied experimentally over a decade ago [122, 136, 141]. We investigate the representation of the pre-quench state in the post-quench eigenbasis, which is the initial condition for all subsequent time-evolution. We also analyse how that time-evolution affects the values of observables such as the moments of the fermions' spatial density profile.

Since our fermions are non-interacting, the population of each post-quench single-particle eigenstate is a constant of motion, and the system is trivially integrable. Nonetheless, as we change the trap-jump distance Δj and the strength of the disorder W we observe considerable variation in the timescales on which different observables relax to their time-averaged values, and in the extent to which those time-averaged values agree with equilibrium predictions.

The plan of the remainder of this chapter is as follows. In Sec. 5.1, we introduce the model and discuss the quench protocol. In Sec. 5.2, we then present the zero hopping case ($J = 0$) as the simplest version of the model in order to build some physical intuition for the system and its quench dynamics. In Sec. 5.3, we analyse the experimentally relevant case with hopping. In particular we analyse the post-quench eigenfunctions, which will play a crucial role in the system's dynamics (see 5.3.1), and the representation of the pre-quench state in the post-quench basis — the initial condition for the post-quench time-evolution — for a range of trap-jump sizes Δj (see 5.3.3).

Sec. 5.4 provides an analysis of the time-evolution of the moments of the density and investigates the short and long time properties of the density itself. We also include the influence of disorder on the dynamics, elucidating the competition between the two forms of localisation in the system. We conclude with Sec. 5.5, in which we briefly summarise our results, and also discuss further planned and already realised research, particularly the focus on the addition of inter-particle interactions.

5.1 MODEL AND QUENCH PROTOCOL

We consider spinless fermions moving in one dimension on a lattice of L sites with open boundary conditions. The Hamiltonian reads

$$\hat{H}_i = -J \sum_{j=1}^{L-1} \left(c_j^\dagger c_{j+1} + c_{j+1}^\dagger c_j \right) + \sum_{j=1}^{L} \left[\frac{1}{2} \kappa a^2 \left(j - j_0 \right)^2 + \epsilon_j \right] c_j^\dagger c_j. \quad (5.1)$$

Here the operator $c_j^\dagger$ creates a fermion on site j, and J is the hopping matrix element between neighbouring sites. The on-site energy consists of a harmonic trapping potential of spring constant κ centred at j_0 plus additional uncorrelated on-site disorder taken from a uniform box distribution: $\epsilon_j \in [-W, W]$. For convenience we shall henceforth set both $\hbar$ and the lattice constant a to unity. We find the single-particle eigenstates $\{\alpha_k\}$ of $\hat{H}_i$ and populate the lowest N of them to obtain the initial ground state of the N-fermion problem. Alternatively we can choose a chemical potential μ and populate all single-particle eigenstates for which the eigenenergy $E_k^{(i)}$ is smaller than μ.

In this chapter, we study the non-equilibrium dynamics of this model that arise from a particular spatially inhomogeneous global quench. At time $t = 0$ the centre of the harmonic trapping potential is displaced from site j_0 to site j_1, while the disorder potential is left unchanged. Thus the post-quench Hamiltonian $\hat{H}$ is exactly the same as (5.1) but with $j_0 \to j_1$. This Hamiltonian has a set of single-particle eigenstates $\{\beta_k\}$ with eigenenergies E_k. We define the 'jump size' Δj as $|j_1 - j_0|$.

The subsequent time-evolution of the many-body state of the system can be understood as a dephasing of the contributions of the individual post-quench eigenstates, due to their different eigenenergies. The pre-quench state, represented in the post-quench basis, serves as the initial condition for this time-evolution. In the coming sections, we study further the nature of this initial condition, and of the subsequent time-evolution of physical observables such as the centre-of-mass of the atom cloud.

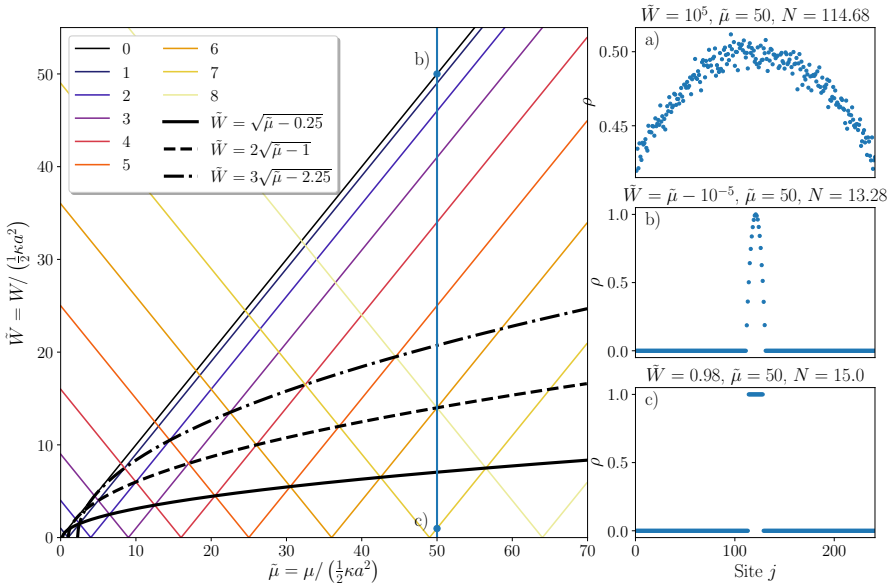

Figure 5.1: Left panel: An illustration of the disorder-broadening of the single-particle energy levels of a finite-size system. Possible level crossings as a function of $\tilde{W}$ and $\tilde{\mu}$, which are scaled by the harmonic trapping potential for clarity, lie on parabolic curves showing the critical disorder strength at which neighbouring (black solid line), second-neighbour (black dashed line), third-neighbour (black dotted line), etc. levels can cross. Right panels: The disorder-averaged density profile for three different disorder strengths. Parameters: number of lattice sites $L = 241$; trap spring constant $\kappa = 0.0025$; hopping integral $J = 0$; trap centre $j_0 = 121$.

5.2 THE ZERO-HOPPING CASE

By far the simplest case arises when the hopping matrix element between neighbouring sites is zero, i. e. when $J = 0$. The system is now not only trivially integrable, but in fact trivially diagonal as without any hopping, the pre- and post-quench eigenfunctions can be chosen to be eigenfunctions of position. This means that the values of the on-site potential in (5.1) are the eigenenergies E. However, in order to connect smoothly to the $J \neq 0$ case, we instead take the excited states to be bonding and antibonding superpositions of the pair of parity-related degenerate position eigenstates. We now explore what cases can arise when altering the remaining parameters, the disorder strengths W, the chemical potential μ and the jump size Δj.

5.2.1 *Pre-quench density*

Without disorder, the ground-state density will be a simple block of fermions occupying all sites whose energy level is below the chemical potential. This will be the case even for finite disorder as long as

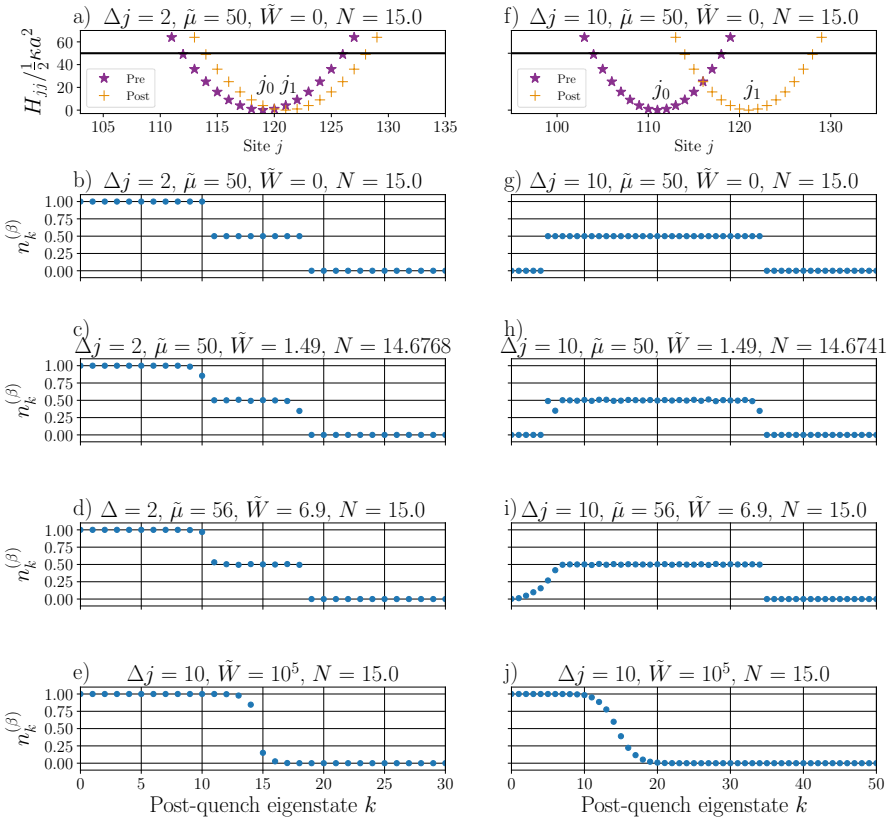

Figure 5.2: An illustration of the different qualitative forms of the post-quench occupation function in the absence of hopping ($J = 0$), for different jump sizes Δj, scaled chemical potentials $\tilde{\mu} \equiv 2\mu/\kappa a^2$, and scaled disorder strengths, $\tilde{W} = 2W/\kappa a^2$. (a) The pre- and post-quench trapping potentials. In the absence of hopping and with no disorder, this is also a graph of the eigenvalues of the pre- and post-quench Hamiltonians. The black line denotes the chemical potential $\tilde{\mu}$. (b) The post-quench occupation function after a small trap-jump, as a function of eigenstate quantum number k. (c) The same as (b), but with moderate disorder. The deviation from half-unit values is mainly because changing the disorder at fixed chemical potential changes the total particle number. (d) The same as (c), but with a choice of $\tilde{W}$ and $\tilde{\mu}$ that restores the original particle number N. Note that there are still residual deviations from half-unit values. (e) The occupation function in the case of very large $\tilde{W}$. (f)-(j) As panels (a)-(e), but for a larger jump size, $\Delta j = 10$. Parameters: number of lattice sites $L = 241$; trap spring constant $\kappa = 0.0025$; hopping integral $J = 0$; pre-quench trap centre $j_0 = 121$. Each disorder-average in this chapter is performed over 10000 disorder realisations, unless mentioned otherwise.

the disorder is not able to bring an energy level above the chemical potential (see Fig. 5.1c). The left panel of Fig. 5.1 visualises how disorder can broaden the discrete energy levels of the harmonic trap. It permits us to determine possible level crossings and level occupations for given values of the chemical potential μ and the disorder strength W. The parabolic curves show the disorder strength at which neighbouring (next-neighbour, etc.) levels first cross. However, the only line of relevance in the continuum case is in fact the line $W = \mu$, which denotes the broadening of (what was in the clean case) the single-particle ground state. This divides the (W, μ) parameter space into two distinct regions.

The right panels illustrate the qualitative difference in the form of the ground-state density between these two regions. Panel (a) shows a case where $W \gg \mu$. Here all lattice sites are occupied with roughly equal probabilities, though the breaking of particle-hole symmetry due to the trapping potential is still visible. Panel (c) shows a contrasting case where $W \ll \mu$. Here the spatial density profile has a 'top hat' form. Panel (b) shows the density at the point $W = \mu$: here the average occupation of (what was in the clean case) the lowest energy site is just about to deviate from unity.

5.2.2 *The post-quench occupation function without hopping*

Without hopping there will be no dynamics. Our considered quench, displacing the trap, therefore merely changes the energies of the occupied sites with no effect on the dynamics 'post-quench'. Here, we want to investigate the so-called post-quench occupation nonetheless, as it will predict and explain many of the structures we will see in the hopping case later, where the post-quench occupation becomes very important. Thus if we want to determine the time-evolution of the system for times $t > 0$, we need to know the state at time $t = 0$, i. e. we need to represent the pre-quench state in the post-quench basis. This will consist of a superposition of many different Slater determinants, each corresponding to a different assignment of the N fermions to the L post-quench single-particle eigenstates. A simple function that captures its essence, however, is the expectation value of the occupation of each post-quench single-particle eigenstate, $n_k^{(\beta)}$. Here $k = 1, 2, \ldots, L$ labels the post-quench single-particle eigenfunctions.

In order to determine $n_k^{(\beta)}$ we express the pre-quench ground state $|\psi_0^{(N)}\rangle$ for N particles as,

$$|\psi_0^{(N)}\rangle = \alpha_N^\dagger \alpha_{N-1}^\dagger \ldots \alpha_2^\dagger \alpha_1^\dagger |0\rangle, \tag{5.2}$$

where the operator $\alpha_k^\dagger$ creates a fermion in pre-quench single-particle eigenstate α_k, and $|0\rangle$ is the fermionic vacuum. The post-quench occupation function is then defined as,

$$n_k^{(\beta)} \equiv \langle \psi_0^{(N)} | \beta_k^\dagger \beta_k | \psi_0^{(N)} \rangle = \sum_{q=1}^{N} \left| O_{qk}\left(\Delta j\right) \right|^2, \tag{5.3}$$

where $\beta_k^\dagger$ creates a fermion in post-quench single-particle eigenstate β_k, and the overlap matrix $O_{qk}(\Delta j)$ is defined as,

$$O_{qk}(\Delta j) \equiv \langle \alpha_q | \beta_k \rangle. \tag{5.4}$$

Since there is a one-to-one mapping between the eigenstate quantum numbers k and the eigenenergies E_k, we may equivalently represent the occupation function as $n(E)$, which we sample at the points $E = E_k$.

A careful analysis of Fig. 5.1 is necessary to understand the occupation function obtained in the $J = 0$ quench problem, some examples of which are shown in Fig. 5.2. Due to the lack of hopping, in a single disorder realisation the density can only take the values 0 or 1. The same is true of the occupation function — except in the clean case, where our choice of bonding and antibonding forms of the eigenstates allows also a value of $1/2$. The disorder-averaging, of course, permits other values to emerge as weighted averages of these.

In panels (a) and (f) we visualise the quench protocol by showing the diagonal matrix elements (which for zero hopping are also the eigenvalues) of $\hat{H}_i$ and $\hat{H}$. The translation of the trap explains the shape of the disorder-free occupation function for the different jump sizes in panels (b) and (g). These are in the case $W \ll \mu$, so the real-space pre-quench density is of top-hat form, i. e. just one continuous block of occupied sites. Where the two sites corresponding to a degenerate pair of post-quench eigenstates both exist within that block, those states get occupation 1; where only one of the sites overlaps with the original density profile, they get occupation $1/2$; and where both sites lie outside the block, they get occupation 0.

Adding disorder to the system allows the levels to cross, and also leads, for a fixed chemical potential, to a change of the total particle number. This means that disorder distorts the clean post-quench distribution function in two qualitatively different ways. These are shown separately in panels (c), (d), (h), and (i).

Panels (c) and (h) show the occupation function when μ and W are chosen so as not to mix any neighbouring levels (i. e. below the thick black parabola in Fig. 5.1). However, different disorder realisations may still push the highest occupied level through the chemical potential, resulting in an average total particle number that is non-integer.

In panels (d) and (i) the disorder is strengthened, but the chemical potential is also raised. This results in the opposite situation: now the disorder cannot empty a previously occupied state, but there is

on the other hand a strong possibility of the lower levels being permuted. Since the energy-level permutation is more likely at lower energies, the departure from the clean behaviour is asymmetric, unlike in panels (c) and (h).

Lastly, we have included the case of very strong disorder, for comparison with Fig. 5.5.

5.3 THE HOPPING CASE

In the following we want to discuss the experimentally more relevant case where $J \neq 0$. The pre- and post-quench eigenfunctions are now not limited to single sites as a particle can lower its energy by spreading according to the kinetic term in (5.1). Since we are studying a non-interacting model, the occupation of the post-quench eigenstates cannot be altered via scattering. In other words, the occupation of the post-quench eigenstates is the system's initial condition that prevails to infinite times and prevents the system trivially from thermalising. Therefore, the postquench eigenfunctions (see 5.3.1) and their occupancy (see 5.3.3) are the central quantities we want to discuss in the non-interacting case.

5.3.1 *Post-quench single-particle eigenstates*

Fig. 5.3 shows some of the post-quench single-particle eigenstates, obtained by numerical exact diagonalisation [1]. The nature of these eigenstates was first discussed in [87, 152]; here we briefly summarise their properties.

In the clean case, and in the absence of the harmonic trap, i. e. when $\kappa = W = 0$, our model is just a tight-binding model with a band dispersion $E(k) = -2J\cos k$, where k is the wave number. In this limit the density of states is only non-zero for $|E| \leq 2J$, the region which we call the band. We will use the terminology of the band, especially 'top' and 'bottom' to refer to $E = \pm 2J$ respectively, even when $\kappa \neq 0$. We also consider only states in the lowest band, i. e. that any higher band is far enough in energy to not play a role in the dynamics.

Adding a harmonic trap, i. e. setting $\kappa \neq 0$, imposes a finite spatial extent on the eigenfunctions. As discussed in [87], this may be determined semiclassically by considering the orbit of a particle whose total energy is given by $E = -2J\cos k + \kappa x^2/2$. For $E < 2J$, the orbit has only the conventional classical turning points, where $k = 0$,

$$j = j_1 \pm j_c, \quad j_c = \sqrt{\frac{2E + 4J}{\kappa}}. \tag{5.5}$$

1 In the cases where the exponentially small energy splitting between the symmetric and antisymmetric eigenstates of the problem is beyond the resolution of our numerical solver, we have 'manually' taken linear combinations of the results to produce the correct symmetric and antisymmetric eigenstates

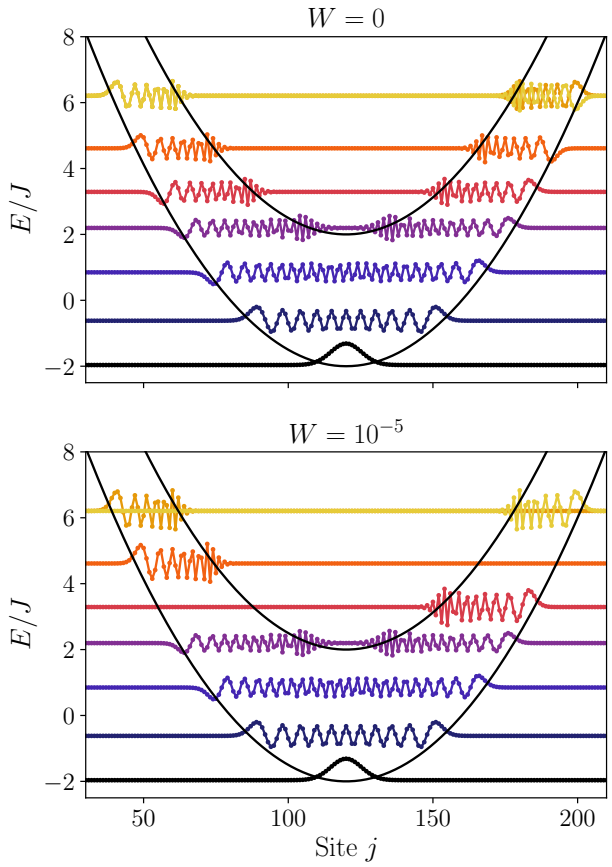

Figure 5.3: Selected post-quench single-particle eigenfunctions, determined by exact diagonalisation. Each eigenfunction is offset vertically by its eigenenergy. The highest-lying eigenfunction is shown together with its almost degenerate partner. The outer parabola shows the classical turning points as a function of energy while the inner parabola shows the Bragg turning points. Upper panel: clean case ($W = 0$). Lower panel: very weak disorder ($W = 10^{-5}$). Parameters: number of lattice sites $L = 241$; trap spring constant $\kappa = 0.0025$; hopping integral $J = 1$; post-quench trap centre $j_1 = 121$.

By contrast, for energies $E \geq 2J$ the orbit acquires in addition two Bragg turning points, where $k = \pm\pi$,

$$j = j_1 \pm j_b, \quad j_b = \sqrt{\frac{2E - 4J}{\kappa}}. \tag{5.6}$$

Bragg reflection exponentially suppresses the wave function in the region between the two Bragg turning points. We call this region 'Bragg-forbidden' and the states that exhibit such suppression 'Bragg-localised'. As can be seen in Fig. 5.3, these turning points provide a good description of the spatial extent of the numerically determined eigenfunctions.

How are these eigenstates affected by the addition of disorder? In the clean ($W = 0$) case, the Hamiltonian H is symmetric under a

reflection about the trap centre j_1. Hence each eigenstate is either odd or even under such a reflection. For energies E well above $2J$, i. e. well into the Bragg-localised regime, each even eigenstate has an odd partner with almost the same energy. These may be thought of as bonding and anti-bonding combinations of a left Bragg-localised and a right Bragg-localised state. In the $E \to \infty$ limit, the energy splitting between the bonding and anti-bonding states tends to zero, and the left- and right-localised states become exact eigenstates of the problem. But for any finite eigenenergy they are hybridised by a non-zero tunnelling matrix element T,

$$T \approx e^{-j_b(E)/\xi(E)}, \tag{5.7}$$

where the decay length $\xi(E)$ is given approximately by

$$\xi(E) = -\frac{1}{\ln\left(\frac{E}{2J} - \sqrt{\left(\frac{E}{2J}\right)^2 - 1}\right)}. \tag{5.8}$$

The details of the derivation of (5.7) and (5.8) are discussed below (see 5.3.2).

However, the introduction of very weak disorder, $W \sim T$, is sufficient to suppress this hybridisation, thus making the left- and right-localised states the true eigenstates of the problem. This phenomenon is illustrated in Fig. 5.3. The two highest-energy eigenfunctions in the upper panel are the hybridisation-split bonding and anti-bonding states; the two highest-energy eigenfunctions in the lower panel are the left- and right-localised states. The hybridisation between them has been suppressed even though the disorder strength is more than five orders of magnitude smaller than the bandwidth. This implies that the post-quench time evolution is sensitively dependent on even very weak disorder. Some examples of this will be shown in Sec. 5.4.

5.3.2 *Hybridisation between Bragg-localised states*

We now show in detail how to obtain an approximate form for the matrix element T responsible for the hybridisation of left- and right-Bragg-localised states. The calculation is similar in structure to that of the hopping integral in a tight-binding model.

We first split the Hamiltonian into three parts,

$$H = H_{\text{kin}} + V_0 + V_1. \tag{5.9}$$

Here H_{kin} is the lattice kinetic energy,

$$H_{\text{kin}} = -2J\cos(k), \tag{5.10}$$

while the potential terms V_0 and V_1 are defined as follows,

$$\begin{aligned} V_0(x) &= \frac{1}{2}\kappa x^2\,\Theta(-x), \\ V_1(x) &= \frac{1}{2}\kappa x^2\,\Theta(x), \end{aligned} \tag{5.11}$$

where $\Theta(x)$ is the step function. $H_L \equiv H_{\text{kin}} + V_0$ has only left-localised eigenstates, while $H_R \equiv H_{\text{kin}} + V_1$ has only right-localised ones. We may thus calculate the hopping integral from the left- to the right-localised states by introducing V_1 as a perturbation to H_L.

Following [87], we use a WKB approximation for the left-localised eigenstate, i. e. an eigenstate of H_L with eigenenergy E,

$$\phi_L(x) \sim \exp\left(i \int_{x_0}^{x} k(x')dx' \right), \tag{5.12}$$

where the wavenumber $k(x)$ is the solution to the equation

$$-2J\cos(k) + V_0(x) = E, \tag{5.13}$$

and x_0 is an arbitrary reference point. We see that, for $x > 0$, k is independent of x. The calculation is not very sensitive to the structure of $\phi_L(x)$ for $x < 0$, so we make the following rather crude approximation:

$$\phi_L(x) = \begin{cases} 0 & x \le -x_c; \\ \dfrac{1}{\sqrt{x_c(E) - x_b(E) + \xi(E)}} & -x_c < x \le -x_b; \\ \dfrac{e^{-x/\xi(E)}}{\sqrt{x_c(E) - x_b(E) + \xi(E)}} & x > -x_b. \end{cases} \tag{5.14}$$

Here $x_c(E)$ and $x_b(E)$ are respectively the classical and Bragg turning points of the semiclassical orbit,

$$x_c(E) = \sqrt{\frac{2E + 4J}{\kappa}}, \qquad x_b(E) = \sqrt{\frac{2E - 4J}{\kappa}}, \tag{5.15}$$

and $\xi(E)$ is the decay length in the Bragg-forbidden region,

$$\xi(E) = -\frac{1}{\ln\left(\frac{E}{2J} - \sqrt{\left(\frac{E}{2J}\right)^2 - 1} \right)}. \tag{5.16}$$

Since the transformation $x \to -x$ transforms H_L into H_R, it follows that the eigenstate of H_R with energy E is given by $\phi_R(x) = \phi_L(-x)$. The hopping integral is

$$T = \int_{-\infty}^{\infty} \phi_L^*(x)\, V_1(x)\, \phi_R(x)\, dx. \tag{5.17}$$

This integral is dominated by the region in which $\phi_R(x)$ is constant; hence

$$T \approx \frac{\kappa}{2} \int_{x_b(E)}^{x_c(E)} \frac{x^2\, e^{-x/\xi(E)}}{x_c(E) - x_b(E) + \xi(E)} dx. \tag{5.18}$$

For large energies we can approximate this integral as

$$T(E) \approx \frac{\kappa}{2} \left[x_b(E)\right]^2 \exp\left(-\frac{x_b(E)}{\xi(E)}\right), \tag{5.19}$$

which is the form quoted in (5.7).

5.3.3 *Post-quench occupation function*

We have already introduced and defined the post-quench occupation function in Sec. 5.2.2. We now discuss it in the presence of hopping. Since the fermions are still non-interacting, each $n_k^{(\beta)}$ is a constant of the motion. This trivially prevents the system from thermalising; nonetheless, particular observables — e.g. the centre-of-mass of the atom cloud — may still relax to their thermal equilibrium values.

In Fig. 5.4 we plot this post-quench occupation function for four different jump sizes in the clean case. For comparison, we also show the occupation function calculated in the continuum (see Sec. 5.3.4), and the thermal occupation function for the same total energy and particle number.

The post-quench occupation function exhibits a remarkable amount of structure. Unlike the thermal distribution, it has a very steep slope when departing from zero and unity. For a wide range of small jump-sizes it also shows an almost linear structure around the Fermi energy $E_F = 0$ that has a plateau-like substructure.

The continuum approximation works better for small trap jumps than for larger ones. The reason is that small jumps mainly occupy low-lying single-particle eigenstates of the post-quench Hamiltonian. These resemble the eigenstates of a continuum harmonic oscillator [87]. Thus the 'athermal' structure of the occupation function in these cases arises from the harmonic-oscillator nature of the eigenstates, rather than from the influence of the lattice.

For larger jump sizes, where the quench populates the higher-lying single-particle eigenstates, the continuum approximation becomes worse. In particular, for energies $E \geq 2J$ the true occupation function and the continuum approximation to it disagree sharply. This is because, as we learned in Sec. 5.3.1, the single-particle eigenstates with energies $E \geq 2J$ are (to use the terminology of [87]) Bragg-localised: instead of extending between the two classical turning points, they go only as far as the atom can propagate before being Bragg-reflected from the optical lattice.

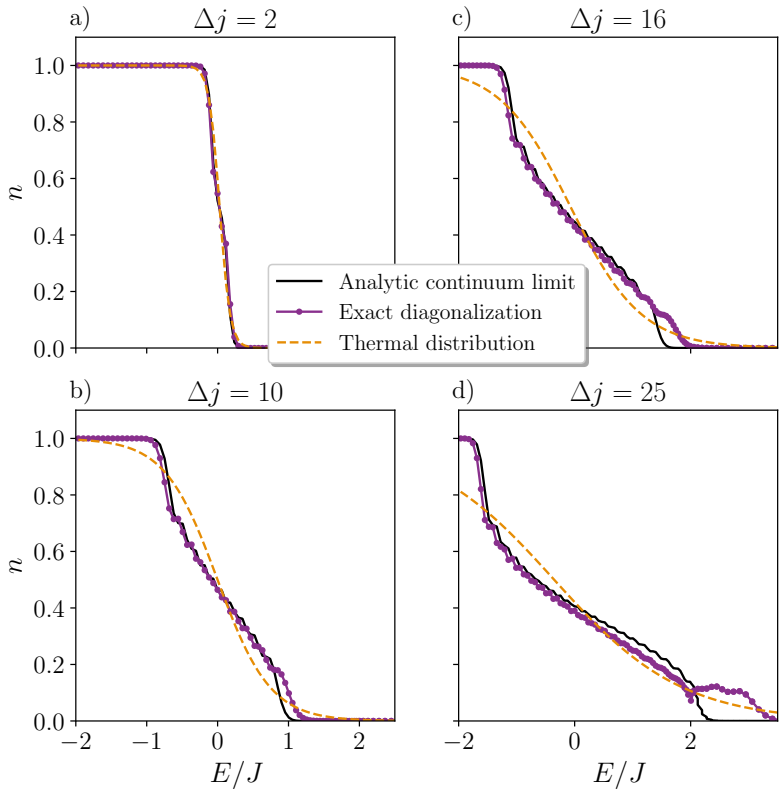

Figure 5.4: The post-quench occupation function $n(E)$ (purple; circles) for four different jump sizes Δj. For comparison we also plot the continuum result (black; solid line) and the result for a thermal state with the same total energy and particle number (orange; dashed line). For small Δj (panels (a) and (b)), the continuum approximation is a good one. As soon as we start populating states above $E = 2J$, i. e. Bragg localised states, the continuum approximation fails (panels (c) and (d)). Parameters: number of lattice sites $L = 241$; trap spring constant $\kappa = 0.0025$; hopping integral $J = 1$; chemical potential $\mu = 0$; post-quench trap centre $j_1 = 121$; disorder strength $W = 0$.

5.3.4 *Continuum approximation to the post-quench occupation function*

In order to tell which features of the post-quench occupation function are due to the structure of the underlying lattice and which, by contrast, are present also in a continuum treatment, we calculate the overlap $O_{qk}(\Delta j)$ for harmonic oscillator wave functions in the continuum; i. e. we compute the overlap of two harmonic oscillator eigenfunctions corresponding to the trap potential, one of which is displaced with respect to the other by Δj. Some results on this continuum limit have already been obtained in [142].

For convenience, we centre the two eigenfunctions respectively at $x = \pm x_0$. The overlap is given by

$$O_{qk}^{\text{cont.}}(x_0) \equiv \int_{-\infty}^{\infty} \psi_q^*(x + x_0)\, \psi_k(x - x_0)\, dx, \tag{5.20}$$

where the normalised harmonic oscillator eigenfunction is given by

$$\psi_k(x) = \frac{1}{\sqrt{2^k k!}} \pi^{-1/4} e^{-x^2/2} H_k(x). \tag{5.21}$$

Here $H_k(x)$ denotes the kth (physicists') Hermite polynomial, and we have chosen units in which $\hbar = m = \omega = 1$. Using Eq. (7.377) in [71], one finds,

$$O_{qk}^{\text{cont.}}(x_0) = \sqrt{\frac{2^\alpha \beta!}{2^\beta \alpha!}}\, (-1)^{\max(k-q,0)}\, e^{-x_0^2}\, x_0^{\alpha-\beta}\, L_\beta^{\alpha-\beta}(2x_0^2), \tag{5.22}$$

where $\alpha \equiv \max(k, q)$, $\beta \equiv \min(k, q)$, and $L_n^k(x)$ are the associated Laguerre polynomials.

To complete our derivation we must relate the continuum shift of the eigenfunctions x_0 to the displacement of the harmonic trap in lattice units Δj. The natural length scale of the continuum quantum harmonic oscillator is $\zeta = 1/\sqrt{m\omega}$. For the lattice problem, we may obtain expressions for m and ω by Taylor-expanding the lattice kinetic energy $-2J \cos k$ around $k = 0$. This gives for the effective mass,

$$m^* = \frac{1}{2J}, \tag{5.23}$$

while the effective frequency is given by

$$\omega^* = \sqrt{\frac{\kappa}{m^*}} = \sqrt{2\kappa J}. \tag{5.24}$$

The result is $\zeta = (2J/\kappa)^{1/4}$. We thus find that $2x_0 = \Delta j/\zeta$.

5.3.5 *Post-quench occupation function with moderate disorder*

We can further analyse what happens to the occupation function when we introduce moderate disorder into the $J \neq 0$ system. (Here 'moderate' means a disorder strength high enough to do more than just lift the degeneracy between neighbouring Bragg-localised states.) The results of this analysis are shown in Fig. 5.5. In order to have comparable results upon disorder averaging we have chosen a fixed particle number N rather than a fixed chemical potential μ. We have plotted the occupation function not as a function of energy, but rather eigenstate quantum number k ordered by energy.

The results show that as the disorder becomes stronger, the trap jump has an increasingly minor effect upon the post-quench occupation function. This is as expected, since the disorder profile, unlike

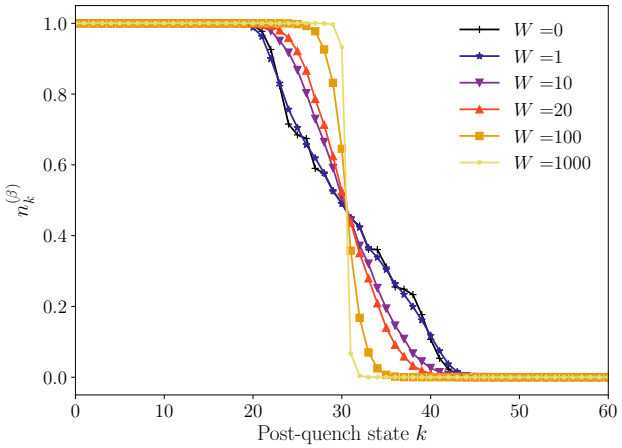

Figure 5.5: The post-quench occupation function $n_k^{(\beta)}$ in the presence of hopping J and moderate disorder W. For convenience we have picked a constant particle number $N = 31$. Parameters: number of lattice sites $L = 241$; trap spring constant $\kappa = 0.0025$; hopping integral $J = 1$; pre-quench trap centre $j_0 = 115$, post-quench trap centre $j_1 = 121$. Each disorder-average is performed over 10000 disorder realisations.

the trapping potential, is not displaced at the moment of the quench. Furthermore we see that in the case of very strong disorder the occupation functions for the $J = 0$ model (see Fig. 5.2) and that for the $J \neq 0$ model become qualitatively similar. This is again as it should be, since the nearest-neighbour coherence $\left|\left\langle Jc_i^\dagger c_{i+1}\right\rangle\right| \approx \frac{J^2}{W}$ for large disorder.

5.4 TIME-EVOLUTION OF EXPERIMENTAL OBSERVABLES

The occupation function analysed in the previous section is the initial condition for the post-quench time-evolution of the atom cloud. We now turn to the question of how this initial condition translates into the time-evolution of the cloud's spatial density profile.

The density of atoms at lattice site j is given by the diagonal elements of the following equal-time Green's function:

$$C_{ij}(t) \equiv \langle c_i^\dagger(t) c_j(t)\rangle. \tag{5.25}$$

With a little algebra (see 5.4.1), we may write this in terms of the single-particle post-quench eigenfunctions and their eigenenergies. This allows us to obtain the density profile at any time $t > 0$,

$$\rho_j(t) = \sum_{l=1}^{N} \left| \sum_{a=1}^{L} O_{al} e^{-iE_a t} \psi_{aj} \right|^2. \tag{5.26}$$

Here E_a is the eigenenergy of post-quench eigenstate β_a, and ψ_{aj} is its (lattice) wave function.

The contributions of single-particle eigenstates β_a and β_b to post-quench observables dephase on a timescale $\tau_{ab} \sim 1/(E_a - E_b)$. This is largest for neighbouring energy levels, E_a and E_{a+1}. This dephasing does not, of course, imply that the observables actually become time-independent, even at long times. However, if we examine an observable — such as the density profile — averaged over a time interval τ_{av},

$$\bar{\rho}_j(\tau_{\mathrm{av}}) \equiv \frac{1}{\tau_{\mathrm{av}}} \int_0^{\tau_{\mathrm{av}}} \rho_j(t) dt, \tag{5.27}$$

we find that this tends to a limiting form as $\tau_{\mathrm{av}} \to \infty$,

$$\bar{\rho}_j \equiv \lim_{\tau_{\mathrm{av}} \to \infty} \left(\bar{\rho}_j(\tau_{\mathrm{av}}) \right) = \sum_{a=1}^{L} n_a \left| \psi_{aj} \right|^2 . \tag{5.28}$$

Following Deutsch [53], we call $\bar{\rho}_j$ the time-averaged density.

In the clean system (see Fig. 5.3, upper panel), the density profile of every post-quench single-particle eigenstate is symmetric about the post-quench trap centre j_1. Hence the time-averaged density (5.28) will be centred at j_1 as well. However, because the eigenenergies of the bonding and anti-bonding Bragg-localised states are very nearly degenerate, the restoration of this symmetry about $j = j_1$ occurs very slowly. This is demonstrated in Fig. 5.6, where the cloud's centre-of-mass seemingly equilibrates at a position between the original trap centre j_0 and the new trap centre j_1. In reality, though, a very slow drift — not visible on experimental timescales — will eventually restore the centre-of-mass to $j = j_1$ (see Fig. 5.9).

However, this symmetry-restoring drift ceases to occur as soon as the disorder is able to disrupt the hybridisation between the left- and right-localised states. As discussed above, this occurs for any $W \gtrsim T$, where T — given in (5.7) — is exponentially small in $2j_b(E)$, the width of the Bragg-forbidden region. Therefore, even for such weak disorder, the parity-breaking imposed by the initial conditions remains visible in the infinite-time density profile (see Fig. 5.10). This is a localisation mechanism for the atom cloud which is conceptually quite distinct from Anderson localisation.

As a diagnostic for this we define the jump efficiency η, which expresses the post-quench displacement of the centre-of-mass as a fraction of the jump size Δj. Fig. 5.11 shows a plot of the jump efficiency as a function of jump size for various disorder strengths. This clearly demonstrates the distinction between Bragg and Anderson localisation.

In the remainder of this section we will study two facets of the post-quench density profile — its early-time behaviour and its time-averaged value — in more detail. The early-time behaviour, analysed in Sec. 5.4.2, is similar for the clean and weakly disordered cases. The

time-averaged state, however, is not; therefore, we analyse the clean case in Sec. 5.4.3, and then the disordered cases in Sec. 5.4.4.

5.4.1 *The equal-time Green's function*

Before studying the dynamics in detail, we want to present the general derivation of the form of the equal-time Green's function (5.25). This is useful for our purposes because its diagonal form gives the density; but it is also useful for following work (see Ch. 6), calculating such quantities as the entanglement entropy [140].

Defining the following basis transformations,

$$\begin{aligned} c_j &= \phi^*_{kj}\alpha_k, \\ c_j &= \psi^*_{kj}\beta_k, \\ \beta_k &= O_{kq}\alpha_q, \end{aligned} \tag{5.29}$$

we can expand (5.25) to

$$C_{ij}(t) = \langle \psi_0^{(N)} | e^{iHt}\phi_{ki}\phi^*_{qj}\alpha^\dagger_k\alpha_q e^{-iHt} | \psi_0^{(N)} \rangle. \tag{5.30}$$

(Here and in the rest of this chapter we use the Einstein convention that repeated indices are summed over.) From Blaizot's book [30] (2.19) we get the following identity:

$$e^{\frac{1}{2}\tilde{\nu}K\nu+\bar{l}\nu}\nu_i e^{-\frac{1}{2}\tilde{\nu}K\nu-\bar{l}\nu} = \sum_{j=1}^{2L}\left[\left(e^{-\sigma K}\right)_{ij}\nu_j + l_j\sigma_{ji}\right], \tag{5.31}$$

where $\tilde{\nu} = \nu^{\mathrm{T}} = (\alpha_1, \ldots, \alpha_L, \alpha_1^\dagger, \ldots, \alpha_L^\dagger)$, K is a $2L \times 2L$ matrix, and

$$\sigma = \begin{pmatrix} 0_{L\times L} & \mathbb{1}_{L\times L} \\ \mathbb{1}_{L\times L} & 0_{L\times L} \end{pmatrix}.$$

In order to bring (5.30) into the form of (5.31), we write the Hamiltonian as:

$$H = \omega_s\beta^\dagger_s\beta_s = \omega_s O^*_{sq}O_{sp}\alpha^\dagger_q\alpha_p \equiv H_{qp}\alpha^\dagger_q\alpha_p, \tag{5.32}$$

where in the last step we have defined $H_{qp} \equiv \omega_s O^*_{sq}O_{sp}$. It is convenient to choose K such that $(K^*)^{\mathrm{T}} = \overline{K}^* = -K$. To achieve this, we symmetrise the Hamiltonian, making use of the anticommutation properties of the fermionic operators:

$$e^{iHt} = e^{iH_{qp}\alpha^\dagger_q\alpha_p t} = e^{iH_{qp}\left(\frac{1}{2}\alpha^\dagger_q\alpha_p - \frac{1}{2}\alpha_p\alpha^\dagger_q + \frac{1}{2}\delta_{qp}\right)t}. \tag{5.33}$$

In this form we have $e^{\frac{1}{2}\tilde{\nu}K\nu}$ with $K = \begin{pmatrix} 0 & -i\overline{H}t \\ iHt & 0 \end{pmatrix}$ and hence obtain: $e^{-\sigma K} = \begin{pmatrix} e^{-iHt} & 0 \\ 0 & e^{i\overline{H}t} \end{pmatrix}$.

We now are in a position to apply (5.31) to (5.30), which leaves us with the following equation:

$$C_{ij}(t) = A_{kiqj} \sum_{m,n}^{2L} \left(e^{-\sigma K}\right)_{k+L,m} \left(e^{-\sigma K}\right)_{q,n} Q_{mn}, \tag{5.34}$$

where the matrix element Q_{mn} is defined as follows:

$$Q_{mn} = \langle \psi_0^{(N)} | \nu_m \nu_n | \psi_0^{(N)} \rangle, \tag{5.35}$$

and $A_{kiqj} = \phi_{ki}\phi^*_{qj}$. The sums are restricted due to the shape of K and the Fermi-energy, limiting when Q_{mn} is non-zero. We therefore obtain:

$$C_{ij}(t) = \sum_{m=1}^{N} \sum_{k=1}^{L} \sum_{q=1}^{L} \phi_{ki}\phi^*_{qj} \left(e^{i\overline{H}t}\right)_{km} \left(e^{-iHt}\right)_{qm} \tag{5.36}$$

As a final step we diagonalise the Hamiltonian by reversing (5.32) using (5.29) which allows us to transform the ϕ's and write the solution in the following form:

$$C_{ij}(t) = \sum_{a,c=1}^{L} \sum_{m=1}^{N} O_{am} O^*_{cm} e^{-i(\omega_a - \omega_c)t} \psi_{ci} \psi^*_{aj}. \tag{5.37}$$

Setting $i = j$ in this formula recovers the expression for the density $\rho_j(t)$ given in (5.26).

5.4.2 *Early-time behaviour*

To characterise the time-evolution of the density (5.26) shortly after the quench, we consider in particular two of its moments: the first moment, x_1, which corresponds to the atom cloud's centre-of-mass; and the third (standardised) moment, x_3, which corresponds to its skewness. These are defined respectively as

$$x_1(t) \equiv \frac{1}{N} \sum_{j=1}^{L} j\, \rho_j(t) \tag{5.38}$$

and

$$x_3(t) \equiv \frac{\frac{1}{N}\sum_j \left(j - x_1(t)\right)^3 \rho_j(t)}{\left(\frac{1}{N}\sum_j \left(j - x_1(t)\right)^2 \rho_j(t)\right)^{3/2}}. \tag{5.39}$$

We plot them as functions of time in Fig. 5.6, for two different jump sizes.

The dominant effect is clearly the oscillation of the centre-of-mass, the frequency of which may be accurately predicted by a classical oscillator calculation using the band mass as the mass of the particle —

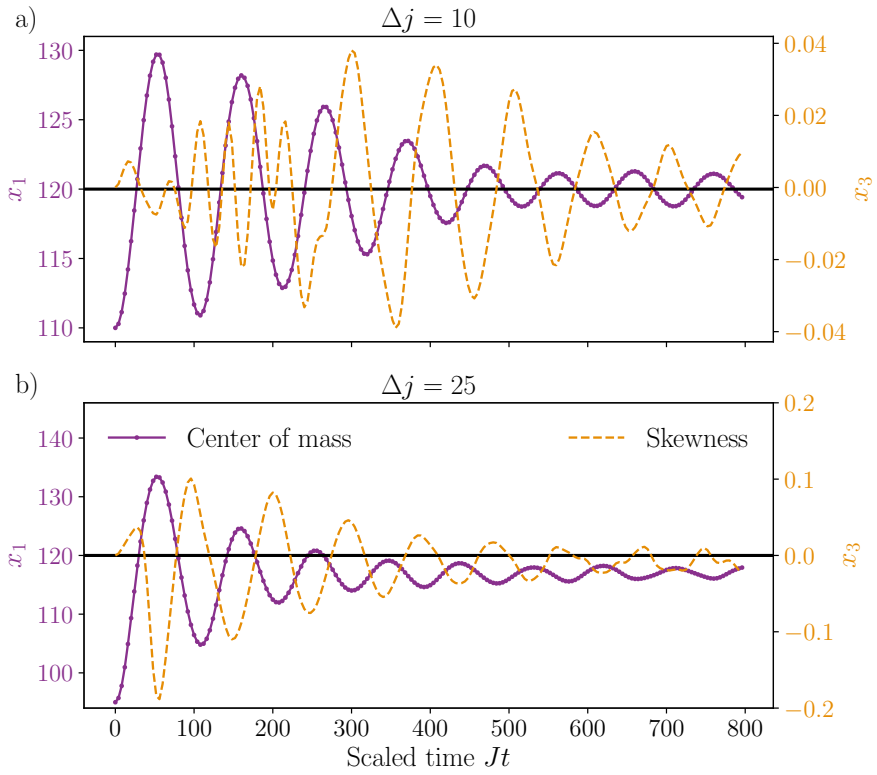

Figure 5.6: (a) centre-of-mass x_1 (purple curve with circles; left-hand scale) and skewness x_3 (orange dashed curve; right-hand scale) as functions of time, for a quench with trap-jump size $\Delta j = 10$. The centre-of-mass oscillates around the post-quench trap centre (solid black line). (b) The same, but for a larger trap-jump size $\Delta j = 25$. Again, the post-quench trap centre is indicated by the solid black line; but now, even though there is no disorder, on observable time-scales the centre-of-mass instead oscillates around a different point, between pre- and post-quench trap centres. Parameters: number of lattice sites $L = 241$; trap spring constant $\kappa = 0.0025$; hopping integral $J = 1$; chemical potential $\mu = 0$; post-quench trap centre $j_1 = 120$; disorder strength $W = 0$.

see (5.24). In this case, a spring constant of $\kappa = 0.0025$ and a hopping integral of $J = 1$ yield a frequency of $f/J = 0.01125$, which matches the oscillation frequency of x_1 in Fig. 5.6.

For the smaller jump size, this oscillation occurs about the post-quench trap centre, j_1, which is shown by the solid horizontal (black) line. For the larger jump size, however, it appears to occur around a different point, somewhere between j_0 and j_1. As discussed above, this is because the quench with the larger jump size populates some of the left Bragg-localised states, which on the timescales shown have not yet tunneled across to their partners on the right.

The oscillations in the skewness are much smaller-scale than those of the centre-of-mass. In Fig. 5.7, we elucidate their origin by plotting the contributions of selected individual pre-quench single-particle ei-

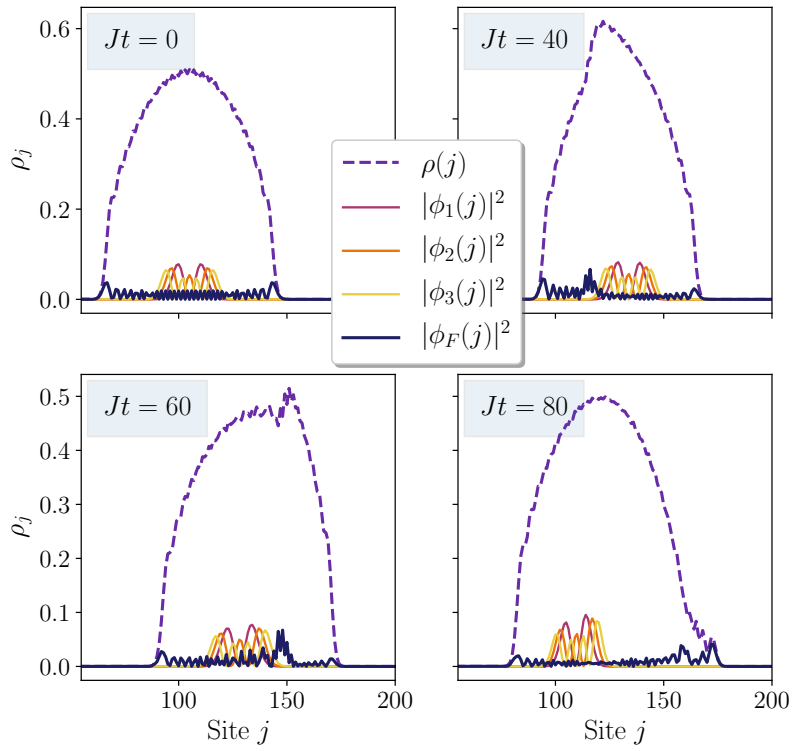

Figure 5.7: The density profile of the atom cloud at various times after the quench (purple dashed curve), showing the contributions of selected individual pre-quench single-particle eigenstates (solid curves, various colours). The skewness oscillations are caused by the mobile 'bump' in the profile, which lags behind the centre-of-mass oscillations, and which appears to be due principally to the highest-lying occupied eigenfunction $\phi_F(j)$. Parameters: number of lattice sites $L = 241$; trap spring constant $\kappa = 0.0025$; hopping integral $J = 1$; chemical potential $\mu = 0$; pre-quench trap centre $j_0 = 106$; post-quench trap centre $j_1 = 121$; disorder strength $W = 0$.

genfunctions to the overall density profile. This decomposition of the density strongly suggests that the skewness oscillation is a finite-size effect. This is supported by exact diagonalisation for larger values of the chemical potential, which suggests that the skewness oscillations are suppressed as N increases, and also by the solution of the fermionic Gross-Pitaevskii equation [99], which suggests that they are absent in the continuum. Nonetheless, for typical experimental set-ups, in which one may have $N \sim 100$ atoms per quasi-one-dimensional tube, they may well be observable.

5.4.3 *Time-averaged state (clean case)*

In the complete absence of disorder, parity is eventually restored by the dephasing of the Bragg-localised states, as all single-particle ei-

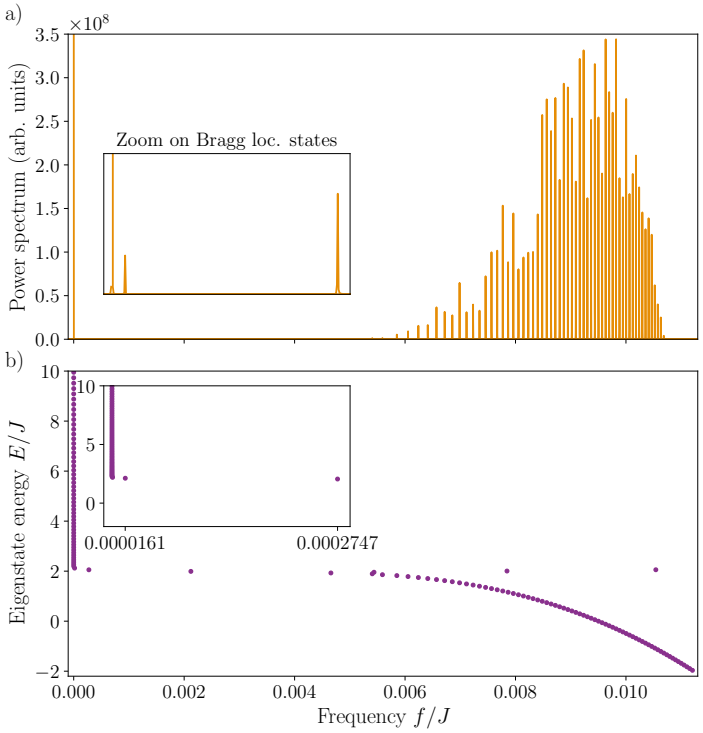

Figure 5.8: The correspondence between the long-time part of the centre-of-mass oscillations and the dephasing of nearly degenerate Bragg-localised states. (a) The power spectrum of the centre-of-mass oscillations of the atom cloud. (b) Energy differences of neighbouring single-particle energy levels converted to frequencies (horizontal axis) for a pair of single-particle states near energy E (vertical axis). Insets: a zoomed-in version to very small frequencies f/J of the same, showing the first two Bragg-localised states. Note the excellent quantitative match between the frequency content of the upper and lower panels which share a common x-axis. Parameters: number of lattice sites $L = 241$; trap spring constant $\kappa = 0.0025$; hopping integral $J = 1$; chemical potential $\mu = 0$; pre-quench trap centre $j_0 = 105$; post-quench trap centre $j_1 = 121$; disorder strength $W = 0$.

genstates have densities symmetric about the post-quench trap centre. However the timescale on which this occurs is extremely long. Thus on experimentally relevant timescales the clean case is not actually materially different from the weakly disordered one discussed below. In both, for example, the centre-of-mass oscillates not about the new centre of the trap, but about a point between the pre- and post-quench trap centres (see Fig. 5.6). The question whether the centre-of-mass reaches the new trap centre, and in particular the role of Bragg localised states [152] and the existence of parity doublets [159], was already raised following the original experiment [122].

As emphasised above, in the clean case all single-particle eigenstates have densities symmetric about the post-quench trap centre,

which means that the time-averaged density profile will have this symmetry too. Therefore, we should be able to see in the power spectrum of the centre-of-mass oscillations the slow modes that restore this symmetry at long times. As shown in Fig. 5.8, indeed we can. Fig. 5.8a shows the frequencies present in the power spectrum, with an inset concentrating on the low-frequency spectrum. Fig. 5.8b is a histogram of the frequencies obtained from the gaps between neighbouring post-quench single-particle energy levels. The quantitative match between these graphs is striking. Furthermore, the oscillation frequency calculated above ($f/J = 0.01125$) provides an upper bound to the frequency spectrum.

This analysis demonstrates how long a time scale one would need to go to to see the atomic cloud oscillating about the new trap centre. This time may be estimated as the dephasing time of the highest occupied Bragg-localised state, i. e.

$$\tau_{\text{long}} \approx 1/T_F = e^{j_b(E_F)/\xi(E_F)}, \tag{5.40}$$

where E_F denotes the eigenenergy of that state, and the functions $j_b(E)$ and $\xi(E)$ are defined in (5.6) and (5.8) respectively. This should be compared with the time scale associated with the centre-of-mass oscillations immediately after the quench, which is given by

$$\tau_{\text{short}} \approx 1/f^* = \frac{2\pi}{\sqrt{2\kappa J}}. \tag{5.41}$$

Only for times $\tau_{\text{av}} \gg \tau_{\text{long}}$ will a time-averaged density profile match the symmetric prediction of (5.28).

While this time-averaged density has a centre-of-mass which clearly matches the thermal equilibrium prediction, other moments of the time-averaged and thermal profiles do not agree, as shown in Fig. 5.9. Due to the reflection symmetry about $j = j_1$, the centre-of-mass, the skewness, and in fact all odd moments of the density do 'thermalise'. However, the same is not true for the even moments: even for small trap jumps, the two densities are different. Related questions have also been discussed for hard-core bosons [153].

In addition to the two densities obtained from the occupation functions, we have plotted an average density over many consecutive time steps at very large times. This underlines that (a) there is a long period of time over which the density reaches a 'finite-time-averaged' state, where the in-band single-particle states have dephased but the weakly-hybridised pairs of Bragg-localised states have not, and (b) the true time-averaged density emerges only at significantly longer times than used in this example.

5.4.4 *Time-averaged state (disordered case)*

Upon adding disorder to the system one can immediately see that the clean case is very fragile with respects to parity symmetry breaking

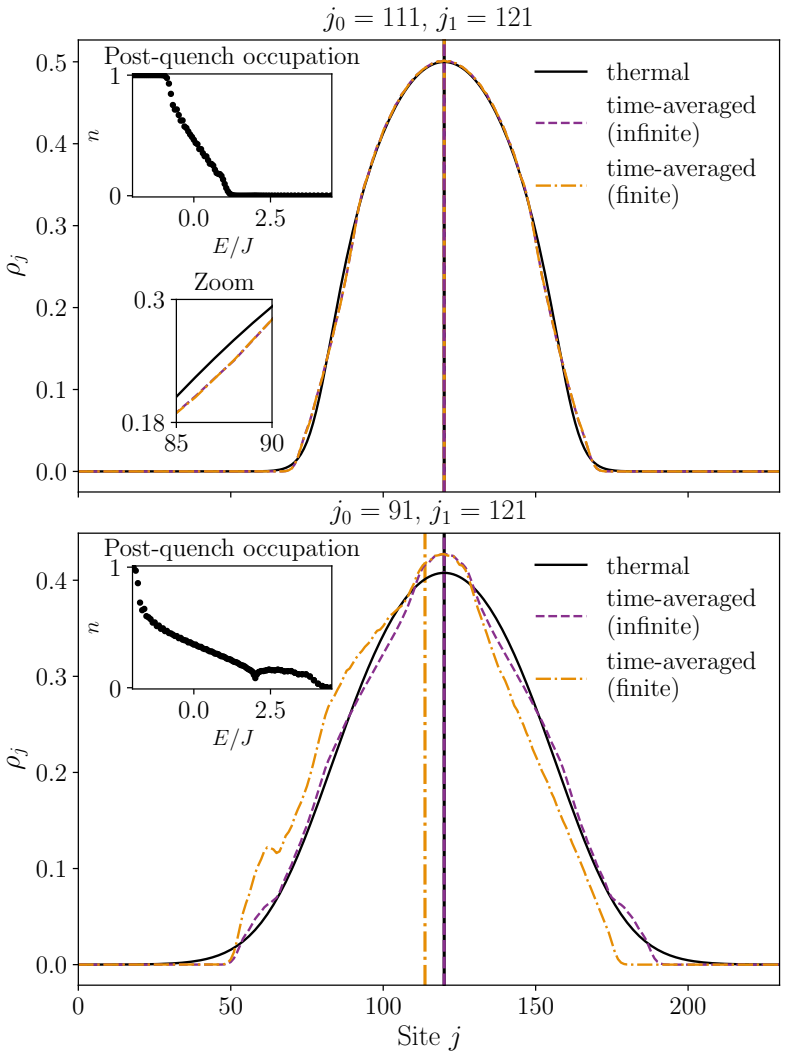

Figure 5.9: A comparison between three densities: the time-averaged density calculated from expression (5.28) ('time-averaged (infinite)'); the time-average of consecutive densities at large but finite times ('time-averaged (finite)') (similar to (5.27)); and the density of a thermal equilibrium state with the same total energy and number of atoms ('thermal'). The finite average was taken at $Jt = 50000$ for 1000 consecutive time steps separated by $\Delta t = 1/J$. The vertical lines denote the position of the centre-of-mass for the corresponding density. The time-averaged density does not perfectly match the thermal prediction for any non-zero jump size. For larger jump sizes (bottom), as the Bragg-localised states are populated, the approach to the time-averaged state becomes very slow. This happens because Bragg localisation generates a very long time-scale (5.40), below which a time-average deviates strongly from the infinite-time result. This is shown by the disparity between the 'time-averaged (finite)' and 'time-averaged (infinite)' curves in the lower panel. Parameters: number of lattice sites $L = 241$; trap spring constant $\kappa = 0.0025$; hopping integral $J = 1$; chemical potential $\mu = 0$; disorder strength $W = 0$.

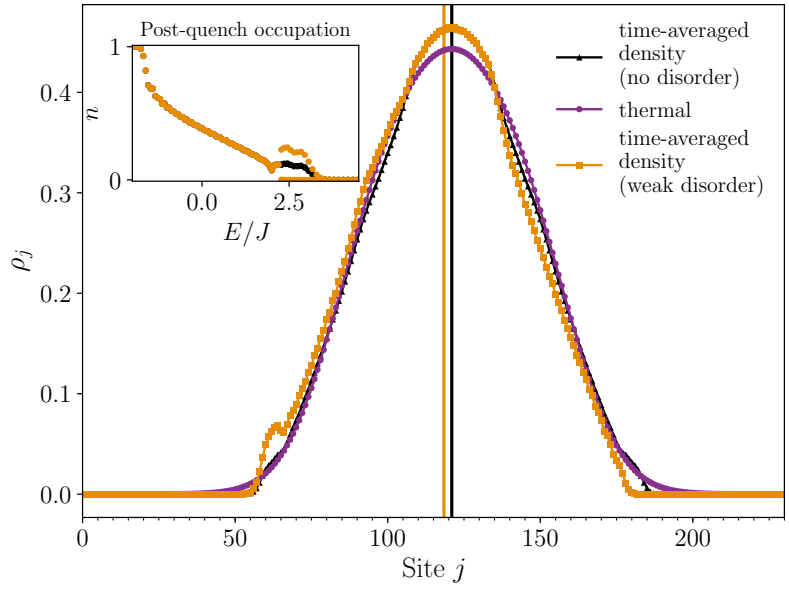

Figure 5.10: Main panel: We compare the real-space time-averaged density profile of the fermions without disorder (black curve with triangles) and in the case of very weak disorder (orange curve with squares) to the equilibrium prediction for a system with the same number of particles and the same total energy (purple curve with circles). Note that even the centre-of-mass of the weakly disordered time-averaged profile (solid orange line) does not coincide with the equilibrium or clean case prediction (solid black line). Inset: The occupation function of the post-quench states ordered by their energy in the weakly disordered (orange) and clean (black) cases. Note the occupation of states with energies $E > 2J$: these states are Bragg-localised. Parameters: number of lattice sites $L = 241$; trap spring constant $\kappa = 0.0025$; hopping integral $J = 1$; chemical potential $\mu = 0$; pre-quench trap centre $j_0 = 96$; post-quench trap centre $j_1 = 121$; disorder strength $W = \{0, 10^{-5}\}$.

of the trap. For large enough trap jumps, even when the disorder is extremely weak, we find that the violation of parity present in the initial conditions is now preserved in the infinite-time ($t \to \infty$) density profile. This represents a dramatic failure to match the form predicted by equilibrium statistical mechanics (see Fig. 5.10). This is not due to Anderson localisation. Rather, it is associated with the extreme disorder-sensitivity of the Bragg-localised states in the upper part of the single-particle spectrum. Weak disorder, provided that it is large compared to the splitting between symmetric and anti-symmetric Bragg-localised states, breaks the hybridisation of those states and thus causes the time-averaged density to be significantly asymmetric about the new trap centre.

The reason for asymmetry in case of arbitrary disorder strength however is twofold. First, an arbitrarily weak disorder potential breaks

the parity symmetry of the clean Hamiltonian. This has the consequence, for $W \gtrsim T$ (see (5.7) for definition of T), that the eigenstates become localised on the left or the right of the trap. Second, as disorder is made stronger, this effect extends to the delocalised states in the centre of the trap, which may be attributed to Anderson localisation.

For clarity, it should be stated that Bragg localisation and Anderson localisation are conceptually quite distinct. While the latter is defined as the absence of diffusion in the presence of randomness (see Sec. 3.3), the former occurs in a setting here where such a definition is not natural, because the unbounded trap potential in any case eventually prevents diffusion. A natural description of Bragg localisation is rather that there are high-lying eigenstates that are exponentially localised on a shorter length-scale than the classically allowed region set by the trap. While we use uncorrelated on-site disorder for simplicity, any term in the Hamiltonian that breaks the parity symmetry, e.g. an Aubry-André (AA) potential, where $\epsilon_j \equiv W\cos(2\pi\alpha j)$ with $\alpha = \frac{1+\sqrt{5}}{2}$ [14] or even a non-integer post-quench trap position j_1, would yield analogous effects with respect to the effect attributed to Bragg localisation.

The significance of the AA potential is that it facilitates experimental setups significantly. As previously discussed, the current experimental advances surrounding quantum quenches and quantum thermalisation are mostly realised in cold atom systems where it is not easy to simulate uncorrelated disorder, and usually some sort of correlation between on-site energies is present. However the AA quasi-periodic potential (which can be considered a kind of correlated disorder) exhibits a localisation-delocalisation transition. Moreover, systems with this quasi-periodic potential can be more easily simulated in an experimental setup [117, 167].

To quantify the influence of disorder, we define the 'jump efficiency' η as follows,

$$\eta \equiv \frac{x_1^{t\to\infty} - x_1^{t=0}}{\Delta j}. \tag{5.42}$$

Here the pre-quench centre-of-mass position of the cloud, $x_1^{t=0}$, is calculated from the pre-quench distribution; the time-averaged post-quench centre-of-mass position, $x_1^{t\to\infty}$, is calculated from (5.28). Put simply, this jump efficiency describes (as a number between 0 and 1) how much of the way from the pre-quench trap centre to the post-quench trap centre the atom-cloud moves.

Fig. 5.11 shows the jump efficiency as a function of jump size for different disorder strengths. The most striking feature is that, even in the limit where the jump size $\Delta j \to 0$, the jump efficiency does not remain unity; rather, it has the form

$$\eta_{\mathrm{p}} \equiv \lim_{\Delta j\to 0} [\eta(\Delta j)] \approx 1 - \alpha W^2. \tag{5.43}$$

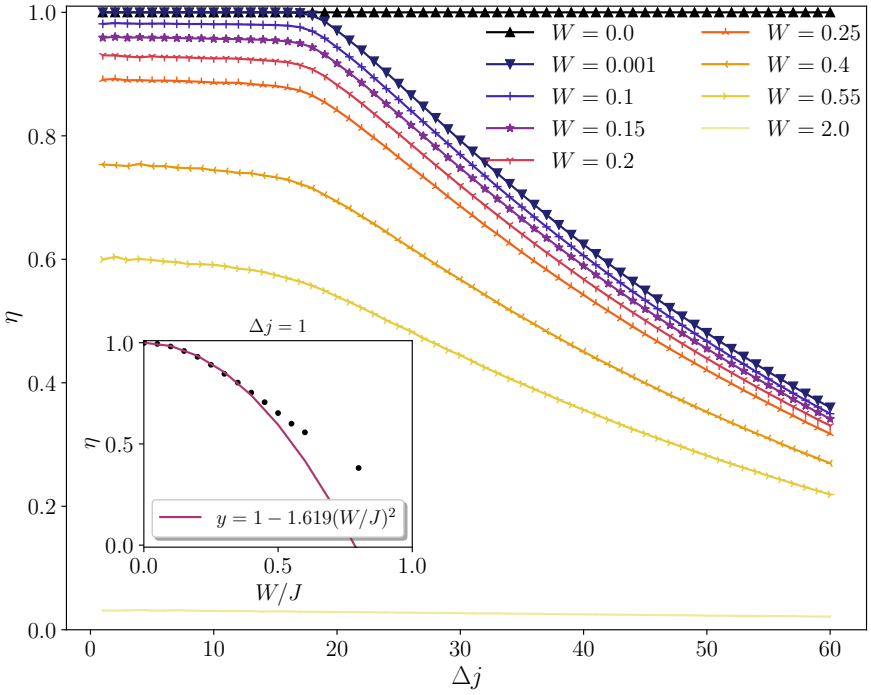

Figure 5.11: The jump efficiency η as a function of the jump size Δj, for various disorder strengths. This graph illustrates the qualitative distinction between Anderson and Bragg localisation. For $W = 0$ the jump efficiency η is always unity. For the disordered cases Bragg localisation appears in the form of a Δj-dependent decrease in η. Inset: The jump efficiency η as a function of disorder strength W/J for a fixed jump size $\Delta j = 1$. Parameters: number of lattice sites $L = 241$; trap spring constant $\kappa = 0.0025$; hopping integral $J = 1$; chemical potential $\mu = 0$; post-quench trap centre $j_1 = 121$. Each disorder-average is performed over 10000 disorder realisations.

This may be understood as the development of a correlation between (a) whether the disorder potential shifts the centre-of-mass of a particular post-quench eigenfunction to the left or to the right, and (b) whether the post-quench occupation of that eigenfunction goes up or down. Each of these effects is first-order in the disorder potential $V(x)$, but each by itself would average to zero. However, the development of a correlation between them gives an effect of order W^2 that survives the disorder average. Below (Sec. 5.4.5), we present a toy calculation that displays this physics.

As the jump size is increased, the plateau in $\eta(\Delta j)$ at some point gives way to a decrease in the jump efficiency. This is because the jump size is now large enough to populate some of the Bragg-localised states of the post-quench trapping potential. As discussed above, these are sensitive to even weak disorder, and once localised they effectively

contribute almost nothing to the jump efficiency. Indeed, the shape of the curves in Fig. 5.11 may be well approximated by the equation

$$\eta = f_{\mathrm{d}}\eta_{\mathrm{P}}, \tag{5.44}$$

where f_{d} is the fraction of the pre-quench atoms that are projected into non-Bragg-localised states, and η_{p} is the 'plateau value' of the jump efficiency defined in (5.43). As previously stated, to obtain the Bragg localisation effects visible in Fig. 5.11 we require only a parity-breaking potential while features associated with Anderson localisation require randomness.

5.4.5 *Jump efficiency*

In this final section, we present a toy calculation that allows us to understand the $1 - \alpha\tilde{W}^2$ dependence of the jump efficiency at small jump sizes (see inset of Fig. 5.11). We define $\tilde{W} \equiv W/J$ as the dimensionless disorder strength.

It represents the pre-quench single-particle eigenfunctions by,

$$\begin{aligned}\phi^{+}_{nj} &= \frac{1}{\sqrt{2}}\left(\delta_{j,j_0+n} + \delta_{j,j_0-n}\right),\\ \phi^{-}_{nj} &= \frac{1}{\sqrt{2}}\left(\delta_{j,j_0+n} - \delta_{j,j_0-n}\right).\end{aligned} \tag{5.45}$$

We have denoted the symmetric and antisymmetric eigenfunctions separately, while the quantum number $n = 1, 2, 3, \ldots$ (we ignore the $n = 0$ case). Essentially, this amounts to a cartoon of each harmonic oscillator eigenfunction in the form of two peaks at its classical turning points, retaining the information about whether the function is symmetric or antisymmetric. We thus obtain the densities:

$$|\phi^{+}_{nj}|^2 = |\phi^{-}_{nj}|^2 = \frac{1}{2}\left(\delta_{j,j_0+n} + \delta_{j,j_0-n}\right). \tag{5.46}$$

We need to occupy the symmetric and antisymmetric versions of $N/2$ eigenstates to get the correct particle number, i. e. we occupy the states with $1 \leqslant n \leqslant N/2$, such that the total density becomes

$$\rho_j = \sum_{n=1}^{N/2}\left(\delta_{j,j_0-n} + \delta_{j,j_0+n}\right). \tag{5.47}$$

This is a 'block' in real space, covering the region $j_0 - N/2 \leqslant j \leqslant j_0 + N/2$ (with a hole at $j = j_0$, but this causes only a $1/N$ effect, which we neglect).

Second, we assume that the post-quench eigenfunctions in the presence of disorder may similarly be approximated by,

$$\begin{aligned}\psi^{+}_{nj} &= \sqrt{\frac{1+\sigma_n\tilde{W}}{2}}\,\delta_{j,j_1+n} + \sqrt{\frac{1-\sigma_n\tilde{W}}{2}}\,\delta_{j,j_1-n},\\ \psi^{-}_{nj} &= \sqrt{\frac{1+\sigma_n\tilde{W}}{2}}\,\delta_{j,j_1+n} - \sqrt{\frac{1-\sigma_n\tilde{W}}{2}}\,\delta_{j,j_1-n},\end{aligned} \tag{5.48}$$

where the random variable $\sigma_n = \pm 1$ is chosen independently for each value of n to encode the presence of disorder. Note that for both the pre- and post-quench eigenfunctions we have made the simplifying assumption that the position of the classical turning points is proportional to the energy of the eigenstate. This corresponds to choosing a linear trapping potential rather than a quadratic one.

With the above choice of eigenfunctions we can determine $x_{1,n}$, the disorder-dependent centre-of-mass of post-quench eigenfunction n:

$$x_{1,n} = \sum_j j|\psi^+_{nj}|^2 = \sum_j j|\psi^-_{nj}|^2 = j_1 + \sigma_n n\tilde{W}, \tag{5.49}$$

which is linear in $\tilde{W}$ and independent of the symmetry of the eigenfunction.

In order to determine the post-quench occupation function n_β, we first determine the overlap between a particular pair of pre- and post-quench eigenfunctions:

$$\begin{aligned} O^{S_0S_1}_{n_0n_1} &\equiv \sum_j \phi^{S_0}_{n_0j}\psi^{S_1}_{n_1j} \\ &= \frac{\sqrt{1+\sigma_{n_1}\tilde{W}}}{2}\left(\delta_{j_0+n_0,j_1+n_1} + S_0\delta_{j_0-n_0,j_1+n_1}\right) \\ &+ \frac{\sqrt{1-\sigma_{n_1}\tilde{W}}}{2}S_1\left(\delta_{j_0+n_0,j_1-n_1} + S_0\delta_{j_0-n_0,j_1-n_1}\right). \end{aligned} \tag{5.50}$$

Here $S_0, S_1 \in \{-1,+1\}$ are the symmetries of the pre- and post-quench eigenfunctions, and n_0 and n_1 are their quantum numbers. Assuming without loss of generality that $j_1 > j_0$, the pure S_0 term is always zero, so that we obtain as squared overlap

$$\begin{aligned} \left|O^{S_0S_1}_{n_0n_1}\right|^2 &= \frac{1+\sigma_{n_1}\tilde{W}}{4}\delta_{j_0+n_0,j_1+n_1} \\ &+ \frac{1-\sigma_{n_1}\tilde{W}}{4}\left(\delta_{j_0+n_0,j_1-n_1} + \delta_{j_0-n_0,j_1-n_1}\right). \end{aligned} \tag{5.51}$$

The post-quench occupation function then takes the form

$$\begin{aligned} n^{S_1}_{n_1} &= \sum_{n_0=1}^{N/2}\sum_{S_0=\pm1}\left(\frac{1+\sigma_{n_1}\tilde{W}}{4}\delta_{j_0+n_0,j_1+n_1}\right. \\ &\left. + \frac{1-\sigma_{n_1}\tilde{W}}{4}\left(\delta_{j_0+n_0,j_1-n_1} + \delta_{j_0-n_0,j_1-n_1}\right)\right). \end{aligned} \tag{5.52}$$

Since n_1 has to be positive, we obtain ($\Delta \equiv j_1 - j_0$):

$$n_{n_1}^{S_1} = \begin{cases} 1 & n_1 \leq N/2 - \Delta; \\ \dfrac{1 - \sigma_{n_1}\tilde{W}}{2} & N/2 - \Delta < n_1 \leq N/2 + \Delta; \\ 0 & \text{otherwise.} \end{cases} \tag{5.53}$$

Hence the post-quench centre-of-mass is

$$\begin{aligned} x_1 &= \frac{2}{N} \sum_{n_1=1}^{L/2} \left(j_1 + \sigma_{n_1} n_1 \tilde{W}\right) n_{n_1}^{S_1} \\ &= \frac{2}{N} \sum_{n_1=1}^{N/2-\Delta} \left(j_1 + \sigma_{n_1} n_1 \tilde{W}\right) \\ &\quad + \frac{2}{N} \sum_{n_1=N/2-\Delta+1}^{N/2+\Delta} \left(j_1 + \sigma_{n_1} n_1 \tilde{W}\right) \left(\frac{1 - \sigma_{n_1}\tilde{W}}{2}\right). \end{aligned} \tag{5.54}$$

Upon disorder-averaging, any term containing an odd power of σ_{n_1} vanishes, while the average of any even power of σ_{n_1} is unity. Hence

$$\begin{aligned} \overline{x_1} &= \frac{1}{N}\left[2j_1\left(\frac{N}{2} - \Delta\right) + j_1\,(2\Delta)\right] \\ &\qquad - \frac{\tilde{W}^2}{N} \sum_{n_1=N/2-\Delta+1}^{N/2+\Delta} n_1 \\ &= j_1 - \Delta\tilde{W}^2 \frac{N+1}{N} \\ &\approx j_1 - \Delta\tilde{W}^2. \end{aligned} \tag{5.55}$$

The jump efficiency is given by the difference between this post-quench centre-of-mass and the pre-quench one in units of the jump size:

$$\begin{aligned} \eta &\equiv \frac{\overline{x_1} - j_0}{\Delta} \\ &\approx \frac{\Delta - \Delta\tilde{W}^2}{\Delta} \\ &= 1 - \tilde{W}^2. \end{aligned} \tag{5.56}$$

This is the qualitative behaviour that we observe for small jump sizes in Fig. 5.11.

5.5 SUMMARY

In this chapter we have studied a particular type of relatively simple quantum quench: a sudden trap displacement applied to a one-dimensional system of non-interacting lattice fermions with disorder. The

central theme of this chapter was to provide an understanding of how confinement, lattice structure and disorder conspire to provide various dynamical regimes to the coherent post-quench time evolution. We discussed these questions using a number of relatively straightforward real-space observables.

Our main observation was that the disorder in this system has two distinct localising effects: Anderson localisation, which occurs via the same mechanism as in the untrapped system, and Bragg localisation, which arises from the presence in the single-particle spectrum of the post-quench Hamiltonian of nearly degenerate bonding and antibonding states that are spatially localised near the edges of the trap.

As a result of Bragg localisation, the time-evolution of the density profile of the clean system after a quench shows two regimes. In the short-time regime, the dynamics are driven by the dephasing of the 'in-band' states (those with energies $|E| < 2J$), and look like collective oscillations about a position which may not match that of the actual post-quench trap centre. In the long-time regime, the dephasing of the Bragg-localised states causes a slow drift of the centre-of-mass from this position to the centre of the trap.

The role of disorder in the long-time evolution is very pronounced. Since the splitting between the symmetric and antisymmetric combinations of the Bragg-localised states is exponentially suppressed in their separation, extremely weak disorder can dominate over this splitting, resulting in a time-averaged state which magnifies the weak parity-breaking of the disorder potential into a macroscopic effect. Indeed, for the system parameters we have studied, as seen in Fig. 5.11, a disorder strength of less than a thousandth of the bandwidth of the single-particle hopping band can reduce the jump efficiency by a factor of more than two!

We have assumed throughout that the Bragg-localised level pairs form a discrete spectrum, and in that sense all of this analysis is for a finite-size system. This is the case for which experiments are perhaps most likely to be realised initially. However, it is interesting to ask what would happen if we took the thermodynamic limit. Then the disorder potential would make one left-Bragg-localised state resonant with a different right-Bragg-localised state. Would this still suppress the jump efficiency from unity? If so, by what fraction?

The question that is most imminent however, and which is been therefore studied following this initial research is the introduction of interactions between the fermions. Perhaps the most curious idea that has emerged from the research presented above is whether the logarithmic growth of entanglement entropy seen in MBL systems (see Sec. 3.4.2) also occurs when interactions are added to the Bragg-localised case. In fact, while not seeking complete analogy, we started to investigate how much of the MBL phenomenology translates to the

Bragg-localised case. We therefore focus on a very simplified model of the proposed Stark many-body localisation (as Bragg localisation focussed on the case where a tunnelling partner state is present). In the next chapter (Ch. 6) we thus shift from a closed-system non-interacting problem to a simplified closed-system interacting problem. We treat the more complicated general addition of interactions to the quench presented in this chapter in an unpublished overview in Ch. 7.

Overall, we believe that this kind of quantum quench provides an ideal platform for studying the interplay of spatial inhomogeneity, disorder and interactions for the dynamics in a quantum coherent setting.

6

STARK MANY-BODY LOCALISATION

The phenomenon of Bragg localisation introduced in Ch. 5 is a special case of the better known Wannier-Stark localisation [197], where one does not find a tunnelling partner. As a consequence, the wave function is completely localised in space. A more sophisticated mechanism for localisation is Anderson localisation as discussed in Sec. 3.3. It established that the eigenfunctions of a quantum particle moving in a disordered potential landscape in one or two dimensions are exponentially localised. At the same time we also discussed the phenomenon now termed many-body localisation (see Sec. 3.4). It was shown that Anderson localisation can persist even for finite densities of fermions with repulsive interparticle interactions.

A very natural question that immediately arises is whether disorder is at all an essential ingredient for observing MBL phenomenology, or whether it is possible for thermalisation to fail in interacting systems for other reasons. One obvious way already encountered in this thesis is the case of integrable systems (see Sec. 3.2). However those cases turned out to constitute isolated points in parameter space, with arbitrarily small generic variations in the Hamiltonian parameters restoring ergodicity. An important question is then whether there can be *robust* non-ergodic phases in models without quenched disorder. There have so far been several proposals for this, ranging from models inspired by classical glassy physics [86, 188] to variants of the Bose Hubbard model [49, 70]; however, there are also counterarguments that the localisation in some of these systems is a long-lived intermediate-time phenomenon which eventually yields to thermalisation at very long times [33, 208].

It is from the work in Ch. 5 that we were inspired to investigate to what extent one could find many of the above mentioned signatures of MBL without disorder, by introducing interactions into a single-particle model that exhibits Wannier-Stark localisation [173]. A very large trap jump on a finite lattice, where the tunnelling partners on the other side of the trap vanish, constitutes a Wannier-Stark localised system in the limit where the curvature is negligible. We investigate the physics of such an idealised 'large trap jump' and compare the resulting physics, which we call Stark many-body localisation, with the well known many-body disorder localised case. The setup for this system is depicted in Fig. 6.1.

For fields with slight spatial gradients, we find that Stark-MBL is robust and shares many similarities with MBL. Specifically, the entanglement entropy grows logarithmically with time after a quench

(Fig. 6.3), and the many-body eigenenergies of the Stark-MBL problem generically show Poissonian level statistics (Fig. 6.4). We moreover predict the results in our Stark-MBL system of a quench experiment starting from a charge-density wave state of the type conducted in [167], and we obtain graphs similar to those seen in the MBL case. For the case of a strictly uniform field, entanglement entropy and level statistics deviate from MBL phenomenology, although certain slow features appear to survive.

The plan for the remainder of this chapter is as follows. In Sec. 6.1 we briefly introduce the model. We then investigate the logarithmic entanglement growth analytically and numerically in Sec. 6.2. Subsequently we look at the level statistics (Sec. 6.3) and a possible imbalance experiment (Sec. 6.4).

6.1 MODEL

The Hamiltonian of our model is

$$\begin{aligned}\hat{H} =& \frac{J}{2}\sum_{j=0}^{L-2}\left(c_j^\dagger c_{j+1} + \text{h.c.}\right) + \sum_{j=0}^{L-1} W_j\left(n_j - \frac{1}{2}\right) \\ &+ V\sum_{j=0}^{L-2}\left(n_j - \frac{1}{2}\right)\left(n_{j+1} - \frac{1}{2}\right).\end{aligned} \tag{6.1}$$

Here the operator $c_j^\dagger$ creates a fermion on lattice site j, and the associated number operator $n_j = c_j^\dagger c_j$. $J/2$ is the hopping matrix element between neighbouring sites, V is the strength of the nearest-neighbour repulsion, and L is the number of sites of the lattice, the boundary conditions of which we take to be open. This Hamiltonian is very similar to (5.1) except for the inter-particle interactions V. The slight deviations due to constant terms are chosen such that a Jordan-Wigner transformation of (3.42) is equivalent to (6.1), apart from the on-site field. This emphasises the proximity to the XXZ model in which most of the MBL phenomenology is explained (see Sec. 3.4.2).

W_j is the on-site potential energy due to the applied electric field. For a uniform field γ, it takes the form $W_j = -\gamma j$ and represents a linear potential. For a non-uniform field, it acquires some simplified form of curvature, $W_j = -\gamma j + \alpha j^2/L^2$. This means that the potential has the same value and slope as the linear one at $j = 0$, but differs at the other end of the chain by α from the purely linear case (see the inset of Fig. 6.3).

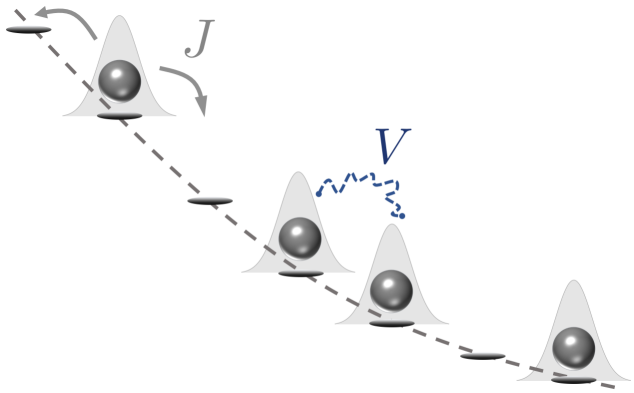

Figure 6.1: Schematic illustration of the model. On a *finite* lattice in one dimension, the single particle states of spinless fermions, which can delocalise via hopping J, are exponentially localised via a strong electric field. For a purely uniform field (i. e. a linear electric potential), this is usually referred to as Wannier-Stark localisation [197]. When the particles interact via nearest-neighbour interactions V, they share many properties with the well studied MBL phenomenology.

6.2 ENTANGLEMENT ENTROPY GROWTH

6.2.1 *Analytic treatment*

A quantity that is often used to diagnose and characterise MBL is the entanglement entropy (see Sec. 2.3 and Sec. 3.4.2). For Anderson localised systems this entanglement entropy does not rise beyond a value essentially set by the localisation length of the system. In contrast, it was found that the value grows without limit in the MBL regime, albeit *logarithmically* in time. To recap, in order to calculate this entanglement entropy, a spatial bipartition into two halves is made by cutting a particular bond. The reduced density matrix of the subsystem, ρ_{red}, is calculated, and the entropy determined via $S = -\text{Tr}\,(\rho_{\text{red}}\,\log(\rho_{\text{red}}))$. Serbyn *et al.* [177] gave an argument for the logarithmic growth at long times, i. e. that $S(t) \sim S_0 \ln(Vt)$, on the basis of the general physical picture of 'l-bits' in the MBL regime. This argument is explained in detail in Sec. 3.4.2. We now show that the long-time entanglement growth in the Stark-MBL system behaves similarly for sufficient non-uniformity of the field, though with some modification reflecting the fact that the tails of Wannier-Stark-localised wave functions are not pure exponentials.

We begin by deriving the form of these tails. We will then use this information and the logic of [177] to predict $S(t)$. Similar to the calculation in Sec. 5.3.2, we obtain the functional form of the tails of the single-particle Wannier-Stark wave functions from a semiclassical

WKB type argument. This involves using a WKB expression for the wave function,

$$\psi(x) \sim \exp\left(i \int^x k(x')dx'\right), \tag{6.2}$$

with $k(x)$ obtained from the condition of local energy conservation (setting the lattice constant a to unity),

$$J\cos(k) + V(x) = E. \tag{6.3}$$

To first order in x, the potential takes the form $V(x) = -\gamma x$; hence the energy-conservation condition reads $J\cos(k) - \gamma x = E$, which implies that

$$k(x) = \arccos\left(\frac{\gamma x + E}{J}\right). \tag{6.4}$$

This identifies three different regimes of x:

1. $-J < \gamma x + E < J$. In this region the wavenumber is real, and the solutions are plane-wave-like. As previously this is the *classically-allowed* region.

2. $\gamma x + E > J$. In this region the argument of the arccosine is greater than 1, and thus the wavenumber becomes purely imaginary, leading to a decaying wave function. We call this the *classically-forbidden* region.

3. $\gamma x + E < -J$. In this region the argument of the arccosine is less than -1, and thus the wavenumber becomes π/a plus an imaginary part. This leads to a wave function that oscillates while decaying. This was termed the *Bragg-forbidden* region [174]. In view of the missing tunnelling partner, this could equally be called *Stark-forbidden*.

From the point of view of entanglement, only the envelope of the decay will be important — there can be no interference, since the oscillating tail of the wave function of one particle will always meet the non-oscillating tail of the other. That envelope is given by the imaginary part of the arccosine, which is always a logarithm:

$$\mathrm{Im}\left[k(x)\right] \approx \ln\left(\left|\frac{\gamma x}{J}\right|\right), \qquad |\gamma x + E| \gg J. \tag{6.5}$$

For simplicity, we may take x to be large and positive so that the modulus under the logarithm may be dropped. Then the exponent in the WKB wave function is given by

$$-\int^x \ln\left(\frac{\gamma x'}{J}\right) dx' \approx -x \ln\left(\frac{\gamma x}{J}\right), \tag{6.6}$$

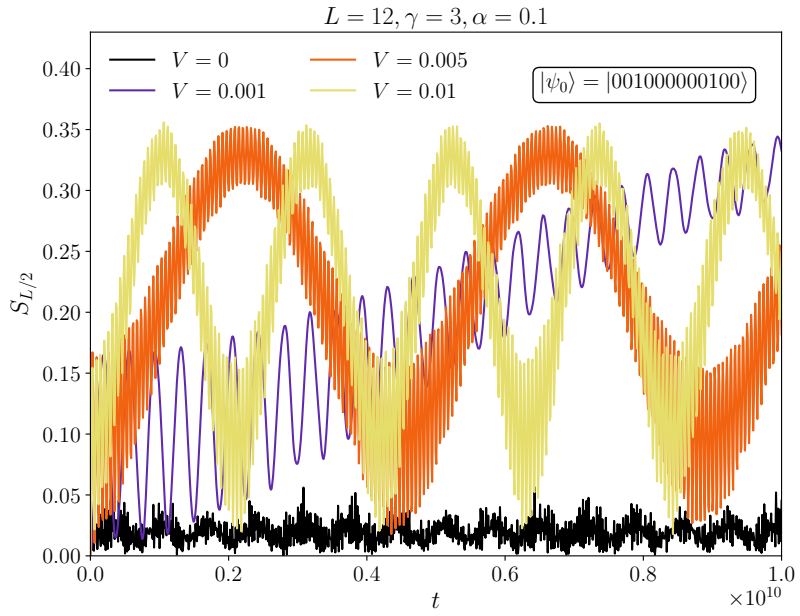

Figure 6.2: Entanglement growth for a two-particle system. An initial product state with two particles equidistant at either side of the bipartition is exposed to a strong non-uniform field, i. e. a linear plus a quadratic potential. We see that the entanglement entropy oscillates at a very small maximum value in the case of no interactions ($V = 0$), while many-body energy dephasing effects cause a very slow rise of the entanglement entropy to the maximum value possible for this pair. The $V \neq 0$ curves scale as a function of Vt. Note that we have scaled the $V = 0$ results by a factor of 50 for illustration purposes.

where we have dropped a linear-in-x term that does not have a logarithm. Hence the form of the tail of the wave function is

$$\psi(x) \sim \exp\left(-x \ln\left(\frac{\gamma x}{J}\right)\right). \tag{6.7}$$

This shows that in essence one still finds exponential decay of the single-particle wave functions in a Wannier-Stark localised system. On this basis, we follow [177] to estimate the entanglement entropy as a function of time.

First, we consider just a pair of particles, $|l\rangle$ and $|r\rangle$, one on either side of the bipartition used in calculating the entanglement entropy. Let each particle have been projected, at the quench, into a superposition of two nearby Stark-localised states. If the particles are separated by a distance x, then the overlap between their wave functions has the same form as one of the tails, i. e. (6.7). Hence the matrix element of the nearest-neighbour repulsion between them is approximately

$$\langle l|\hat{V}|r\rangle \approx V \exp\left(-x \ln\left(\frac{\gamma x}{J}\right)\right). \tag{6.8}$$

This is also a good approximation for the energy difference between the state where the particles are further apart and the state where they are closer together. This energy difference controls the dephasing of these different many-body eigenstates, and hence the dephasing time is

$$t_{\text{deph}} \approx V^{-1} \exp\left(x \ln\left(\frac{\gamma x}{J}\right)\right). \tag{6.9}$$

This is the time at which the entanglement entropy due to this pair will rise from zero to its maximum value. There are several important points to note here. On the one hand, the two-particle Wannier-Stark case should not show any difference to the two-particle disorder case, because the single-particle energy levels play no role at this point of the calculation. On the other hand, there is one crucial difference; all two-particle many-body states are degenerate as long as they have the same centre of mass. This allows for delocalisation in a strictly linear potential, but not in a curved one.

We show the results for two particles in a slightly curved potential in Fig. 6.2. As in [177], there is a very slow growth of entanglement due to dephasing for the case where $V \neq 0$, consistent with the prediction of (6.9). In addition this dephasing happens on a time-scale such that $Vt \sim 1$, confirming the prediction further. We find similarly slow features for the case of a strictly linear potential, but on a different time-scale and less clean. This difference is more pronounced in the many-body case, where it fundamentally changes the behaviour of $S(t)$. Before discussing this in more detail, we show the consequences for a many-particle Wannier-Stark system and the total entanglement entropy between the subsystem to the left of the cut and the subsystem to the right.

This can be thought of as an 'entanglement front' moving through the system from the cut as t increases. At a time t, this front will have moved a distance $x(t)$, which is obtained by solving (6.9) for x. The entanglement entropy at that time will thus be given by $S(t) = S_{\max}\frac{x(t)}{L}$, where L is the length of the subsystem to the left of the cut. Solving (6.9) for $x(t)$, we obtain

$$x(t) = \frac{\ln(Vt)}{p\left(\frac{\gamma \ln(Vt)}{J}\right)}, \tag{6.10}$$

where $p(u)$ is the solution of the equation $p\, e^p = u$. Thus the entanglement entropy is given by

$$S(t) = \frac{S_{\max}}{L} \frac{\ln(Vt)}{p\left(\frac{\gamma \ln(Vt)}{J}\right)}. \tag{6.11}$$

The results of (6.11) can be found in Fig. 6.3, where they match the numeric treatment fairly well.

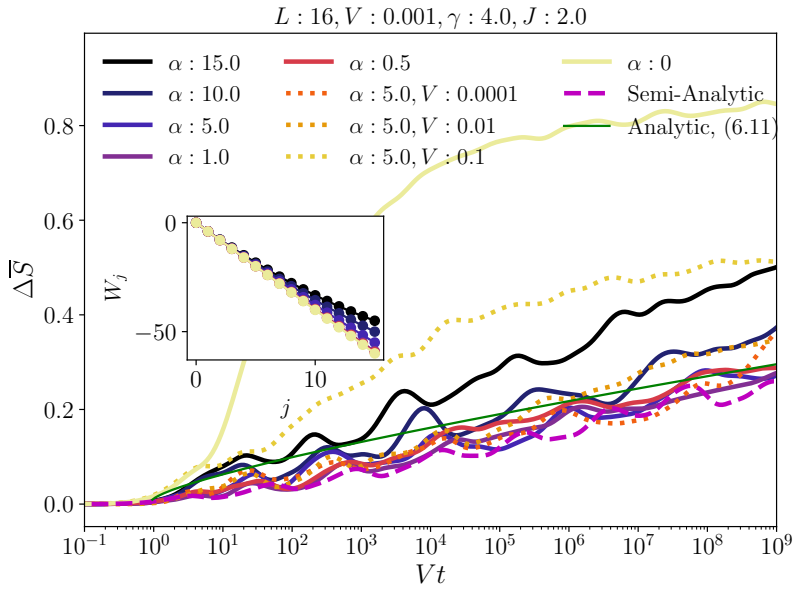

Figure 6.3: Difference $\Delta\overline{S}$ between the bipartite entanglement in the interacting and non-interacting cases. The parameter α denotes the cumulative effect of field non-uniformity on the potential at the end site. For sufficiently small α and suitably large field γ there is good qualitative agreement with our semi-analytic calculation (magenta dashed line) and full analytic calculation (green line and (6.11)). For larger α, the entanglement growth becomes stronger than predicted due to the progressive delocalisation of some of the single-particle orbitals as the field gets weaker. For the purely uniform field, there is an initial steep rise which we attribute to additional degeneracies of the many-body spectrum. The numerical curves have been smoothed by convolution with a Gaussian, $w(n) = e^{-(n/\sigma)^2/2}$, with $\sigma = 4$. Inset: Potential used in the respective main curves.

We can supplement this analytic calculation by computing a 'semi-analytical' form for the entanglement entropy which allows us to circumvent full diagonalisation of the Hamiltonian (6.1). We shall assume that the number of sites, L, is even, and that the entanglement entropy is calculated across a cut between sites $(L/2) - 1$ and $L/2$. We choose our zero of potential energy to lie in the middle of that bond. We shall often ignore the V-term, assuming that it is too weak to modify the form of the many-body eigenfunctions significantly, i. e. we consider the leading effect of V on energies, not wave functions.

Our initial condition involves placing fermions at the sites $S = \{j_k\}$, where $k = 1, 2, \ldots, M$, and M is the total number of fermions. Let $M = M_L + M_R$, where M_L and M_R are respectively the number of fermions to the left and right of the cut, and let us assume that the

list S is in order from left to right (i. e. that $j_k < j_{k+1}$ for all relevant k). This initial condition can be written in second-quantised form as

$$|\psi\rangle = c^\dagger_{j_M} c^\dagger_{j_{M-1}} \dots c^\dagger_{j_2} c^\dagger_{j_1} |0\rangle , \tag{6.12}$$

where $|0\rangle$ is the fermionic vacuum. Let us note that the electric potential energy of this state is given by

$$E_0 = -\gamma \sum_{k=1}^{M} j_k, \tag{6.13}$$

where we have neglected the contribution of α.

We can only write the initial condition in the many-body eigenbasis analytically if we ignore V, so we shall do that for now. In that case, we just need to know how to write the on-site creation operator in terms of creation operators for the Stark-localised states. If we assume the strong-field limit, i. e. that $\gamma \gg J$, then we may suppose that

$$c^\dagger_j = \sqrt{1 - 2\left(\frac{J}{\gamma}\right)^2}\, \beta^\dagger_j + \frac{J}{\gamma}\left(\beta^\dagger_{j+1} + \beta^\dagger_{j-1}\right), \tag{6.14}$$

where $\beta^\dagger_j$ creates a fermion in the single-particle Stark-localised state centred at position j. This assumes that the Stark-localised states are restricted to three sites (the central, or 'locator', site and its two nearest neighbours). It also does not account for the mutual orthogonality of the different Stark-localised states, and it does not work at the very ends of the chain.

Substituting (6.14) into (6.12), we obtain the following,

$$|\psi\rangle = \sum_{\{Q\}} f_Q \beta^\dagger_{Q(j_M)} \beta^\dagger_{Q(j_{M-1})} \dots \beta^\dagger_{Q(j_2)} \beta^\dagger_{Q(j_1)} |0\rangle . \tag{6.15}$$

Here Q is an operation that, for each original site label, either moves it one place to the left, moves it one place to the right, or leaves it alone. The factor f_Q is given approximately by

$$f_Q \approx \left(\frac{J}{\gamma}\right)^{\lambda_Q + \rho_Q}, \tag{6.16}$$

where λ_Q counts the number of original site labels that are shifted to the left by Q, and ρ_Q the number that are shifted to the right.

In order to time-evolve (6.15), we attach to each many-body state in the sum a factor of $e^{-iE_Q t}$, where E_Q is the state's energy. As we know from [177], we need to be more precise about the tails of the single-particle wave functions at this stage if we want to capture the entanglement evolution at late times. The energy E_Q is composed of two parts: the electric potential energy, and the repulsive interaction energy of each pair of particles in the system. The electric potential

energy can be calculated by noting which particles have moved compared to the reference state,

$$E_{Q,\text{elec}} = E_0 + \gamma\left(\rho_Q - \lambda_Q\right). \tag{6.17}$$

The repulsive interaction energy may be roughly calculated by taking the probability density in the tail of one Stark-localised state at the centre of the other and multiplying it by V. For two Stark-localised states with locators separated by ξ lattice sites, this gives an energy of approximately

$$V\left(\frac{J}{\gamma}\right)^{2\xi-2}. \tag{6.18}$$

Thus the complete energy of the component Q of $|\psi\rangle$ is given approximately by

$$E_Q \approx E_0 + \gamma\left(\rho_Q - \lambda_Q\right) + \frac{V}{2}\sum_k \sum_{p\neq k}\left(\frac{J}{\gamma}\right)^{2\left|Q(j_k)-Q(j_p)\right|-2}, \tag{6.19}$$

where the sums over k and p run from 1 to M.

We can thus approximate the state of the M-fermion system at an arbitrary time t as

$$|\psi(t)\rangle = \sum_Q f_Q e^{-iE_Q t}\beta^\dagger_{Q(j_M)}\beta^\dagger_{Q(j_{M-1})}\cdots\beta^\dagger_{Q(j_2)}\beta^\dagger_{Q(j_1)}|0\rangle, \tag{6.20}$$

where f_Q is given by (6.16) and E_Q is given by (6.19). To turn this into a density operator it is more convenient to write it in first-quantised notation,

$$\begin{aligned}|\psi(t)\rangle = \sum_Q f_Q e^{-iE_Q t}\Big[\,&|Q(j_1)\rangle\otimes|Q(j_2)\rangle\otimes\cdots\\ &\otimes|Q(j_{M-1})\rangle\otimes|Q(j_M)\rangle\Big],\end{aligned} \tag{6.21}$$

where $|j\rangle$ is the single-particle state in which the particle is on site j. This allows us to calculate the time-evolved reduced density matrix of any subsystem, from which we obtain $S(t)$ via diagonalisation. The results can be found in Fig. 6.3 and again match the numerical curves very well, qualitatively more accurate than (6.11) even.

6.2.2 *Numerical simulations*

We now compare the above results against numerical simulations of the model (6.1). Hopping is set to $J = 2$ and we consider an $L = 16$ chain at half-filling. The field on one end has strength γ and decreases uniformly, so that the value of the potential on the final site of the chain differs by an amount α from its value in the purely linear case. We use all possible initial product states (at half-filling) that do not

have a particle on the two sites directly adjacent to the cut, which we choose to be at the middle bond. For $L = 16$, this amounts to 1225 states. Using ED, we compute the time-evolution for a given initial state, and obtain the entanglement entropy $S(t)$ for an equal bipartition of the lattice. We then average over all of the above mentioned initial states.

Our results for $\gamma = 4$ and various values of α are shown in Fig. 6.3. In order to show the effect of interactions, we display $\Delta\overline{S}(t) \equiv \overline{S}(t) - \overline{S}_0(t)$, where $S_0(t)$ is the entropy in the non-interacting case, and the bar denotes an average over the initial conditions as discussed above. Consistent with previous findings, the entanglement growth due to many-body dephasing effects commences at times $Vt \sim 1$. The curves scale as a function of Vt, until the interactions become strong enough to alter the eigenstates significantly.

For sufficiently nonuniform field, this growth continues logarithmically up to a maximum value, which is finite for a finite system size. This growth agrees qualitatively with our semi-analytic calculation presented above, confirming our intuition that the physics of this system is well described by (6.15) and (6.19). We have also compared the pure analytic calculation (6.11) against the numerics. Here $S_{\max}$ is taken to be the diagonal entropy S_{diag} resulting from the reduced density matrix obtained by (6.21). S_{diag} denotes the maximum achievable entropy for a given initial state, assuming that the interactions do not significantly change the form of the eigenstates and that time allows for complete dephasing of all off-diagonal elements [145, 177].

In the case of a strictly linear potential, there is instead a steep rise of the entanglement entropy followed by slow growth. We attribute this to the many exact degeneracies in the non-interacting version of the problem, which arise from the fact that all two-particle states with the same centre of mass are degenerate, and can therefore hybridise strongly.

The logarithmic entanglement growth given by (6.11) can thus fail for two different reasons: too little non-uniformity, or too small a field. The former allows delocalisation of the two-particle states into a broad band, with a correspondingly short dephasing time, leading to steep initial growth of $\Delta\overline{S}(t)$. On the other hand the latter causes the localisation to weaken in parts of the chain, in turn making the accumulation of entanglement in that part stronger. Both cases are visible in Fig. 6.3. However, in between them there is a large range of curvature values for which an MBL-like entanglement growth is observed. We thus conclude that in terms of entanglement growth, the Stark-MBL case is not materially different from the disorder MBL regime. As already mentioned in the introduction to this chapter, with disorder-free MBL models, there is always the caveat that a phenomenon might be slow, but ultimately would give way to thermalising behaviour at very large times. We therefore turn towards a

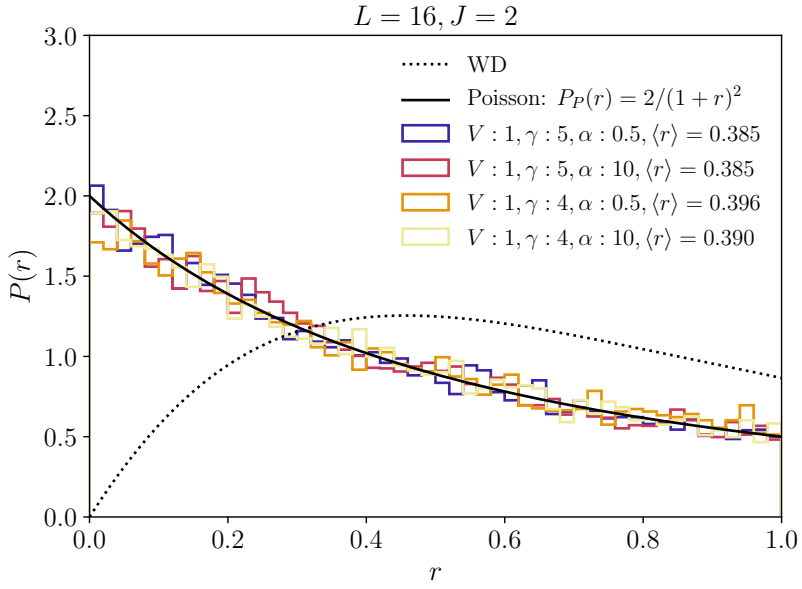

Figure 6.4: The many-body level statistics for the case of nonzero field gradient α. For all displayed values of field strength γ and α the probability distribution of the gap-ratio parameter, $r_n = \min(\delta_n/\delta_{n+1}, \delta_{n+1}/\delta_n)$ (where δ_n is the gap between the n^{th} and $(n-1)^{\text{th}}$ energy eigenvalues), agrees with the prediction for Poisson level statistics expected for integrable or localised models. For comparison we have included the prediction for Wigner-Dyson statistics.

measure for localisation that is basis independent, the many-body level statistics.

6.3 MANY-BODY LEVEL STATISTICS

A powerful and basis-independent diagnostic to determine whether a model is localised is its spectral statistics [116, 130]. Fig. 6.4 shows our exact diagonalisation results for the gap-ratio parameter in a chain of length $L = 16$ with open boundary conditions, for a range of field strengths γ and gradients α. These were obtained in exactly the same fashion as introduced in Sec. 3.4.2, but as a recap, we recall that the gap-ratio parameter is defined as $r_n = \min(\delta_n/\delta_{n+1}, \delta_{n+1}/\delta_n)$, where δ_n is the gap between the n^{th} and $(n-1)^{\text{th}}$ energy eigenvalues. Plotting a histogram of the gap-ratio parameter eliminates a dependence on the density of states, such that we can use the whole spectrum as long as there is no mobility edge present. We have verified this and the results are qualitatively the same for all ranges and energy densities used.

The probability distribution of the gap-ratio parameter for Poisson statistics of the level spacings reads $P_P(r) = 2/(1+r)^2$, which is in ex-

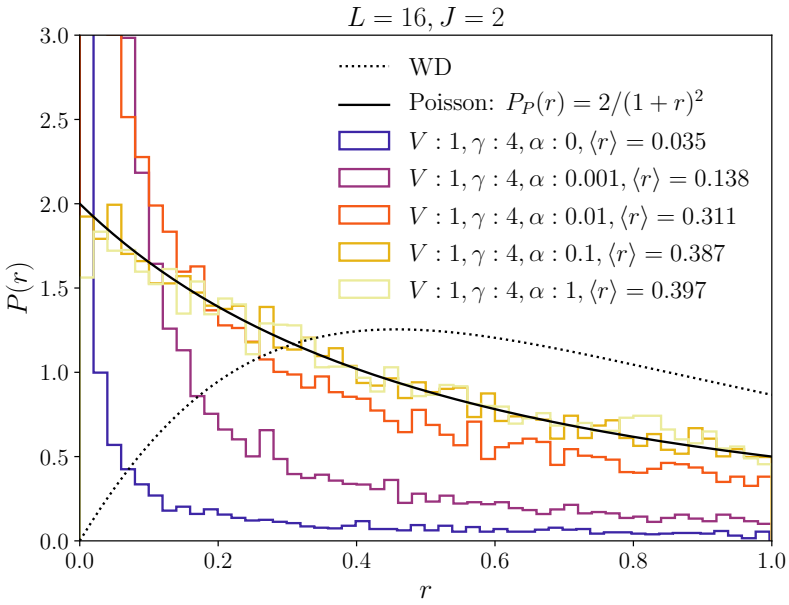

Figure 6.5: The many-body level statistics for the case in which Poisson level stastics are not found. In the case of very small or zero field gradient α, we find that the probability distribution for the gap-ratio parameter is consistent neither with Poissonian nor with Wigner-Dyson statistics. We attribute this to the many exact degeneracies in the non-interacting problem creating a disproportionally large weight for small r_n in the many body spectrum.

cellent agreement with our results over most of our parameter range. In the case of very small or zero field gradient α however, we find results that are consistent neither with Poissonian nor with Wigner-Dyson statistics. We attribute this to the many exact degeneracies in the non-interacting problem creating a disproportionally large weight for small r_n in the many body spectrum. This failure to obey Poisson level statistics is shown in Fig. 6.5. It may also be observed in the regime where $V/\gamma \ll 1$, i. e. in the case of a strong uniform component but weak interactions. In this case, as well as the parametrically opposite case of $V \to \infty$, we do not expect the level statistics to give reliable predictions due to the proximity to a non-interacting model, or an effective non-interacting model in the case of large V.

6.4 QUENCH FROM CHARGE-DENSITY WAVE

While the entanglement and spectral statistics are experimentally difficult to extract, there are other indicators of localisation. One of the simplest setups consists of monitoring the relaxation of an initial charge-density wave (CDW) order, in which all even sites are occu-

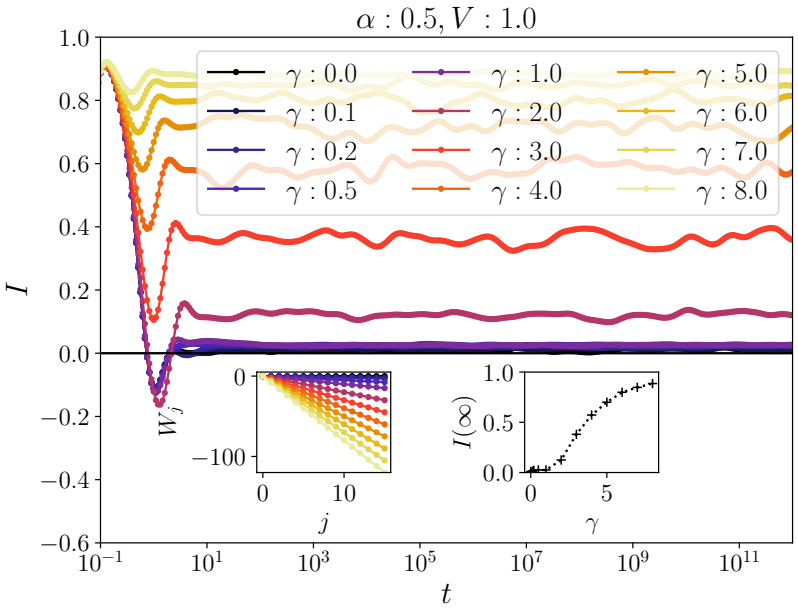

Figure 6.6: The $L = 16$ study of a hypothetical imbalance experiment, where an initial charge-density wave relaxes under unitary time-evolution. The different curves represent different field strengths γ with $\alpha = 0.5$. Inset left: Visualisation of the corresponding potential. Inset right: Average imbalance $\mathcal{I}$ at times $10^{14} \geq t/J \geq 10^{11}$. The numerical curves have been smoothed by convolution with a Gaussian, $w(n) = e^{-(n/\sigma)^2/2}$, with $\sigma = 4$.

pied [167]. An associated observable is the imbalance $\mathcal{I}$ between the occupation on odd and even sites, N_o and N_e respectively,

$$\mathcal{I} = \frac{N_e - N_o}{N_e + N_o}. \tag{6.22}$$

In the ergodic, thermalising case it should quickly decay to zero, which it does in the case $\gamma = 0$ when there is no Wannier-Stark localisation. For a many-body localised system, on the other hand, the value of the imbalance should remain non-zero up to infinite times.

In Fig. 6.6, we show exact diagonalisation results of the time-evolution of an initial CDW state under unitary time-evolution given by the Hamiltonian (6.1). After initial transient behavior, the imbalance (6.22) remains non-zero for arbitrarily long times in the case of sufficiently large fields.

6.5 SUMMARY

In summary, we have shown that the experimentally natural case of a finite system in an electric field, a simple Wannier-Stark-localised system, shows properties that coincide with those of the MBL phase.

While the case of a purely uniform field, $\alpha = 0$, remarkably turns out to be a non-generic limit, even moderate curvature gives consistent and robust MBL-like features. The bipartite entanglement entropy $S(t)$ exhibits a slow, logarithmic growth to a value much larger than that obtained in the non-interacting case. The spectral statistics, a dynamics-independent measure for localisation, are Poissonian. And finally, localisation seems equally persistent in a now standard imbalance experiment, where the relaxation of CDW order is measured.

In the limit of large system sizes, the energy density can grow without bound on account of the unbounded potential implied by a uniform component of the electric field. This precludes an asymptotic definition of exponential localisation, which should however not pose a problem in practice given the attainability of short localisation lengths. While the set-up of Stark-MBL is quite different from conventional disorder MBL, the similar phenomenology is quite striking. The MBL phase is described in terms of l-bits, while other disorder-free localised systems have also identified integrals of motion. Here, l-bits emerge naturally and robustly as Stark locators, again without the use of any quenched disorder.

7

INTERACTING TRAP JUMP

In Ch. 5 and Ch. 6, we considered the physics of a non-interacting trap jump quench and an idealised interacting system respectively. In this chapter we are now interested in the more complicated case of a trap jump quench including interparticle interactions. Chronologically, some of this work was done in parallel with or even prior to the work in Ch. 6. In fact it is the more complicated trap jump that ultimately led us to the discovery of Stark many-body localisation. This chapter is thus a relatively brief summary and overview of some of the investigated features. It consists of mostly unpublished and unfinished work, such that in many places definite conclusions may not be drawn and in some cases may be speculation. We note that the addition of interactions is not the unique unifying feature, but merely the most common denominator. A very important part is dedicated to the entanglement properties of the system in the absence of disorder and interactions (see 7.2).

We now have in essence three main parameters, namely disorder strength W, interaction strength V and trap jump distance Δj. Due to the increased complexity of the problem, we therefore attempt to summarise the main features in a phase diagram in Fig. 7.1. Throughout this chapter we will refer back to this figure at many instances.

7.1 MODEL AND QUENCH PROTOCOL

Similar to Ch. 5, we consider spinless fermions moving in one dimension on a lattice of L sites with open boundary conditions. In this chapter, we add nearest-neighbour interactions, such that the Hamiltonian reads

$$H = -J\sum_{j=1}^{L-1}\left(c_j^\dagger c_{j+1} + c_{j+1}^\dagger c_j\right) + \sum_{j=1}^{L}\left[\frac{1}{2}\kappa a^2\left(j-j_0\right)^2 + \epsilon_j\right]c_j^\dagger c_j + V\sum_{j=1}^{L-1} n_j n_{j+1}. \tag{7.1}$$

Here the operator $c_j^\dagger$ creates a fermion on site j, and J is the hopping matrix element between neighbouring sites. The on-site energy consists of a harmonic trapping potential of spring constant κ centred at j_0 plus additional uncorrelated on-site disorder taken from a uniform box distribution: $\epsilon_j \in [-W, W]$. The nearest-neighbour interaction strength is denoted by V. For convenience we shall henceforth set both $\hbar$ and the lattice constant a to unity.

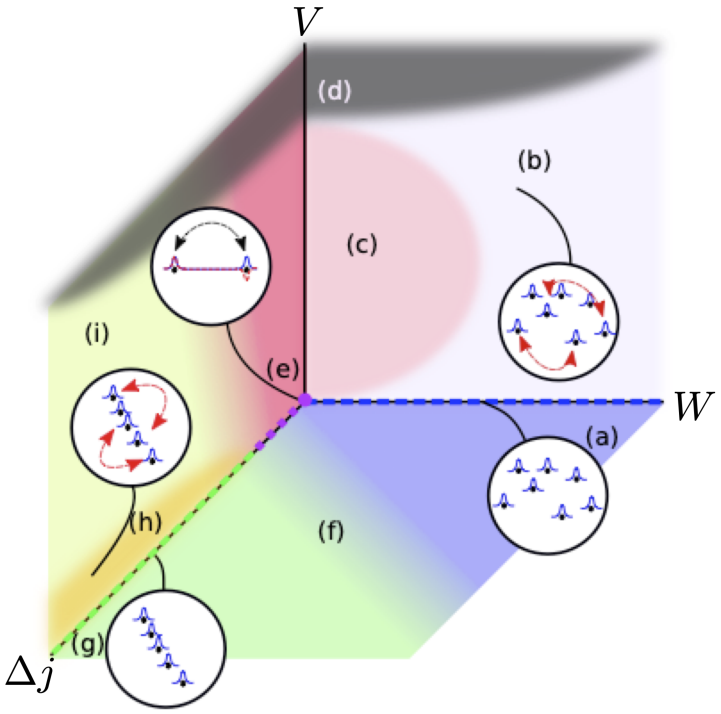

Figure 7.1: Phase diagram of a trapped fermion quench: a) Anderson insulator. b) Many-body localised phase. c) Delocalised phase. d) Domain-wall physics. e) Bragg-localised phase (quasi-logarithmic entanglement growth). f) Competition between Stark- and Anderson localisation. g) Pure Stark localisation. h) Stark many-body localisation. i) Stark many-body localisation and interaction assisted tunnelling. More detailed explanations may be found in the main text. The diagrams illustrates the single-particle eigenfunctions and the underlying mechanism of entanglement growth in the system at that parameter range.

As in Ch. 5 we study a spatially inhomogeneous global quench in order to investigate the non-equilibrium dynamics of this model. Starting with some initial state, we time-evolve the system from time $t = 0$ according to (7.1), where we replace j_0 by j_1, such that the jump size is defined as $\Delta j \equiv |j_1 - j_0|$. We discriminate between two different types of initial condition. In the case that $\Delta j > 0$, the initial state consists of the ground state of (7.1) with a chemical potential chosen such that no Bragg-localised state be occupied. The quench is then indeed a trap jump in the way discussed in Ch. 5. The ground-state is generally obtained numerically using the DMRG algorithm (see Sec. 4.4). On the other hand, the case in which $\Delta j = 0$, i. e. the V-W plane in Fig. 7.1, would not constitute a quench as the ground state of (7.1) is an eigenstate of the system. In this case we choose the initial state to be a simple product state, in which sites have a definite particle number at time $t = 0$. The caveat here is that if we choose particles to be far away from the trap centre, they might be in the Bragg-forbidden region of the trap. We will mention the precise form

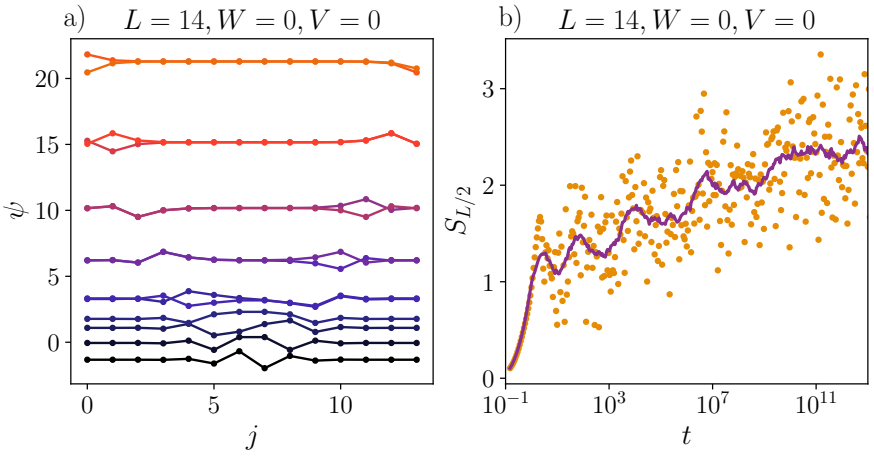

Figure 7.2: a) As a reminder, the single-particle eigenfunctions of the clean Hamiltonian (7.1) displaced by their eigenenergy as a function of position j. High-energy eigenstates show Bragg localisation as previously discussed. b) We can observe an approximately logarithmic-in-time entanglement growth (yellow points) of the bipartite entanglement entropy $S_{L/2}$ as defined in (7.2) with time after quenching a charge density wave (CDW) into (7.1). Further parameters were $J = 1, \kappa = 0.5$ and $j_0 = L/2 + 0.5$. The purple line represents a convolution with a box function including 20 points to smoothen out the data.

of the initial condition when discussing this region. This slightly complicated quench procedure makes it possible to summarise the entire content of this chapter in Fig. 7.1. In order to simplify the analysis, we first discuss the special point in which $V = W = \Delta j = 0$. This is depicted as a purple point in Fig. 7.1. We then describe the remaining phase diagram.

7.2 THE CLEAN AND INTERACTION-FREE CASE

An interesting special point in the study of entanglement properties of (7.1) is the case when $V = W = \Delta j = 0$, marked in purple in Fig. 7.1. In this special case, given a parity symmetric Hamiltonian, we may obtain quasi-logarithmic entanglement growth with neither interactions nor disorder.

The Hamiltonian we quench into consists of (7.1), with the harmonic trapping potential centred at $j_i = L/2 + 1/2$ (L even), i. e. precisely between the lattice sites of the middle bond. The initial condition is a product state, either a charge density wave (CDW) with all particle on odd or even sites respectively, or a domain wall, where we place all particles in one half of the lattice and as such on one side of the trap. We will see that especially the domain wall initial condition is particularly suited to explaining the problem.

Many of the underlying phenomena presented below are linked to the physics discussed in Ch. 5. However, entanglement was not part of the initial work, for which reason we present the unpublished results in the following. We want to focus on two things. Firstly, can we reproduce the bipartite logarithmic-in-time entanglement growth [21] of the MBL phase with a simple non-interacting (and realistic) system? And secondly, how does this change if we add interactions or disorder? The entanglement entropy was previously defined (2.20), but we remind ourselves that it is the von Neumann entropy

$$S = -\mathrm{Tr}\left(\rho_A \log \rho_A\right) = -\mathrm{Tr}\left(\rho_B \log \rho_B\right) \tag{7.2}$$

of the reduced density matrix of either subsystem A or B of the whole system. In this Section, we always form the two subregions by dividing the system at the centre bond (denoted by $S_{L/2}$ for the entanglement).

The fundamental idea for logarithmic-in-time entanglement growth, namely dephasing due to interaction-induced shifts in the many-body energies, is absent in this calculation as there are no interactions. However, as discussed in Ch. 6, the essential ingredient to logarithmic entanglement growth is a series of superpositions of localised single particle orbitals that can dephase with respect to a bipartition on an exponential hierarchy of time-scales. This is in fact what we described in Sec. 5.4.3 with respect to the density, where for a parity symmetric Hamiltonian Bragg-localised states can dephase states on an exponentially large time-scale. This physics can be translated into observations about the entanglement entropy.

Importantly, when quenching from a product state, we are using a superposition of eigenstates that have equal weighting on either side of the bipartition (the Bragg-localised states). Unlike the eigenstates of a simple tight-binding two-site system, they dephase very (exponentially) slowly. Upon dephasing, the Bragg localised states build up the maximum possible entanglement entropy of $S_{\max} = \log(2)$ each. A series of such dephasing Bragg-localised states with approximately exponential increase of the dephasing period then yields approximately logarithmic entanglement growth as shown in Fig. 7.2.

7.2.1 *Role of Bragg-localised states in entanglement growth*

With the general result established, we now aim to explain the mechanism behind the log-growth observed in Fig. 7.2. A very clear way to show this is by actually not using a charge density wave as the initial conditon, but rather a domain wall, or even single particles at specific positions. The dynamics of the corresponding bipartite entanglement growth is then dependent on the exact locations of the particle(s) before the quench and which post-quench single-particle states are necessary to describe the particle in that position. This is

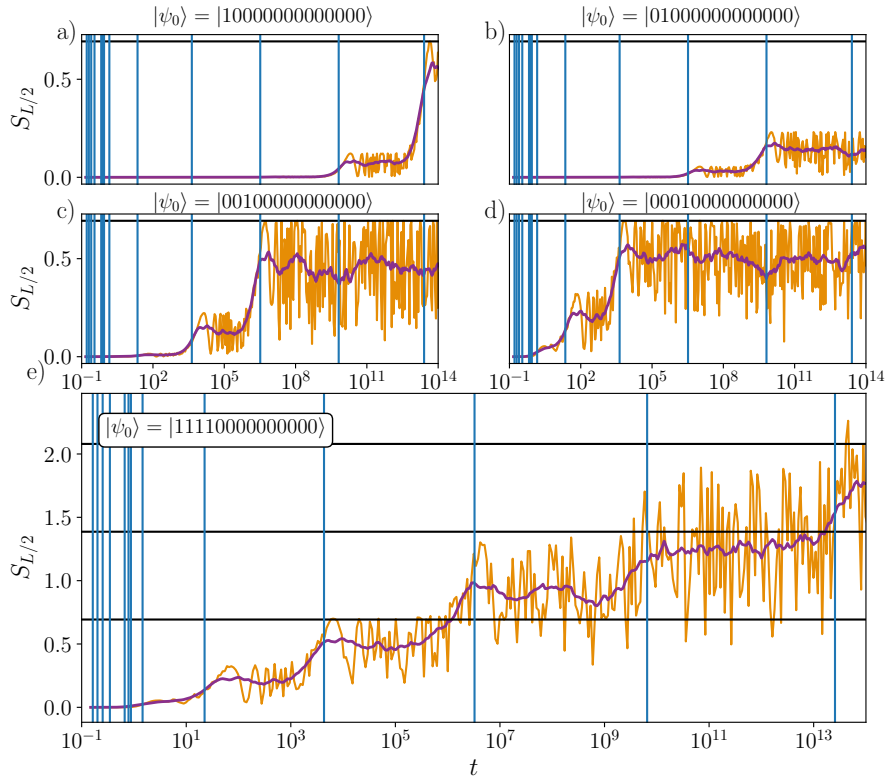

Figure 7.3: a) - d): The entanglement entropy $S_{L/2}$ across the middle bond plotted as a function of time on a logarithmic time scale for different initial particle positions. We can clearly observe how the different initial positions of the single particles lead to different times at which the entanglement S reaches its maximal value of $\log(2)$. The fact that the entanglement rises to a non-maximal plateau first is due to the fact that the Bragg-localised states are not single-site localised and hence Bragg-localised states at multiple eigenenergies make up one initial particle. To smooth out the data, we used a convolution with a box distribution including 20 points (purple line). e): The initial condition now consists of a domain-wall state with four particles. We observe that at every blue vertical line a new plateau of log(2) is filled (represented by a black horizontal line). At late times we do not sample the entanglement often enough in time to capture the instants in which all entanglement oscillations constructively add to the maximal value. Further parameters were $L = 14, J = 1, V = 0, \kappa = 0.5$ and $j_0 = L/2 + 0.5$.

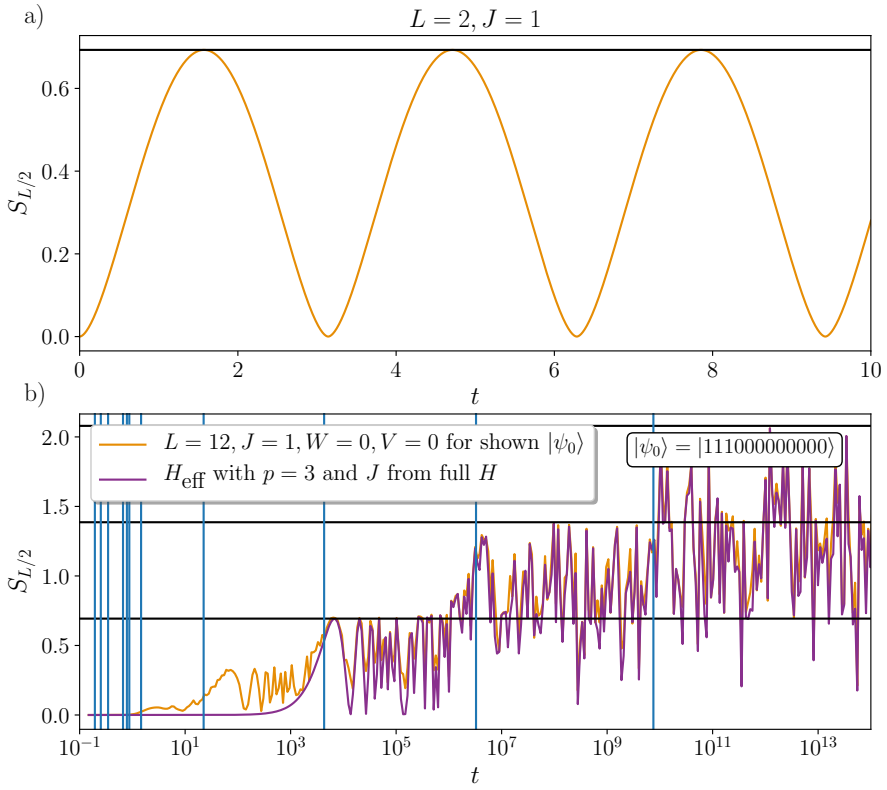

Figure 7.4: a) Bipartite entanglement entropy $S(t)$ (7.5) for a two-site system ($J = 1$). b) Comparison between the numerical exact solution of the bipartite entanglement and the tentative effective two-site system (7.6). Generally speaking the models agree well. In this case, $p = 3$ as we have three particles.

exactly what is shown in Fig. 7.3. Depending on the starting position of the only particle in the problem, the entanglement develops on a different time-scale. This time scale corresponds exactly to the hybridisation energy level splitting of the principal involved Bragg-localised pair states. The level splitting converted to periods is illustrated in Fig. 7.3 as blue vertical lines, similar to what was done in Fig. 5.8. We also note that the maximal entanglement for a single particle is always $\log(2)$, which must be the case for this parity symmetric Hamiltonian, as we will always be able to produce a completely diagonal reduced density matrix with equal eigenvalues. Combining these single particle initial conditions into a domain wall initial condition results in the last panel of Fig. 7.3, where multiples of $\log(2)$ are represented by black horizontal lines as guides to the eye.

7.2.2 *Effective two-site model*

Much of this behaviour can be explained by a simple two-site model with a single particle or a series thereof. Let us suppose we want to

calculate the bipartite entanglement entropy of a particle that is on a two-site lattice and time-evolving according to the Hamiltonian

$$H = -J\left(c_0^\dagger c_1 + c_1^\dagger c_0\right), \tag{7.3}$$

where J is the hopping parameter. This is actually the form of (7.1) in the case of $N = 2$. Starting from a product state $\psi_0 = |10\rangle$ (i. e. the particle initially placed on the left), we can, after tracing out the right side of the system, obtain a reduced density matrix for the left site:

$$\rho_L(t) = \begin{pmatrix} \frac{1}{2} + \frac{1}{2}\cos(Jt) & 0 \\ 0 & \frac{1}{2} - \frac{1}{2}\cos(Jt) \end{pmatrix}. \tag{7.4}$$

Its eigenvalues can of course be just be read off and hence we obtain a bipartite entanglement of:

$$\begin{aligned} S(t) = &-\frac{1}{2}\left(1+\cos(Jt)\right)\log\left[\cos\left(\frac{Jt}{2}\right)^2\right] \\ &+\frac{1}{2}\left(-1+\cos(Jt)\right)\log\left[\sin\left(\frac{Jt}{2}\right)^2\right]. \end{aligned} \tag{7.5}$$

For $J = 1$, the time-evolution of (7.5) is illustrated in Fig. 7.4a. We can use this very simple form to derive a tentative effective Hamitonian that approximately describes the whole system:

$$\hat{H}_{\text{eff}} = \sum_{n=1}^{p} -J_n\left(c_{-n}^\dagger c_n + \text{h.c.}\right), \tag{7.6}$$

where p is the desired number of two-site systems, n describes a specific two-site system, and J_n is the level-dependent tunnelling strength (equivalent to the energy-splitting between hybridised levels). This is of course the central quantity and we attempted to estimate it in Sec. 5.4.3 with (5.40). The bipartition is taken to be at the hypothetical site $n = 0$. In order for pure logarithmic entanglement growth to occur, we need this tunnelling rate to be a pure exponential, which it does not seem to be exactly in reality. It does however come very close. In Fig. 7.4b, we can observe an illustration of the real and the effective model in comparison. Note that the frequencies are *not* obtained via (5.40), but straight from the energy differences in the eigenenergies of (7.1), so one might argue that Fig. 7.4b is still somewhat artificial.

7.2.3 *Influence of disorder*

Another idea that we stressed in Ch. 5 is the sensitivity to disorder of the Bragg-localised states. There we saw that this sensitivity leads to an equilibrium density disproportionately asymmetric compared to the strength of the disorder. Here it inhibits the logarithmic growth

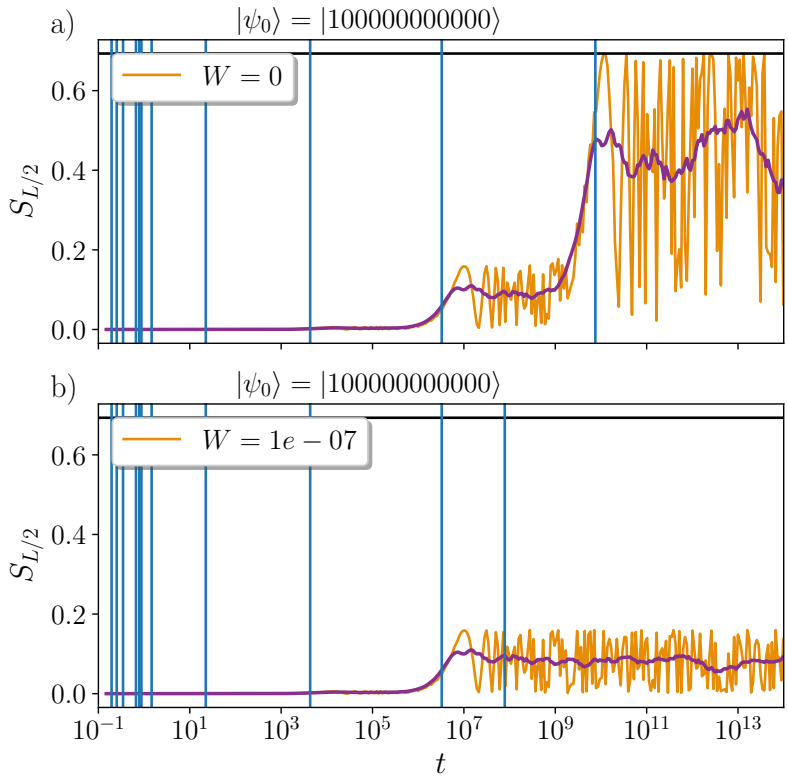

Figure 7.5: Illustrates of how disorder caps the logarithmic entanglement growth for level splittings smaller than the disorder strength W. Depending on whether we use hybridised Bragg-localised states, or those that are completely localised on either side of the bipartition we get a different entanglement growth. a) The clean case for a single particle as already seen in Fig. 7.3. b) The weakly disordered case does not rise to the maximal entanglement value of $S_{L/2} = \log(2)$ as the higher lying Bragg-localised states do not hybridise any more. Further parameters were $L = 12, V = 0, J = 1, \kappa = 0.5$ and $j_0 = L/2 + 0.5$.

of the entanglement beyond a hybridisation level splitting approximately of the order of the disorder strength. This is of course due to the fact that when the hybridisation is prevented, the post-quench states are localised separately on either side of the bipartition and there is no dephasing that would cause the entanglement to grow. An illustration where disorder prevents the hybridisation of the two highest-lying Bragg-localised states (but no others!) is given in Fig. 7.5.

7.2.4 *Influence of interactions*

A very interesting question that follows is what changes when we add nearest-neighbour interactions (i. e. $V \neq 0$ in (7.1))? We did not have much intuition in this case, nor did we perform even approximate analytic calculations. However, we added interactions in a few

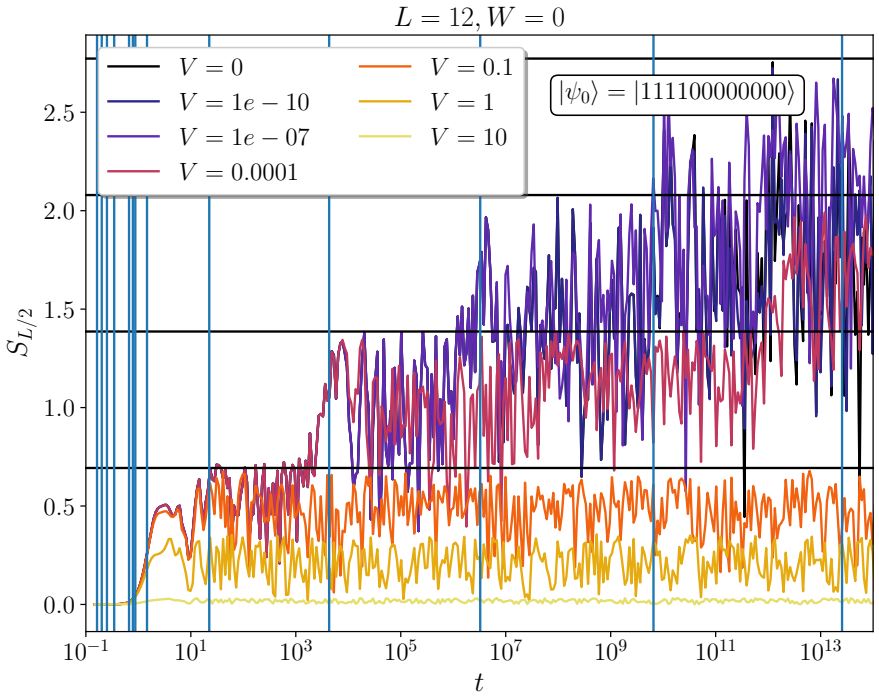

Figure 7.6: Comparing a domain wall initial condition for different interaction strengths V. The behaviour seems very reminiscent of the role of disorder, but we did not study this further. The system parameters were $J = 1, \kappa = 0.5$ and $j_0 = L/2 + 0.5$.

basic cases in order to see numerically what changes. From what we can tell, interactions play a very similar role to disorder for the simulated time-scales (up to $t \sim 10^{14}$), in that interactions of different orders of magnitude seem to prevent the hybridisation between Bragg-localised states with an energy splitting of similar order. Since interactions do not, unlike disorder, break the parity symmetry of the Hamiltonian and its eigenstates, we believe that the energy splitting between symmetric and anti-symmetric eigenstates has merely been decreased further. As such we ultimately do not expect this apparent lack of hybridisation to be visible at even longer time-scales and expect dephasing and hence the maximally achievable entropy.

7.3 DYNAMICS FOR SIMPLIFIED PARAMETERS

In this section we discuss the phase-diagram Fig. 7.1 further. We start by introducing the physics of the two-parameter planes, where one of the three main parameters $(W, V, \Delta j)$ is zero.

7.3.1 *No trap jump*

In the framework of Fig. 7.1 and the quench protocol described above, the V-W plane is a problematic singular point. There is, as mentioned above, technically no quench, and as such we may not probe its non-equilibrium dynamics in the same way as in Ch. 5. If there were no trap either ($\kappa = 0$), then we could reduce the problem to the well known cases of Anderson localisation (see Sec. 3.3) and many-body localisation (see Sec. 3.4). A key feature of Anderson localisation, which in one and two dimensions exists for arbitrarily small W, is the exponentially suppressed nature of the wave functions as schematically depicted in Fig. 7.1a. From an entanglement perspective this case ($V = 0$) is well understood too. After a quantum quench, entanglement entropy is generated very quickly (over times of the order of the inverse hopping strength). This continues to a point of saturation which depends on the nature of the initial condition and the nature of the quench, i. e. the final Hamiltonian, and remains at that value (not considering recurrences due to finite size effects) [177]. Upon adding interactions between the particles ($V \neq 0$), the system may be in either a many-body localised phase (see Sec. 3.4) or a delocalised, ergodic phase. Its phase diagram then corresponds to Fig. 1 in [20]. With respect to entanglement it is known that small interactions do not alter the nature of the eigenstates significantly, but small shifts in the many-body eigenenergies allow for dephasing (schematically depicted in Fig. 7.1b) and as a consequence, a slow and logarithmic build-up of entanglement beyond the initial saturation. The ergodic region is shown in Fig. 7.1c.

The presence of a trap changes the above picture significantly. The semi-unbounded energy spectrum clearly introduces classically forbidden regions with vanishing energy density. As such ergodicity in the sense of equiprobable density across the entire chain will of course be broken for any kind of trapping potential as the classically forbidden region will remain inaccessible even with interactions (as long as those are below the energy-scale of the trap).

While interactions may delocalise the Bragg-localised states in some fashion, it is hard to imagine that they would do so in a way that makes the entirety of real space equally probable. As a consequence, the actual MBL phase diagram does not translate directly. However, on a finite lattice, the experimentally relevant case, some features can be retained. There is no a priori reason why MBL as probed on finite lattices should not persist, a case which we will discuss in Sec. 7.4.1. While the ergodic phase as described above clearly cannot exist any more as such, a finite number of particles could still delocalise. It may be the case that an atomic cloud would take a shape as predicted by an equilibrium thermal distribution for a harmonic potential (c.f. Sec. 5.4.3) and thus constitute a thermal state for a constrained sys-

tem. In that sense we take the V-W plane as a useful guide to discuss the physics of the rest of the phase diagram.

7.3.2 *No interactions*

The physics of the W-Δj plane is described in great detail in Ch. 5. The idea is that the larger our trap displacement (Δj), the steeper the potential and hence the more (exponentially) Stark localised the eigenstates become, as schematically depicted in Fig. 7.1g. This competes with the Anderson localisation (Fig. 7.1a) that stems from disorder and has no clear transition point (Fig. 7.1f) other than that we are able to compare the respective localisation lengths of the single particle wave functions. For the clean system, the situation is particularly interesting. Without a trap jump we are in the special situation of a parity symmetric initial Hamiltonian, which allows for the existence of a maximal number of Bragg-localised pairs (Fig. 7.1e). From an entanglement perspective they follow the same paradigm as the density. Given sufficient time they will dephase and as such develop maximal bipartite entanglement entropy. The hierarchy of energy splittings of these states is quasi-exponential from which follows a quasi-logarithmic entanglement growth. As entanglement was not discussed in Ch. 5, we discussed this case in more detail in Sec. 7.2. The further the trap is displaced, the more partner states are lost on one side and hence the system becomes fully Stark localised (Fig. 7.1g), the case that eventually turned into the idea for Stark many-body localisation, which is discussed in Ch. 6. As there are no interactions, the question of ergodicity or at least some form of delocalisation is not relevant in this plane.

7.3.3 *No disorder*

The physics of the V-Δj plane exhibits several interesting features. First of all it allows for the extension of Wannier-Stark localisation to the case of Stark many-body localisation, where again eigenfunctions remain exponentially localised in space, but small interactions allow for dephasing (schematically depicted in Fig. 7.1h) causing a logarithmic-in-time growth of entanglement. This was discussed in detail in Ch. 6, where it was also shown that further MBL signatures such as Poisson level statistics take the same form in the Stark MBL phase. The delocalisation in the low-energy part of the trap as discussed for Fig. 7.1c does survive up to the jump size Δj where the centre of the trap is displaced beyond the edge of the chain (here depicted as the end of the purple dashed line), as then the entire chain is Stark localised (and missing a tunnelling partner state). Fig. 7.1h describes the region of the phase diagram which exhibits Stark-MBL, but where the statements about entanglement growth do not neces-

sarily hold any more, as the interactions would change the nature of the eigenstates (similar to conventional MBL).

7.4 DYNAMICS OF THE COMPLETE PROBLEM

In the above discussion of the two-parameter planes, we have seen that Stark localisation with its interaction extension to Stark MBL behaves, at least on a finite lattice, very similarly to Anderson localisation with its extension in MBL. The main difference is the replacement of disorder by a strong electric field. Both phenomena are also robust to small perturbations. It was briefly mentioned in Ch. 6, but not discussed in great detail, how these two cases connect. Essentially this boils down to the question whether and how the crossover line depicted in Fig. 7.1f translates when adding interactions, i. e. when going out of plane. Since there is no reason to believe that anything special happens, we would conclude that MBL and Stark-MBL (regions Fig. 7.1b and Fig. 7.1h) are continuously connected and essentially remain a competition between localisation lengths. Further research to elucidate the nature of this region would be worthwhile.

7.4.1 *Large trap jump or strong disorder*

The case of large trap jumps Δj, finite interaction strength V and no disorder corresponds to the physics of Stark-MBL. It was mainly discussed in Ch. 6, where the initial state consisted of an idealised product state. The basis for this work was TEBD simulations on large trap jumps in the usual quench protocol, i. e. starting from the ground-state of (7.1). The results (not shown here) show a fast entanglement oscillation that is superposed by slower oscillations (not fully visible), ultimately leading to the connection to MBL, where the logarithmic growth is explained by such a mechanism. The entanglement also scales as a function of Vt, similar to the pure MBL case. The absence of a strictly linear entanglement growth made this regime feasible for numerical investigation with TEBD, at least on moderate time scales. Another such limit is the usual strong disorder limit, where conventional MBL is expected.

We also performed the usual quench protocol for the case of small V, strong W (≥ 5) and non-zero Δj. The results (see Fig. 7.7) indicate that we acquire the well known logarithmic-in-time bipartite entanglement growth (here averaged over every bond with finite particle density to either side in order to eliminate density effects) known in MBL that scales with Vt. The interesting feature is that the slope of this growth is Δj dependent. Further investigation ideas for this case were to investigate the Δj dependence of the inverse participation ratio (see (3.51)) of the initial condition in more detail, similar to what is described in [177].

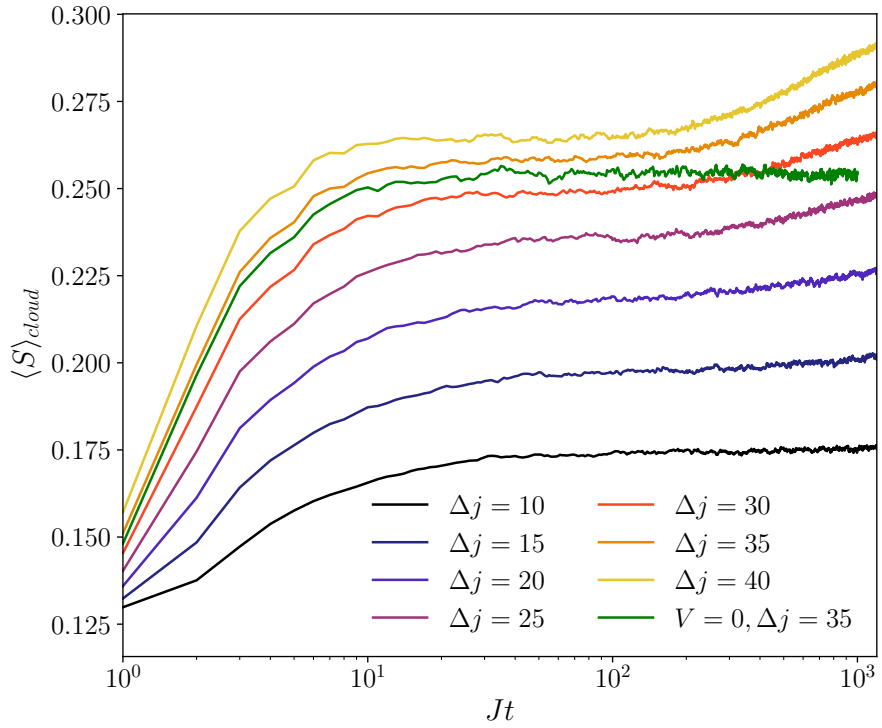

Figure 7.7: The entanglement entropy S averaged over every bond with finite particle density to either side (in order to eliminate density effects in the entanglement entropy). For small interaction V and strong disorder W, we observe the usual MBL log-growth with Δj dependent slope. The system and quench parameters are $L = 121, \kappa = 0.03, j_0 = 25, W = 5, V = 0.01$.

7.4.2 *Strong interaction strength*

All of the above is done for the limiting cases of no, small or very large W and Δj, and for no or small V. One remaining 'axis' is the limit of very strong interaction V. In this limit, the elementary excitations of the system are domain walls, which could possibly obey the same Bragg/Anderson/Stark physics as the non-interacting system (Fig. 7.1d). There are a few things discussed so far.

1. Above the ground state, our fundamental excitations are domain walls. In the limit of $V \to \infty$ we can see them again as free particles hopping around on a harmonic trap. This is very similar to our initial free particle situation and so we could investigate whether domain walls also get 'Bragg-localised'.

2. In the limit of $V \to \infty$ and half filling our ground state will be a charge density wave. Depending on the number of particles and whether we have an odd or even number of sites, this ground state can be unique or doubly degenerate. Ultimately this has always to do with the parity symmetry of the trap. Disorder

or placing the trap non-symmetrically on the lattice breaks this symmetry.

3. Due to the parity symmetry there are many doubly degenerate many-body eigenstates in the system, and we can calculate their energy splitting by degenerate perturbation theory. This is then very reminiscent of the Bragg-physics above and could potentially show similar signatures in certain cases.

The above are directions that were considered for further research, but we have not yet had time to investigate further.

Part III

HYDRODYNAMICS IN SYMMETRY-BROKEN SPIN CHAINS

8

TRANSPORT PRECEDING THE MANY-BODY LOCALISATION TRANSITION

In Part ii, much of the discussion revolved around out-of-equilibrium physics in localised regimes. Whether Bragg, Wannier-Stark, Anderson, Stark many-body or many-body localised, all of these cases share the common feature that transport of conserved quantities such as energy, magnetisation or particles is absent in the regimes that are deemed localised. There are however many other features which distinguish these forms of localisation. In the case of disorder induced localisation it is possible to show a localisation-delocalisation transition at finite disorder (even zero in some case - see Sec. 3.3 and Sec. 3.4). This transition does not exist in the discussed disorder free cases of localisation. A good candidate would have been Stark localisation (with or without interactions) with a strictly linear potential. However, as we saw in Ch. 6, the strictly linear potential did not reveal the same kind of localisation features in terms of level spacing statistics and entanglement growth as the disorder counterpart. In all other cases, the addition of curvature precludes localisation in some parts of the system at all times and makes the formulation of the thermodynamic limit more difficult [87] if not impossible at times.

This clear separation of localised and delocalised regimes via a transition makes the study of disorder induced localisation even more fascinating. After all, the study of classical and quantum phase transitions has been one of the main tasks of condensed matter physics in the latter half of the twentieth century. As discussed in Sec. 3.3, the case of Anderson localisation is more or less resolved. This is less the case with MBL where there are ongoing debates about the differences between one-dimensional chains and higher-dimensional lattices [37, 50, 91], and about the existence or non-existence of a transition in energy at fixed disorder strength [51, 108, 116]. However, as shown in Sec. 3.4, the basic physics of the MBL phase is nonetheless fairly well understood by now. By contrast, we also showed that very little progress has been made on the properties of the transition between the ergodic and MBL phases. In particular the region immediately preceding it on the low-disorder side is not properly understood. Numerics in the critical and pre-critical regions of the isolated system scarcely converge, and the critical exponents that emerge from a scaling analysis appear to be ruled out by general considerations [39, 116, 143]. One problem ubiquitously present in numerical studies that do converge are severe finite size effects. It is thus useful to observe that one can access much larger system sizes by considering open-

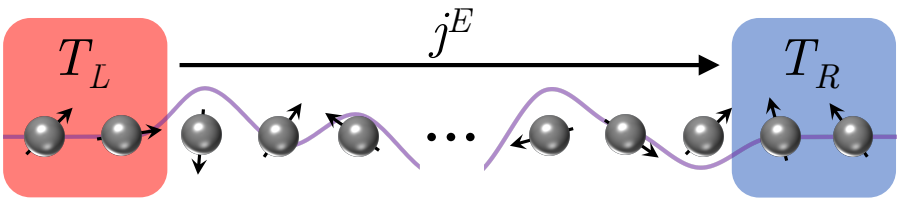

Figure 8.1: A disordered spin-1/2 XYZ chain, with Lindblad driving applied to the pair of spins at each end to impose a temperature gradient. In our time-evolving block decimation (TEBD) studies, we time-evolve such a system until it reaches its non-equilibrium steady state (NESS). This analysis was supplemented by Scott Taylor via exact diagonalisation (ED) studies on closed (and much shorter) chains.

system dynamics. Previous work has pursued this idea to characterise transport in XXZ spin chains, where the z-projection of the total spin is conserved: spin transport in [5, 20, 212], and energy transport in [190] though with severely limited numerics. The most convincing numerical study [212] shows that there is a small region of diffusive transport and a large, pre-critical region of anomalous subdiffusive transport.

In this chapter we aim to investigate the rich physics of the ergodic phase further (see Sec. 3.5) by investigating the disordered spin-1/2 XYZ chain [175]. We choose this model because it is a quantum spin chain in which all conservation laws are violated except energy. In particular, the U(1) symmetry (see Sec. 2.4) of the XXZ model, which corresponds in a fermionic picture to fermion number conservation, is broken in the XYZ model. A setup of how the non-equilibrium transport is studied via boundary driving can be seen in Fig. 8.1. This allows us to ask two main questions. How do underlying symmetries affect the hydrodynamics of a model, and what are the consequences of symmetry breaking for the localisation transition (if it still happens)? The question of hydrodynamics has been my main contribution to this project, while the transition study was mostly done by Scott Taylor. The results are summarised in the following.

First, we verify that in the absence of disorder ($W = 0$) the transport is ballistic [213], in contrast with the classical model [160] where the non-linear interaction between the spin modes causes spin waves to diffuse. We attribute this behaviour to the integrability of the quantum model [26], as non-integrable or classical spin chains typically show diffusive transport (see for example [126, 131]).

Second, for weak but non-zero disorder ($0 < W \lesssim 0.7$) there is a region in which energy transport is diffusive. This diffusive region persists up to a finite critical disorder strength, $W_{c1}(\eta)$, which depends on the XY anisotropy η (i. e. on how strongly the U(1) symmetry of the XXZ chain is broken). Third, for increasing disorder

strengths $W > W_{c1}(\eta)$ energy transport becomes increasingly subdiffusive, while increasing the XY anisotropy η counteracts this effect and brings the system back towards the regime of diffusive energy transport. We can follow this behaviour up to disorder strengths of $W \approx 2.2$, where we see subdiffusive exponents up to $\gamma \approx 2.7$.

Fourth, the system exhibits an MBL transition at a disorder strength $W_{c2}(\eta)$, which increases significantly as the XY anisotropy η is increased. Due to the above mentioned lack of a U(1) symmetry in the XYZ chain, this transition cannot be thought of as directly following from the arguments for localisation of [23]. It is, however, in line with the most recent research on the topic which relies less on the particle interpretation [92] and more on non-proliferation of resonances. Scott Taylor determined W_{c2} via ED analysis of chains with lengths up to $L = 17$ spins, using the standard tests of the eigenstates and spectrum of the Hamiltonian [101, 116, 130, 185]. A phase diagram summarising these results is shown in Fig. 8.2.

The remainder of the chapter is organised as follows. We introduce the model and the implementation of the open-system drive in Sec. 8.1. In Sec. 8.3 we then discuss the hydrodynamics of this model including the clean and disordered cases. We finish by a short summary of the results regarding the localisation transition (Sec. 8.4).

8.1 MODEL

The Hamiltonian of the disordered XYZ spin chain reads

$$\begin{aligned} H &= \sum_{n=1}^{L-1} \left[(1+\eta) s_n^x s_{n+1}^x + (1-\eta) s_n^y s_{n+1}^y + \Delta s_n^z s_{n+1}^z \right] \\ &\quad + \sum_{n=1}^{L} h_n s_n^z. \end{aligned} \tag{8.1}$$

Here $s_n^\alpha = \frac{1}{2}\sigma_n^\alpha$ are spin-1/2 operators (σ_n^α are Pauli matrices (2.17)), η is the XY anisotropy of the coupling (the parameter that breaks the U(1) symmetry of the XXZ model), Δ is the Ising anisotropy (in our case always $\Delta = 1.2$ unless mentioned otherwise), and $h_n \in [-W, W]$ are uncorrelated disorder fields randomly drawn from a uniform distribution. The $\eta \to 0$ limit of this model is the well-studied XXZ spin chain; $\eta \neq 0$ introduces a term equal to

$$\eta \sum_n \left(s_n^+ s_{n+1}^+ + s_n^- s_{n+1}^- \right) /2,$$

which violates the conservation of the z-component of the total magnetisation. In the fermion language this corresponds to a nearest-neighbour pairing term.

We probe the hydrodynamics of this system using TEBD as introduced in Sec. 4.3. To this end, we couple the ends of the chain to

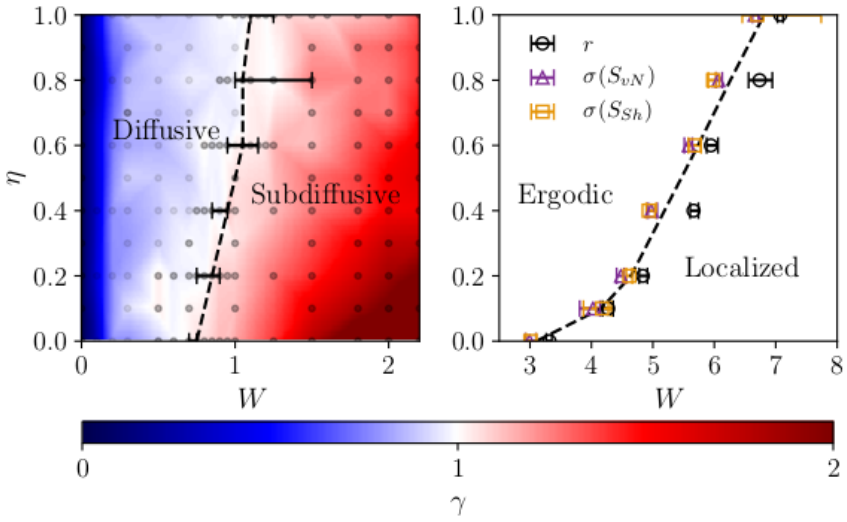

Figure 8.2: The resulting 'phase diagram' of the boundary-driven disordered spin-1/2 XYZ chain, for an Ising anisotropy of $\Delta = 1.2$. Here η is the XY anisotropy of the exchange interaction between the spins, and W is the strength of the random-field disorder. In the left-hand panel, the dashed line shows the border between diffusive and subdiffusive energy transport determined from our TEBD studies, and the bars are error estimates. The colour scale shows the transport exponent γ estimated via interpolation between the numerically determined values, which are indicated by gray points. The right-hand panel shows the location of the MBL transition, determined by three different analyses of ED results: the crossover in level statistics from random-matrix to Poissonian, r; the peak in the standard deviation of the Shannon entropy, $\sigma(S_{\mathrm{Sh}})$; and the peak in the standard deviation of the von Neumann entropy, $\sigma(S_{\mathrm{vN}})$.

two thermal baths at different temperatures, and describe the time-evolution of the resulting non-equilibrium open system depicted in Fig. 8.1 using the Lindblad equation (2.14) introduced in Sec. 2.1.4:

$$\frac{d\rho}{dt} = -i\,[H,\rho] + \kappa\left\{\mathcal{L}_L(\rho) + \mathcal{L}_R(\rho)\right\}. \tag{8.2}$$

The first term on the right-hand side of (8.2) describes the coherent dynamics; the Lindblad terms $\mathcal{L}_L(\rho)$ and $\mathcal{L}_R(\rho)$, defined as in (2.14), correspond to the left and right reservoirs respectively, and κ is the strength with which we couple them to the chain. This two-site thermal driving protocol has been used in similar transport studies [148, 210]. In particular, it drives an isolated pair of spins to a thermal state with temperature T, $\rho \propto \exp(-H/T)$. We drive the pair of spins on the left-hand end of the chain towards a high temperature T_L, and the right-hand pair towards a lower temperature T_R. For the remainder of this chapter we use the target temperatures $T_L = \infty$ and $T_R = 20$. We will now introduce how to engineer such a driving.

8.1.1 *Two-site driving protocol*

Our aim is to construct operators $\mathcal{L}_L(\rho)$ and $\mathcal{L}_R(\rho)$, i. e. determine the corresponding Lindblad operators L_k, which produce a unique stationary state $\rho_{\mathrm{L(R)}}$ at the two spins on the left (right) of the chain to which they are applied. This stationary two-site density matrix will act as a *bath* and take the form of $\rho_B = \exp(-h/T_B)/\mathrm{Tr}(\exp(-h/T_B))$, a local thermal (Gibbs) state with respect to the two-site Hamiltonian $h_{n,n+1}$ (such as Eq. 8.6). The two-site density operator ρ_B is a $2^2 \times 2^2$ matrix. In order to be the stationary state resulting from (8.2) we require that ρ_B be a unique eigenvector (in the superoperator formalism) of $\mathcal{L}_B$ with eigenvalue 0, while all other eigenvalues are negative. By only fixing one eigenvector and eigenvalue, the choice of L_μ (see (2.14)) will not be unique, so that it makes sense to demand that all other negative eigenvalues be -1 to ensure fast convergence [148]. In order to make the construction easier, we can diagonalise ρ_B, so that it takes the form $d = \mathrm{diag}(d_0, d_1, d_2, d_3)$. We now show that the set of 16 Lindblad operators L_μ (μ is now a double index (ij)) of the form

$$L_{ij} = \sqrt{\frac{d_m}{32}} r^i \otimes r^j, \qquad i,j = 0,1,2,3, \qquad m = (i \bmod 2) + 2(j \bmod 2), \tag{8.3}$$

where $r^0 = \sigma_x + i\sigma_y$, $r^1 = \sigma_x - i\sigma_y$, $r^2 = \mathbb{1} + \sigma_z$, $r^3 = \mathbb{1} - \sigma_z$, indeed result in a $\mathcal{L}_B^{\mathrm{diag}}$ satisfying the above conditions. The superscript 'diag' denotes that we have constructed an operator that will drive the two-site density matrix into a thermal state in its diagonal basis. In order to represent $\mathcal{L}_B^{\mathrm{diag}}$ as a superoperator following (4.46), we need to again choose a basis. Most convenient would be of course the Pauli basis, which for a two-site Hilbert space takes the form of $\sigma_{\underline{\alpha}} = \sigma_{\alpha_1} \otimes \sigma_{\alpha_2}$, with $\alpha_1, \alpha_2 = 0, x, y, z$. We therefore obtain a superoperator via $A^{\#}_{\underline{\alpha},\underline{\beta}} = 1/4\ \mathrm{Tr}(A^\dagger \sigma_{\underline{\beta}} A \sigma_{\underline{\alpha}})$. The only non-zero matrix elements $\left(\mathcal{L}^{\mathrm{diag},\#}\right)_{\alpha,\beta}$ with $\alpha, \beta \in \{0, \ldots, 15\}$ are, if we assume positive d_i and that $\mathrm{Tr}(d) = 1$,

$$\begin{aligned}
\left(\mathcal{L}_B^{\mathrm{diag},\#}\right)_{\alpha,\alpha} &= -1, \qquad \alpha = 1, \ldots, 15, \\
\left(\mathcal{L}_B^{\mathrm{diag},\#}\right)_{15,0} &= d_0 - d_1 - d_2 + d_3, \\
\left(\mathcal{L}_B^{\mathrm{diag},\#}\right)_{12,0} &= d_0 + d_1 - d_2 - d_3, \\
\left(\mathcal{L}_B^{\mathrm{diag},\#}\right)_{3,0} &= d_0 - d_1 + d_2 - d_3.
\end{aligned} \tag{8.4}$$

Diagonalising (8.4), we find indeed that the above conditions are fulfilled, in particular that the eigenvector with corresponding eigenvalue of 0 is d. We now need to find the form of $\mathcal{L}^{\mathrm{diag},\#}$ for non-diagonal ρ_B, e. g. for a ρ_B in the basis of the Hamiltonian. To that

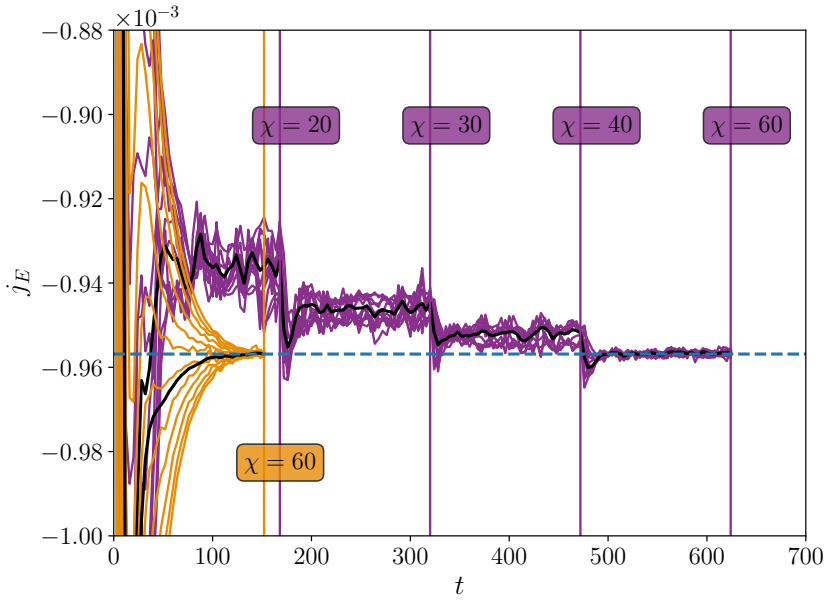

Figure 8.3: Relaxation of the energy current to its NESS value for $L = 16$, $\eta = 0.2$, $\Delta = 1.2$, and $W = 0.4$. The orange curves show the currents through each site as a function of time using $\chi = 60$ throughout. The purple curves show the currents through each site as a function of time using the iterative procedure of increasing χ. The vertical lines indicate the points where χ increases, the dashed horizontal line shows the NESS value of the current. The black curves show the value of the current averaged over all sites.

end, we use the rotation matrix V that diagonalises $\rho_B = V^\dagger dV$ in order to formulate a rotation on $\mathcal{L}_B^{\text{diag},\#}$. We apply this rotation as a superoperator in the Pauli basis such that we finally obtain

$$\exp(\mathcal{L}_B^{\#} t) = V^{\dagger\#} \exp(\mathcal{L}_B^{\text{diag},\#} t) V^{\#}. \tag{8.5}$$

8.1.2 *Obtaining the non-equilibrium steady state*

To study the energy transport across the disordered chain, we simulate the non-equilibrium configuration depicted in Fig. 1(a) of Eq. (8.2) with the baths engineered as shown above. These thermal baths are coupled with strength κ (in our simulations always $\kappa = 0.5$) to the end spins, where we set $h_i = 0$ ($i \in \{0, 1, L-2, L-1\}$). These end spins are then coupled to the rest of the chain which evolves coherently according to the Hamiltonian (8.1). In order to obtain results for sufficiently long chains, we use a TEBD method to drive the chain until a NESS is obtained. In particular, we encode the density matrix of the system as a state vector and make use of the superoperator

formalism to evolve it in time [97, 214]. In our simulations, we were able to reach system sizes of up to $L = 400$.

To obtain the NESS for each set of parameters W, Δ, and η, we consider M realisations of the disordered magnetic field h_n. For each realisation, we take $\rho(0)$ to be a product of completely mixed local density matrices, and we time-evolve it to obtain an approximation to the steady state density matrix of the lattice, $\rho_\infty = \lim_{t\to\infty}\rho(t)$ [148]. Our TEBD method is a variant of the open source library TeNPyLight [82], which implements the superoperator formalism for states. We use a time-step $dt = 0.4$ and a fourth-order Trotter decomposition [182] for our two-site local updates. At any time, our global density matrix ρ is described by a MPS of matrix dimension of up to $\chi = 300$.

This process is performed until a series of convergence criteria is fulfilled. Spatial homogeneity and temporal uniformity of the energy current (described in the next section) are the most suitable indicators of convergence. We choose as our spatial criterion that the standard deviation of the individual currents on every bond k (excluding those subjected directly to the Lindblad driving) relative to the average current be $\sigma(j_k)/\overline{j_k} < 2\%$. The temporal criterion is that the standard deviation of the average current over the previous 100 time-steps is less than 0.3% of the average over the same period.

We then use the obtained NESS as the initial state for a simulation with a higher maximal matrix dimension χ. As the NESS is unique [148], we make the reasonable assumption, which we back up below, that every increase of χ will bring our numerical approximation of j_E closer to the true value. We repeat this process of increasing the matrix dimension until the average energy current $\overline{j_E}$ is basically independent of χ, i. e. when $\Delta\overline{j_E}/\overline{j_E} < 0.4\%$. If any of the convergence criteria are not satisfied then the result has not converged and the data is excluded from the study. We require that the TEBD must successfully converge to a steady state for at least 98.5% of disorder realisations, or the data is discarded to avoid biased sampling of the true current distribution. After the NESS is obtained for M realisations (M ranging 20 to 600), the energy current (already averaged along the chain) is averaged over realisations, resulting in a statistical uncertainty of $\sigma(\overline{j_k})/\sqrt{M} \approx 1.5\%$ or less for most chains ($< 3-4\%$ for the strong disorder runs).

In order to make the entire process more tangible, we have shown a sample run for a single disorder realisation in Fig. 8.3. The purple lines represent energy current measurements at different bonds of the chain for a simulation as described above. Every time a steady state (SS) according to the chosen criteria is reached, we use this SS and run the simulation at a higher maximal bond-dimension χ. In comparison, we show in yellow that a simulation run at the maximal χ from the start converges to the same SS. In that sense, we confirm that the SS is indeed unique and that a variable χ can help reaching

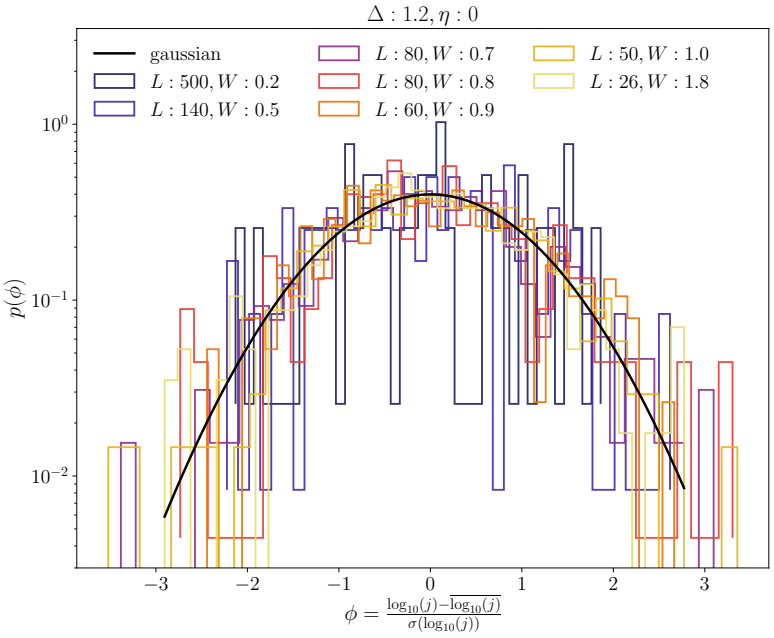

Figure 8.4: We plot the NESS energy current distribution of the scaled logarithm of currents $p(\phi)$, where $\phi \equiv \frac{\log_{10}(j) - \overline{\log_{10}(j)}}{\sigma(\log_{10}(j))}$. For a wide range of disorder strengths we find that the probability distribution is well described by a log-normal distribution. This may be in contrast with observations about subdiffusion in [5].

the true SS faster because it allows for initial states to have a larger overlap with the actual SS.

Lastly we note that one may also study the whole NESS energy current probability distribution $p(j_E)$ for the entire disorder ensemble (see Fig. 8.4). This is important for two reasons. Firstly we need to verify the shape of the distribution in order to determine whether it is well-behaved, i. e. posseses a well-defined mean. We find that the distribution of the log-currents seems to be stable and described by a normal distribution, i. e. the distribution of currents is log-normal. Secondly, it was claimed in [5] that subdiffusion, such as also found in this study, may result from chain-resistivities R ($R \sim 1/j$) having broad distributions in their respective disorder ensemble. The width of these distributions diverges at low frequency in response theory and therefore the distribution becomes scale-free. This leads then to anomalous transport coefficients signifying subdiffusion. Interestingly our current distributions do not agree with this prediction of a broadening distribution. We plan to address this further in future research and hope to provide an alternative mechanism for subdiffusion.

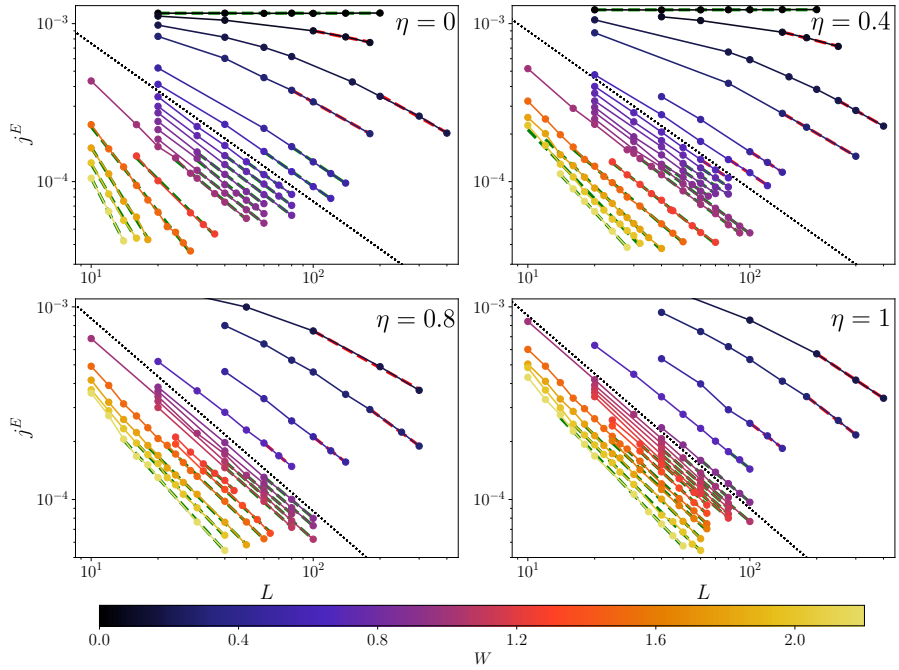

Figure 8.5: Transport properties of the XYZ model for a range of disorder strengths W, including zero. We show the current scaling for different values of the XY anisotropy η. Each panel shows the NESS disorder-averaged energy current j^E as a function of chain length L. The finite-size effects discussed in the text are clearly visible for small W. The coloured dashed lines indicate the power-law fit we use to obtain the transport exponent γ. The length of the dashed line shows the range of system sizes that were used: either all chains longer than the estimated $L^\star$ (green), or the last three obtained data points (red). The latter are indicated by hollow symbols in Fig. 8.2 and Fig. 8.8. The dotted line corresponds to a transport exponent of $\gamma = 1$. Here $\Delta = 1.2$.

8.2 CURRENT SCALING

We are now in a position to determine the transport properties based on the NESS as obtained above. For that matter, we extract a transport coefficient γ similar to what was first introduced in Fig. 3.11 for spin currents. It is obtained by scaling the NESS energy current as a function of system size L (see Fig. 8.5). The energy current operator is determined from the continuity equation for the bond energy operator

$$\begin{aligned}\tilde{H}_{n,n+1} =&(1+\eta)s_n^x s_{n+1}^x + (1-\eta)s_n^y s_{n+1}^y + \Delta s_n^z s_{n+1}^z \\ &+ \frac{1}{2}\left(h_n s_n^z + h_{n+1} s_{n+1}^z\right),\end{aligned} \tag{8.6}$$

and in the XYZ model the current operator for the nth site is:

$$\begin{aligned} j_n^E &= i\left[\tilde{H}_{n-1,n}, \tilde{H}_{n,n+1}\right] \\ &= \sum_{\alpha,\beta,\gamma} J_\alpha J_\gamma s_{n-1}^\alpha s_n^\beta s_{n+1}^\gamma \varepsilon_{\alpha\beta\gamma} + \frac{1}{2} h_n J_x \left(s_{n-1}^x s_n^y - s_n^y s_{n+1}^x\right) \\ &\quad + \frac{1}{2} h_n J_y \left(s_n^x s_{n+1}^y - s_{n-1}^y s_n^x\right) \end{aligned} \tag{8.7}$$

where $\varepsilon_{\alpha\beta\gamma}$ is the Levi-Civita tensor, $\alpha, \beta, \gamma \in \{x, y, z\}$, and J_α is the nearest-neighbour coupling between the α components of the spins. In our case they take the values $1+\eta$, $1-\eta$ and Δ respectively.

The diffusion equation (see (3.28)) for the transport of energy E, where $E = \langle \tilde{H}_{n,n+1} \rangle$ corresponds to the bond-energy density as obtained by (8.6), reads $j^E = -D\nabla E = -D\Delta E/L$. This is sometimes also referred to as Ohm's or Fick's law. Here D is the diffusion constant, ∇E is the gradient of E, and ΔE is the difference between its boundary values. We therefore expect the current to scale in a diffusive regime as $\sim 1/L$. We may stress again that as derived in Sec. 3.3.1, *diffusion* is the expected form of transport in a disordered medium. The mean-square displacement in this case asymptotically reads $\Delta x^2 \sim Dt$. We use this to define a time t_* it takes an excitation (spin, particle, energy) to traverse the system, sometimes referred to as Thouless time [115], namely $t_* \equiv L^\beta$. A fixed bias should make an extensive number of excitations available for transport, so that the stationary current will be given as $j \propto \frac{L}{t_*} = \frac{1}{L^{\beta-1}}$. The diffusive case corresponds to $\beta = 2$ and agrees with the expectation from the diffusion equation. In the ballistic case, $\beta = 1$, the current is expected to be independent of system size.

Defining for simplicity $\gamma \equiv 1 - \beta$, In the thermodynamic limit we expect the NESS current scaling to give $j^E \sim L^{-\gamma}$. In this case $\gamma = 1$ corresponds to normal diffusive energy transport, i. e. Fick's law. When Fick's law breaks down, the transport is no longer diffusive, and we may observe slower subdiffusive ($\gamma > 1$) or faster superdiffusive ($\gamma < 1$) transport. This corresponds to anomalous transport as briefly discussed in Sec. 3.5.

A series of such scaling measurements, where we plot the energy current as a function of system size, for a wide range of parameters is shown in Fig. 8.5. Here the coloured dashed lines indicate the scaling range used in order to obtain the transport coefficient γ (in this case the slope). We discuss the consequences and physics of these scaling measurements in the following section.

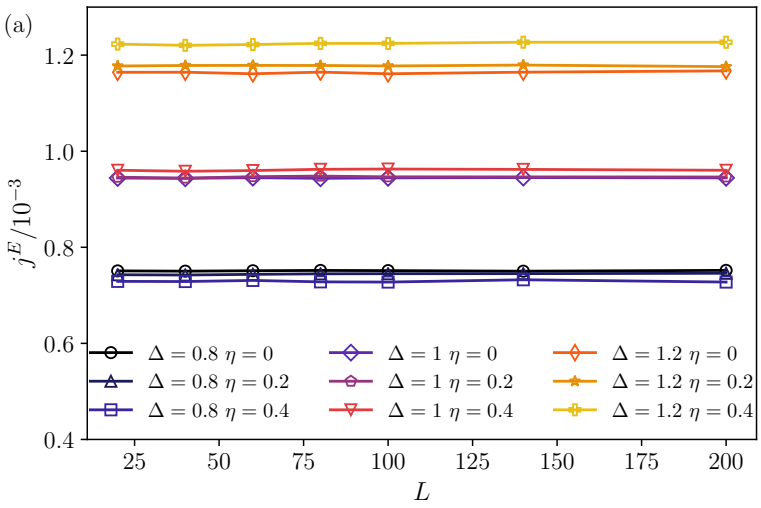

Figure 8.6: Transport study of the XYZ model without disorder. TEBD results for the dependence of the energy current j^E on the chain length L, showing ballistic transport for several values of the Ising anisotropy Δ and the XY anisotropy η.

8.3 ERGODIC PHASE AND HYDRODYNAMICS

8.3.1 *No disorder: ballistic energy transport*

Before investigating the transport behaviour in the disordered system, we quickly want to verify that results for the clean ($W = 0$) case agree with existing literature [213]. In the zero-disorder limit the XYZ model has been shown to be solvable by Bethe Ansatz methods. However, the "reference state" is not known, so only a limited number of exact results are available [26, 93]. We find that the energy current j^E is independent of the length of the system, which signals that the energy transport is ballistic; this is consistent with previous work on the XYZ model [213]. Ballistic energy transport has been linked to the integrability of quantum systems [120], a characteristic which is also visible in the Poissonian statistics of the Hamiltonian's eigenenergy spectrum [36]. For $0 < \Delta \leq 2$ and $0 < \eta \leq 1$ it was shown that the average of r falls close to the Poissonian value $r_P = \ln 4 - 1$ over the entire spectrum [175]. However, as far as we are aware, there have hitherto been no transport or eigenvalue studies of this sort for the XYZ model.

Fig. 8.6 shows our TEBD results for the energy current j^E as a function of the chain length L, for a range of η and Δ. Each curve clearly shows that j^E is independent of the chain-length L, as expected for ballistic transport. Our results are therefore consistent with the established analytical predictions for spin chains in the absence of disorder [213].

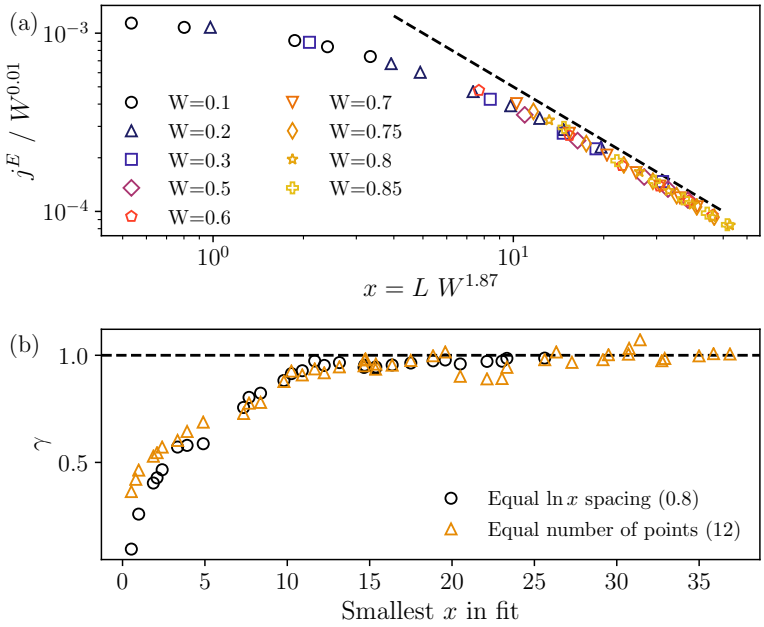

Figure 8.7: Testing whether our chains are long enough for the scaling limit to have been reached. In this example the XY anisotropy parameter $\eta = 0.4$. (a) The numerical collapse of the energy current j^E as a function of chain length L onto a single curve under suitable scaling by the disorder strength W. Note the typical crossover from ballistic behaviour in short chains to diffusive behaviour — indicated by the dashed line — in longer ones. (b) The 'running exponent' $\gamma(x)$, determined from tangential power-law fits to the universal curve, showing that γ reaches the diffusive value of 1 above the critical length scale $x^\star \approx 25 - 30$.

8.3.2 *Weak disorder: stable diffusive phase*

At weak but non-zero disorder, $0 < W < W_{c1}(\eta)$, the transport is diffusive as can be seen in Fig. 8.5, where any non-zero disorder causes the energy current to be system size dependent. This has previously been shown for spin and energy transport in the XXZ chain ($\eta = 0$) [121], but we show it for the first time in the XYZ case. An important note we take from Fig. 8.5 is that as in previous studies, we find severe finite-size effects in the results at weak disorder. For small system sizes the transport appears faster, continuously 'bending' towards a linear asymptotic regime. This asymptotic scaling behaviour of $j^E(L)$ corresponds to diffusion ($\gamma = 1$) and is observed only for values of L exceeding a critical length $L^\star$, where $L^\star$ increases with decreasing W. For a ballistic-to-diffusive crossover, it can be shown that this length scale should scale as $L^\star \sim W^{-2}$ [212]. This relies on a result already derived previously. Essentially this length scale represents the mean free path, i. e. the distance an excitation of energy ϵ may travel before it changes momentum k due to disorder. We use

(3.32) then to estimate the time τ for the first collision. Before that, the excitations travel freely and ballistically with a dispersion relation of $\epsilon_k = 2J\cos(k)$. We use this to substitute the density of states into (3.34) and thus obtain $\tau \sim J/W^2$ for excitations in the middle of the spectrum or at infinite temperature. Again using the idea that $x \sim t^{1/\beta}$, for the ballistic-to-diffusive ($\beta = 1$) case we finally arrive at $L_* \sim 1/W^2 \equiv 1/W^\nu$. We further note that the diffusion coefficient must also be disorder dependent and scales for a ballistics-to-diffusive crossover as $D \sim 1/W^2 \equiv 1/W^\delta$. If we apply our analysis naïvely to a chain of length $L < L^\star$, it yields an exponent $\gamma < 1$, and thus falsely suggests superdiffusive energy transport.

However, we can use the scaling properties of $j^E(L)$ to test whether the scaling regime has been reached in any given case. In Fig. 8.7a we demonstrate that, by scaling the data using $x \equiv LW^\nu$ and additionally $y \equiv j^E W^{\delta-\nu}$, it is indeed possible to collapse all points onto a single universal curve. For the example shown, $\eta = 0.4$, the best empirical scaling exponent is $\nu \approx 1.87$, in reasonable agreement with the predicted value of 2. We also find that $\nu - \delta = 0.01$, which is close to the predicted behaviour of $\nu = \delta$ [212].

We estimate $x^\star$, the value of x above which the running exponent determined from the scaling of the energy current $j^E(x)$ no longer changes, by performing a tangential fit to the universal diffusive curve formed by the scaled $j^E(L)$ data — see Fig. 8.7a. We perform two fits, the first taken over all of the data points within a region of constant size in $\ln x$ and the second taken over a constant number of data points. The results of these fits are shown in Fig. 8.7b as a function of the smallest x used in each fit. Our estimate of $x^\star$ is the value at which $\gamma(x)$ has become 1.

This allows us to identify the points in Fig. 8.2 and Fig. 8.8 where we are therefore confident that the reported value of γ is not reflective of the thermodynamic limit (indicated by hollow markers). We note that the value of $x^\star$ increases for increased η.

The diffusive phase is not materially altered when the XY anisotropy is increased, except insofar as it extends to stronger disorder, i. e. $W_{c1}(\eta)$ increases with η (see left-hand panel in Fig. 8.2). We determine the value for the disorder strength $W_{c1}(\eta)$ at which energy transport changes from diffusive to subdiffusive as follows. We set the upper bound of the transition, i. e. the disorder strength at which we are confident that energy transport has become subdiffusive, where our average γ is more than two standard deviations away from 1. The lower bound is set to the disorder value at which the NESS current scaling comfortably falls on top of the universal scaling curve (see Fig. 8.7). The dashed line in the left-hand panel of Fig. 8.2 represents the disorder strength at which our average γ is more than one standard deviation away from 1.

8.3.3 *Intermediate disorder: subdiffusive energy tran-sport*

Increasing the disorder strength further we find that the disordered XYZ model exhibits subdiffusive energy transport at $W > W_{c1}(\eta)$. In contrast to the diffusive region, in the subdiffusive phase the transport exponent γ varies continuously as a function of both the disorder strength W and the XY anisotropy η. This variation shows two main trends. First, as shown in Fig. 8.8a, a larger η results in a smaller γ, i. e. breaking the U(1) symmetry pushes the system back towards diffusive transport. Second, as shown in Fig. 8.8b, increasing disorder strength W leads to an increased value of γ for all values of η, i. e. increasing disorder pushes the system further away from the diffusive regime. While we cannot follow this behaviour all the way to the MBL transition, the location of which we determine by other means, we expect that γ would diverge there.

It has to be restated that subdiffusive transport corresponds to anomalous transport and therefore is not the 'norm' in disordered systems. While in U(1) symmetric systems, one could visualise such an effect as particles physically getting stuck, in the case of energy transport this is an even more intriguing effect and an open area of research.

8.4 LOCALISED PHASE

8.4.1 *Strong disorder: many-body localisation*

Because the convergence of our TEBD method worsens at stronger disorder, we cannot use it all the way to the MBL transition. Therefore, it becomes necessary to perform ED studies on short, closed chains. The numerical work was carried out by Scott Taylor and the results are briefly summarised below. The ED was carried out on chain length of up to $L = 17$ spins for the XXZ model and $L = 16$ spins for the XYZ model with periodic boundary conditions.

In Sec. 3.4.2 we discussed several measures to identify the location of the MBL transition. The most prominent one consists of determining the crossover from random-matrix to Poissonian statistics in the eigenenergy spectrum, as measured by the gap-ratio parameter. Further to that we also showed that one can locate the peak in the fluctuations of the Shannon entropy $S_{\mathrm{Sh}} = -\sum_i \rho_{ii} \ln \rho_{ii}$, where ρ is the full density matrix of the spin chain. Finally, it is also possible to locate the peak in the fluctuations of the half-chain entanglement entropy $S_{\mathrm{vN}} = -\mathrm{Tr}(\rho_A \ln \rho_A)$, where ρ_A is the reduced density matrix of the half-chain. In the present case these quantities were evaluated using the 200 eigenstates closest to the middle of the many-body energy spectrum, and then averaged over disorder realisations. Employing a finite-size scaling analysis of the disorder-averaged results leads to

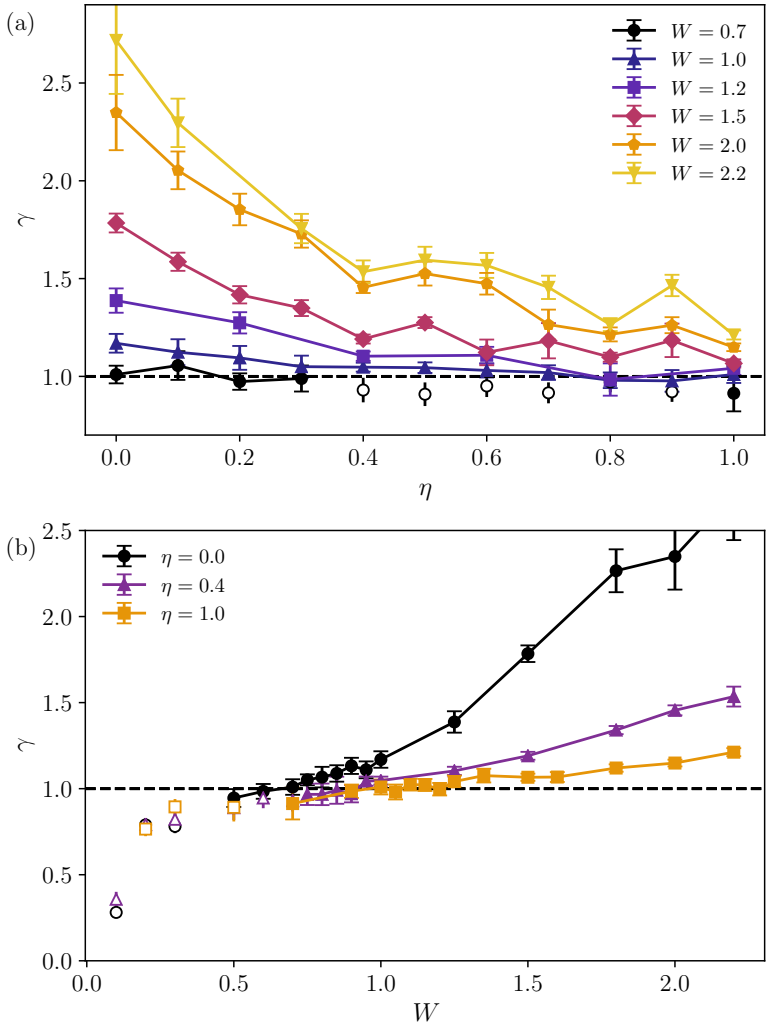

Figure 8.8: The energy-transport exponent γ in the disordered spin-1/2 XYZ chain at weak to moderate disorder strengths, as determined from our TEBD numerical results. All results reported are for an Ising anisotropy of $\Delta = 1.2$. (a) The exponent γ as a function of the XY anisotropy η, for various values of the disorder strength W. $\gamma = 1$ corresponds to diffusive energy transport; for $\gamma > 1$, energy transport is subdiffusive. (b) The exponent γ as a function of the disorder strength W, for various values of the XY anisotropy η. The open symbols in both panels indicate cases in which the chain was not long enough to achieve fully diffusive behaviour, and these points should therefore be disregarded (see Fig. 8.7 and corresponding text). The error bars shown correspond to two standard deviations of uncertainty resulting from the γ fit to the results shown in Fig. 8.5. We have not included any uncertainties stemming from a non-optimal SS or from the disorder averaging of SS values of j^E as these were generally small.

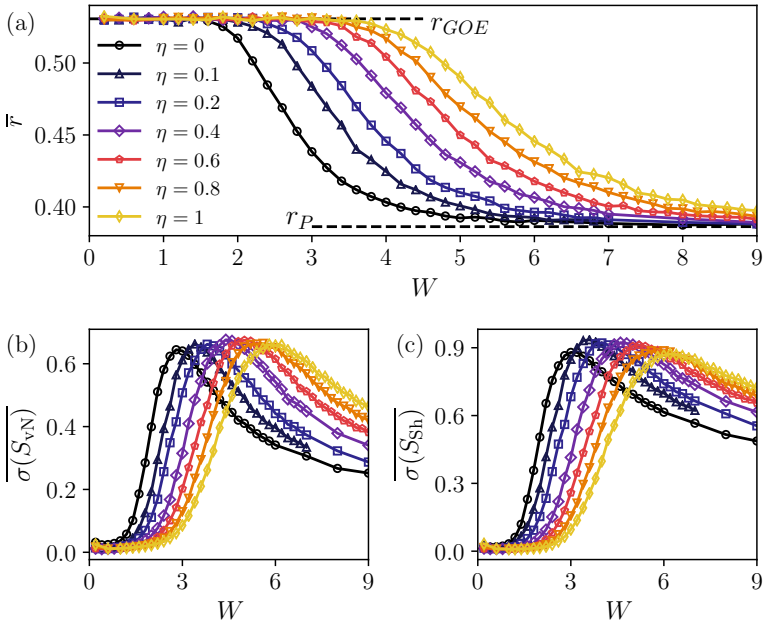

Figure 8.9: This figure presents the numerical results carried out by Scott Taylor. They locate the MBL transition via exact diagonalisation via (a) the level statistics r parameter, (b) the standard deviation of the entanglement entropy distribution, and (c) the standard deviation of the Shannon entropy distribution, all as a function of disorder strength W for several values of the XY anisotropy parameter η. These results were obtained from exact diagonalisation of the Hamiltonian for a disordered XYZ spin chain of length $L = 15$ with periodic boundary conditions. The error bars are smaller than the symbol size.

the MBL transition points found in Fig. 8.2. The analysis of the individual quantities is shown in Fig. 8.9. All three measures demonstrate a pronounced increase of the critical disorder strength for the MBL transition, W_{c2}, as the XY anisotropy parameter η is increased. This is very much in line with the observation of the shift in transition from diffusive to subdiffusive behaviour for a varying XY anisotropy parameter.

8.5 SUMMARY

In this chapter, we have provided evidence that there are four phases in the disordered spin-1/2 XYZ chain: a ballistic phase at zero disorder; a diffusive phase for a finite range of disorder from 0^+ to a critical value $W_{c1}(\eta)$; a subdiffusive phase for a finite range of disorder from $W_{c1}(\eta)$ to the MBL transition $W_{c2}(\eta)$; and a many-body localised phase for disorders above $W_{c2}(\eta)$. Importantly, the model that we have studied takes us beyond cases — such as the previously

studied XXZ chain — that can be thought of in terms of the strongly-interacting dynamics of a fixed number of particles.

The two main conclusions to be drawn from this chapter are as follows: disorder tends to localise; XY anisotropy tends to delocalise. It is not immediately intuitive how to think of the latter. One possible way to understand delocalisation is to think of it in the fermionic picture, in which the XY anisotropy η appears as a pair-creation (and of course a partner pair-annihilation) term. This means that the system, in its time-evolution, can visit sectors with other fermion numbers, which it could not in the XXZ case. If subdiffusion is pictured as excitations (and in this illustration particles) 'getting stuck' and thus moving slower than diffusively, an additional transport channel might help them travel though the chain faster. Barring significant phase-coherence effects between the states in the N and $N+2$-particle sectors (which there seems to be no reason to expect), we would therefore expect enhanced delocalisation of energy density excitations. This would presumably carry over to the localisation transition of the MBL phase and explain the transition point at much larger values of disorder strength.

Further interesting questions include testing this for quasi-periodic disorder as well as elaborating further on the mechanics for subdiffusion, something that is not fully understood at this point. These questions are currently being addressed in ongoing research.

Part IV

CONCLUSION, OUTLOOK & FUTURE WORK

9

CONCLUSIONS AND OUTLOOK

In this thesis, we have studied various aspects of the spin-1/2 XYZ model and its fermionic equivalent. There are two main results. Firstly, we showed that a disorder-free, Wannier-Stark localised system exhibits many-body localisation phenomenology upon adding interactions between its constituent particles. While lacking an asymptotic description in the thermodynamic limit, this is the first disorder-free model containing only one particle species that exhibits non-transient many-body localisation phenomenology. Secondly, we characterise the energy transport of the spin-1/2 XYZ chain under U(1) symmetry breaking. We showed that symmetry breaking delays localisation and enhances transport, while retaining previously found forms of anomalous transport.

9.1 CONTEXT AND RELEVANCE

The underlying reason for our research, as motivated in the introduction, is that the mechanism for quantum systems to thermalise is not sufficiently understood. (Idealised) model systems such as the XYZ spin chain provide a promising venue to uncover fundamental laws of collective quantum phenomena. Still, these complex systems are often analytically intractable and numerics, on the other hand, become unfeasible due to an exponential increase in required computer resources when increasing the investigated system size. It is often due to ingenious numerical techniques or the scaling of small system size exact numerics that progress can be made.

This leaves the question whether it is useful at all to study a specific system, its short time dynamics as well as its long time steady state. After all, in theoretical physics, we are most interested in universal behaviour applicable to a wide class of problems. To answer this, it is worthwhile to take a step back and look at the history of condensed matter physics. The earliest forms of condensed matter science are broadly speaking connected with the prehistoric ages such as the stone, bronze and iron age. While they were very different in the nature of their science, we must not forget that the idea of quenching, an important topic in this thesis, has its possibly first prominent written mention in Book 9 of Homer's Odyssey describing the stabbing of the Cyclops' one eye.

'as when a man who works as a blacksmith plunges a screaming great axe blade or adze into cold water, treating it for temper, since this is the way

steel is made strong, even so Cyclops' eye sizzled about the beam of the olive.' (9:393) [158]

The modern, scientific condensed matter theory emerges in the middle of the nineteenth century with the classification of crystal symmetries, the Wiedemann-Franz law (for thermal and electrical conductivity) and not least with J. J. Thomson's discovery of the electron in 1897. In the many decades to follow, theorists and experimentalists discovered and explained many of the most fundamental concepts to the present day: band-structures, magnetism, superconductivity, superfluidity and many more. Importantly, theorists at the time were mostly concerned with calculating properties measurable or already measured in the laboratory.

A paradigm shift can be seen with the discovery of the renormalisation group. The idea of scale invariance and universality classes has since then made a profound impact on the field. While initially most prominent in the study of phase transitions, universal scaling behaviour was discovered in many others areas, not least in the recently very active area of topological insulators. Universality is of course a powerful concept in physics. It distils nature's essence in a unique way and is ultimately a time saver, simply put.

The danger with ever increased abstraction is, however, that things become far more difficult to realise in experiment. In that sense, we may be observing a paradigm shift again. The advent of cold atom experiments, among other promising avenues, has allowed us to probe concrete quantum systems in a way impossible before. This unparalleled level of control has brought questions of non-universal nature back to the forefront of physics.

9.2 INTERPLAY OF DISORDER, CONFINEMENT, INTERACTIONS

Prompted by the above, we studied in the first part of this thesis a particular type of relatively simple quantum quench: a sudden trap displacement applied to a one-dimensional system of non-interacting lattice fermions with disorder (the interacting case was also considered and discussed). The central theme of the first chapter in that part was to provide an understanding of how confinement, lattice structure and disorder, three key ingredients in cold atom experiments of the present day, conspire to provide various dynamical regimes to the coherent post-quench time evolution. We discussed these questions using a number of relatively straightforward real-space observables.

The main conclusion drawn for the non-interacting case was that the disordered potential has two distinct localising effects: Anderson localisation, which occurs via the same mechanism as in the untrapped system, and Bragg localisation, which arises from the presence in the single-particle spectrum of the post-quench Hamiltonian

of nearly degenerate bonding and antibonding states that are spatially localised near the edges of the trap. These effects have profound impact on the short- and long-time dynamics of the system.

Especially the role of disorder or parity breaking in the long-time evolution is very pronounced. Very weak disorder or a non-integer trap jump may stop the hybridisation of Bragg-localised states causing a macroscopic parity violation by steady state density.

The study of this specific case raised a more general question. In the case of large trap displacements, when the so-called Bragg-localised states lose their partner states on the other side of the confinement, the system is Wannier-Stark localised (in a non uniform field). The underlying mechanism for localisation is different from Anderson localisation; however, many emerging properties such as exponentially localised eigenstates remain. How much of this phenomenology remains when adding interparticle interaction?

In the second chapter of the first part we have shown that the experimentally natural case of a finite system in an electric field, a simple Wannier-Stark-localised system, shows properties that coincide with those of the MBL phase. The bipartite entanglement entropy $S(t)$ exhibits a slow, logarithmic growth to a value much larger than that obtained in the non-interacting case. The spectral statistics, a dynamics-independent measure for localisation, are Poissonian. And finally, localisation seems equally persistent in a now standard imbalance experiment, where the relaxation of CDW order is measured.

This striking similarity of Stark-MBL and disorder-induced MBL shows the emergence of interesting fundamental properties from concrete physical systems. While in the limit of large system sizes, Stark-MBL may be difficult to motivate on account of the unbounded potential implied by a uniform component of the electric field, in any realistic experiment this should not pose a problem. The realisation of MBL phenomenology without the use of any quenched disorder in a single-species particle model opens up the route to new research investigating the crossover regime between the two cases.

9.3 SYMMETRY AND HYDRODYNAMICS

While the first part of this thesis is mainly concerned with various forms of localisation in one-dimensional fermionic systems, the second part is dedicated to transport in disordered but delocalised systems. To that end we investigated the disordered spin-1/2 XYZ chain. It has recently become clear that spin systems which localise at strong disorder, have a complex phase diagram in the parameter region preceding the localisation transition. One interesting property is that spin and energy transport are believed to behave anomalously, in that they show subdiffusive instead of diffusive transport prior to the loc-

alisation transition. A completely open question in the hydrodynamic studies was the influence of underlying symmetries.

We found that breaking the U(1) symmetry present in the the previously studied XXZ chain (by introducing an XY anisotropy) influences the energy transport as well as the localisation transition. In total we found four phases: a ballistic phase at zero disorder; a diffusive phase for a finite range of disorder from 0^+ to a critical value $W_{c1}(\eta)$; a subdiffusive phase for a finite range of disorder from $W_{c1}(\eta)$ to the MBL transition $W_{c2}(\eta)$; and a many-body localised phase for disorders above $W_{c2}(\eta)$. Importantly, the model in question takes us beyond cases — such as the previously studied XXZ chain — that can be thought of in terms of the strongly-interacting dynamics of a fixed number of particles. The two main conclusions to be drawn from this part are as follows: disorder tends to localise; XY anisotropy tends to delocalise. In future research it would be interesting to address the mechanism behind subdiffusion further. This form of transport, while possibly a transient phenomenon (in time or space), remains a peculiar property even at the time- and length-scales currently investigated.

9.4 OPEN QUESTIONS AND OUTLOOK

In summary, we hope to have provided a detailed rendition of the last four years of work dedicated to the study of localisation, thermalisation and transport in one-dimensional systems. We found that the study of concrete experimental realities such as harmonic confinement gave rise to abstract new ways of thinking about localisation, as is the case for Stark-MBL. Further to this, even in the ergodic region of disordered systems, once dubbed a mere 'bad metal', things are far from understood. The mechanism for anomalous subdiffusive transport remains disputed, while other flavours of ergodicity such as the fractal dimension equally show irregular behaviour.

As a closing remark we note that while this work only touched upon a very small area of non-equilibrium condensed matter physics, the emerging answers and new questions are broad and profound. We therefore expect that many new and exciting concepts will arise in this field in the years to come. What a time to be alive (and to be doing physics of course!).

BIBLIOGRAPHY

1. Abanin, D. A. & Papić, Z. Recent progress in many-body localization. *Ann. Phys.* **529,** 1700169 (2017).
2. Abou-Chacra, R, Thouless, D. J. & Anderson, P. W. A selfconsistent theory of localization. *J. Phys. C Solid State Phys.* **6,** 1734–1752 (1973).
3. Abrahams, E., Anderson, P. W., Licciardello, D. C. & Ramakrishnan, T. V. Scaling theory of localization: Absence of quantum diffusion in two dimensions. *Phys. Rev. Lett.* **42,** 673–676 (1979).
4. Affleck, I., Kennedy, T., Lieb, E. H. & Tasaki, H. Rigorous results on valence-bond ground states in antiferromagnets. *Phys. Rev. Lett.* **59,** 799–802 (1987).
5. Agarwal, K., Gopalakrishnan, S., Knap, M., Müller, M. & Demler, E. Anomalous diffusion and Griffiths effects near the many-body localization transition. *Phys. Rev. Lett.* **114,** 160401 (2015).
6. Alet, F. & Laflorencie, N. Many-body localization: An introduction and selected topics. *Comptes Rendus Phys.* (2018).
7. Alet, F., Damle, K. & Pujari, S. Sign-Problem-Free Monte Carlo Simulation of Certain Frustrated Quantum Magnets. *Phys. Rev. Lett.* **117,** 197203 (2016).
8. Altman, E. & Vosk, R. Universal dynamics and renormalization in many body localized systems. *Annu. Rev. Cond. Matt. Phys.* **6,** 383–409 (2015).
9. Altshuler, B., Krovi, H. & Roland, J. Anderson localization makes adiabatic quantum optimization fail. *Proc. Natl. Acad. Sci. U.S.A.* **107,** 12446–12450 (2010).
10. Anderson, P. W. Absence of diffusion in certain random lattices. *Phys. Rev.* **109,** 1492–1505 (1958).
11. Aspect, A. & Inguscio, M. Anderson localization of ultracold atoms. *Phys. Today* **62,** 30–35 (2009).
12. Aspuru-Guzik, A. & Walther, P. Photonic quantum simulators. *Nat. Phys.* **8,** 285–291 (2012).
13. Atas, Y. Y., Bogomolny, E., Giraud, O. & Roux, G. Distribution of the ratio of consecutive level spacings in random matrix ensembles. *Phys. Rev. Lett.* **110,** 084101 (2013).
14. Aubry, S. & André, G. Analyticity breaking and Anderson localization in incommensurate lattices. *Ann. Isr. Phys. Soc.* **3,** 133–140 (1980).

15. Baldwin, C. L., Laumann, C. R., Pal, A & Scardicchio, A. Clustering of Nonergodic Eigenstates in Quantum Spin Glasses. *Phys. Rev. Lett.* **118,** 127201 (2017).

16. Balents, L. Spin liquids in frustrated magnets. *Nature* **464,** 199–208 (2010).

17. Banerjee, S. & Roy, A. *Linear Algebra and Matrix Analysis for Statistics* p. 129 (Chapman and Hall/CRC, 2014).

18. Bar-Lev, Y. & Reichman, D. R. Dynamics of many-body localization. *Phys. Rev. B* **89,** 220201(R) (2014).

19. Bar-Lev, Y. & Reichman, D. R. Slow dynamics in a two-dimensional Anderson-Hubbard model. *EPL* **113,** 46001 (2016).

20. Bar-Lev, Y., Cohen, G. & Reichman, D. R. Absence of diffusion in an interacting system of spinless fermions on a one-dimensional disordered lattice. *Phys. Rev. Lett.* **114,** 100601 (2015).

21. Bardarson, J. H., Pollmann, F. & Moore, J. E. Unbounded growth of entanglement in models of many-body localization. *Phys. Rev. Lett.* **109,** 017202 (2012).

22. Barthel, T. Precise evaluation of thermal response functions by optimized density matrix renormalization group schemes. *New J. Phys.* **15,** 073010 (2013).

23. Basko, D. M., Aleiner, I. L. & Altshuler, B. L. Metal-insulator transition in a weakly interacting many-electron system with localized single-particle states. *Ann. Phys. (N. Y).* **321,** 1126–1205 (2006).

24. Bauer, B. & Nayak, C. Area laws in a many-body localized state and its implications for topological order. *J. Stat. Mech,* P09005 (2013).

25. Baxter, R. J. Dimers on a rectangular lattice. *J. Math. Phys.* **9,** 650–654 (1968).

26. Baxter, R. J. *Exactly Solved Models in Statistical Mechanics* (Academic, London, 1982).

27. Bera, S., De Tomasi, G., Weiner, F. & Evers, F. Density Propagator for Many-Body Localization: Finite-Size Effects, Transient Subdiffusion, and Exponential Decay. *Phys. Rev. Lett.* **118,** 196801 (2017).

28. Bertrand, C. L. & García-García, A. M. Anomalous Thouless energy and critical statistics on the metallic side of the many-body localization transition. *Phys. Rev. B* **94,** 144201 (2016).

29. Billy, J., Josse, V., Zuo, Z., Bernard, A., Hambrecht, B., Lugan, P., Clément, D., Sanchez-Palencia, L., Bouyer, P. & Aspect, A. Direct observation of Anderson localization of matter waves in a controlled disorder. *Nature* **453,** 891–894 (2008).

30. Blaizot, J. *Quantum Theory of Finite Systems* p. 38 (MIT, Cambridge, MA, 1986).

31. Blatt, R. & Roos, C. F. Quantum simulations with trapped ions. *Nat. Phys.* **8,** 277–284 (2012).

32. Bloch, I., Dalibard, J. & Nascimbène, S. Quantum simulations with ultracold quantum gases. *Nat. Phys.* **8,** 267–276 (2012).

33. Bols, A. & De Roeck, W. Asymptotic localization in the Bose-Hubbard model. *J. Math. Phys.* **59,** 021901 (2018).

34. Buluta, I. & Nori, F. Quantum Simulators. *Science* **326,** 108–111 (2009).

35. Carleo, G. & Troyer, M. Neural Networks. *Science* **355,** 602–606 (2017).

36. Caux, J.-S. & Mossel, J. Remarks on the notion of quantum integrability. *J. Stat. Mech.* P02023 (2011).

37. Chandran, A., Pal, A., Laumann, C. R. & Scardicchio, A. Many-body localization beyond eigenstates in all dimensions. *Phys. Rev. B* **94,** 144203 (2016).

38. Chandran, A., Khemani, V., Laumann, C. R. & Sondhi, S. L. Many-body localization and symmetry-protected topological order. *Phys. Rev. B* **89,** 144201 (2014).

39. Chandran, A., Kim, I. H., Vidal, G. & Abanin, D. A. Constructing local integrals of motion in the many-body localized phase. *Phys. Rev. B* **91,** 85425 (2015).

40. Childress, L, Gurudev Dutt, M. V., Taylor, J. M., Zibrov, A. S., Jelezko, F, Wrachtrup, J, Hemmer, P. R. & Lukin, M. D. Coherent Dynamics of Coupled Electron and Nuclear Spin Qubits in Diamond. *Science* **314,** 281–285 (2006).

41. Choi, J.-Y., Hild, S., Zeiher, J., Schauß, P., Rubio-Abadal, A., Yefsah, T., Khemani, V., Huse, D. A., Bloch, I. & Gross, C. Exploring the many-body localization transition in two dimensions. *Science* **352,** 1547–1552 (2016).

42. Cramer, M. & Eisert, J. Correlations, spectral gap and entanglement in harmonic quantum systems on generic lattices. *New J. Phys.* **8** (2006).

43. D'Alessio, L., Kafri, Y., Polkovnikov, A. & Rigol, M. From quantum chaos and eigenstate thermalization to statistical mechanics and thermodynamics. *Adv. Phys.* **65,** 239–362 (2016).

44. Daley, A. J., Kollath, C., Schollwöck, U. & Vidal, G. Time-dependent density-matrix renormalization-group using adaptive effective Hilbert spaces. *J. Stat. Mech.* P04005 (2004).

45. Daley, A. J., Taylor, J. M., Diehl, S., Baranov, M. & Zoller, P. Atomic three-body loss as a dynamical three-body interaction. *Phys. Rev. Lett.* **102,** 040402 (2009).

46. Daley, A. J. Quantum trajectories and open many-body quantum systems. *Adv. Phys.* **63,** 77–149 (2014).

47. Dalichaouch, R., Armstrong, J. P., Schultz, S., Platzman, P. M. & McCall, S. L. Microwave localization by two-dimensional random scattering. *Nature* **354,** 53–55 (1991).

48. De Luca, A. & Scardicchio, A. Ergodicity breaking in a model showing many-body localization. *EPL* **101,** 37003 (2013).

49. De Roeck, W. & Huveneers, F. Asymptotic Quantum Many-Body Localization from Thermal Disorder. *Commun. Math. Phys.* **332,** 1017–1082 (2014).

50. De Roeck, W. & Huveneers, F. Stability and instability towards delocalization in many-body localization systems. *Phys. Rev. B* **95,** 155129 (2017).

51. De Roeck, W., Huveneers, F., Müller, M. & Schiulaz, M. Absence of many-body mobility edges. *Phys. Rev. B* **93,** 014203 (2016).

52. Deutsch, D. Quantum theory, the Church-Turing principle and the universal quantum computer. *Proc. R. Soc. Lond. A* **400,** 97–117 (1985).

53. Deutsch, J. M. Quantum statistical mechanics in a closed system. *Phys. Rev. A* **43,** 2046–2049 (1991).

54. Dias da Silva, L. G.G. V., Heidrich-Meisner, F., Feiguin, A. E., Büsser, C. A., Martins, G. B., Anda, E. V. & Dagotto, E. Transport properties and Kondo correlations in nanostructures: Time-dependent DMRG method applied to quantum dots coupled to Wilson chains. *Phys. Rev. B* **78,** 195317 (2008).

55. Dukelsky, J., Martín-Delgado, M. A., Nishino, T., Sierra, G., Martin-Delgado, M. A., Nishino, T. & Sierra, G. Equivalence of the variational matrix product method and the density matrix renormalization group applied to spin chains. *EPL* **43,** 457 (1998).

56. Eckhardt, R. Stan Ulam, John Von Neumann, and the Monte Carlo Method. *Los Alamos Sci.* 131–143 (1987).

57. Einstein, A., Podolsky, B. & Rosen, N. Can quantum-Mechanical Description of Physical Reality Be Considered Complete? *Phys. Rev.* **47,** 777–780 (1935).

58. Eisert, J. Entanglement and tensor network states. *arXiv,* 1308.33–18 (2013).

59. Eisert, J., Cramer, M. & Plenio, M. B. Colloquium: Area laws for the entanglement entropy. *Rev. Mod. Phys.* **82,** 277–306 (2010).

60. Eisert, J., Friesdorf, M. & Gogolin, C. Quantum many-body systems out of equilibrium. *Nat. Phys.* **11,** 124–130 (2015).

61. Essler, F. H. L., Frahm, H., Göhmann, F., Klümper, A. & Korepin, V. *The one-dimensional Hubbard model* p. 54 (Cambridge University Press, 2005).

62. Fermi, E, Pasta, J & Ulam, S. Studies of Nonlinear Problems. *Los Alamos Rep,* 1 –20 (1955).

63. Feynman, R. P. Simulating physics with computers. *Int. J. Theor. Phys.* **21,** 467–488 (1982).

64. Foulkes, W. M. C., Mitas, L., Needs, R. J. & Rajagopal, G. Quantum Monte Carlo simulations of solids. *Rev. Mod. Phys.* **73,** 33–83 (2001).

65. Fröhlich, J. & Spencer, T. Absence of diffusion in the Anderson tight binding model for large disorder or low energy. *Commun. Math. Phys.* **88,** 151–184 (1983).

66. Furstenberg, H. & Kesten, H. Products of random matrices. *Annanls Math. Stat.* **31,** 457–469 (1960).

67. Georgescu, I. M., Ashhab, S. & Nori, F. Quantum simulation. *Rev. Mod. Phys.* **86,** 153–185 (2014).

68. Goldshtein, I., Molchanov, S. A. & Pastur, L. A pure point spectrum of the stochastic one-dimensional Schrödinger operator. *Funct. Anal. Appl.* **11,** 1–10 (1977).

69. Goold, J, Gogolin, C, Clark, S. R., Eisert, J, Scardicchio, A & Silva, A. Total correlations of the diagonal ensemble herald the many-body localization transition. *Phys. Rev. B* **92,** 180202(R) (Nov. 2015).

70. Gornyi, I. V., Mirlin, A. D. & Polyakov, D. G. Interacting electrons in disordered wires: Anderson localization and low-T transport. *Phys. Rev. Lett.* **95,** 206603 (2005).

71. Gradshteyn, I. S. & Ryzhik, I. M. *Table of Integrals, Series, and Products* 6th, p. 797 (Academic, New York, 2000).

72. Griffiths, R. B. Nonanlytic behavior above the critical point in a random Ising ferromagnet. *Phys. Rev. Lett.* **23,** 17–19 (1969).

73. Gull, E., Millis, A. J., Lichtenstein, A. I., Rubtsov, A. N., Troyer, M. & Werner, P. Continuous-time Monte Carlo methods for quantum impurity models. *Rev. Mod. Phys.* **83,** 349–404 (2011).

74. Haake, F. *Quantum Signatures of Chaos* (Springer-Verlag New York, 2006).

75. Haldane, F. D. M. Continuum dynamics of the 1-D Heisenberg antiferromagnet: Identification with the O(3) nonlinear sigma model. *Phys. Lett. A* **93,** 464–468 (1983).

76. Haldane, F. D. M. Nonlinear field theory of large-spin Heisenberg antiferromagnets: Semiclassically quantized solitons of the one-dimensional easy-axis Néel state. *Phys. Rev. Lett.* **50,** 1153–1156 (1983).

77. Hallberg, K. A. Density-matrix algorithm for the calculation of dynamical properties of low-dimensional systems. *Phys. Rev. B* **52,** R9827–R9830 (1995).

78. Hallberg, K. A. New trends in density matrix renormalization. *Adv. Phys.* **55,** 477–526 (2006).

79. Hartmann, M. J., Prior, J., Clark, S. R. & Plenio, M. B. Density matrix renormalization group in the Heisenberg picture. *Phys. Rev. Lett.* **102,** 057202 (2009).

80. Hastings, M. B. An Area Law for One Dimensional Quantum Systems. *J. Stat. Mech,* P08024 (2007).

81. Hastings, M. B. & Koma, T. Spectral Gap and Exponential Decay of Correlations. *Commun. Math. Phys* **265,** 781–804 (2006).

82. Hauschild, J. & Pollmann, F. Efficient numerical simulations with Tensor Networks: Tensor Network Python (TeNPy). *SciPost Phys. Lect. Notes* **5,** 1–32 (2018).

83. Hecker Denschlag, J, Simsarian, J. E., Häffner, H, McKenzi, C, Browaeys, A, Cho, D, Helmerson, K, Rolston, S. L. & Phillips, W. D. A Bose-Einstein condensate in an optical lattice. *J. Phys. B At. Mol. Opt. Phys* **35,** 3095–3110 (2002).

84. Heisenberg, W. Zur Theorie des ferromagnetismus. *Zeitschrift für Phys.* **49,** 619–636 (1928).

85. Henelius, P. & Sandvik, A. W. Sign problem in Monte Carlo simulations of frustrated quantum spin systems. *Phys. Rev. B* **62,** 1102–1113 (2000).

86. Hickey, J. M., Genway, S. & Garrahan, J. P. Signatures of many-body localisation in a system without disorder and the relation to a glass transition. *J. Stat. Mech,* 054047 (2016).

87. Hooley, C. & Quintanilla, J. Single-atom density of states of an optical lattice. *Phys. Rev. Lett.* **93,** 080404 (2004).

88. Houck, A. A., Türeci, H. E. & Koch, J. On-chip quantum simulation with superconducting circuits. *Nat. Phys.* **8,** 292–299 (2012).

89. Hundertmark, D. *A short introduction to anderson localization* 194–218 (Oxford Scholarship Online, 2008).

90. Huse, D. A., Nandkishore, R. & Oganesyan, V. Phenomenology of fully many-body-localized systems. *Phys. Rev. B* **90,** 174202 (2014).

91. Huveneers, F. Classical and quantum systems: transport due to rare events. *Ann. Phys.* **529,** 1600384 (2017).

92. Imbrie, J. Z. On Many-Body Localization for Quantum Spin Chains. *J. Stat. Phys.* **163,** 998–1048 (2016).

93. Inami, T. & Konno, H. Integrable XYZ spin chain with boundaries. *J. Phys. A. Math. Gen.* **27,** L913 (1994).

94. Jaksch, D. & Zoller, P. The cold atom Hubbard toolbox. *Ann. Phys. (N. Y).* **315,** 52–79 (2005).

95. Jeckelmann, E. Dynamical density-matrix renormalization-group method. *Phys. Rev. B* **66,** 045114 (2002).

96. Jördens, R., Strohmaier, N., Günter, K., Moritz, H. & Esslinger, T. A Mott insulator of fermionic atoms in an optical lattice. *Nature* **455,** 204–207 (2008).

97. Joshi, C., Nissen, F. & Keeling, J. Quantum correlations in the one-dimensional driven dissipative XY model. *Phys. Rev. A* **88,** 063835 (2013).

98. Kassal, I., Whitfield, J. D., Perdomo-Ortiz, A., Yung, M.-H. & Aspuru-Guzik, A. Simulating chemistry using quantum computers. *Annu. Rev. Phys. Chem.* **62,** 185–207 (2011).

99. Kim, Y. E. & Zubarev, A. L. Time-dependent density-functional theory for trapped strongly interacting fermionic atoms. *Phys. Rev. A* **70,** 033612 (2004).

100. Kinoshita, T., Wenger, T. & Weiss, D. S. A quantum Newton's cradle. *Nature* **440,** 900–903 (2006).

101. Kjäll, J. A., Bardarson, J. H. & Pollmann, F. Many-body localization in a disordered quantum ising chain. *Phys. Rev. Lett.* **113,** 107204 (2014).

102. Kollath, C., Schollwöck, U. & Zwerger, W. Spin-charge separation in cold fermi gases: A real time analysis. *Phys. Rev. Lett.* **95,** 176401 (2005).

103. Kondov, S. S., McGehee, W. R., Xu, W. & DeMarco, B. Disorder-induced localization in a strongly correlated atomic Hubbard gas. *Phys. Rev. Lett.* **114,** 083002 (2015).

104. Kramer, B. & MacKinnon, A. Localization: theory and experiment. *Reports Prog. Phys.* **56,** 1469–1564 (1993).

105. Kravtsov, V. E., Khaymovich, I. M., Cuevas, E. & Amini, M. A random matrix model with two localization transitions. *New J. Phys.* **17,** 122002 (2015).

106. Kühner, T. D. & White, S. R. Dynamical Correlation Functions using the Density Matrix Renormalization Group. *Phys. Rev. B* **60,** 335–343 (1999).

107. Lanczos, C. An iteration method for the solution of the eigenvalue problem of linear differential and integral operators. *J. Res. Natl. Bur. Stand. (1934).* **45,** 255–282 (1950).

108. Laumann, C. R., Pal, A. & Scardicchio, A. Many-body mobility edge in a mean-field quantum spin glass. *Phys. Rev. Lett.* **113,** 200405 (2014).

109. Laumann, C. R., Moessner, R, Scardicchio, A & Sondhi, S. L. Quantum annealing: The fastest route to quantum computation? *Eur. Phys. J. Spec. Top.* **224,** 75–88 (2015).

110. Lewenstein, M., Sanpera, A., Ahufinger, V., Damski, B., Sen, A. & Sen, U. Ultracold atomic gases in optical lattices: Mimicking condensed matter physics and beyond. *Adv. Phys.* **56,** 243–379 (2007).

111. Lightman, A. P. *The discoveries: great breakthroughs in twentieth-century science, including the original papers* p. 8 (Vintage; Reprint edition, Toronto, 2005).

112. Lloyd, S. Universal Quantum Simulators. *Science* **273,** 1073–1078 (1996).

113. Luitz, D. J. Long tail distributions near the many-body localization transition. *Phys. Rev. B* **93,** 134201 (2016).

114. Luitz, D. J. & Bar-Lev, Y. Anomalous Thermalization in Ergodic Systems. *Phys. Rev. Lett.* **117,** 170404 (2016).

115. Luitz, D. J. & Lev, Y. B. The Ergodic Side of the Many-Body Localization Transition. *Ann. Phys.* 1600350 (2016).

116. Luitz, D. J., Laflorencie, N. & Alet, F. Many-body localization edge in the random-field Heisenberg chain. *Phys. Rev. B* **91,** 081103(R) (2015).

117. Lüschen, H. P., Bordia, P., Scherg, S., Alet, F., Altman, E., Schneider, U. & Bloch, I. Observation of Slow Dynamics near the Many-Body Localization Transition in One-Dimensional Quasiperiodic Systems. *Phys. Rev. Lett.* **119,** 260401 (2017).

118. Lye, J. E., Fallani, L., Modugno, M., Wiersma, D. S., Fort, C. & Inguscio, M. Bose-Einstein condensate in a random potential. *Phys. Rev. Lett.* **95,** 070401 (2005).

119. McCulloch, I. P. From density-matrix renormalization group to matrix product states. *J. Stat. Mech.* P10014 (2007).

120. Mendoza-Arenas, J. J., Clark, S. R. & Jaksch, D. Coexistence of energy diffusion and local thermalization in nonequilibrium XXZ spin chains with integrability breaking. *Phys. Rev. E* **91,** 042129 (2015).

121. Mendoza-Arenas, J. J., Znidaric, M., Varma, V. K., Goold, J., Clark, S. R. & Scardicchio, A. Asymmetry in energy versus spin transport in certain interacting, disordered systems. *arXiv,* 1803.11555 (2018).

122. Modugno, G, Ferlaino, F, Heidemann, R, Roati, G & Inguscio, M. Production of a Fermi gas of atoms in an optical lattice. *Phys. Rev. A* **68,** 011601(R) (2003).

123. Mott, N. F. Metal-insulator transition. *Rev. Mod. Phys.* **40,** 677–683 (1968).

124. Mott, N. F. & Twose, W. D. The theory of impurity conduction. *Adv. Phys.* **10,** 107–163 (1961).

125. Mott, N. F. & Davis, E. *Electronic Processes in Non-Crystalline Materials* (Clarendon Press, Oxford, 1971).

126. Mukerjee, S., Oganesyan, V. & Huse, D. Statistical theory of transport by strongly interacting lattice fermions. *Phys. Rev. B* **73,** 035113 (2006).

127. Nandkishore, R. & Huse, D. A. Many body localization and thermalization in quantum statistical mechanics. *Annu. Rev. Condens. Matter Phys.* **6,** 15–38 (2015).

128. Nielsen, M. A. & Chuang, I. L. *Quantum Computation and Quantum Information* (Cambridge University Press, 2010).

129. Noether, E. Invariante Variansprobleme. *Nachr. D. König. Gesellsch. D. Wiss. Zu Göttingen, Math-phys. Klasse, S,* 235–257 (1918).

130. Oganesyan, V. & Huse, D. A. Localization of interacting fermions at high temperature. *Phys. Rev. B* **75,** 155111 (2007).

131. Oganesyan, V., Pal, A. & Huse, D. A. Energy transport in disordered classical spin chains. *Phys. Rev. B* **80,** 115104 (2009).

132. Oitmaa, J., Hamer, C. & Zheng, W. *Series expansion methods for strongly interacting lattice models* (Cambridge University Press, 2006).

133. Orús, R. & Vidal, G. Infinite time-evolving block decimation algorithm beyond unitary evolution. *Phys. Rev. B* **78,** 155117 (2008).

134. Orús, R. A practical introduction to tensor networks: Matrix product states and projected entangled pair states. *Ann. Phys. (N. Y).* **349,** 117–158 (2014).

135. Östlund, S. & Rommer, S. Thermodynamic limit of density matrix renormalization. *Phys. Rev. Lett.* **75,** 3537–3540 (1995).

136. Ott, H., de Mirandes, E., Ferlaino, F., Roati, G., Modugno, G. & Inguscio, M. Collisionally induced transport in periodic potentials. *Phys. Rev. Lett.* **92,** 160601 (2004).

137. Page, D. N. Average Entropy of a Subsystem. *Phys. Rev. Lett.* **71,** 1291–1294 (1993).

138. Pal, A. & Huse, D. A. Many-body localization phase transition. *Phys. Rev. B* **82,** 174411 (2010).

139. Pekker, D., Clark, B. K., Oganesyan, V. & Refael, G. Fixed Points of Wegner-Wilson Flows and Many-Body Localization. *Phys. Rev. Lett.* **119,** 075701 (2017).

140. Peschel, I. Special Review: Entanglement in Solvable Many-Particle Models. *Brazilian J. Phys.* **42,** 267–291 (2012).

141. Pezzè, L., Pitaevskii, L., Smerzi, A., Stringari, S., Modugno, G., de Mirandes, E., Ferlaino, F., Ott, H., Roati, G. & Inguscio, M. Insulating behavior of a trapped ideal fermi gas. *Phys. Rev. Lett.* **93,** 120401 (2004).

142. Pezzè, L., Hambrecht, B. & Sanchez-Palencia, L. Dipole oscillations of a Fermi gas in a disordered trap: Damping and localization. *EPL* **88,** 30009 (2009).

143. Pietracaprina, F., Parisi, G., Mariano, A., Pascazio, S. & Scardicchio, A. Entanglement critical length at the many-body localization transition. *J. Stat. Mech,* 113102 (2017).

144. Plenio, M. B., Eisert, J., Dreißig, J. & Cramer, M. Entropy, entanglement, and area: Analytical results for harmonic lattice systems. *Phys. Rev. Lett.* **94,** 060503 (2005).

145. Polkovnikov, A. Microscopic diagonal entropy and its connection to basic thermodynamic relations. *Ann. Phys. (N. Y).* **326,** 486–499 (2011).

146. Polkovnikov, A., Sengupta, K., Silva, A. & Vengalattore, M. Colloquium: Nonequilibrium dynamics of closed interacting quantum systems. *Rev. Mod. Phys.* **83,** 863–883 (2011).

147. Porter, M. A., Zabusky, N. J., Hu, B. & Campbell, D. K. Fermi, Pasta, Ulam and the Birth of Experimental Mathematics. *Am. Sci.* **97,** 214–221 (2009).

148. Prosen, T. & Žnidarič, M. Matrix product simulations of non-equilibrium steady states of quantum spin chains. *J. Stat. Mech.* P02035 (2009).

149. Rademaker, L. & Ortuño, M. Explicit Local Integrals of Motion for the Many-Body Localized State. *Phys. Rev. Lett.* **116,** 010404 (2016).

150. Raghunathan, M. S. A proof of Oseledec's multiplicative ergodic theorem. *Isr. J. Math.* **32,** 356–362 (1979).

151. Ramirez, A. P. Strongly Geometrically Frustrated Magnets. *Ann. Rev. Mater. Sci.* **24,** 453–480 (1994).

152. Rigol, M. & Muramatsu, A. Confinement control by optical lattices. *Phys. Rev. A* **70,** 043627 (2004).

153. Rigol, M., Muramatsu, A. & Olshanii, M. Hard-core bosons on optical superlattices: Dynamics and relaxation in the superfluid and insulating regimes. *Phys. Rev. A* **74,** 053616 (2006).

154. Rigol, M., Dunjko, V., Yurovsky, V. & Olshanii, M. Relaxation in a completely integrable many-body Quantum system: An Ab initio study of the dynamics of the highly excited states of 1D lattice hard-core bosons. *Phys. Rev. Lett.* **98,** 050405 (2007).

155. Rigol, M., Dunjko, V. & Olshanii, M. Thermalization and its mechanism for generic isolated quantum systems. *Nature* **452,** 854–858 (2008).

156. Roati, G., D'Errico, C., Fallani, L., Fattori, M., Fort, C., Zaccanti, M., Modugno, G., Modugno, M. & Inguscio, M. Anderson localization of a non-interacting Bose-Einstein condensate. *Nature* **453,** 895–898 (2008).

157. Ros, V., Müller, M. & Scardicchio, A. Integrals of motion in the many-body localized phase. *Nucl. Phys. B* **891,** 420–465 (2015).

158. Russo, R. The heart of steel: A metallurgical interpretation of iron in Homer. *Bull. Hist. Chem.* **30,** 23–29 (2005).

159. Ruuska, V. & Törmä, P. Quantum transport of non-interacting Fermi gas in an optical lattice combined with harmonic trapping. *New J. Phys.* **6,** 59 (2004).

160. Savin, A. V., Tsironis, G. P. & Zotos, X. Thermal conductivity of a classical one-dimensional Heisenberg spin model. *Phys. Rev. B* **72,** 140402(R) (2005).

161. Scalapino, D. J. The 2D Hubbard Model and the High Tc Cuprate Problem. *J. Supercond. Nov. Magn.* **19,** 195–200 (2007).

162. Scalapino, D. J., Loh, E. & Hirsch, J. E. D-wave pairing near a spin-density-wave instability. *Phys. Rev. B* **34,** 8190–8192 (1986).

163. Scardicchio, A. & Thiery, T. Perturbation theory approaches to Anderson and Many-Body Localization: some lecture notes. *arXiv,* 1710.01234 (2017).

164. Schneider, C., Porras, D. & Schaetz, T. Experimental quantum simulations of many-body physics with trapped ions. *Reports Prog. Phys.* **75,** 024401 (2012).

165. Schollwöck, U. The density-matrix renormalization group. *Rev. Mod. Phys.* **77,** 259–315 (2005).

166. Schollwöck, U. The density-matrix renormalization group in the age of matrix product states. *Ann. Phys. (N. Y).* **326,** 96–192 (2011).

167. Schreiber, M., Hodgman, S. S., Bordia, P., Lüschen, H. P., Fischer, M. H., Vosk, R., Altman, E., Schneider, U. & Bloch, I. Observation of many-body localization of interacting fermions in a quasirandom optical lattice. *Science* **349,** 842–845 (2015).

168. Schrödinger, E. Die gegenwärtige Situation in der Quantenmechanik. *Naturwissenschaften* **48,** 807–812 (1935).

169. Schrödinger, E. Die gegenwärtige Situation in der Quantenmechanik. *Naturwissenschaften* **49,** 823–828 (1935).

170. Schrödinger, E. Discussion of Probability Relations Between Separated Systems, 555–563 (1935).

171. Schrödinger, E. Probability Relations Between Separated Systems, 446–452 (1936).

172. Schulte, T., Drenkelforth, S., Kruse, J., Ertmer, W., Arlt, J., Sacha, K., Zakrzewski, J. & Lewenstein, M. Routes towards Anderson-like localization of Bose-Einstein condensates in disordered optical lattices. *Phys. Rev. Lett.* **95,** 170411 (2005).

173. Schulz, M., Hooley, C. A., Moessner, R. & Pollmann, F. Stark Many-Body Localization. *Phys. Rev. Lett.* **122,** 040606 (2019).

174. Schulz, M., Moessner, R. & Hooley, C. A. Slow relaxation and sensitivity to disorder in trapped lattice fermions after a quench. *Phys. Rev. A* **94,** 063643 (2016).

175. Schulz, M., Taylor, S. R., Hooley, C. A. & Scardicchio, A. Energy transport in a disordered spin chain with broken U(1) symmetry: diffusion, subdiffusion, and many-body localization. *Phys. Rev. B* **98,** 180201(R) (2018).

176. Serbyn, M. & Moore, J. E. Spectral statistics across the many-body localization transition. *Phys. Rev. B* **93,** 41424 (2016).

177. Serbyn, M., Papić, Z. & Abanin, D. A. Universal slow growth of entanglement in interacting strongly disordered systems. *Phys. Rev. Lett.* **110,** 260601 (2013).

178. Serbyn, M., Papić, Z. & Abanin, D. A. Thouless energy and multifractality across the many-body localization transition. *Phys. Rev. B* **96,** 104201 (2017).

179. Srednicki, M. Chaos and quantum thermalization. *Phys. Rev. E* **50,** 888–901 (1994).

180. Stagraczyński, S., Chotorlishvili, L., Schüler, M., Mierzejewski, M. & Berakdar, J. Many-body localization phase in a spin-driven chiral multiferroic chain. *Phys. Rev. B* **96,** 054440 (2017).

181. Sugiyama, G. & Koonin, S. E. Auxiliary field Monte-Carlo for quantum many-body ground states. *Ann. Phys. (N. Y).* **168,** 1–26 (1986).

182. Suzuki, M. Fractal decomposition of exponential operators with applications to many-body theories and Monte Carlo simulations. *Phys. Lett. A* **146,** 319–323 (1990).

183. Suzuki, M. General theory of fractal path integrals with applications to many-body theories and statistical physics. *J. Math. Phys.* **32,** 400–407 (1991).

184. Thouless, D. J. Anderson's theory of localized states. *J. Phys. C Solid State Phys.* **3,** 1559–1566 (1970).

185. Torres-Herrera, E. J. & Santos, L. F. Extended nonergodic states in disordered many-body quantum systems. *Ann. Phys.* **529,** 1600284 (2017).

186. Torres-Herrera, E. J., Karp, J., Távora, M. & Santos, L. F. Realistic many-body quantum systems vs. full random matrices: Static and dynamical properties. *Entropy* **18,** 1–20 (2016).

187. Troyer, M. & Wiese, U.-J. Computational complexity and fundamental limitations to fermionic quantum Monte Carlo simulations. *Phys. Rev. Lett.* **94,** 170201 (2005).

188. Van Horssen, M., Levi, E. & Garrahan, J. P. Dynamics of many-body localization in a translation-invariant quantum glass model. *Phys. Rev. B* **92,** 100305(R) (2015).

189. Van Tiggelen, B. *Localization of Waves* 1–60 (Springer, 1999).

190. Varma, V. K., Lerose, A., Pietracaprina, F., Goold, J. & Scardicchio, A. Energy diffusion in the ergodic phase of a many body localizable spin chain. *J. Stat. Mech.* 053101 (2017).

191. Vasseur, R. & Moore, J. E. Nonequilibrium quantum dynamics and transport: From integrability to many-body localization. *J. Stat. Mech,* 064010 (2016).

192. Verstraete, F., García-Ripoll, J. J. & Cirac, J. I. Matrix product density operators: Simulation of finite-temperature and dissipative systems. *Phys. Rev. Lett.* **93,** 207204 (2004).

193. Vidal, G., Latorre, J. I., Rico, E. & Kitaev, A. Entanglement in Quantum Critical Phenomena. *Phys. Rev. Lett.* **90,** 227902 (2003).

194. Vidal, G. Efficient classical simulation of slightly entangled quantum computations. *Phys. Rev. Lett.* **91,** 147902 (2003).

195. Vidal, G. Efficient simulation of one-dimensional quantum many-body systems. *Phys. Rev. Lett.* **93,** 040502 (2004).

196. Vojta, T. Rare region effects at classical, quantum and nonequilibrium phase transitions. *J. Phys. A. Math. Gen.* **39,** R143–R205 (2006).

197. Wannier, G. Dynamics of Band Electrons in Electric and Magnetic Fields. *Rev. Mod. Phys.* **34,** 645–655 (1962).

198. Weiße, A. & Fehske, H. *Exact diagonalization techniques* 529–544 (Springer-Verlag Berlin Heidelberg, 2008).

199. White, M., Pasienski, M., McKay, D., Zhou, S. Q., Ceperley, D. & DeMarco, B. Strongly interacting bosons in a disordered optical lattice. *Phys. Rev. Lett.* **102,** 055301 (2009).

200. White, S. R. Density matrix formulation for quantum renormalization groups. *Phys. Rev. Lett.* **69,** 2863–2866 (1992).

201. White, S. R. Density-matrix algorithms for quantum renormalization groups. *Phys. Rev. B* **48,** 10345–10356 (1993).

202. White, S. R. Spin Gaps in a Frustrated Heisenberg Model for CaV4O9. *Phys. Rev. Lett.* **77,** 3633–3636 (1996).

203. White, S. R. & Affleck, I. Spectral function for the S=1 Heisenberg antiferromagetic chain. *Phys. Rev. B* **77,** 134437 (2008).

204. White, S. R. & Feiguin, A. E. Real-time evolution using the density matrix renormalization group. *Phys. Rev. Lett.* **93,** 076401 (2004).

205. Wiersma, D. S., Bartolini, P., Lagendijk, A. & Righini, R. Localization of light in a disordered medium. *Nature* **390,** 671–673 (1997).

206. Wilczek, F. Quantum time crystals. *Phys. Rev. Lett.* **109,** 160401 (2012).

207. Wilson, K. G. The renormalization group: Critical phenomena and the Kondo problem. *Rev. Mod. Phys.* **47,** 773–840 (1975).

208. Yao, N. Y., Laumann, C. R., Cirac, J. I., Lukin, M. D. & Moore, J. E. Quasi-Many-Body Localization in Translation-Invariant Systems. *Phys. Rev. Lett.* **117,** 240601 (2016).

209. Zelevinsky, V., Brown, B., Frazier, N. & Horoi, M. The nuclear shell model as a testing ground for many-body quantum chaos. *Phys. Rep.* **276,** 85–176 (1996).

210. Žnidarič, M. Dephasing-induced diffusive transport in the anisotropic Heisenberg model. *New J. Phys.* **12** (2010).

211. Žnidarič, M., Prosen, T. & Prelovšek, P. Many-body localization in the Heisenberg XXZ magnet in a random field. *Phys. Rev. B* **77,** 064426 (2008).

212. Žnidarič, M., Scardicchio, A. & Varma, V. K. Diffusive and Subdiffusive Spin Transport in the Ergodic Phase of a Many-Body Localizable System. *Phys. Rev. Lett.* **117,** 040601 (2016).

213. Zotos, X., Naef, F. & Prelovšek, P. Transport and conservation laws. *Phys. Rev. B* **55,** 11029–11032 (1997).

214. Zwolak, M. & Vidal, G. Mixed-state dynamics in one-dimensional quantum lattice systems: A time-dependent superoperator renormalization algorithm. *Phys. Rev. Lett.* **93,** 207205 (2004).

COLOPHON

This document was typeset using the typographical look-and-feel `classicthesis` developed by André Miede. The style was inspired by Robert Bringhurst's seminal book on typography "*The Elements of Typographic Style*". `classicthesis` is available for both LaTeX and LyX:

https://bitbucket.org/amiede/classicthesis/

Happy users of `classicthesis` usually send a real postcard to the author, a collection of postcards received so far is featured here:

http://postcards.miede.de/

Final Version as of 31st January 2019 (`classicthesis` version 7.0).